ADVERTIMENT. L'accés als continguts d'aquesta tesi queda condicionat a l'acceptació de les condicions d'ús establertes per la següent llicència Creative Commons: 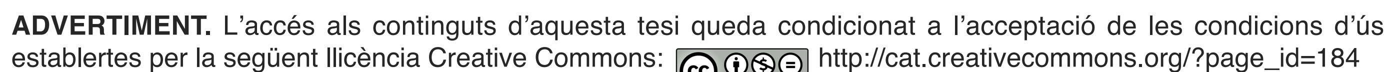 http://cat.creativecommons.org/?page_id=184

ADVERTENCIA. El acceso a los contenidos de esta tesis queda condicionado a la aceptación de las condiciones de uso establecidas por la siguiente licencia Creative Commons: http://es.creativecommons.org/blog/licencias/

WARNING. The access to the contents of this doctoral thesis it is limited to the acceptance of the use conditions set by the following Creative Commons license: 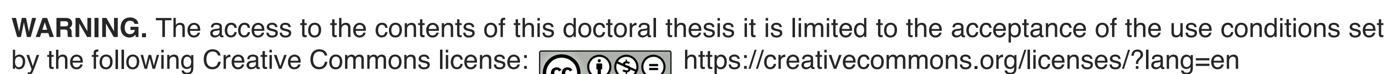 https://creativecommons.org/licenses/?lang=en

Growth and Optical Characterization of Strain-Engineered Semiconductor Nanostructures

Alessandro Bernardi

Director: Dr. Maria Isabel Alonso
Co-director: Prof. Alejandro R. Goñi
Tutor: Prof. Jordi Pascual

PhD Thesis

Doctorado en Ciencia de Materiales
Departamento de Física

2015

Ai miei genitori

Abstract

In this work we explored different pathways to exploit the strain stored into nanoscale layers of materials as a driving force to self-assemble 3D structures.

In particular, we have studied the epitaxial growth of self-assembled Ge quantum dots when a submonolayer of carbon is deposited prior to the growth of the dots. Using atomic-force microscopy combined with RHEED and optical techniques like Raman scattering and ellipsometry, we performed a systematic study of the role played by thermally activated Si interdiffusion and the composition of the wetting layer on dot density and morphology. The results give experimental evidence of a kinetically limited growth mechanism in which Ge adatom mobility is determined by chemical interactions among C, Si, and Ge. We suggest a two-stage growth procedure for fine-tuning the dot topography (density, shape and size), useful for possible optoelectronic applications.

Moreover we investigated the dynamics of strain relaxation during the capping of islands, which is useful for engineering devices based on multistacks of quantum dots. We also analysed the evolution of Ge nanostructures grown by combining nanostenciling and pulsed laser deposition, as a promising approach for the parallel patterning of semiconductor nanostructures for optoelectronics.

Apart from the growth of 3D islands, we applied strain-driven engineering to release rolled-up microtubes, obtained from strained semiconductor heterostructures. Through micro-Raman spectroscopy we were able to determine the residual strain, which results in a frequency shift of phonon modes measured on the tube as compared with reference unstrained material. We developed a simple elastic model to describe the measured phonon-frequency shifts, from which we estimate the strain status of the microtube. Results demonstrate the power of Raman spectroscopy as a diagnostic tool for engineering of strain-driven self-positioning microelectromechanical systems.

We tested the potential application of this rolled-up nanotechnology to obtain a lab-in-a-tube device where light is used as a biochemical sensor. We fabricated rolled up microtubes consisting of Si/SiO_x integrated on a Si chip and we analysed their properties to use them as a refractometric sensor. An aqueous sugar solution was inserted into the microtube, which leads to a change in refractive index and, as a result, to a detectable spectral shift of the whispering gallery modes. This prototype proved that the monolithic on-chip integration of strain-engineered microtubes is a promising approach to design optofluidic channels for lab-on-a-chip applications.

Contents

1 Introduction 7

2 Results and Discussion 9

2.1 Self-assembling of Carbon-induced Germanium quantum dots 9

2.1.1 Effect of silicon interdiffusion on thermally activated wetting layers 10

2.1.2 Growth dynamics on SiGe strained layers and fine tuning of island density 11

2.1.3 Morphology, strain and composition during capping of dots 13

COMPENDIUM ARTICLES 17

2.2 Growth and characterization of SiGe nanostructures 19

2.2.1 Raman characterization of SiGe dots under high pressure 19

CORE RESEARCH ARTICLES 21

2.2.2 SiGe alloys: measurement of phonon strain-shift coefficients 23

COMPLEMENTARY ARTICLES 25

2.2.3 Multilayers of Ge quantum dots 27

COMPLEMENTARY ARTICLES 29

2.2.4 Ge nanostructures via PLD nanostencilling 31

CORE RESEARCH ARTICLE 33

COMPLEMENTARY ARTICLE 35

2.2.5 Optical characterization of Ge nanocrystals 37

COMPLEMENTARY ARTICLES 39

2.3 Rolled-up semiconductor microtubes 41

2.3.1 Probing strain in microtubes by micro-Raman spectroscopy 42

2.3.2 Lab-in-a-tube: on-chip integration of an optical ring resonator for biochemical sensing 44

CORE RESEARCH ARTICLES 47

3 Conclusions 49

4 References 53

5 Acknowledgements 55

1 Introduction

Before you start reading this thesis, could you please raise your head for a second and take a look around you? There must be somebody typing on his last generation smartphone to send messages to the world at an incomparable speed of data processing. Samsung just unveiled [1] its 14-nanometer chipset powering the new Galaxy S6 that it said offers better battery life and performance. When compared to Samsung's 20-nanometer process technology, the new 14-nanometer process enables up to 20 percent higher speed, 35 percent less power consumption and 30 percent productivity gain.

We already have now in the market, as an industry standard, a nanoscale technology that at the beginning of this thesis appeared to be futuristic but that has been evolving pretty fast, in fact. In order to optimize production and scale devices to match the market requirements, the semiconductor engineers require deep know-how on surface science and ways to manipulate and characterize materials with nanometric precision.

The core research of this work focuses on self-assembling of strain-engineered semiconductor nanostructures, i.e. controlling the amount of strain stored in the materials as a driving force to release 3D structures, with the challenge to manipulate their positioning and direct integration on a chip. In addition to the bottom-up techniques, this thesis is highly oriented to the optical characterization and development of phenomenological models.

The optical characterization is used at first as a way to investigate the chemical composition and the strain distribution inside of the nanostructured systems. We demonstrate how optical mapping can be an excellent non-invasive probing tool to test integrated nanostructured semiconductor devices, as recently reported also for mapping of SiGe nanowires [2].

On the other hand, once a strain-engineered nanostructured device is fabricated, detectable variations of its optical properties can easily reveal subtle changes of the boundary conditions, making it possible to assemble a miniaturized sensor integrated on a semiconductor chip: a prototype of a so called Lab-on-a-chip.

In the next chapter of results and discussion, the papers published by the author of this thesis are organized in different thematic sections, covering the different areas of research and dealing with different types of strain-engineered nanostructured systems.

The core of the thesis deals with self-assembling of carbon induced Ge quantum dots by molecular beam epitaxy (2.1). Besides optimizing the preparation of materials, the growth dynamics have been investigated by *in situ* RHEED[1] and the

[1] Reflection High Energy Electron Diffraction

resulting morphology of nanostructures has been probed by AFM[2]. The use of impurities and stressors later inspired the work of some other research groups focusing on ordering of SiGe islands [3,4] and our results were presented in some recent reports on self-assembling of SiGe nanostructures [5,6]. The same growth technique, Molecular Beam Epitaxy, is used to deposit strained semiconductor multilayers that have been processed to release freestanding microtubes [7], with potential application as microfluidic devices and optical resonators (2.3). After our first prototype, the fabrication process evolved to permit the preparation of large arrays of multifunctional microtubes [8] and several futuristic applications of lab-in-a-tube [9,10,11,12,13,14] were discussed. Apart from the strain-engineered processing, the optical characterization (mainly Raman Spectroscopy) of the microtubes is also an important contribution to this thesis work. Our original approach, combining elastic models with the phonon strain-shift theory, has been reviewed as a technique to study the mechanical behaviour of microdevices [15] and nanostructures [16,17,18,19,20,21].

Elastic strain plays a key role in the growth dynamics and optical properties of a number of other semiconductor nanostructures, which have been fabricated or characterized as a result of different collaborations, emerged during this thesis. Defining good measurement protocols for the determination of strain and composition of SiGe nanostructures was crucial for this work and it has been still a challenge in several other experiments following up [22]. Our results provide useful insights for potential application in optoelectronic and nanocalorimetry of some interesting strain-engineered semiconductor nanostructures, ranging from strained epitaxial SiGe alloys (2.2.2), multistacks of quantum dots (1.1.1), Ge nanostructures on patterned substrates (2.2.4) and crystallized Ge nanocrystals (2.2.5).

Within the different works presented, there is a hierarchy that can be summarized like this:

A. **COMPENDIUM ARTICLES**: work officially presented for this thesis and approved by the scientific doctorate committee to be the constituent of the compendium.

B. **CORE RESEARCH ARTICLES**: papers collecting the main results of the research conducted during the doctorate, directly related with the compendium articles and in which the author of this thesis has a leading role conducting experiments and discussing results.

C. **COMPLEMENTARY ARTICLES**: other works which are fruit of different scientific collaborations in which the author of this thesis has a secondary role, generally restricted to the growth and optical characterization of samples.

[2] Atomic Force Microscopy

2 Results and Discussion

2.1 Self-assembling of Carbon-induced Germanium quantum dots

Size, density, shape uniformity, and ordering of quantum dots QDs are crucial parameters when self-assembling is considered for applications in optoelectronic devices. In recent years, different smart strategies have been proposed to address the problem of dot engineering. Increase of dot density at very low substrate temperatures and/or high deposition rates is a well-established technique but in most cases it is not of practical interest for applications due to the degradation of crystalline quality. Perfect position control keeping high quality of dot ensembles can be achieved by means of artificially nanopatterned substrates. This approach is, however, less suitable for potential high surface and low cost applications. An alternative are spontaneous bottom up approaches such as the use of template layers to guide the selective nucleation of dots, which has demonstrated to be a good method to control the positioning of dots by inducing self-ordering processes during growth. A strain-driven instability in SiGe/Si(001) pseudomorphic layers leads to the formation of periodic surface undulations ripples acting as a natural template pattern that can be controlled by thickness, composition, and selection of vicinal Si(001) surfaces. Other routes include Ge deposition on relaxed SiGe/Si buffer layers and deposition on buried dislocation networks. Another relevant bottom up strategy towards efficient dot engineering involves surface modification through deposition of sub monolayer amounts of impurities that can reduce the diffusion length i.e., enhancing dot density and altering the energetics of nucleation.

In this work we focused our attention on the growth of carbon-induced QDs, getting insight into the surface processes which are relevant at the stage of island nucleation. Up to now the C-induced growth of Ge quantum dots (C-QDs) has been discussed in terms of a single-stage process determined by growth parameters like substrate temperature and amount of C. In that way, it is not possible to experimentally decouple different phenomena that take place at the same time, namely silicon incorporation in the QDs and kinetic aspects of the 3D growth. Here we aimed at putting in evidence the previously ignored role of silicon interdiffusion. Based on experimental observation we propose a mechanism of growth where enhanced lattice mismatch, limited kinetic conditions and chemical interaction altogether contribute to complete an overall picture of the processes involved in C-induced growth.

In order to fully understand the growth dynamics we present results grouped in three scenarios:

- Self-assembling of dots on top of Ge wetting layers (WLs) grown at different temperatures, where the intermixing with the silicon substrate plays a crucial role (2.1.1).

- Growth of dots on top of strained SiGe layers of different composition. This case is somehow reproducing conditions similar to those of the deposition on top of an intermixed WL, but with the possibility to better control the chemistry at the surface. This approach represents a possible strategy for engineering and tuning dots size and density (2.1.2).

- Capping Ge dots with silicon affects the chemical composition of the islands and their strain status. On one side we follow the pathway of strain-relaxation driving the self-assembling of dots (with and without carbon) and on the other side, after capping, we observe partial recompression and variable silicon interdiffusion depending on the morphological characteristics of the islands. 3D growth and silicon intermixing are competitive mechanisms to relief the built-in strain and our results shed some light on how to engineer capped dot devices and multistacks of strained nanostructures (2.1.3).

2.1.1 Effect of silicon interdiffusion on thermally activated wetting layers

A set of samples was prepared by solid-source molecular beam epitaxy, always according to the following procedure: after oxide desorption at 900 °C and 50 nm thick Si buffer layer deposition, a 3.7 Å thick Ge WL was grown at given fixed temperature T_{WL} ranging from 330 to 750 °C. Subsequently, the temperature was stabilized to 500 °C before depositing 0.1 monolayers (MLs) of carbon from a calibrated sublimation filament. Finally, keeping the temperature fixed at 500 °C for all samples, a top 5.8 Å thick layer of Ge was grown, leading to almost instantaneous formation of self-assembled C-QDs without reaching the typical critical thickness for the conventional 2D–3D growth mode transition which occurs in the absence of carbon. The growth was monitored in situ by RHEED and the island topography was studied ex situ by AFM.

In order to evaluate the composition and residual strain, samples were characterized by optical measurements at room temperature. Raman spectroscopy was carried out with the 514.5 nm line of an Ar-ion laser for excitation. Light was focused onto the sample with a spot size of about 1 μm and a laser power of 4 mW. In order to suppress contributions from second-order processes, we used the scattering geometry $z(xy)\bar{z}$, where x, y and z are the [100], [010] and [001] crystallographic directions, respectively. The ellipsometric spectra were collected using a rotating polarizer ellipsometer in the 1.4–4.8 eV spectral range.

The main original results of this work can be summarized in the following points:

- Increasing only the deposition temperature of the Ge WL leads to gradually higher QD densities, in apparent contradiction with what is well established in literature, where maximum dot densities are generally obtained in low growth temperature processes

- Since we kept the substrate temperature always fixed to 500 ºC during the QD nucleation stage, we exclude any Arrhenius-type of kinetic dependence on temperature of Ge adatom mobility. Then, the observed topography strictly reflects the intrinsic characteristics of the surface material. A change in the growth temperature during the WL deposition can be related to the amount of silicon incorporated in the Ge overlayers.

- Data obtained from Raman and spectroscopic ellipsometry are consistent: the material constituting the QDs is nearly pure Ge and the amount of silicon intermixed in the islands goes up to 10% when increasing the T_{WL} from 330 ºC to 750 ºC. For the highest temperature we estimate a large Si content in the WL, around 75%.

- A clear correlation between topographic features and Si intermixing can be inferred. Increasing temperature favours Si interdiffusion in the nominally pure Ge WL and eventually in the QD layer, until a saturation value is reached due to Ge overgrowth. The QD density follows the same trend with a maximum saturation density in this experiment one order of magnitude lower (8.0×10^9 islands/cm^2) than for growth of C-QDs on bare Si(001).

- The presence of a certain amount of Si in the WL due to thermally activated interdiffusion could contribute to partially stabilize carbon on top surface layers, considering that Si–C bonds are much more stable than Ge–C ones. From this perspective a higher growth temperature TW_L means a higher Si content in the WL. Consequently, C can arrange in metastable surface reconstruction patches, which are responsible for the decrease of adatom mobility, thus explaining the observed increase in dot density.

- By close inspection of the C-QD topography we found out that even the smallest islands are all dome-shaped with no evidence of flatter pyramid-like dots (with aspect ratio <0.10). The main effect of carbon predeposition is to shrink the in-plane lattice parameter because of C-rich patches formed on the surface. The resulting enhancement of the lattice mismatch is responsible for the growth-mode change from Stranski–Krastanow to Volmer–Weber. In fact, our RHEED observations suggest the onset of islanding when we start Ge growth immediately after the C-submonolayer deposition, even if the WL thickness is subcritical.

- The presence of carbon also affects the energetics of the pyramid–dome shape transition. The main reason for the reduction of the critical volume for the appearance of dome-shaped islands is the locally enhanced lattice misfit.

2.1.2 Growth dynamics on SiGe strained layers and fine tuning of island density

We present a different route for manipulating Ge island self-assembling based on the combination of epitaxial growth on strained SiGe buffer layers and carbon

predeposition. Inspired by the results on the influence of Si interdiffusion (2.1.1) and the Ge–C repulsive interaction on the resulting Ge dot topography we make use of the effect that a submonolayer deposition of C has on the Ge adatom diffusion. Our results point to a reduction by two orders of magnitude of dot density with increasing Ge content in the buffer layer.

A thin strained $Si_{1-x}Ge_x$ buffer layer with Ge composition (x) ranging from 0% to 60% was deposited on a silicon substrate at 400 °C. For all the samples the SiGe buffer layer thickness remained below the limit of metastability, preventing three-dimensional nucleation of SiGe quantum dots, as confirmed by in situ RHEED monitoring. The temperature was then raised and maintained at 500 °C during the deposition of 0.1 ML of carbon by a sublimation filament and the subsequent evaporation of 6 Å of Ge at a fixed growth rate of 0.04 Å/s, leading to self-assembling of quantum dots. The growth was monitored in situ by RHEED using 20 keV electrons and a CCD camera to record the diffraction pattern displayed on a phosphor screen.

The main original results of this work can be summarized in the following points:

- The first striking result of this work concerns the observed tendency of the dot density which exhibits a significant, monotonous decrease by two orders of magnitude with increasing Ge content in the buffer layer from 0% up to 60% whereas the interdot separation (λ) increases. Our results follow a trend which is exactly the opposite of what we could expect if the nucleation of dots was driven by morphological instabilities (ripples) or induced by the average roughness of a Ge rich strained layer. In order to explain our experimental findings we need to take into account the effects of the submonolayer of carbon.

- We propose a mechanism by which the chemical interactions among Si, Ge, and C drive the growth process. The Si–C attractive interaction favors C condensation, leading to the appearance of c(4×4) reconstruction patches also associated with an enhanced surface roughness. If the carbon is deposited on a layer containing Ge, the Ge–C repulsion induces phase separation and, depending on Ge content, the C-induced reconstruction patches become increasingly fragmented, being the C atoms progressively incorporated at random sites in the film. The key point is that the formation of the reconstruction patches produces a significant quenching of the Ge adatom diffusion, which within the kinetic model implies the self-assembled growth of a high density of Ge dots. With increasing Ge content of the buffer layer the C-induced patches gradually disappear, the surface roughness diminishes, and the Ge adatom diffusivity becomes enhanced, resulting in lower dot densities.

- The RHEED patterns collected *in situ* reveal interesting insights about the growth dynamics. Monitoring the intensity of the 3D spotty pattern and simultaneously extracting the distance between streaks (or spots) it is possible to quantify the strain relaxation associated to the dot growth, which appears to take place from the very beginning of the dot growth. The

evolution of Ge dots on C-alloyed strained SiGe surfaces proceeds via a Volmer-Weber mode, similarly to the case (2.1.1) of C-induced Ge dots on Si(001).

- When the Ge deposition starts we detect a certain delay of time before the appearance of a spotty pattern: this observation is consistent with the estimated critical volume required for RHEED detection of a 3D cluster, in the range of 0.5-7× 10^3 nm^3 with increasing Ge content in the buffer layer. The obtained values match with the sizes of the smallest dome-shaped islands determined from AFM images.

2.1.3 Morphology, strain and composition during capping of dots

In the present work we describe an experimentally observed growth mode change from Stranski–Krastanow (SK) in the absence of C to Volmer–Weber (VW) when depositing Ge on a C-enriched Si substrate. The evolution of the surface lattice parameter is followed up to large Ge coverage where both elastic and plastic mechanisms of relaxation are active. We also study the process of capping the islands with silicon to understand how it affects the final composition and the elastic recompression of the dots. Finally, we also focus on the structural properties of the cap layer and obtain evidence of the existence of compressive stress induced by local strain fields associated with carbon-rich patches.

Samples under investigation were prepared by solid-source molecular beam epitaxy. After oxide desorption at 900 °C and 100 nm thick Si buffer layer deposition, the substrate temperature was set to 500 °C. Subsequently, ~0.1 monolayers (MLs) of carbon were predeposited on the Si surface from a calibrated sublimation filament. The self-assembling of carbon-induced quantum dots (C-QDs) was achieved by evaporation of 12 MLs of Ge. A reference sample was prepared following exactly the same growth procedure as above, but omitting the step of carbon predeposition. As a result standard Stranski–Krastanow quantum dots (SK QDs) were obtained. Finally, part of the surface of the samples was capped with a 10 nm thick Si layer deposited at 300 °C, in order not to alter the shape of buried dots. Growth was monitored in situ by RHEED and the island topography was studied ex situ by AFM.

By using complementary surface science tools we were able to study different aspects of the growth of strained Ge/Si islands. RHEED was used to *in situ* monitor the evolution of the *in-plane* lattice parameter, allowing us to determine the set in of strain relaxation due to nucleation of 3D clusters. In the absence of C, we observed the formation of a flat 2D wetting layer (WL), taking place before the gain in elastic energy becomes dominant over the energetic term associated with the increase of surface (SK growth). In this case, the first stage of island growth accounts for the relaxation of less than 50% of the lattice mismatch and it can be attributed to the nucleation of small and shallow pyramids. When the islands get bigger, they transform into domes or dislocated Ge clusters that can relax the

strain more efficiently, so that after 10 MLs of coverage we already measure a lattice parameter approaching the value of bulk Ge.

The strain-relaxation pathway changes quite dramatically when carbon is used to engineer the dot topography. In this case, the presence of carbon-rich patches and the repulsive Ge–C interaction prevent the formation of a WL, i.e., it is energetically more convenient to increase the Ge surface with nucleation of 3D clusters, rather than wetting the carbon-alloyed surface. As a result, the lattice parameter relaxation associated with the 3D nucleation can be observed starting from the very first stages of Ge deposition, which is experimental evidence of the growth mode change from Stranski–Krastanow to Volmer–Weber. In the case of C-QDs, we do not observe two regimes of strain relaxation (shallow and steeper islands) but a continuous progressive evolution of the lattice parameter, and this observation is consistent with the AFM topography characterized only by dome-shaped clusters. The density of domes is exceptionally high ($\sim 10^{11}$ cm^{-2}) due to reduced mobility of Ge on a roughened carbon-alloyed surface.

The reduced surface diffusion that explains the high dot density is likely to be also responsible for the quenching of Si intermixing in the islands. Both island morphology and composition keep evolving while the growth or annealing proceeds. Intermixing dynamics is thought to be dominated by surface rather than bulk diffusion, especially at temperatures below 500 °C. Therefore, it is possible that in the presence of C, the process of Si intermixing is kinetically limited. Then, capped C-QDs are less intermixed and retain larger strain than SK-QDs, as experimentally observed. The limited intermixing as a partial strain-reliever and the presence of local inhomogeneous strain fields are both consistent with the extreme decrease of the critical volume for the pyramid-to-dome transition, to the point where only dome-shaped clusters can be observed.

As a result of the deposition of 12 MLs of Ge, the dots completely relax their strain towards their apex, as can be measured by RHEED probing the topmost atomic layers. Raman spectroscopy becomes a useful tool to study instead the average strain distribution inside the volume of the islands. The relevant question arising when evaluating the Raman results is to decide which is the adequate elastic model to describe the strain status of a quantum dot. Once we have measured the LO phonon frequency shift associated with the lattice deformation, in order to quantify the strain, we need to know the relation existing between the *in-plane* ($\epsilon_{\parallel}$) and *out-of-plane* ($\epsilon_{\perp}$) components. A tiny shallow island is somehow similar to a pseudomorphic 2D layer and its strain status is likely described by a biaxial model (i.e., the lattice is compressed in the *in-plane* direction and it is free to expand in the *out-of-plane* direction, according to Hooke's law). For steeper islands embedded in a matrix (capped dots), the strain status of dots can be rather described by a hydrostatic model ($\epsilon_{\perp} = \epsilon_{\parallel}$).

- According to the results the uncapped dots (both SK and C-QDs) retain only between 10% and 30% of the strain, depending on whether we consider a hydrostatic or biaxial model, respectively.

- After capping with a 10 nm thick Si layer, the islands are recompressed and we can clearly recognize in Raman spectra features corresponding to two contributions from portions of material with different composition and strain. The experimental piece of evidence is that we are probing regions of material with rather different structural properties; thus, it is unlikely that they refer to different portions of the same island. This argument leads us to ascribe the contributions to two separate families of islands: the smaller coherent islands are fully recompressed (according to the biaxial model) whereas the bigger relaxed domes are less affected by the thin cap layer.

- Raman spectroscopy turns out to be a powerful technique capable of pointing out the presence of local structural inhomogeneities of the quantum dots, complementing the information achieved by RHEED analysis. When probing dot ensembles most of the characterization tools are sensitive to the 3D clusters due to the grazing incidence geometry and shadowing (this is the case of RHEED) or for confinement of carriers in the islands and the absence of a signal collectable from the WL (like in Raman spectroscopy. In this context, ellipsometry provides unique information on the average strain field of the silicon cap layer, which indicates a local compressive strain in the regions between islands associated with the carbon-rich patches.

COMPENDIUM ARTICLES

Article n: 1

Authors: A. Bernardi, J. O. Ossó, M. I. Alonso, A. R. Goñi and M. Garriga

Title: Influence of Si interdiffusion on carbon-induced growth of Ge quantum dots: a strategy for tuning island density

Journal: Nanotechnology

Doi: 10.1088/0957-4484/17/10/026

Article n: 2

Authors: A. Bernardi, M. I. Alonso, A. R. Goñi, J. O. Ossó, and M. Garriga

Title: Density control on self-assembling of Ge islands using carbon-alloyed strained SiGe layers

Journal: Applied Physics Letters

Doi: 10.1063/1.2349317

Article n: 3

Authors: A. Bernardi, M.I. Alonso, A.R. Goñi, J.O. Ossó, M. Garriga

Title: Growth dynamics of C-induced Ge dots on $Si_{1-x}Ge_x$ strained layers

Journal: Surface Science

Doi: 10.1016/j.susc.2006.12.048

Article n: 4

Authors: A. Bernardi, M. I. Alonso, J. S. Reparaz, A. R. Goñi, P. D. Lacharmoise, J. O. Ossó and M. Garriga

Title: Evolution of strain and composition during growth and capping of Ge quantum dots with different morphologies

Journal: Nanotechnology

Doi: 10.1088/0957-4484/18/47/475401

INSTITUTE OF PHYSICS PUBLISHING NANOTECHNOLOGY

Nanotechnology **17** (2006) 2602–2608 doi:10.1088/0957-4484/17/10/026

Influence of Si interdiffusion on carbon-induced growth of Ge quantum dots: a strategy for tuning island density

A Bernardi, J O Ossó, M I Alonso, A R Goñi[1] and M Garriga

Institut de Ciència de Materials de Barcelona-CSIC, Esfera UAB, 08193 Bellaterra, Spain

E-mail: abernardi@icmab.es

Received 3 January 2006, in final form 14 February 2006
Published 28 April 2006
Online at stacks.iop.org/Nano/17/2602

Abstract
We have studied the epitaxial growth of self-assembled Ge quantum dots when a submonolayer of carbon is deposited on a Ge wetting layer (WL) prior to the growth of the dots. Using atomic-force microscopy combined with optical techniques like Raman and ellipsometry, we performed a systematic study of the role played by thermally activated Si interdiffusion on dot density, composition and morphology, by changing only the growth temperature T_{WL} of the WL. Strikingly, we observe that higher dot densities and a narrower size distribution are achieved by increasing the deposition temperature T_{WL}, i.e. by enhancing Si interdiffusion from the substrate. We suggest a two-stage growth procedure for fine tuning of dot topography (density, shape and size) useful for possible optoelectronic applications.

1. Introduction

Bottom-up approaches for the fabrication of nanostructures have attracted great interest in recent years, appearing as a viable path towards a new generation of nanotechnological devices [1]. Self-assembling of epitaxial germanium quantum dots (QDs) has been extensively studied in the last decade and fundamental physical processes governing heteroepitaxy have been described and modelled elegantly [2]. The next goal will be to attain full capability to tailor material properties and to modify the growth dynamics in order to match specific requirements, depending on the physical process one needs to exploit for a given field of application. In particular, the design of a new class of silicon-based optoelectronic devices [3] requires a high density of QDs with narrow size distribution. However, conventional self-assembling of Ge QDs on Si(001) leads to a bimodal distribution of island shapes and sizes [4, 5]. The addition of impurity atoms has been demonstrated [6–11] to be a valid option for modifying the growth mode and to produce more homogeneous ensembles of islands.

Several possible approaches have been explored by various research groups: one well established way for controlling morphology consists in predeposition of a surfactant like Sb [6], or alternative dopants like P [7] or B [8]. For instance, predeposition of carbon is an especially successful pathway [9–11]. All these cases share a lot of similarities in the growth dynamics: the addition of extremely low coverages of impurities leads to a significant increase of dot density and consequent reduction of average dot size. Previous experimental work evidenced the role of carbon in terms of reduction of the Ge diffusion length at the substrate surface, which is reflected in the increase of dot density. Direct observation of carbon-induced $c(4\times4)$ reconstruction on Si(001) surface [12] hints at a selective deposition of Ge in carbon-free regions in agreement with theoretical predictions which consider the repulsive interaction between Ge and C [13]. Carbon has been predeposited both on bare silicon substrates [12] and eventually on Ge wetting layers (WLs) [14], but, besides observing a systematic increase of dot density, no explanation has been yet proposed to understand why the addition of carbon directly to silicon leads to dot densities roughly one order of magnitude higher. Other basic questions on the kinetic evolution and on the thermodynamically favoured equilibrium shape of C-induced islands remain yet unanswered.

In this work we focused our attention on the growth of carbon-induced QDs, getting insight into the surface processes which are relevant at the stage of island nucleation. Up to now the C-induced growth of Ge quantum dots (C-QDs) has

[1] ICREA Research Professor.

been discussed in terms of a single-stage process determined by growth parameters like substrate temperature and amount of C [10, 11]. In that way, it is not possible to experimentally decouple different phenomena that take place at the same time, namely silicon incorporation in the QDs and kinetic aspects of the 3D growth. Here we aimed at putting in evidence of the previously ignored role of silicon interdiffusion. Based on experimental observation we propose a mechanism of growth where enhanced lattice mismatch, limited kinetic conditions and chemical interaction altogether contribute to complete an overall picture of the processes involved in C-induced growth.

We will show that the density of QDs increases when the WL has a higher Si content due to higher growth temperature T_{WL}. Carbon on a Si-rich surface can arrange in metastable reconstruction patches that reduce the adatom mobility, giving an increase of dot density. On a Ge-rich WL, such as obtained at lower T_{WL}, deposited C tends to be buried into deeper layers and have less influence on the adatom mobility, thus allowing the growth of larger and less dense islands.

2. Experimental details

A set of samples was prepared by solid-source molecular beam epitaxy, always according to the following procedure: after oxide desorption at 900 °C and 50 nm thick Si buffer layer deposition, a 3.7 Å thick Ge WL was grown at given fixed temperature T_{WL} ranging from 330 to 750 °C. Subsequently, the temperature was stabilized to 500 °C before depositing 0.1 monolayers (MLs) of carbon from a calibrated sublimation filament. Finally, keeping the temperature fixed at 500 °C for all samples, a top 5.8 Å thick layer of Ge was grown, leading to almost instantaneous formation of self-assembled C-QDs without reaching the typical critical thickness for the conventional 2D–3D growth mode transition which occurs in the absence of carbon. The growth was monitored *in situ* by reflection high energy electron diffraction (RHEED), and the island topography was studied *ex situ* by atomic force microscopy. In order to evaluate the composition and residual strain, samples were characterized by optical measurements at room temperature. Raman spectroscopy was carried out with the 514.5 nm line of an Ar-ion laser for excitation. Light was focused onto the sample with a spot size of about 1 μm and a laser power of 4 mW. In order to suppress contributions from second-order processes, we used the scattering geometry $z(xy)\bar{z}$, where x, y and z are the [100], [010] and [001] crystallographic directions, respectively. The ellipsometric spectra were collected using a rotating polarizer ellipsometer in the 1.4–4.8 eV spectral range.

3. Results

3.1. Topography by atomic force microscopy

Figure 1 shows the topographic images of three representative samples. In all cases the typically observed morphology is that of dome-shaped islands with not clear faceting, in agreement with published work [9–11] on carbon-induced Ge QDs. Nevertheless, quite a surprising behaviour can be pointed out: increasing only the deposition temperature of the Ge WL leads to gradually higher QD densities, in apparent contradiction with what is well established in literature, where maximum dot densities are generally obtained in low growth temperature processes [11, 14].

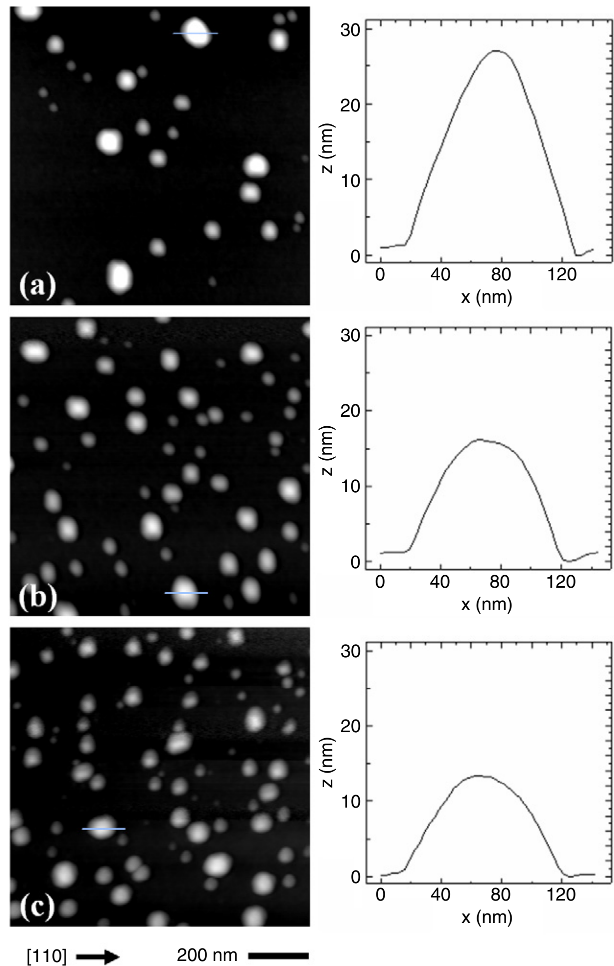

Figure 1. Topographic images (1 μm × 1 μm) of C-QDs obtained for different growth temperatures of the wetting layer (WL) at (a) 330 °C, (b) 400 °C and (c) 750 °C. The right-hand panels show representative island profiles of each image.

(This figure is in colour only in the electronic version)

Since we kept the substrate temperature always fixed to 500 °C during the QD nucleation stage, we exclude any Arrhenius-type of kinetic dependence on temperature of Ge adatom mobility. Then, the observed topography strictly reflects the intrinsic characteristics of the surface material. A change in the growth temperature during the WL deposition can be related to the amount of silicon incorporated in the Ge overlayers; in order to explain the observed topographic changes, interdiffusion processes need to be taken into account. The questions arising about the correlation of the dot density with the composition of the QDs will be addressed by optical characterization techniques in the following sections.

3.2. Raman spectroscopy

Raman spectroscopy has been demonstrated to be a surface-sensitive technique that is useful for extracting information about composition and strain inside the QDs [15]. From the

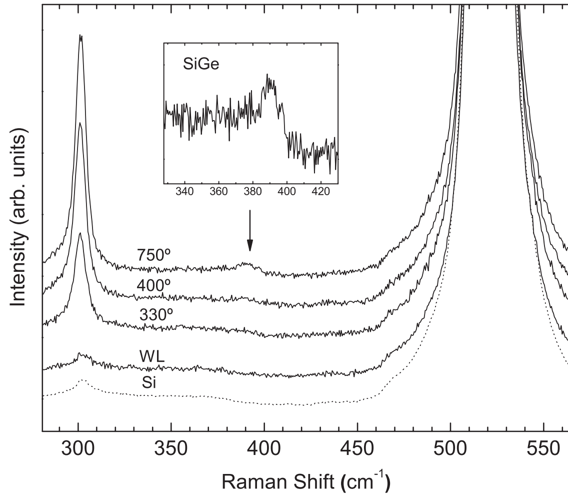

Figure 2. Raman spectra of C-QD samples obtained for different T_{WL} and compared with the spectra of the substrate (dotted line) and a reference sample having only a Ge WL. The fingerprints of the QDs are the Ge–Ge peak at 301.3 cm^{-1} and a much weaker Si–Ge phonon mode (see the inset). The intensity is normalized to that of the strong Si phonon mode of the substrate. The spectra are vertically shifted for clarity.

Raman spectra shown in figure 2, we can extract the following information.

- Apart from the strong silicon peak at 520.5 cm^{-1} coming from the LO phonon mode of the substrate, a Ge–Ge vibration peak can be detected at 301.3 cm^{-1}. In contrast, the spectrum of a reference sample, where only the thin Ge WL at 750 °C was deposited, exhibits a small peak in the 300 cm^{-1} range, which is attributed because of its shape and intensity to the residual second-order 2TA phonon feature, also detectable in the silicon substrate. We conclude that the Ge–Ge phonon mode observed in the different samples can be ascribed to scattering only from the QDs without contribution of the WLs.
- In the 400 cm^{-1} range, it is possible to resolve a peak at ∼390 cm^{-1} (see inset to figure 2) for the sample corresponding to the highest temperature (T_{WL} = 750 °C) for the WL growth stage. This peak is attributed to the Si–Ge phonon mode and its presence hints at interdiffusion of silicon through the WL into the QDs. The spectral positions (in cm^{-1}) of the Ge–Ge and Si–Ge peaks allow us to extract the composition (x) of the $Si_{1-x}Ge_x$ alloy and the *in-plane* strain ($\epsilon_\parallel$) by applying the empirical relations [15]

$$\omega_{Ge-Ge} = 284 + 5x + 12x^2 + b_{Ge-Ge}\,\epsilon_\parallel, \quad (1)$$

$$\omega_{Si-Ge} = 400 + 29x - 95x^2 + 213x^3 - 170x^4 + b_{Si-Ge}\,\epsilon_\parallel. \quad (2)$$

Using the phonon strain-shift coefficients $b_{Ge-Ge} = -400$ cm^{-1} and $b_{Si-Ge} = -575$ cm^{-1} determined by Tan *et al* [16] for Ge-rich self-assembled QDs, for T_{WL} = 750 °C we obtain from equations (1) and (2) a Ge composition of $x_{Ge} = 0.94 \pm 0.02$ and a compressive strain equal to $\epsilon_\parallel \approx -0.5 \pm 0.2\%$ (errors are estimated considering the dispersion of strain-shift coefficients found in literature [17]). For T_{WL} < 750 °C, the Si–Ge peak cannot be resolved, indicating an even higher Ge content in QDs. Therefore, for a quantitative determination of composition from just the Ge–Ge peak an assumption about the strain of the islands is required. Since the measured frequency of the Ge–Ge phonon mode is the same for all the samples (301.3 cm^{-1}), our interpretation is that small variations of composition, if any, induce shifts that are easily compensated by slightly different degrees of strain relaxation. Just for an estimation, it is reasonable to expect that for T_{WL} = 330 °C the Si interdiffusion process is completely quenched, i.e. the overgrown QDs are almost of pure Ge. Consequently, evaluating the strain from equation (1), we obtain $\epsilon_\parallel \approx -0.1 \pm 0.2\%$. In other words, bigger islands obtained at lower T_{WL} are found to be more relaxed than smaller domes, in agreement with the expected strain-dependent scaling of QD size [18].

- Another remarkable feature of the collected spectra concerns the different intensities of the Ge–Ge peaks, even though the amount of Ge deposited is the same for all the samples. This can be understood by taking into account Raman resonance effects. In fact, the incident laser light has an energy of 2.414 eV quite close to the E_1 electronic interband transition in $Si_{1-x}Ge_x$. An increase of Ge content in the islands causes a redshift of the electronic transition with the consequent progressive loss of the resonance condition. Thus, the observed reduction in intensity for decreasing T_{WL} is consistent with the expected Ge enrichment of the islands.

3.3. Spectroscopic ellipsometry

Spectroscopic ellipsometry *ex situ* represents a powerful diagnostic tool to probe extremely thin layers of Ge on a Si substrate. By measuring the complex reflectance ratio $\rho = \tan\psi e^{i\Delta}$ it is possible to determine the effective thickness of the deposited material and to extract its dielectric function with an accurate fitting procedure and inversion algorithm, as discussed elsewhere [15]. In figure 3 we compare the spectra obtained from the QD samples with the dielectric function of a silicon substrate for reference. The presence of the Ge epilayers, apart from causing a change in intensity of the E_1 and E_2 electronic transitions of the substrate (corresponding to the two main peaks in figure 3), yields a contribution apparent as a low-energy shoulder. It corresponds to interband electronic transitions E_1 and $E_1 + \Delta_1$ present in Ge-rich alloys. These transitions can only be resolved by taking the second derivative of the calculated dielectric functions, depicted in the inset to figure 3. Fitted energies range from E_1 = 2.149 eV and $E_1 + \Delta_1$ = 2.401 eV for T_{WL} = 330 °C to E_1 = 2.254 eV and $E_1 + \Delta_1$ = 2.498 eV for T_{WL} = 750 °C. From the known energy shift as a function of composition [15] it is possible to obtain quantitative information about the average Si content. The material constituting the QDs is nearly pure Ge and the amount of silicon intermixed in the islands goes up to 10% when increasing T_{WL} from 330 to 750 °C. We could not determine the composition of the thin WLs with enough accuracy but the ellipsometry spectra of reference WLs indicate much higher Si contents than in the QD samples. For the highest temperature (T_{WL} = 750 °C) we estimate a large Si content in the WL, around 75%.

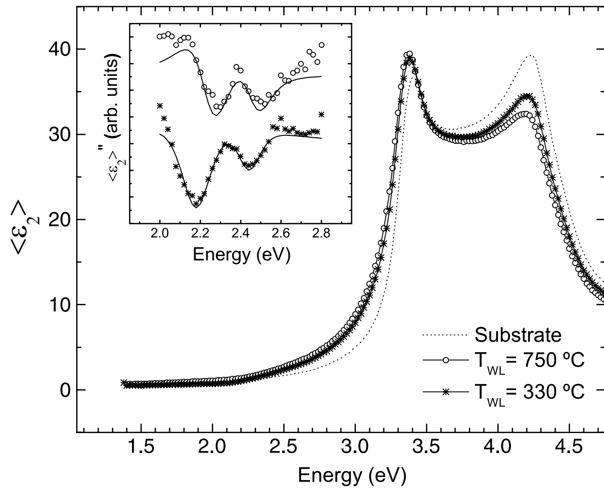

Figure 3. Ellipsometry spectra of C-QDs displayed as the imaginary part of the dielectric function for samples with different T_{WL} compared to the spectrum of a silicon substrate. The contribution of the Ge dots arises in the spectral range around 2.5 eV. The inset shows second derivative spectra with respect to energy, from which the contributing electronic transitions can be extracted.

The compositions of QDs obtained from spectroscopic ellipsometry are consistent with the Raman results. The excitation energy used for the Raman measurements (λ = 514 nm, corresponding to 2.414 eV) falls just between the Ge-like interband transitions observed in ellipsometry for T_{WL} = 750 °C, for which maximum resonance is then expected. With decreasing T_{WL} the energies of these optical transitions shift to the red, in good agreement with the gradual loss of the resonance condition, and the Ge–Ge Raman peak becomes weaker. We point out that this behaviour of the optical transition energies and, thus, of the Raman resonance cannot be explained in terms of quantum confinement effects [19]. Although the average dot size depends on T_{WL} through the dot density (see figure 1), the typical dimensions of dots are not small enough to ascribe the observed interband energy shifts to changes in confinement. In conclusion, both Raman and ellipsometry experiments give clear evidence of Si intermixing in the Ge QDs with increasing growth temperature T_{WL} of the wetting layer.

4. Discussion

4.1. Interdiffusion and dot density

In the previous sections we have shown that depending on the WL growth temperature different dot densities can be achieved. Islands are found to have very high Ge contents and are characterized by almost total strain relaxation. In figure 4 we summarize the dependence on WL growth temperature T_{WL} of both the dot density obtained from AFM images and the QD Si composition fitted from ellipsometry. The error bars in the island density reflect the dispersion in analysis of several AFM images for each sample, at different spots and imaged areas. The uncertainties of the compositions are calculated from the errors of the fitted E_1 energies. A clear correlation between topographic features and Si intermixing can be inferred. Increasing temperature favours Si interdiffusion in the nominally Ge WL and eventually in the QD layer, until a saturation value is reached due to Ge overgrowth, as predicted by atomic-scale simulations [20]. The QD density follows the same trend with a maximum saturation density in this experiment one order of magnitude lower than for growth of C-QDs on bare Si(001).

The obtained relationship between dot density and composition is a striking result, since an increase of Si content in the WL is conventionally associated with a lower density, leading to bigger lateral size of dome-shaped islands due to the composition dependence of the critical volume [21] for the pyramid-to-dome shape transition (this aspect will be discussed in more detail below). On the contrary, we observe that the QD density as well as the Si content increases with higher deposition temperature. Under such conditions the average lateral size of the islands is minimized, tending to the limiting case of deposition of C-QDs on bare Si(001). Our results point to a more pronounced instability of carbon atoms on the surface of predeposited Ge WL in relation with its silicon content.

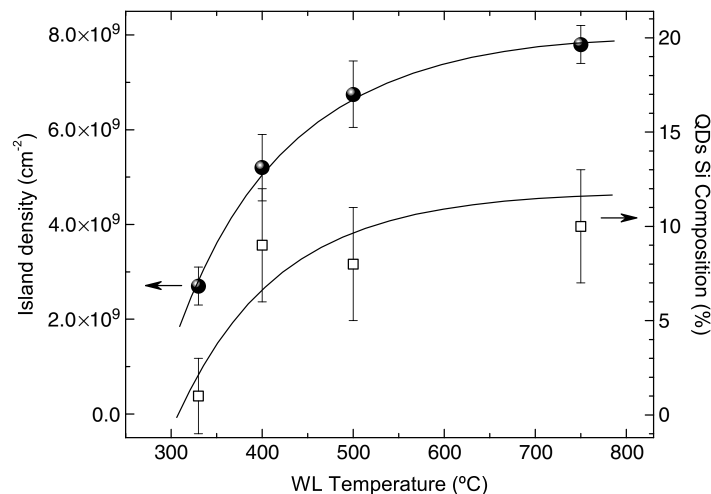

Figure 4. Island density and average silicon content of the QDs versus growth temperature of the wetting layer. The composition is obtained from ellipsometric data. The curves are a guide to the eye.

Carbon is known [12] to cause stable $c(4 \times 4)$ reconstruction patches on a Si(001) surface, and the presence of these carbon-rich regions causes a reduction of surface diffusion length of Ge, leading to an increased dot density in a kinetically self-limited growth regime. Reduced surface adatom mobility can be compensated by raising the growth temperature at the moment when the nucleation of islands sets in. This explains the previously established dependence [11, 14], where at high temperature the lateral size of the QDs increases at the expenses of dot density. However, these experiments could not distinguish between pure temperature-induced kinetic effects and other factors dealing with surface energetics related to composition and strain. By keeping the temperature during the nucleation stage of C-QDs fixed at 500 °C but varying only the growth temperature of the subcritical wetting layer, we succeeded in distinguishing between the different superficial phenomena taking place during island nucleation, whose effects are reflected in the dot topography.

In the case of C predeposition on Si(001) substrates no consensus has been reached yet on the microscopic understanding of the observed $c(4 \times 4)$ reconstruction [22]. However, *ab initio* calculations and Monte Carlo simulations [23] shed some light on the fundamental consequences of the presence of low amounts of carbon: despite the great lattice mismatch, impurity atoms occupy equilibrium substitutional sites in close proximity to the surface, forming Si–C bonds. In the case of coverage with Ge, it was predicted that due to the repulsive chemical interaction between Ge and C [13], carbon atoms are forced into deeper layers. Applying this scenario to C deposition on a Ge surface, it is reasonable to expect that C is unstable on top surface layers, as buried occupation sites the equilibrium configuration. The presence of a certain amount of Si in the WL due to thermally activated interdiffusion could contribute to partially stabilize carbon on top surface layers, considering that Si–C bonds are much more stable than Ge–C ones [13]. From this perspective a higher growth temperature T_{WL} means a higher Si content in the WL. Consequently, C can arrange in metastable surface reconstruction patches which are responsible for the decrease of adatom mobility, thus explaining the observed increase in dot density. In contrast, at low temperature no significant Si interdiffusion occurs and the deposited C is buried, possibly down to the interface with the Si substrate, contributing merely to an overall modulation of the strain field.

4.2. Thermodynamics of island growth

By close inspection of the C-QD topography (see section 3.1) we found out that even the smallest islands are all dome-shaped with no evidence of flatter pyramid-like dots. In figure 5 we display the measured aspect ratios for islands of different sizes in our samples. For comparison the conventional growth pathway [24, 25] in the absence of carbon is sketched by arrows. Smaller islands are generally shallow pyramids with low aspect ratio (⩽0.10) until a critical volume is reached and a shape transition to domes with higher aspect ratio occurs. The dome-shaped geometry turns out to be energetically favourable when the increase of surface energy is compensated by the possibility to minimize the elastic energy stored inside the island. As discussed above, C-QD nucleation occurs in a

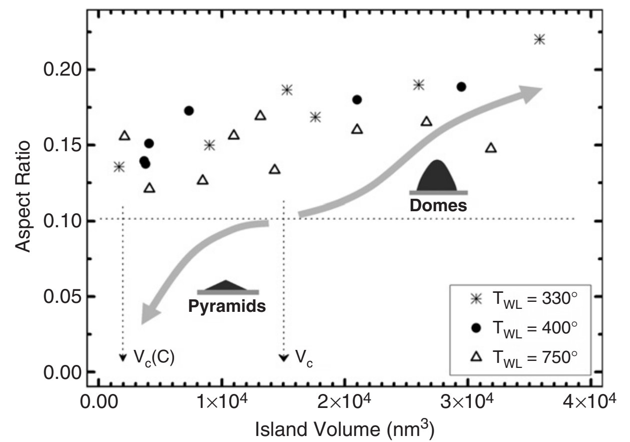

Figure 5. Aspect ratio (height over the square root of the basis area) versus island volume for samples with three different T_{WL} values. The dashed arrows indicate critical volumes V_c and $V_c(C)$ for pyramid–dome transition in the absence or presence of predeposited carbon, respectively.

kinetically limited growth regime also confirmed by the fact that dots do not exhibit clear faceting. Nevertheless, the absence of shallow islands in principle cannot be explained only in terms of simple kinetic considerations but implies important changes on the surface thermodynamics.

The main effect of carbon predeposition is to shrink the in-plane lattice parameter because of C-rich patches formed on the surface [12]. Such in-plane surface relaxation is possible in submonolayer coverages such as that used here. The resulting enhancement of the lattice mismatch is responsible for the growth-mode change from Stranski–Krastanow to Volmer–Weber [26] observed on C-alloyed bare Si substrates [12]. In our case RHEED observations suggest the onset of islanding when we start Ge growth immediately after the C-submonolayer deposition. This happens even if the WL thickness is subcritical. Thus, the growth mode cannot be described as Stranski–Krastanow. More detailed RHEED experiments are underway to clarify this point, and the results will be published elsewhere. Apart from the alteration of the elastic energy term, carbon can lead to a modification of the surface energy and, as suggested recently [27], the dependence of surface energy with strain should also be taken into account. Some preliminary quantitative evaluations are possible considering that the free energy of an island with facets having an inclination α can be parameterized as a function of volume (V) and lattice misfit (ϵ) [4] as

$$\Delta F\,(V, \alpha, \epsilon) = -K\epsilon^2 V\alpha + \Gamma V^{\frac{2}{3}}\alpha^{\frac{4}{3}}, \tag{3}$$

where the first term represents the elastic energy relief (K includes the elastic properties of the material) and the second term accounts for the energy increase due to the additional surface of the dots (Γ contains the surface tension). A shape transition from shallow facets ($\alpha = 11°$ for pyramids) to steeper ones ($\alpha' = 25°$ for domes) occurs when the two shapes are degenerate in energy at the critical dot volume V_c obtained from (3)

$$V_c = \left(\frac{\Gamma'\alpha'^{\frac{4}{3}} - \Gamma\alpha^{\frac{4}{3}}}{\alpha' - \alpha}\right)\frac{1}{K^3\epsilon^6}. \tag{4}$$

Assuming that for low carbon coverage the mechanical properties and the superficial energies do not change significantly, (4) implies a strong dependence of the critical volume on lattice mismatch. For instance, (4) can explain the stability of bigger pyramids when the lattice mismatch decreases because of Si intermixing due to capping at relatively high temperatures [21]. In our C-QDs, we expect a significant increase of lattice mismatch and a corresponding lowering of the critical volume $V_c(C)$ for dome-shaped island stability.

Monte Carlo simulations [23] predict carbon concentrations up to 8% in the topmost layers of a silicon substrate for a C coverage corresponding to 0.36 ML, which is in the same range as the amount used in our experiment. Overgrowth with Ge has been shown to displace the C atoms towards the first subsurface layers and we estimate an average C composition not lower than 3% as a typical reference value for our samples. The introduction of such an amount of carbon into silicon or silicon–germanium alloys would shrink the lattice parameter with strong deviation from Vegard's rule, but taking into account recent experimental results [28] we calculate a reduction of ≈0.074 Å compared to the lattice parameter of bulk Si. Thus, for Ge overgrowth we estimate a misfit of roughly 6%. If we consider that the effect of carbon predeposition is mainly this change of lattice mismatch, from (4) it follows that

$$\frac{V_c\,(C)}{\epsilon^6_{\mathrm{Ge-Si}}} \cong \frac{V_c}{\epsilon^6_{\mathrm{Ge-SiC}}}. \tag{5}$$

The critical volume reported recently [21] is $V_c \approx 15 \times 10^3$ nm^3 for Ge-rich QDs. Using (5) we obtain in our case a significant reduction to a value of $V_c(C) \approx \frac{15\times10^3\ \mathrm{nm}^3}{(-0.06)^6}(-0.042)^6 \cong 2000$ nm^3. Both V_c and $V_c(C)$ values are indicated by vertical arrows in figure 5. The smallest detectable islands have typical volumes which match nicely the predicted critical volume for stable carbon-induced domes, thus supporting the validity of the proposed phenomenology.

When discussing the factors that can modify the energetics of the pyramid–dome transition, especially by comparing QD ensembles characterized by different island densities, it is crucial to account also for the island–island interaction. In fact, the critical volume is expected to decrease with increasing dot density [29, 30]. In figure 5, although we plot data corresponding to samples having different island density, there is no significant change in aspect ratio. We conclude that island–island interaction is negligible in this density range.

5. Conclusions

In summary, we have studied the modified epitaxial growth mechanism of self-assembled Ge QDs in the case of submonolayer carbon predeposition. Our results point to Si interdiffusion combined with the Ge–C repulsive interaction as key factors in understanding the surface dynamics driving the whole process.

We have suggested a two-stage growth process which enables one to finely tune the island density just by controlling the deposition temperature of the WL before the growth of the C-induced Ge dots. We found out that the highest dot densities are achieved at higher temperature, in apparent contrast with literature results.

By means of optical characterization techniques we were able to accurately determine the composition and strain of the C-induced QD ensembles, demonstrating that the variation of island density correlates with the amount of interdiffused silicon from the substrate through the WL. The larger the amount of thermally activated silicon intermixing, the better is the carbon stability on the surface. This modifies the diffusion length of the Ge adatoms, leading to different topographies.

Another striking result is that the average dot size is minimized when the silicon content is increased, whereas in the literature Si intermixing is usually related to an enlargement of the islands. This, again, can be understood only by considering that the diffusion length of Ge is modified by the presence of carbon-rich clusters due to Si intermixing in the wetting layer. The presence of carbon also affects the energetics of the pyramid–dome shape transition. The main reason for the reduction of the critical volume for the appearance of dome-shaped islands is the locally enhanced lattice misfit.

Acknowledgments

We acknowledge financial support from Air Products and Chemicals, MATGAS 2000 AIE, and from the Dirección General de Investigación from Spain under project MAT2003-00738. AB is also grateful to the Spanish Ministry of Education and Science for an FPI fellowship.

References

[1] Rosei F 2004 Nanostructured surfaces: challenges and frontiers in nanotechnology *J. Phys.: Condens. Matter* **16** S1373–436
[2] Stangl J, Holy V and Bauer G 2004 Structural properties of self-organized semiconductor nanostructures *Rev. Mod. Phys.* **76** 725
[3] Konle J, Presting H and Kibbel H 2003 Self-assembled Ge-islands for photovoltaic applications *Physica* E **16** 596–601
[4] Ross F M, Tersoff J and Tromp R M 1998 Coarsening of self-assembled Ge quantum dots on Si(001) *Phys. Rev. Lett.* **80** 984
[5] Medeiros-Ribeiro G, Bratkovski A M, Kamins T I, Ohlberg D A A and Williams R S 1998 Shape transition of germanium nanocrystals on a silicon (001) surface from pyramids to domes *Science* **279** 353–5
[6] Portavoce A, Berbezier I and Ronda A 2004 Sb-surfactant-mediated growth of Si and Ge nanostructures *Phys. Rev.* B **69** 155416
[7] Qin J, Xue F, Wang Y, Bai L H, Cui J, Yang X J, Fan Y L and Jiang Z M 2005 Phosphorus-mediated growth of Ge quantum dots on Si(001) *J. Cryst. Growth* **278** 136–41
[8] Shi W H, Li C B, Luo L P, Cheng B W and Wang Q M 2005 Growth of Ge quantum dot mediated by boron on Ge wetting layer *J. Cryst. Growth* **279** 329–34
[9] Beyer A, Muller E, Sigg H, Stutz S, Grutzmacher D, Leifeld O and Ensslin K 2000 Size control of carbon-induced Ge quantum dots *Appl. Phys. Lett.* **77** 3218–20
[10] Wakayama Y, Gerth G, Werner P, Gosele U and Sokolov L V 2000 Structural transition of Ge dots induced by submonolayer carbon on Ge wetting layer *Appl. Phys. Lett.* **77** 2328–30
[11] Kim J Y, Ihm S H, Seok J H, Lee C H, Lee Y H, Suh E K and Lee H J 2000 Growth temperature dependence on the formation of carbon-induced Ge quantum dots *Thin Solid Films* **369** 96–9
[12] Leifeld O, Beyer A, Grutzmacher D and Kern K 2002 Nucleation of Ge dots on the C-alloyed Si(001) surface *Phys. Rev.* B **66** 125312

[13] Kelires P C 1995 Monte Carlo studies of ternary semiconductor alloys: application to the Si[sub 1 − *x* − *y*]Ge[sub *x*]C[sub *y*] system *Phys. Rev. Lett.* **75** 1114–7
[14] Wakayama Y, Sokolov L V, Zakharov N, Werner P and Gosele U 2003 Precise control of size and density of self-assembled Ge dot on Si(100) by carbon-induced strain-engineering *Appl. Surf. Sci.* **216** 419–23
[15] Alonso M I, de la Calle M, Ossó J O, Garriga M and Goñi A R 2005 Strain and composition profiles of self-assembled Ge/Si(001) islands *J. Appl. Phys.* **98** 033530
[16] Tan P H, Brunner K, Bougeard D and Abstreiter G 2003 Raman characterization of strain and composition in small-sized self-assembled Si/Ge dots *Phys. Rev.* B **68** 125302
[17] Stoehr M, Aubel D, Juillaguet S, Bischoff J L, Kubler L, Bolmont D, Hamdani F, Fraisse B and Fourcade R 1996 Phonon strain-shift coefficients of $Si_{1-x}Ge_x$ grown on Ge(001) *Phys. Rev.* B **53** 6923
[18] De Seta M, Capellini G, Evangelisti F and Spinella C 2002 Intermixing-promoted scaling of Ge/Si(100) island sizes *J. Appl. Phys.* **92** 614–9
[19] Talochkin A B, Teys S A and Suprun S P 2005 Resonance Raman scattering by optical phonons in unstrained germanium quantum dots *Phys. Rev.* B **72** 115416
[20] Wagner R J and Gulari E 2004 Simulation of Ge/Si intermixing during heteroepitaxy *Phys. Rev.* B **69** 195312
[21] Rastelli A, Kummer M and von Känel H 2001 Reversible shape evolution of Ge islands on Si(001) *Phys. Rev. Lett.* **87** 256101
[22] Kim H, Kim W, Lee G and Koo J-Y 2005 Two-dimensional carbon incorporation into Si(001): C amount and structure of Si(001)-$c(4 \times 4)$ *Phys. Rev. Lett.* **94** 076102
[23] Hadjisavvas G, Sonnet Ph and Kelires P C 2003 Stress and composition of C-induced Ge dots on Si(100) *Phys. Rev.* B **67** 241302
[24] Rastelli A, Stoffel M, Tersoff J, Kar G S and Schmidt O G 2005 Kinetic evolution and equilibrium morphology of strained islands *Phys. Rev. Lett.* **95** 026103
[25] Montalenti F *et al* 2004 Atomic-scale pathway of the pyramid-to-dome transition during Ge growth on Si(001) *Phys. Rev. Lett.* **93** 216102
[26] Daruka I and Barabási A-L 1997 Dislocation-free island formation in heteroepitaxial growth: a study at equilibrium *Phys. Rev. Lett.* **79** 3708
[27] Shklyaev O E, Beck M J, Asta M, Miksis M J and Voorhees P W 2005 Role of strain-dependent surface energies in Ge/Si(100) island formation *Phys. Rev. Lett.* **94** 176102
[28] De Salvador D, Petrovich M, Berti M, Romanato F, Napolitani E and Drigo A 2000 Lattice parameter of $Si_{1-x-y}Ge_xC_y$ alloys *Phys. Rev.* B **61** 13005
[29] Floro J A, Lucadamo G A, Chason E, Freund L B, Sinclair M, Twesten R D and Hwang R Q 1998 SiGe island shape transitions induced by elastic repulsion *Phys. Rev. Lett.* **80** 4717–20
[30] Capellini G, De Seta M and Evangelisti F 2003 Ge/Si(100) islands: growth dynamics versus growth rate *J. Appl. Phys.* **93** 291–5

Density control on self-assembling of Ge islands using carbon-alloyed strained SiGe layers

A. Bernardi,[a] M. I. Alonso, A. R. Goñi, J. O. Ossó, and M. Garriga
Institut de Ciència de Materials de Barcelona-CSIC, Esfera UAB, 08193 Bellaterra, Spain

(Received 26 May 2006; accepted 18 July 2006; published online 8 September 2006)

The authors show that by deposition of 0.1 ML of carbon prior to the self-assembled growth of Ge quantum dots on a strained $Si_{1-x}Ge_x$ buffer layer a striking decrease in dot density by two orders of magnitude from about 10^{11} to 10^9 cm^{-2} occurs when the Ge content of the buffer layer increases from 0% to 64%. Their results give experimental evidence for a kinetically limited growth mechanism in which Ge adatom mobility is determined by chemical interactions among C, Si, and Ge. Thus, by adjusting the Ge content of the SiGe buffer layer onto which a carbon submonolayer is deposited they are able to fine tune the density of the carbon-induced Ge quantum dots. © *2006 American Institute of Physics*. [DOI: 10.1063/1.2349317]

Size, density, shape uniformity, and ordering[1,2] of quantum dots (QDs) are crucial parameters when self-assembling is considered for applications in optoelectronic devices. In recent years, different smart strategies have been proposed to address the problem of dot engineering.[3] Increase of dot density at very low substrate temperatures and/or high deposition rates is a well established technique but in most cases it is not of practical interest for applications due to the degradation of crystalline quality. Perfect position control keeping high quality of dot ensembles can be achieved by means of artificially nanopatterned substrates.[4] This approach is, however, less suitable for potential high-surface and low cost applications. An alternative are spontaneous bottom up approaches such as the use of template layers to guide the selective nucleation of dots, which has demonstrated to be a good method to control the positioning of dots by inducing self-ordering processes during growth. A strain-driven instability[5,6] in SiGe/Si(001) pseudomorphic layers leads to the formation of periodic surface undulations (ripples) acting as a natural template pattern[7,8] that can be controlled by thickness, composition, and selection of vicinal Si(001) surfaces.[9] Other routes include Ge deposition on relaxed SiGe/Si buffer layers[10,11] and deposition on buried dislocation networks.[12] Another relevant bottom up strategy towards efficient dot engineering involves surface modification through deposition of sub monolayer amounts of impurities[13] that can reduce the diffusion length (i.e., enhancing dot density) and alter the energetics of nucleation. This approach has recently gathered renewed interest, having as examples the cases of surfactant mediated growth in the presence of Sb (Ref. 9) or surface alloying with carbon.[14,15]

In this Letter we present a different route for manipulating Ge island self-assembling based on the combination of epitaxial growth on strained SiGe buffer layers and carbon predeposition. Inspired by our recent results on the influence of Si interdiffusion and the Ge–C repulsive interaction on the resulting Ge dot topography[15] we make use of the effect that a submonolayer deposition of C has on the Ge adatom diffusion. Our results point to a reduction by two orders of magnitude of dot density with increasing Ge content in the buffer layer. This experimental evidence is in frank contrast with currently accepted models for island nucleation in the absence of carbon. We therefore propose a growth scenario in which the Ge–C chemical interaction plays a determinant role.

The growth sequence of the uncapped Ge QDs prepared by solid-source molecular beam epitaxy on Si(001) substrates is as follows. After desorbing the thin oxide of the Si wafer at 900 °C and depositing a 50 nm thick Si buffer layer, the substrate temperature was set to 400 °C to deposit a thin strained $Si_{1-x}Ge_x$ buffer layer with Ge composition x ranging from 0% to ~60%. For all the samples the SiGe buffer layer thickness (see Table I) remained below the limit of metastability,[16,17] preventing three-dimensional nucleation of SiGe quantum dots, as confirmed by *in situ* reflection high-energy electron diffraction monitoring. The temperature was then raised and maintained at 500 °C during the deposition of 0.1 ML of carbon by a sublimation filament and the subsequent evaporation of ~6 Å of Ge at a fixed growth rate of ~0.04 Å/s, leading to self-assembling of quantum dots.

In Fig. 1 we present the topographic images obtained with an atomic force microscope (AFM) resulting from the three-step deposition process (SiGe buffer+carbon+Ge) with different compositions x of the buffer layer, maintaining the remaining growth parameters fixed. At low Ge content in the buffer layer, carbon induces the nucleation of a high density of small dome-shaped dots with monomodal size distribution [see Fig. 1(a)], similar to what was previously observed in the case of C predeposition directly on Si(001).[13] By increasing the Ge composition of the buffer layer we observe a significant decrease of island density [see Figs.

TABLE I. Composition values and layer thicknesses obtained by optical characterization of the $Si_{1-x}Ge_x$ buffer layers using spectral ellipsometry and Raman scattering.

Ellipsometry		Raman	
Thickness (nm)	Composition x	ω_{SiGe} (cm^{-1})	Composition x
5±1	0.08±0.02	404.3±0.5	0.08±0.01
8±1	0.20±0.02	410.3±0.5	0.25±0.05
7±1	0.44±0.01	418.3±0.2	0.43±0.08
6±1	0.64±0.01	421.3±0.1	0.63±0.01

[a]Electronic mail: abernardi@icmab.es

This article is copyrighted as indicated in the article. Reuse of AIP content is subject to the terms at: http://scitation.aip.org/termsconditions. Downloaded to IP: 158.109.223.71 On: Fri, 21 Feb 2014 13:09:02

0003-6951/2006/89(10)/101921/3/$23.00

© 2006 American Institute of Physics

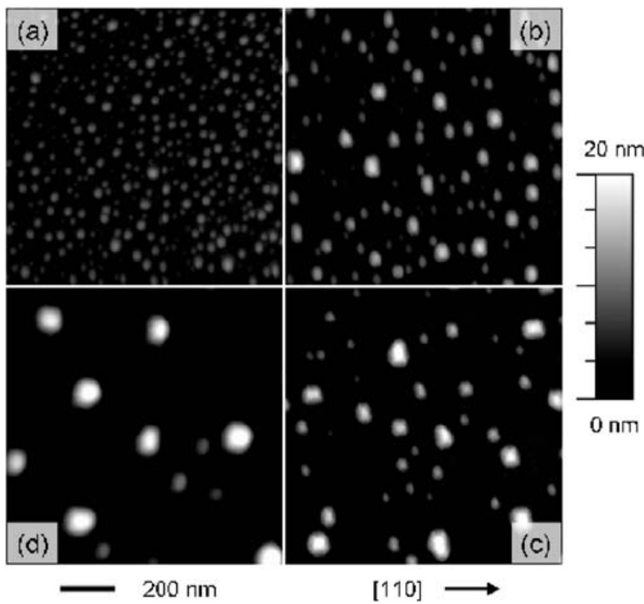

FIG. 1. AFM images of C-induced Ge QDs grown on strained $Si_{1-x}Ge_x$ buffer layers with (a) 8%, (b) 20%, (c) 44%, and (d) 64% Ge contents.

1(b)–1(d)] with the consequent increase in average island size.

Samples have been characterized *ex situ* by Raman spectroscopy to obtain information on strain and composition of the nanostructures. Three representative spectra are shown in Fig. 2. The composition of the SiGe alloy constituting the buffer layer can be determined from the position of the Si–Ge phonon mode apparent in the 400 cm^{-1} spectral range, considering that the built-in strain of the buffer layer is given by its pseudomorphic growth on the Si substrate. For the highest Ge content of the buffer layer (see bottom spectrum in Fig. 2) we can also resolve at least one of the local Si–Si modes of the SiGe alloy. Its position confirms the values of composition and strain from the Si–Ge mode. The peak at

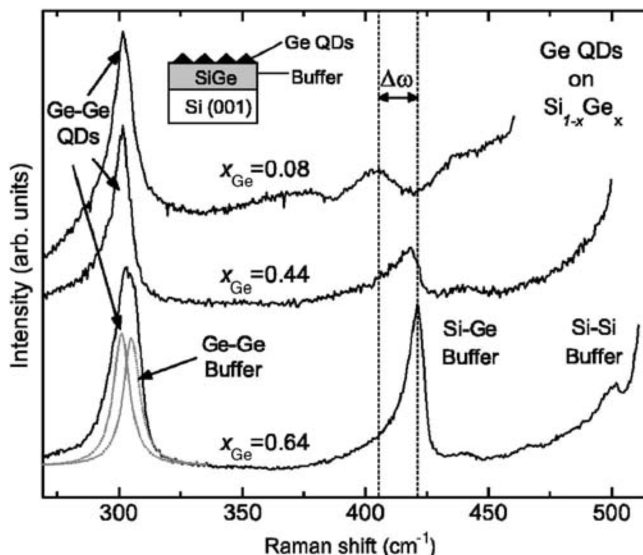

FIG. 2. Raman spectra of QD ensembles grown on $Si_{1-x}Ge_x$ buffer layers with contents of $x=0.08$, 0.44, and 0.64. The assignment of the various Raman peaks to the different local Ge–Ge, Si–Ge, and Si–Si modes of the buffer layer and the dots is indicated. The dashed vertical lines put in evidence the frequency shift of the Si–Ge mode. The inset shows a sketch of a sample with uncapped Ge dots.

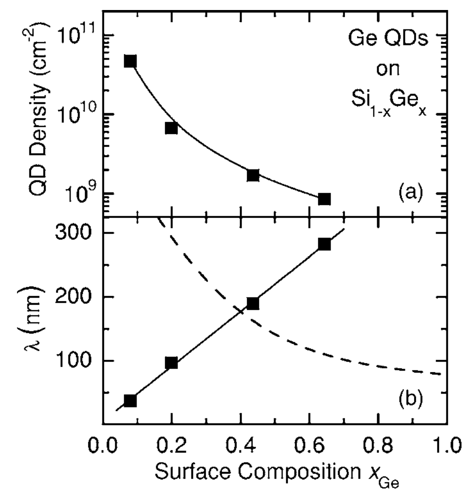

FIG. 3. Solid symbols correspond to (a) the island density and (b) the average interdot spacing vs the Ge content of the buffer layer, as obtained from optical spectroscopy. Solid lines are guides to the eyes. Dashed curve in (b) represents the roughness wavelength for SiGe films on Si calculated in Ref. 17 to explain the experimental data of Refs. 5 and 6.

301.3 cm^{-1} is ascribed to the Ge–Ge phonon mode of the Ge QDs and its spectral position is indicative of a very high Ge content of $x>0.90$ and almost complete strain relaxation ($\epsilon_{\parallel}\approx-0.005$).[15] We point out that for the buffer layer with highest Ge concentration we expected its Ge–Ge mode to be observable in Raman spectra as well at $\sim$305 cm^{-1}. In fact, its contribution to the Ge–Ge phonon peak of the dots can be spectrally deconvoluted by fitting this peak with two Lorentzians, as illustrated by the dotted curves in Fig. 2.

The C-induced positioning of the preferential nucleation sites for the Ge dots is leading to the final topography observed for the different samples of Fig. 1. Such changes in topography are clearly related to the interplay between predeposited carbon and the Ge composition of the buffer layer constituting the surface where Ge adatoms move during growth but before being incorporated into a QD. In Fig. 3 we plot the dot density and average interdot spacing λ versus the Ge composition of the buffer layer, represented by the solid symbols. The striking result of this work concerns the observed tendency of the dot density which exhibits a significant, monotonous decrease by two orders of magnitude with increasing Ge content in the buffer layer from 0% up to $\sim$60% whereas the interdot separation represented by λ increases.

According to thermodynamic models, strained SiGe layers are susceptible to evolve into morphological instabilities (ripples) which can form a cell pattern with a characteristic roughness wavelength λ.[5,6] Although such low aspect ratio mounds are still highly strained, the slight relaxation occurring at their apex is enough to act as a template for preferential nucleation of bigger, further relaxed islands during the subsequent Ge deposition. In this picture the resulting average dot spacing matches the roughness wavelength λ. This model[17] which describes well the experimental results of Refs. 5 and 6 predicts λ to scale as x_{Ge}^{-1} (see dashed curve in Fig. 3). This result is totally at odds with our observation of an almost linear increase of λ with Ge content when carbon has been predeposited onto the SiGe buffer layer.

If, in contrast, ripple formation was not responsible for preferential dot nucleation, one should assume that QDs nucleate at random sites and that the interdot spacing is de-

This article is copyrighted as indicated in the article. Reuse of AIP content is subject to the terms at: http://scitation.aip.org/termsconditions. Downloaded to IP: 158.109.223.71 On: Fri, 21 Feb 2014 13:09:02

termined by the adatom diffusion length in a kinetically limited growth regime.[10] In this case, the dot density depends primarily on the surface Ge adatom mobility which, in turn, is related to the average roughness (but not in the form of ripples!) of the SiGe layer. The latter is known to increase with increasing Ge concentration,[18] implying an increment of dot density in the $(1-3)\times 10^9$ cm^{-2} range as was previously reported.[19] Obviously, this model also fails to pinpoint the growth mechanism at work in our case since results in Fig. 3 show the opposite trend in a much wider range of achievable dot densities (10^9-10^{11} cm^{-2}).

In order to explain our experimental findings we need to take into account the effects of the submonolayer of carbon. Impurity atoms are known to cause enhanced surface roughness,[20] thus resulting in an increased dot density but this alone does not explain straightforwardly the observed dependence on Ge composition of the buffer layer. We propose a mechanism by which the chemical interactions among Si, Ge, and C drive the growth process. The Si–C attractive interaction favors C condensation, leading to the appearance of $c(4\times 4)$ reconstruction patches[14] also associated with an enhanced surface roughness. If the carbon is deposited on a layer containing Ge, the Ge–C repulsion[21] induces phase separation and depending on Ge content the C-induced reconstruction patches become increasingly fragmented, being the C atoms progressively incorporated at random sites in the film.[22] The key point is that the formation of the reconstruction patches produces a significant quenching of the Ge adatom diffusion, which within the kinetic model implies the self-assembled growth of a high density of Ge dots. With increasing Ge content of the buffer layer the C-induced patches gradually disappear, the surface roughness diminishes, and the Ge adatom diffusivity becomes enhanced, resulting in lower dot densities. This scenario is consistent with our recent work addressing the influence of Si interdiffusion when the carbon-induced QDs are grown on pure Ge wetting layers deposited at different temperatures.[15] Again the dot density increases with increasing deposition temperature of the wetting layer, i.e., with higher Si content of the surface onto which the dots nucleate.

In conclusion, we have shown that the self-organized growth of Ge islands is fundamentally affected by the predeposition of a carbon submonolayer on a strained SiGe buffer layer. The relevant parameter which allows for a control of dot topography is the Ge content of the SiGe alloy. The result is a monomodal distribution of Ge rich quantum dots with an areal density which can be adjusted over a wide range (10^9-10^{11} cm^{-2}) just by changing the Ge composition of the SiGe buffer/wetting layer. The results are explained using a kinetically limited model for the growth mechanism which accounts for the interplay of chemical interactions among C, Si, and Ge as the determinant factor influencing Ge adatom mobility. This provides us with a powerful growth protocol for better design of Ge quantum dot nanostructures for device applications.

The authors are grateful to the spanish Ministerio de Educación y Ciencia for support through MAT2003-00738. One of the authors (A.B.) also acknowledges an FPI fellowship. Another author (A.R.G.) is an ICREA Research Professor.

[1] G. Capellini, M. D. Seta, F. Evangelisti, V. A. Zinovyev, G. Vastola, F. Montalenti, and L. Miglio, Phys. Rev. Lett. **96**, 106102 (2006).
[2] F. Ratto, A. Locatelli, S. Fontana, S. Kharrazi, S. Ashtaputre, S. K. Kulkarni, S. Heun, and F. Rosei, Phys. Rev. Lett. **96**, 096103 (2006).
[3] J. M. Baribeau, X. Wu, N. L. Rowell, and D. J. Lockwood, J. Phys.: Condens. Matter **18**, R139 (2006).
[4] A. Karmous, A. Cuenat, A. Ronda, I. Berbezier, S. Atha, and R. Hull, Appl. Phys. Lett. **85**, 6401 (2004).
[5] P. Sutter and M. G. Lagally, Phys. Rev. Lett. **84**, 4637 (2000).
[6] R. M. Tromp, F. M. Ross, and M. C. Reuter, Phys. Rev. Lett. **84**, 4641 (2000).
[7] I. Berbezier, M. Abdallah, A. Ronda, and G. Bremond, Mater. Sci. Eng., B **69–70**, 367 (2000).
[8] B. Ismail, M. Descoins, A. Ronda, F. Bassani, G. Bremond, H. Maaref, and I. Berbezier, J. Vac. Sci. Technol. B **23**, 242 (2005).
[9] I. Berbezier, A. Ronda, A. Portavoce, and N. Motta, Appl. Phys. Lett. **83**, 4833 (2003).
[10] H. J. Kim, Z. M. Zhao, and Y. H. Xie, Phys. Rev. B **68**, 205312 (2003).
[11] M. Shaleev, A. Novikov, O. Kuznetsov, A. Yablonsky, N. Vostokov, Y. Drozdov, D. Lobanov, and Z. Krasilnik, Mater. Sci. Eng., B **124–125**, 466 (2005).
[12] H. Kim, C. Shin, and J. Chang, Appl. Surf. Sci. **252**, 1476 (2005).
[13] O. G. Schmidt, C. Lange, K. Eberl, O. Kienzle, and F. Ernst, Appl. Phys. Lett. **71**, 2340 (1997).
[14] O. Leifeld, A. Beyer, D. Grutzmacher, and K. Kern, Phys. Rev. B **66**, 125312 (2002).
[15] A. Bernardi, J. O. Ossó, M. I. Alonso, A. R. Goñi, and M. Garriga, Nanotechnology **17**, 2602 (2006).
[16] D. Perovic', B. Bahierathan, H. Lafontaine, D. Houghton, and D. McComb, Physica A **239**, 11 (1997).
[17] B. J. Spencer, P. W. Voorhees, and J. Tersoff, Phys. Rev. B **64**, 235318 (2001).
[18] G. G. Jernigan and P. E. Thompson, Surf. Sci. **516**, 207 (2002).
[19] D. Lobanov, A. Novikov, N. Vostokov, Y. Drozdov, A. Yablonskiy, Z. Krasilnik, M. Stoffel, U. Denker, and O. Schmidt, Opt. Mater. (Amsterdam, Neth.) **27**, 818 (2005).
[20] G. G. Jernigan and P. E. Thompson, Thin Solid Films **472**, 16 (2005).
[21] P. C. Kelires, Phys. Rev. Lett. **75**, 1114 (1995).
[22] A. Sakai, Y. Torige, M. Okada, H. Ikeda, Y. Yasuda, and S. Zaima, Appl. Phys. Lett. **79**, 3242 (2001).

This article is copyrighted as indicated in the article. Reuse of AIP content is subject to the terms at: http://scitation.aip.org/termsconditions. Downloaded to IP: 158.109.223.71 On: Fri, 21 Feb 2014 13:09:02

Available online at www.sciencedirect.com
ScienceDirect
Surface Science 601 (2007) 2783–2786
SURFACE SCIENCE
www.elsevier.com/locate/susc

Growth dynamics of C-induced Ge dots on $Si_{1-x}Ge_x$ strained layers

A. Bernardi *, M.I. Alonso, A.R. Goñi, J.O. Ossó, M. Garriga

Institut de Ciència de Materials de Barcelona-CSIC, Esfera UAB, 08193 Bellaterra, Spain

Available online 20 December 2006

Abstract

We address the growth mechanism of Ge quantum dots (QDs) on C-alloyed strained $Si_{1-x}Ge_x$ layers by *in situ* reflection high-energy electron-diffraction (RHEED). We show that C-induced growth on a Si-rich surface leads to a high density (about 10^{11} cm^{-2}) of small dome-shaped islands. On surfaces up to ≈65% richer in Ge we observe a decrease of the dot density by two orders of magnitude, which is associated to the increase of the adatom diffusion. Based on quantitative RHEED analysis, the islands are believed to grow in a Volmer–Weber mode even though their spotty electron transmission pattern is not detectable in the initial stages of growth due to the reduced size of the three-dimensional nucleation islands.
© 2006 Elsevier B.V. All rights reserved.

Keywords: C-induced Ge quantum dots; Molecular-beam epitaxy; RHEED; Spectroscopic ellipsometry

1. Introduction

Self-assembling on modified surfaces [1,2] or nanopatterned substrates [3,4] allows for the control of shape, size, density and ordering of quantum dots (QDs), offering the possibility to tailor their properties for potential application in nanoscale devices [5]. In particular, the deposition of sub-monolayer amounts of impurities, like carbon, enables to dramatically decrease the diffusion length of adatoms on the surface, leading to the enhancement of dot density even at relatively high growth temperatures (500–600 °C) required for good crystalline quality [6]. We recently demonstrated [7] that by the combination of epitaxial growth on SiGe buffer layers and carbon predeposition, we are able to manipulate the growth of Ge dots with the possibility to tune the island density from about 10^{11}–10^{9} cm^{-2} just by increasing the Ge content (up to ≈65%) in the strained buffer layer. We explained these results invoking a kinetically-limited model which accounts for the interplay of chemical interactions among C, Si and Ge that determine the Ge adatom mobility.

In this work we have investigated by *in situ* reflection high-energy electron-diffraction (RHEED) the structural changes occurring at the different stages of the proposed multi-step growth process (SiGe deposition, C alloying and nucleation of Ge dots). In particular, we observe that although at the initial stages of dot nucleation the spotty transmission pattern is not detectable due to the reduced size of the critical nuclei, the strain relaxation is being observed from the very beginning of the Ge deposition, which suggests a Volmer–Weber growth mode.

2. Experimental

A set of Ge QD samples was prepared by solid-source molecular-beam epitaxy using a three-step growth procedure: (1) A thin strained $Si_{1-x}Ge_x$ layer (with x ranging from 0 to ~65%) was grown on Si(001) substrates at 400 °C, (2) the temperature was stabilized at 500 °C for the deposition of 0.1 monolayers (MLs) of carbon by a sublimation filament and (3) finally, ~6 Å of Ge were evaporated, leading to self-assembling of QDs. The growth was monitored *in situ* by RHEED using 20 keV electrons and a CCD camera to record the diffraction pattern displayed on a phosphor screen. Characterization of composition, thickness and strain of the $Si_{1-x}Ge_x$ buffer layers was carried

* Corresponding author. Tel.: +34 935 801 853.
E-mail address: abernardi@icmab.es (A. Bernardi).

0039-6028/$ - see front matter © 2006 Elsevier B.V. All rights reserved.
doi:10.1016/j.susc.2006.12.048

out ex-situ by spectroscopic ellipsometry in the 1.4–4.8 eV spectral range in side-by-side grown samples without step (3). Morphology and QDs density were investigated by atomic force microscopy (AFM).

3. Results and discussion

In Fig. 1 we show a sequence of RHEED patterns typical of the different deposition steps collected along the ⟨1 1 0⟩ azimuth. The Si(0 0 1) surface of the substrate is characterized by a streaky pattern corresponding to the (2 × 1) surface reconstruction (Fig. 1(a)). During the deposition of the $Si_{1-x}Ge_x$ buffer Fig. 1(b) we notice a decrease of intensity along the second order strikes that is attributed to the evolution from Si-(2 × 1) to SiGe-(M × N) reconstruction [8]. No indications of the formation of 3D clusters, neither transmission features nor Chevron lines originating from {1 0 5}-facets, can be detected confirming that by lowering the substrate temperature we successfully quenched the formation of ripples [9,10]. After the deposition of 0.1 ML of C (Fig. 1(c)) the second order strikes almost completely disappear hinting at an enhancement of the surface roughness. Carbon on Si(0 0 1) is known to induce a c(4 × 4) reconstruction [11] associated to increased surface roughness, but it is not known if this also applies to C deposition on SiGe alloys. Considered the Ge–C repulsive interaction [12] and the changing surface reconstruction of SiGe it is likely that with increasing Ge content in the alloy, the c(4 × 4) reconstruction becomes progressively unstable and hardly detectable by RHEED. In the last step of the growth process (Fig. 1(d)), a typical spotty pattern resulting from electron transmission through strain-relieved 3D clusters (Ge islands) appears.

The growth sequence for the samples under investigation is always exactly the same, apart from the deposition of the $Si_{1-x}Ge_x$ buffer of variable x. Spectroscopic ellipsometry allows to accurately probe these thin layers for the determination of the film thickness and dielectric function of the material. By an accurate fitting procedure [13] it is possible to extract the energies of the interband electronic transitions E_1 and $E_1 + \Delta_1$. From these two energies we evaluate both the Ge content in the alloy and the in-plane strain, which, approximately, should be

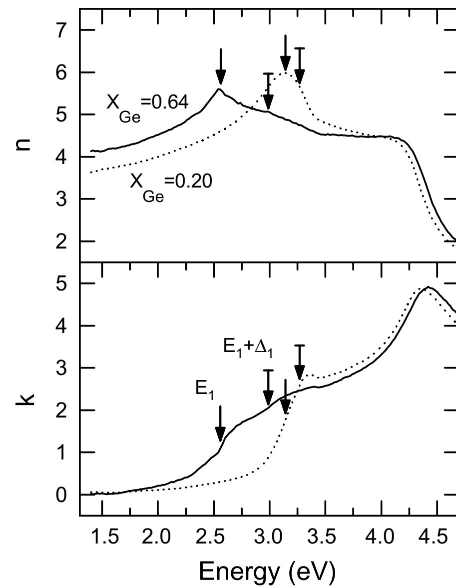

Fig. 2. Optical functions n and k of $Si_{1-x}Ge_x$/Si(0 0 1) buffer layers for $x = 0.20$ (dotted line) and $x = 0.64$ (solid line). Arrows indicate fitted energies of relevant electronic transitions.

$\epsilon_{\parallel}(\%) = -4x$ for pseudomorphic layers. In Fig. 2 we show the fitted spectral dependence of the refractive index n and the extinction coefficient k for two of the buffer layers, with arrows indicating the energies of the transitions obtained from the analysis of the ellipsometric data. Results are summarized in Table 1. In particular, the layers are found to be completely strained, in agreement with a 2D growth, as deduced from RHEED.

The RHEED patterns represented by the sequence in Fig. 1 describe qualitatively all samples. However, interesting differences are revealed upon quantitative analysis of each case. By selecting the line marked by arrows in Fig. 1(a) we extracted profiles of the RHEED patterns collected at different stages of the sample growth. In Fig. 3 we show the evolution of such linescans evidencing the pattern change which corresponds to the appearance of additional transmission spots associated to QD formation. We focus now on this last step of the process during the time when Ge is deposited. We monitor the intensity of the 3D spotty pattern and simultaneously extract the distance between

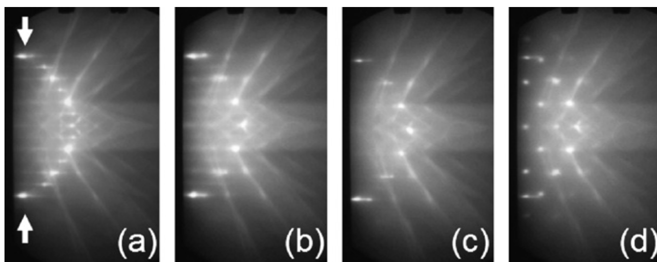

Fig. 1. RHEED pattern sequence taken after deposition of (a) Si buffer, (b) 7 nm-thick $Si_{0.56}Ge_{0.44}$ strained layer, (c) 0.1 ML of carbon and (d) Ge QDs. Arrows in (a) indicate the line along which RHEED profiles were obtained.

Table 1
Results of characterization of the samples. Thicknesses d of the $Si_{1-x}Ge_x$ buffer layers and their transition energies E_1 and $E_1 + \Delta_1$ determined by ellipsometry

d (nm)	E_1 (eV)	$E_1 + \Delta_1$ (eV)	x	$\epsilon_{\parallel}(\%)$	ρ (cm^{-2})
5(1)	3.295(6)	—	0.08(2)	—	4.7×10^{10}
8(1)	3.135(10)	3.245(10)	0.20(2)	−0.7(2)	6.7×10^{9}
7(1)	2.832(5)	3.140(10)	0.44(1)	−1.9(2)	1.7×10^{9}
6(1)	2.560(3)	2.991(5)	0.64(1)	−2.6(1)	8.5×10^{8}

Composition x and in-plane strain $\epsilon_{\parallel}$ are obtained from these energies. Numbers in parentheses represent error bars affecting the last given digits. The tabulated density of QDs ρ was evaluated by AFM for each case with estimated error margin of 10%.

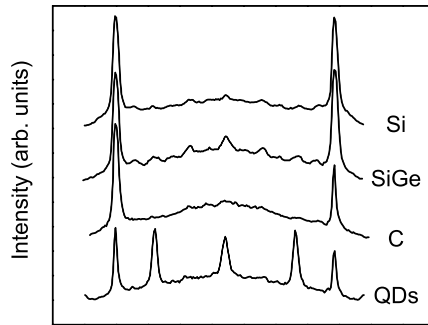

Fig. 3. Linescans of RHEED data typical for the different growth steps shown in Fig. 1.

streaks (or spots) in order to quantify the strain relaxation associated to the dot growth. These results are plotted in Fig. 4. Considering first Fig. 4(a) we observe that the initial growth stages are characterized by a plateau before the rise in intensity of the 3D spots. The lower the Ge content in the $Si_{1-x}Ge_x$ buffer, the longer it takes for the 3D spots to become detectable by RHEED. If we only look at these data we could think that the plateau represents a layer by layer growth compatible with a Stranski–Krastanow (SK) growth mode. From this perspective, we would conclude that for higher Ge content in the buffer (i.e. higher amount of elastic energy stored in the 2D layer), the critical thickness for 2D to 3D growth mode transition is reached earlier, in line with the RHEED data of Fig. 4(a). However, we cannot disregard the key piece of evidence shown in Fig. 4(b), where there is clear indication of an in-plane strain relaxation during Ge growth. For example, we analyze the case of Ge QDs on $Si_{0.92}Ge_{0.08}$, for which the 3D spots do not appear until ~60 s after start of Ge deposition (coverage near 2 MLs). We actually notice that strain relaxation occurs from the very beginning of the Ge growth and when the 3D spots become clearly detectable (see the dotted vertical arrow in Fig. 4(a)) the strain relaxation already accounts for roughly 50% of the value obtained at the end of the deposition. In SK growth mode we would expect no strain relaxation until 3D clusters nucleate. Therefore, we believe that when carbon is involved in the growth process, the evolution of Ge dots on C-alloyed $Si_{1-x}Ge_x$ surfaces proceeds via a Volmer–Weber mode, similarly to the case of C-induced Ge dots on Si(001) [14]. In addition, the observed plateaus indicate that dots must reach a threshold critical volume to produce a detectable spotty pattern.

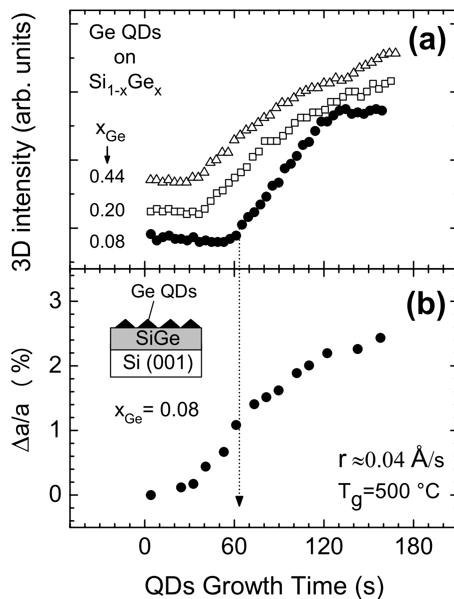

Fig. 4. RHEED parameters obtained by linescan analysis versus Ge growth time. (a) Intensity of the spotty pattern associated with electron transmission through Ge quantum dots for different Ge content in the buffer layer; (b) *in-plane* strain relaxation relative to Si associated to 3D growth. The inset shows a sketch of a sample and the vertical arrow indicates the onset of the spotty pattern for Ge dots grown on $Si_{0.92}Ge_{0.08}$.

In order to explain the dependence of the delay for the observation of transmission spots on the Ge composition of the buffer, we make use of the surface dynamics leading to the final QD topography observed by AFM. We recently proposed [7] that the $c(4\times4)$ reconstruction obtained by depositing C on Si(001) becomes unstable with increasing Ge content of the surface, partly due to the Ge–C repulsive interaction. Consequently, in presence of a SiGe alloy, the C-induced reconstruction patches gradually disappear becoming increasingly fragmented [15]. Because such patches reduce adatom diffusion length, their crumbling opens high mobility paths for the deposited Ge adatoms. The average diffusion length then increases with Ge content causing a gradual decrease in density of dots, as sketched in Fig. 5. At the very first stages of the dot growth, the diffusion length determines the area around the nucleation points, where Ge atoms are likely to be captured into existing Ge islands, instead of forming a new 3D cluster [16,17].

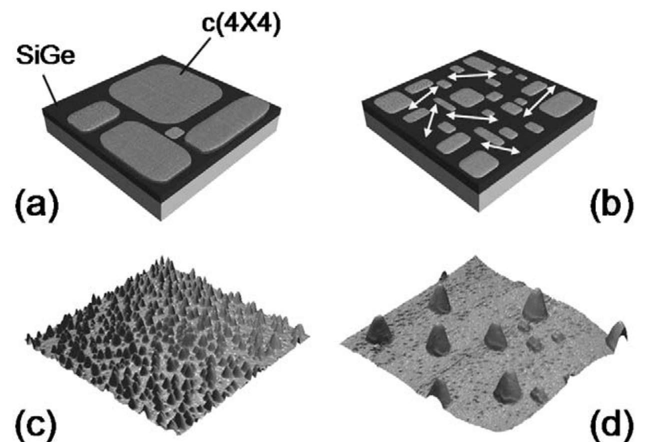

Fig. 5. Top panels are sketches of diffusion limiting $c(4\times4)$ reconstruction patches on $Si_{1-x}Ge_x$ layers with (a) low x and (b) high x. With increasing x the reconstruction becomes unstable and high diffusion paths for Ge adatoms open up, as indicated by arrows. Bottom panels are the corresponding AFM topographic images for Ge QDs grown on C-alloyed $Si_{1-x}Ge_x$ layers with (c) $x=0.08$ and (d) $x=0.64$. Both AFM images are in the same scale: the imaged areas are $2\times2\ \mu m^2$ and the average dot heights (c) 10 nm and (d) 20 nm, respectively.

Hence, the final dot density depends on x and when this value is reached and nucleation of new dots stops, then any additional deposited Ge atom would join the existing islands, whose average volume starts to increase, becoming big enough to produce a spotty pattern. Following this idea, we can estimate the critical volume for RHEED detection as $V_c = \frac{r \cdot t}{\rho}$, where r is the growth rate (≈0.04 Å/s), t is the growth time needed for onset of 3D spots and ρ is the dot density. Then we obtain that V_c is typically in the range $\approx 0.5\text{–}7 \times 10^3\ \text{nm}^3$ with increasing Ge content in the buffer layer. The value V_c can be taken as an upper limit for the critical volume of island formation, and, in fact, the obtained values coincide well with the order of magnitude of very small self-assembled Ge clusters [18] and are in the range of volumes experimentally determined from AFM for the smallest dome-shaped C-induced dots [19], whose critical volume was estimated to be $\approx 2 \times 10^3\ \text{nm}^3$.

4. Conclusions

In conclusion, from strain relief linked to 3D growth observed by RHEED we obtained evidence that the formation of Ge QDs on C-alloyed strained $Si_{1-x}Ge_x$ layers follows a Volmer–Weber growth mode. The presence of C induces nucleation of tiny dots that are not detectable by the characteristic transmission (spotty) pattern before a certain time which depends on the Ge content x in the $Si_{1-x}Ge_x$ buffer layer. This dependence is largely related to the different average adatom diffusion lengths, which determine the time from which no new dots nucleate and the final dot density is reached. Surface diffusion can be manipulated by increasing the Ge content x. Carbon on Si-rich alloys induces the formation of reconstruction patches implying low diffusion and high dot density. The reconstruction is believed to become unstable on Ge-rich surfaces, causing an enhancement of the adatom diffusion length and the consequent decrease of the dot density. Hence, by increasing of Ge content on the surface from zero to 64% the density of dots gradually decreased by roughly two orders of magnitude.

Acknowledgements

We acknowledge financial support from the spanish Ministerio de Educación y Ciencia through MAT2003-00738 and an FPI fellowship (AB). ARG is an ICREA Research Professor.

References

[1] I. Berbezier, A. Ronda, A. Portavoce, N. Motta, Appl. Phys. Lett. 83 (2003) 4833.
[2] J.M. Baribeau, X. Wu, N.L. Rowell, D.J. Lockwood, J. Phys.: Condens. Matter 18 (2006) R139.
[3] F. Rosei, J. Phys.: Condens. Matter 16 (2004) S1373.
[4] A. Karmous, A. Cuenat, A. Ronda, I. Berbezier, S. Atha, R. Hull, Appl. Phys. Lett. 85 (2004) 6401.
[5] J. Stangl, V. Holy, G. Bauer, Rev. Mod. Phys. 76 (2004) 725.
[6] Y. Wakayama, G. Gerth, P. Werner, U. Gosele, L.V. Sokolov, Appl. Phys. Lett. 77 (2000) 2328.
[7] A. Bernardi, M.I. Alonso, A.R. Goñi, J.O. Ossó, M. Garriga, Appl. Phys. Lett. 89 (2006) 101921.
[8] I. Goldfarb, G.A.D. Briggs, Surf. Sci. 433–435 (1999) 449.
[9] D. Perović, B. Bahierathan, H. Lafontaine, D. Houghton, D. McComb, Physica A 239 (1997) 11.
[10] B.J. Spencer, P.W. Voorhees, J. Tersoff, Phys. Rev. B 64 (2001) 235318.
[11] H. Kim, W. Kim, G. Lee, J.-Y. Koo, Phys. Rev. Lett. 94 (2005) 076102.
[12] P.C. Kelires, Phys. Rev. Lett. 75 (1995) 1114.
[13] M.I. Alonso, M. de la Calle, J.O. Ossó, M. Garriga, A.R. Goñi, J. Appl. Phys. 98 (2005) 033530.
[14] M. Stoffel, L. Simon, J.L. Bischoff, D. Aubel, L. Kubler, G. Castelein, Thin Solid Films 380 (2000) 32.
[15] A. Sakai, Y. Torige, M. Okada, H. Ikeda, Y. Yasuda, S. Zaima, Appl. Phys. Lett. 79 (2001) 3242.
[16] H.J. Kim, Z.M. Zhao, Y.H. Xie, Phys. Rev. B 68 (2003) 205312.
[17] F. Ratto, A. Locatelli, S. Fontana, S. Kharrazi, S. Ashtaputre, S.K. Kulkarni, S. Heun, F. Rosei, Phys. Rev. Lett. 96 (2006) 096103.
[18] A. Rastelli, M. Stoffel, J. Tersoff, G.S. Kar, O.G. Schmidt, Phys. Rev. Lett. 95 (2005) 026103.
[19] A. Bernardi, J.O. Ossó, M.I. Alonso, A.R. Goñi, M. Garriga, Nanotechnology 17 (2006) 2602.

Nanotechnology 18 (2007) 475401 (7pp) doi:10.1088/0957-4484/18/47/475401

Evolution of strain and composition during growth and capping of Ge quantum dots with different morphologies

A Bernardi, M I Alonso, J S Reparaz, A R Goñi[1], P D Lacharmoise, J O Ossó[2] and M Garriga

Institut de Ciència de Materials de Barcelona-CSIC, Esfera UAB, 08193 Bellaterra, Spain

E-mail: abernardi@icmab.es

Received 13 July 2007, in final form 26 September 2007
Published 17 October 2007
Online at stacks.iop.org/Nano/18/475401

Abstract

We follow the growth of islands with different shapes by monitoring the strain relaxation by reflection high energy electron diffraction (RHEED). Comparing a bimodal ensemble of pyramids and domes with a monomodal distribution of C-induced domes, we observe different relaxation pathways and a growth mode change from Stranski–Krastanow to Volmer–Weber. We also study the changes induced by the capping process with Si. Small strains in thin cap layers are revealed by spectroscopic ellipsometry. Raman spectroscopy is employed to probe the built-in strain and silicon intermixing in different types of islands, evidencing that smaller islands are enriched in Si and effectively recompressed, whereas bigger relaxed dots remain substantially unaffected.

(Some figures in this article are in colour only in the electronic version)

1. Introduction

The challenge of turning nanostructures like self-assembled quantum dots (QDs) into future nanoscale devices critically depends on the possibility to tailor the island shape, size distribution, composition and strain status [1–3]. In standard Ge/Si heteroepitaxy, 'anomalous' coarsening [4] and Si–Ge intermixing [5] compete as ways for elastic strain relaxation. The typical result is a broad dot-size distribution of coherent islands having different shapes [6–8] (shallow pyramids and steeper domes or barns). For large islands, called superdomes, there is a competition between elastic and plastic relaxation, which depends on the substrate temperature [9–11]. Classifications of island shapes and usual relaxation mechanisms are summarized in [8]. The population of domes and pyramids in an ensemble of islands is related to the total Ge coverage and the growth temperature [12], with bigger pyramids transforming into domes when a critical volume is reached. During annealing, the morphology of strained islands eventually oscillates [8, 13] between shallow and steeper shapes [14] so that the final dot topography is rather unpredictable. The drawback of the coexistence of islands with different shapes is that they are not only inhomogeneous in size but they also exhibit different composition [15] and elastic properties.

To achieve better dot uniformity there are different possible strategies. It is possible to remove large clusters and keep small pyramids by growth interruption and high temperature annealing [16]. In the Ge/Si system pyramids are strongly intermixed and dome-shaped islands with larger aspect ratios and Ge-rich compositions are preferred. In order to obtain small domes, a simple bottom-up strategy involves surface modification by addition of impurities [17–21], which affect the kinetics and alter the energetics of nucleation. Deposition of carbon during the process of QD growth enables a dramatic decrease of the diffusion length of adatoms and a modification of the strain field of the surface. Carbon promotes the growth of domes even at very low Ge coverage and in a wide temperature range [20, 22] without the coexistence of pyramids or hut clusters. The peculiar interplay of chemical interactions between Si, Ge and C and the resulting local enhancement of strain are responsible for

[1] ICREA Research Professor.
[2] Present address: MATGAS 2000 AIE, 08193 Bellaterra, Spain.

 © 2007 IOP Publishing Ltd Printed in the UK

relevant changes in the growth mechanism. In addition to better sample homogeneity, size-reduced domes are attractive for the conception of quantum optoelectronic devices [1]. However, we point out that radiative recombination will typically be indirect in real space (type II), suitable for instance for photodetector operation. Type I structures suitable for stimulated emission are possible at even smaller sizes, as was demonstrated from submonolayer Ge QDs [23].

In the present work we describe an experimentally observed growth mode change from Stranski–Krastanow (SK) in the absence of C to Volmer–Weber (VW) when depositing Ge on a C-enriched Si substrate. The evolution of the surface lattice parameter is followed up to large Ge coverage where both elastic and plastic mechanisms of relaxation are active. We also study the process of capping the islands with silicon to understand how it affects the final composition and the elastic recompression of the dots. Finally, we also focus on the structural properties of the cap layer and obtain evidence of the existence of compressive stress induced by local strain fields associated with carbon-rich patches.

2. Experimental details

Samples under investigation were prepared by solid-source molecular beam epitaxy. After oxide desorption at 900 °C and 100 nm thick Si buffer layer deposition, the substrate temperature was set to 500 °C. Subsequently, ~0.1 monolayers (MLs) of carbon were predeposited on the Si surface from a calibrated sublimation filament. The self-assembling of carbon-induced quantum dots (C-QDs) was achieved by evaporation of 12 MLs of Ge. A reference sample was prepared following exactly the same growth procedure as above, but omitting the step of carbon predeposition. As a result standard Stranski–Krastanow quantum dots (SK QDs) were obtained. Finally, part of the surface of the samples was capped with a 10 nm thick Si layer deposited at 300 °C, in order not to alter the shape of buried dots. Growth was monitored *in situ* by reflection high energy electron diffraction (RHEED) and the island topography was studied *ex situ* by atomic force microscopy. In order to evaluate the composition and residual strain, samples were characterized by optical measurements at room temperature. Raman spectroscopy was carried out with the 514.5 nm line of an Ar-ion laser for excitation. Light was focused onto the sample with a spot size of about 1 μm and a laser power of 4 mW. In order to suppress contributions from second-order processes, we used the scattering geometry $z(xy)\bar{z}$, where x, y and z are the [100], [010] and [001] crystallographic directions, respectively. The ellipsometric spectra were collected using a rotating polarizer ellipsometer in the 1.4–4.8 eV spectral range.

3. Results

3.1. Growth mode and dot topography

When comparing conventional island ensembles with C-induced QDs the first striking feature concerns the morphology. We use the same island shape denominations as those given in [8]. There are two equilibrium island shapes: shallow islands called pyramids (Ps) with {105} crystallographic planes and domes (Ds) with steeper {113} facets. The aspect ratios (defined as the dot height over the square root of the basis area) of these islands are different: pyramids have aspect ratios much smaller than 0.1 and well-developed domes have values around 0.2. The evolution P → D may be rather continuous and the transition islands are called transition domes (TDs), with aspect ratios around 0.15. By changing shapes, islands relax elastically, i.e., Ps and TDs are coherent islands. When TDs evolve into Ds reaching a critical size, plastic relaxation will set in [9, 10] giving rise to larger dome-shaped dislocated islands (superdomes).

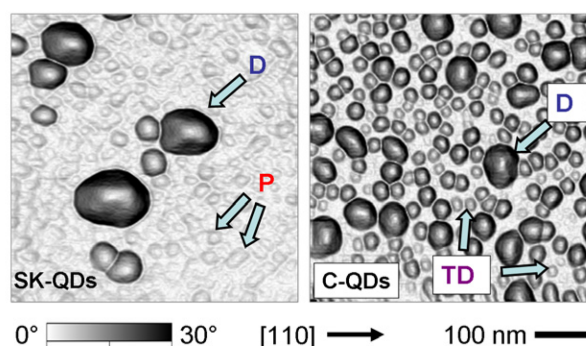

Figure 1. Topographic images of uncapped Stranski–Krastanow quantum dots (SK-QDs) (left) and carbon-induced QDs (C-QDs) (right). The grey scale indicates surface inclination (steeper facets correspond to darker color). Labels in figure refer to pyramids (Ps), transition domes (TDs) and domes (Ds).

We compare the different morphologies in figure 1. We choose a representation with the facet inclination as the z-scale, so that different grey-levels indicate different families of islands. That is, lighter dots are shallow pyramids and darker islands correspond to domes. Ordinary SK self-assembling of Ge islands on Si (left panel) leads to a broad bimodal distribution of pyramids and domes. Addition of carbon to the surface, due to the enhancement of strain fields, stabilizes the dome-shaped islands [24]. In the C-QD ensemble (right panel) even the smaller islands are dome-shaped, with aspect ratios increasing with the dot volume, from ~0.1 for the smaller or transition domes to ~0.2 for the bigger domes. It is evident that the use of carbon yields better island homogeneity with a much narrower dot size distribution, although in this example we go beyond optimal coverage on purpose.

In order to unravel the mechanism leading to such different dot topographies, we performed *in situ* RHEED experiments during the growth of the islands. In figure 2 we show the evolution from the streaky pattern of an atomically flat Si(001) surface to the spotty pattern associated with the surface roughening and nucleation of islands. Apart from a qualitative overview of the growth process from RHEED images it is possible to extract streak intensity profiles which allow us to obtain quantitative information [25] about the strain relaxation mechanism. The spacing of diffraction streaks gives the relative variation of the *in-plane* lattice parameter in real time [26–28].

The measured evolution of in-plane lattice parameter is plotted in figure 3. The top panel corresponds to SK self-assembling. In this case, during the first stage of Ge deposition

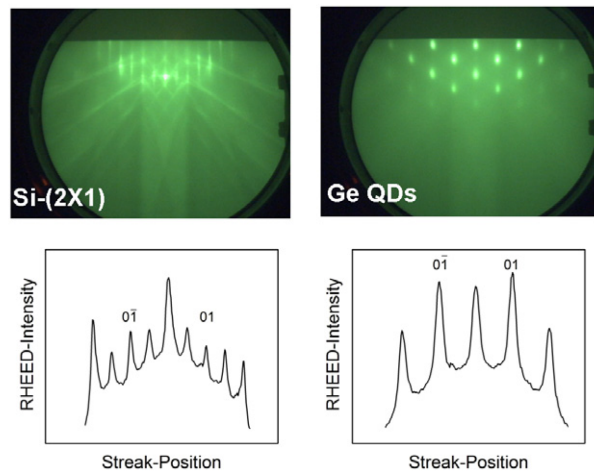

Figure 2. RHEED patterns (top panels) along a ⟨110⟩ azimuth of a flat (2 × 1)-reconstructed Si(001) surface and of transmission diffraction from 3D islands. The bottom panels show the corresponding streak intensity profiles extracted from RHEED images.

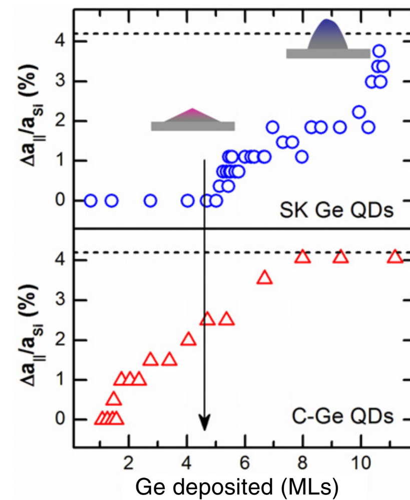

Figure 3. In-plane lattice parameter relaxation associated with the nucleation of 3D islands obtained from RHEED intensity profiles. The vertical arrow indicates the point where dot nucleation for the conventional Stranski–Krastanow islands sets in (top panel).

we do not observe any evolution of the lattice parameter, consistent with the growth of a flat pseudomorphically strained wetting layer (WL). After a critical coverage of 4–5 MLs the streaky pattern starts to evolve into a spotty pattern and from the streak spacing variation we infer a progressive increase of the lattice parameter, which indicates a strain relief associated with the transition from 2D growth to nucleation of 3D clusters. These observations are consistent with the expected Stranski–Krastanow (SK) growth mode. Moreover, from our data we can recognize clearly two stages of strain relaxation. A first plateau around the value $\frac{\Delta a_{\parallel}}{a_{Si}} \lesssim 1\%$ can be attributed to the nucleation and growth of shallow pyramids, and progressive relaxation up to $\lesssim 2\%$ corresponds to their shape transition into steeper domes [7, 12, 14]. After about 10 MLs of Ge coverage we observe a quicker relaxation, almost reaching the lattice mismatch value for Ge bulk (~4%). This can be associated with a more efficient plastic strain relief leading to dislocated domes (also called superdomes). At the final coverage of 12 MLs all these islands coexist.

If we now consider the strain relaxation pathway for C-QDs shown in the bottom panel of figure 3, we observe that the lattice parameter starts to evolve from the very early stages of Ge deposition, indicating that 3D relaxation occurs without the formation of a flat strained WL. This strain relaxation dynamics confirms that the presence of C on the surface induces a change of growth mode from Stranski–Krastanow to Volmer–Weber (VW), as previously demonstrated by other RHEED experiments [29, 30] (qualitative study of the streaky–spotty transition) and scanning tunneling microscopy [31]. In our present quantitative RHEED data analysis of C-QDs growth we cannot appreciate sharply differentiated stages of strain relaxation, suggesting that there is no clear shape transition. This observation is consistent with the measured final AFM topography revealing dot homogeneity, without the presence of islands with different shapes. However, the quick lattice relaxation between 6–8 MLs is likely to involve dislocations.

3.2. Recompression of capped islands and Si intermixing

We now turn to discuss the effects of capping with Si, which changes the strain status of the dots [32, 33] and composition [34–36]. Knowledge of the complex strain field generated inside and outside the dots is determinant for predicting the properties of the nanostructures and for engineering the process of piling up a multistack of vertically correlated islands [2, 37, 38]. During capping, the additional strain is partially relieved by Si intermixing into the islands, so that the composition of the island is expected to change towards a Si enrichment [34]. Notice that capping is done here at substrate temperature of 300 °C, which we checked preserves the island shapes.

Raman spectroscopy is a surface sensitive technique useful to extract information about both composition and strain inside the QDs [10, 24, 35, 36, 39–41]. In figure 4(a) we show the Raman spectra for the investigated samples, where the dominant feature is the Ge–Ge phonon band near 300 cm^{-1}. We always observe that the uncapped samples are characterized by weaker peak intensities, possibly due to partial oxidation of the dots and to the presence of surface states that reduce the electronic lifetimes, affecting the resonant enhancement of the Raman intensity. In contrast, in the capped samples, larger Raman intensity close to resonance is possible in the absence of surface states [32]. Moreover, a Si–Ge band at ~400 cm^{-1}, which was almost absent for uncapped samples (see inset to figure 4(a)), is apparent in the spectra of the capped samples. The relative intensity between Ge–Ge and Si–Ge phonon bands [42, 43] gives at a first glance information on the average composition: uncapped islands are almost pure Ge ($x_{Ge} > 90\%$), whereas capped islands have a composition ranging from $x_{Ge} \sim 80\%$ (for SK QDs) to $x_{Ge} \sim 85\%$ (for C-QDs). The Si intermixing at relatively low temperature is driven by surface diffusion rather than by bulk processes [5, 44, 45], so the reduced adatom mobility associated with the presence of carbon may be the reason why capped C-QDs remain slightly Ge richer.

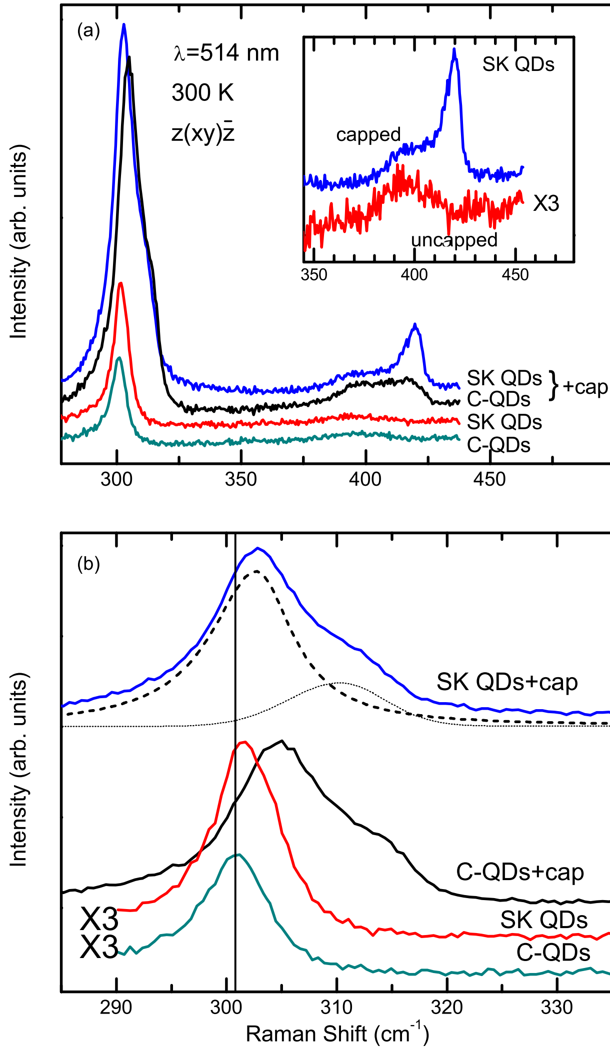

Figure 4. Raman spectra of C-induced and SK QDs for capped and uncapped samples (all with 12 MLs Ge). The inset shows the Si–Ge phonon mode associated with the Si intermixing during the capping process. The bottom panel represents a close-up of the spectra in the region of the Ge–Ge phonon mode. The spectra can be fitted with two asymmetric Gaussians (shown in the figure). The vertical line indicates the Ge–Ge phonon frequency for bulk Ge.

By fitting the peak positions of the phonon bands it is possible to obtain further insight into the nanostructure composition and especially in the strain status. The presence of some dislocated islands does not affect the subsequent analysis, which is completely general. Qualitatively, a red-shift of the Ge–Ge peak is associated with Si enrichment, and a blue-shift is indicative of compressive strain. In figure 4(b) the main Ge–Ge peak is shown with greater detail. The peak position for the Ge–Ge band of uncapped islands ($\sim$301.3 cm^{-1}) is quite close to the frequency expected for relaxed Ge (300.8 cm^{-1}), whereas capped samples are characterized by a blue-shift of the Ge–Ge peak ascribed to the partial recompression of the dots. From figure 4(b) it is remarkable that after capping we are able to resolve two clear contributions to the phonon mode, which can be deconvoluted by fitting two Gaussian terms, giving a low frequency peak at $\omega_{\text{Ge–Ge}} \lesssim 305$ cm^{-1} and a high frequency peak at $\omega_{\text{Ge–Ge}} \gtrsim 310$ cm^{-1}. Similar features observed for nominally monomodal ensembles of dots were recently interpreted as the fingerprints stemming from an intermixed shell and a Ge-rich core, respectively [41]. This core/shell model does not hold for our experiment since the low frequency peak (associated with intermixing during encapsulation of islands) is already present for uncapped dots. Considering the topography of the present samples, we rather ascribe the two contributions to two different families of islands: the high frequency mode is associated with smaller compressed pyramids or transition domes, in the case of the C-QDs, whereas the low frequency peak is mainly related to the bigger relaxed domes with dislocations. Notice in figure 4(a) that the two spectral contributions to the Ge–Ge band can be related to those observed in the Si–Ge band spectral range, namely a lower frequency broad band at $\sim$390 cm^{-1} and a higher frequency peak at $\sim$420 cm^{-1}. The observation of two Ge–Ge modes and their two Si–Ge counterparts allows us to solve for values of composition and strain, as detailed below. The only combination that makes sense is to pair both lower frequency peaks (305 and 390 cm^{-1}) and both higher frequency peaks (310 and 420 cm^{-1}). Taking into account the experimental composition dependence for both the Ge–Ge and Si–Ge LO phonon bands [46], we obtain the following system of two equations where the unknowns are the composition x in $Si_{1-x}Ge_x$ and strain $\epsilon_\parallel$ [24, 10]:

$$\omega_{\text{Ge–Ge}} = 284 + 5x + 12x^2 + b_{\text{Ge–Ge}}\epsilon_\parallel, \quad (1)$$

$$\omega_{\text{Si–Ge}} = 400 + 29x - 95x^2 + 213x^3 - 170x^4 + b_{\text{Si–Ge}}\epsilon_\parallel, \quad (2)$$

provided the strain-shift coefficients b of the last terms of equations (1), (2) are known. The generalized expression is

$$b = \omega(x)(-\tilde{K}_{11}\alpha/2 + \tilde{K}_{12}). \quad (3)$$

In equation (3), $\tilde{K}_{ij}$ are the deformation potentials and $\alpha = -\epsilon_\perp/\epsilon_\parallel$ describes the strain field inside the dots. It is generally assumed that the Ge islands are biaxially strained [2] ($\alpha \simeq 0.75$) like a flat pseudomorphic layer, but this approximation might be inaccurate at least for capped dots with steeper facets (domes) that should tend to an hydrostatic strain field ($\alpha = -1$) [33]. Typical experimental values for $b_{\text{Ge–Ge}}$ of $Si_{1-x}Ge_x$ alloys and Ge quantum dots reported in the literature [40, 42, 43, 47] show considerable dispersion, ranging from -400 to -1000 cm^{-1}, remarkably matching the values that can be obtained from equation (3), if we consider the limiting cases of biaxial and hydrostatic strain (assuming that the deformation potentials of Ge are $\tilde{K}_{11} = -1.57$ and $\tilde{K}_{12} = -2.07$)[Note 3]. Since the values of b directly affect the obtained $\epsilon_\parallel$, we conclude that the main source of uncertainty in determining the strain in the dots comes from the lack of consensus in choosing the proper elastic model to describe a compressed island. Therefore, in table 1 we report two results assuming both limiting cases of biaxial and hydrostatic strain fields.

The dot compositions obtained from this detailed analysis and reported in table 1 are compatible with the average compositions determined above from the peak intensity ratio between the Ge–Ge and Si–Ge modes. Uncapped samples consist of Ge-rich islands ($\sim$90%) and are almost fully relaxed.

[3] Our measurement, unpublished.

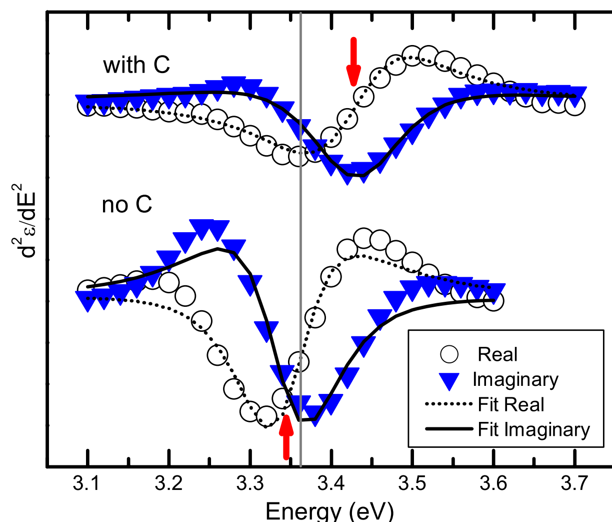

Figure 5. Second derivative with respect to energy of the dielectric function (imaginary and real parts) of the Si cap layer as obtained from the ellipsometry spectra. Arrows represent the fitted energies for the electronic transition E_1. The vertical line shows the E_1 energy for unstrained silicon, and a blue-shift (red-shift) corresponds to compressive (tensile) strain.

Table 1. Composition and strain obtained from the peak positions of the Ge–Ge and Si–Ge phonon modes. For capped samples the results refer to both the high and low frequency contributions to the Raman spectra. We calculate strain assuming both limiting cases of biaxial and hydrostatic strain. In the last column we report as a reference the maximum strain given by the lattice mismatch for each composition.

	x_{Ge} (%)	$\epsilon_{\parallel}^{biaxial}$ (%)	$\epsilon_{\parallel}^{hydrostatic}$ (%)	$\epsilon_{\parallel}^{max}$ (%)
SK QDs	92 ± 2	−1.0	−0.4	−3.7
SK QDs + cap	77 ± 15	−3.0	−1.6	−3.0
	89 ± 3	−1.1	−0.5	−3.5
C-QDs	92 ± 2	−0.8	−0.3	−3.7
C-QDs + cap	82 ± 15	−3.2	−1.9	−3.2
	94 ± 2	−1.3	−0.6	−3.8

After capping, there are two distinct regions showing not only different intermixing but also different strain. This means that some of the islands, presumably the smaller dots, become ~10% richer in silicon and are strongly compressed. In fact, accepting that strain in small islands is well described by a biaxial model [33], then they turn out to be fully compressed upon capping. In contrast, the family of bigger islands remains Ge rich and only slightly recompressed by the cap layer. Results obtained by Raman spectroscopy confirm that the intermixing process during capping is strain-driven and affects mostly the smaller (Ps and TDs) coherent islands.

3.3. Structural properties of the cap layer

Characterization by spectroscopic ellipsometry, complementing the results from RHEED and Raman, is useful in understanding the inhomogeneity of the strain field of the cap layer in the regions above the islands and in between them [37, 48].

Spectroscopic ellipsometry represents a powerful complementary diagnostic tool allowing one, in particular, to probe the thin layer of silicon covering the islands. From the ellipsometric measurement we determine the thickness of deposited

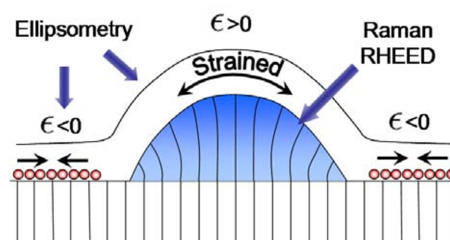

Figure 6. Sketch of the inhomogeneous strain field associated with a C-QD. Relaxed islands induce a tensile strain in the thin cap layer. Nevertheless, the presence of C-rich patches introduces compressive strain in the region of cap layer surrounding the islands.

cap layer and extract its dielectric function with an accurate fitting procedure and inversion algorithm, as discussed elsewhere [10]. By fitting the second derivative spectra of the cap layer dielectric function, we obtain the energy of the E_1 electronic transition [49], indicated by vertical arrows in figure 5. In the reference sample grown without carbon predeposition the E_1 transition is found to be slightly red-shifted compared to bulk Si, indicating the presence of average tensile strain in the cap layer induced by the Ge dots (see the sketch in figure 6). Surprisingly, the E_1 energy for the cap layer deposited on the C-QD sample is blue-shifted, thus reflecting the presence of average compressive strain, in spite of the presence of buried Ge islands which are expected to induce local tensile strain in the overgrown silicon. The structural information obtained by ellipsometry is an areal average of all the sample surface and in contrast to RHEED and Raman measurements does not provide local information related only to the dots. The results indicate that the silicon layer that grows on the C-alloyed surface which surrounds the islands must be compressively strained.

4. Discussion

By using complementary surface science tools we were able to study different aspects of the growth of strained Ge/Si islands. RHEED was used to *in situ* monitor the evolution of the *in-plane* lattice parameter, allowing us to determine the set in of strain relaxation due to nucleation of 3D clusters. In the absence of C, we observed the formation of a flat 2D layer (WL), taking place before the gain in elastic energy becomes dominant over the energetic term associated with the increase of surface (SK growth). In this case, the first stage of island growth accounts for the relaxation of less than 50% of the lattice mismatch and it can be attributed to the nucleation of small and shallow pyramids. When the islands get bigger, they transform into domes or dislocated Ge clusters that can efficiently relax the strain, so that after 10 MLs of coverage we already measure a lattice parameter approaching the value of bulk Ge.

The strain-relaxation pathway changes quite dramatically when carbon is used to engineer the dot topography. In this case, the presence of carbon-rich patches and the repulsive Ge–C interaction prevent the formation of a WL, i.e., it is energetically more convenient to increase the Ge surface with nucleation of 3D clusters, rather than wetting the

carbon-alloyed surface. As a result, the lattice parameter relaxation associated with the 3D nucleation can be observed starting from the very first stages of Ge deposition which is experimental evidence of the growth mode change from Stranski–Krastanow to Volmer–Weber. In the case of C-QDs, we do not observe two regimes of strain relaxation (shallow and steeper islands) but a continuous progressive evolution of the lattice parameter, and this observation is consistent with the AFM topography characterized only by dome-shaped clusters. The density of domes is exceptionally high ($\sim 10^{11}$ cm^{-2}) due to reduced mobility of Ge on a roughened carbon-alloyed surface. Surprisingly, the smaller domes have volumes much below the typical threshold value expected for the pyramid-to-dome shape transition, i.e., the presence of carbon reduces drastically the critical volume associated with the 'anomalous' coarsening. This experimental observation can be accounted for by the enhanced effective mismatch between the substrate and the overlayers [24], without the need to invoke differences of the surface energy between shallower and steeper facets related to the presence of carbon, since the carbon is arranged in patches outside the islands. The reduced surface diffusion that explains the high dot density is likely to be also responsible for the quenching of Si intermixing in the islands. Both island morphology and composition keep evolving while the growth or annealing proceeds. Intermixing dynamics is thought to be dominated by surface rather than bulk diffusion [5, 44], especially at temperatures below 500 °C. Therefore, it is possible that in the presence of C the process of Si intermixing is kinetically limited. Then, capped C-QDs are less intermixed and retain larger strain than SK-QDs, as experimentally observed (see table 1). The limited intermixing as a partial strain-reliever and the presence of local inhomogeneous strain fields are both consistent with the extreme decrease of the critical volume for the pyramid-to-dome transition, to the point where only dome-shaped clusters can be observed.

As a result of the deposition of 12 MLs of Ge, the dots completely relax their strain towards their apex, as can be measured by RHEED probing the topmost atomic layers. Raman spectroscopy becomes a useful tool to study instead the average strain distribution inside the volume of the islands. The relevant question arising when evaluating the Raman results is to decide which is the adequate elastic model to describe the strain status of a quantum dot. Once we have measured the LO phonon frequency shift associated with the lattice deformation, in order to quantify the strain, we need to know the relation existing between the *in-plane* ($\epsilon_{\parallel}$) and *out-of-plane* ($\epsilon_{\perp}$) components. A tiny shallow island is somehow similar to a pseudomorphic 2D layer and its strain status is likely described by a biaxial model (i.e., the lattice is compressed in the *in-plane* direction and it is free to expand in the *out-of-plane* direction, according to Hooke's law). For steeper islands embedded in a matrix (capped dots) [32, 33], the strain status of dots can be rather described by a hydrostatic model ($\epsilon_{\perp} = \epsilon_{\parallel}$). According to the results listed in table 1 the uncapped dots (both SK and C-QDs) retain only between 10% and 30% of the strain, depending on whether we consider a hydrostatic or biaxial model, respectively.

After capping with a 10 nm thick Si layer, the islands are recompressed and we can clearly recognize in Raman spectra features corresponding to two contributions from portions of material with different composition and strain. The experimental piece of evidence is that we are probing regions of material with rather different structural properties; thus, it is unlikely that they refer to different portions of the same island. This argument leads us to ascribe the contributions to two separate families of islands: the smaller coherent islands are fully recompressed (according to the biaxial model) whereas the bigger relaxed domes are less affected by the thin cap layer [33]. Raman spectroscopy turns out to be a powerful technique capable of pointing out the presence of local structural inhomogeneities of the quantum dots, complementing the information achieved by RHEED analysis. When probing dot ensembles most of the characterization tools are sensitive to the 3D clusters due to the grazing incidence geometry and shadowing (this is the case of RHEED) or for confinement of carriers in the islands and the absence of a signal collectable from the WL (like in Raman spectroscopy [24, 40]). In this context, ellipsometry provides unique information on the average strain field of the silicon cap layer, which indicates a local compressive strain in the regions between islands associated with the carbon-rich patches.

5. Conclusions

In summary, we have studied the strain relaxation mechanism during self-assembling of Ge QDs, comparing the conventional Ge/Si heteroepitaxy with the carbon-engineered growth. RHEED analysis permitted us to recognize three stages of strain relaxation after the growth of a pseudomorphic WL, corresponding to the nucleation of pyramids, the shape transition to domes, and dislocation formation. For the sample obtained after pre-depositing carbon on the silicon substrate, we found instead experimental evidence for a growth mode change from Stranski–Krastanow to Volmer–Weber. An ellipsometric study of the silicon cap layer was helpful to point out the presence of compressive strain associated with the local strain field in proximity of the carbon-rich patches in between the islands.

The topography of the quantum dot ensembles was correlated to the structural properties (i.e., strain and composition) measured by Raman spectroscopy. In particular, the capping process put in evidence two distinct regions of the sample with different local composition and elastic properties. We interpreted our experimental results as signals coming from two families of islands, i.e., smaller intermixed dots that get highly recompressed and bigger domes only slightly affected by the deposition of the silicon cap layer.

Optical techniques combined with RHEED and AFM permit one to obtain an overall insight into the growth mechanism of SK and C-QDs, with the possibility to capture features which hint at the local structure of single quantum dots. Nevertheless, in order to unravel the complete accurate picture, single dot spectroscopy or experiments on perfectly monomodal dot ensembles would be required.

Acknowledgments

We are grateful to M S Hegazy for fruitful discussions on RHEED analysis. We acknowledge financial support from the Dirección General de Investigación from Spain under

project MAT2006-02680. AB is also grateful to the Spanish Ministry of Education and Science for a FPI fellowship, JSR acknowledges the Alßan program, and PDL the Spanish Research Council (CSIC) for an I3P fellowship.

References

[1] Baribeau J M, Wu X, Rowell N L and Lockwood D J 2006 *J. Phys.: Condens. Matter* **18** R139
[2] Brunner K 2002 *Rep. Prog. Phys.* **65** 27
[3] Stangl J, Holý V and Bauer G 2004 *Rev. Mod. Phys.* **76** 725
[4] Ross F M, Tersoff J and Tromp R M 1998 *Phys. Rev. Lett.* **80** 984
[5] Ratto F, Costantini G, Rastelli A, Schmidt O G, Kern K and Rosei F 2006 *J. Exp. Nanosci.* **1** 279
[6] Mo Y-W, Savage D E, Swartzentruber B S and Lagally M G 1990 *Phys. Rev. Lett.* **65** 1020
[7] Medeiros-Ribeiro G, Bratkovski A M, Kamins T I, Ohlberg D A A and Williams R S 1998 *Science* **279** 353
[8] Stoffel M, Rastelli A, Stangl J, Merdzhanova T, Bauer G and Schmidt O G 2007 *Phys. Rev.* B **75** 113307
[9] LeGoues F K, Reuter M C, Tersoff J, Hammar M and Tromp R M 1994 *Phys. Rev. Lett.* **73** 300
[10] Alonso M I, de la Calle M, Ossó J O, Garriga M and Goñi A R 2005 *J. Appl. Phys.* **98** 033530
[11] Merdzhanova T, Kiravittaya S, Rastelli A, Stoffel M, Denker U and Schmidt O G 2006 *Phys. Rev. Lett.* **96** 226103
[12] Rudd R E, Briggs G A D, Sutton A P, Medeiros-Ribeiro G and Williams R S 2003 *Phys. Rev. Lett.* **90** 146101
[13] Ledentsov N N, Shchukin V A, Bimberg D, Ustinov V M, Cherkashin N A, Musikhin Y G, Volovik B V, Cirlin G E and Alferov Z I 2001 *Semicond. Sci. Technol.* **16** 502
[14] Rastelli A, Kummer M and von Känel H 2001 *Phys. Rev. Lett.* **87** 256101
[15] Ratto F, Locatelli A, Fontana S, Kharrazi S, Ashtaputre S, Kulkarni S, Heun S and Rosei F 2006 *Small* **2** 401
[16] Ledentsov N N *et al* 2000 *Semicond. Sci. Technol.* **15** 604
[17] Schmidt O G, Lange C, Eberl K, Kienzle O and Ernst F 1997 *Appl. Phys. Lett.* **71** 2340
[18] Beyer A, Muller E, Sigg H, Stutz S, Grutzmacher D, Leifeld O and Ensslin K 2000 *Appl. Phys. Lett.* **77** 3218
[19] Wakayama Y, Gerth G, Werner P, Gösele U and Sokolov L V 2000 *Appl. Phys. Lett.* **77** 2328
[20] Kim J Y, Ihm S H, Seok J H, Lee C H, Lee Y H, Suh E K and Lee H J 2000 *Thin Solid Films* **369** 96
[21] Jernigan G G and Thompson P E 2005 *Thin Solid Films* **472** 16
[22] Wakayama Y, Sokolov L V, Zakharov N, Werner P and Gösele U 2003 *Appl. Surf. Sci.* **216** 419
[23] Makarov A G, Ledentsov N N, Tsatsul'nikov A F, Cirlin G E, Egorov V A, Ustinov V M, Zakharov N D and Werner P 2003 *Semiconductors* **37** 210
[24] Bernardi A, Ossó J O, Alonso M I, Goñi A R and Garriga M 2006 *Nanotechnology* **17** 2602
[25] Wei X H, Li Y R, Zhu J, Zhang Y, Liang Z and Huang W 2005 *J. Phys. D: Appl. Phys.* **38** 4222
[26] Bernardi A, Alonso M I, Goñi A R, Ossó J O and Garriga M 2007 *Surf. Sci.* **601** 2783
[27] Nikiforov A I, Cherepanov V A, Pchelyakov O P, Dvurechenskii A V and Yakimov A I 2000 *Thin Solid Films* **380** 158
[28] Osten H J and Klatt J 1994 *Appl. Phys. Lett.* **65** 630
[29] Dentel D, Bischoff J L, Kubler L, Stoffel M and Castelein G 2003 *J. Appl. Phys.* **93** 5069
[30] Stoffel M, Simon L, Bischoff J L, Aubel D, Kubler L and Castelein G 2000 *Thin Solid Films* **380** 32
[31] Leifeld O, Beyer A, Grutzmacher D and Kern K 2002 *Phys. Rev.* B **66** 125312
[32] Bernardi A, Reparaz J S, Goñi A R, Alonso M I and Garriga M 2007 *Phys. Status Solidi* b **244** 76
[33] Reparaz J S, Bernardi A, Goñi A R, Lacharmoise P D, Alonso M I, Garriga M, Novák J and Vávra I 2007 *Appl. Phys. Lett.* **91** 081914
[34] Lin J H, Yang H B, Qin J, Zhang B, Fan Y L, Yang X J and Jiang Z M 2007 *J. Appl. Phys.* **101** 083528
[35] Baranov A V, Fedorov A V, Perova T S, Moore R A, Yam V, Bouchier D, Thanh V L and Berwick K 2006 *Phys. Rev.* B **73** 075322
[36] Kolobov A V, Morita K, Itoh K M and Haller E E 2002 *Appl. Phys. Lett.* **81** 3855
[37] Tersoff J, Teichert C and Lagally M G 1996 *Phys. Rev. Lett.* **76** 1675
[38] Schmidt O G, Denker U, Christiansen S and Ernst F 2002 *Appl. Phys. Lett.* **81** 2614
[39] Bernardi A, Alonso M I, Goñi A R, Ossó J O and Garriga M 2006 *Appl. Phys. Lett.* **89** 101921
[40] Tan P H, Brunner K, Bougeard D and Abstreiter G 2003 *Phys. Rev.* B **68** 125302
[41] Valakh M Y, Yukhymchuk V, Dzhagan V M, Lytvyn O S, Milekhin A G, Nikiforov A I, Pchelyakov O P, Alsina F and Pascual J 2005 *Nanotechnology* **16** 1464
[42] Tsang J C, Mooney P M, Dacol F and Chu J O 1994 *J. Appl. Phys.* **75** 8098
[43] Volodin V A, Efremov M D, Deryabin A S and Sokolov L V 2006 *Semiconductors* **40** 1314
[44] Leite M S, Medeiros-Ribeiro G, Kamins T I and Williams R S 2007 *Phys. Rev. Lett.* **98** 165901
[45] Katsaros G, Costantini G, Stoffel M, Esteban R, Bittner A M, Rastelli A, Denker U, Schmidt O G and Kern K 2005 *Phys. Rev.* B **72** 195320
[46] Alonso M I and Winer K 1989 *Phys. Rev.* B **39** 10056
[47] Stoehr M, Aubel D, Juillaguet S, Bischoff J, Kubler L, Bolmont D, Hamdani F, Fraisse B and Fourcade R 1996 *Phys. Rev.* B **53** 6923
[48] Marchetti R, Montalenti F, Miglio L, Capellini G, De Seta M and Evangelisti F 2005 *Appl. Phys. Lett.* **87** 261919
[49] See, for instance, Yu P Y and Cardona M 1996 *Fundamentals of Semiconductors* (Berlin: Springer)

2.2 Growth and characterization of SiGe nanostructures

The understanding of the strain-relaxation as a mechanism to drive the growth of nanostructures and the discernment of strain from optical measurements was extended to several SiGe systems, as part of different scientific collaborations. The main contributions of the author of this thesis are the growth of materials and the Raman spectroscopy analysis to determine strain and composition of nanostructures.

2.2.1 Raman characterization of SiGe dots under high pressure

The built-in strain in self-assembled quantum dots has large impact on their physical properties, but both its average value and degree of anisotropy are often unknown. We demonstrate that the pressure coefficient ($d\omega/dP$) of optical phonons might be used as probe to detect the strain status of the dots.

Samples were grown by solid-source molecular beam epitaxy and the Raman spectra were collected with a LabRam HR800 system in backscattering geometry at room temperature using different lines from an argon-ion laser. Measurements under pressure were carried out using the DAC[3] technique. A 4:1 mixture of methanol and ethanol was employed as the pressure-transmitting medium. Pressure was monitored in situ by the shift of the ruby R1 line. The samples loaded in the DAC were previously thinned to about 30 microns by mechanical polishing.

- The pressure coefficient obtained for the Ge mode of relaxed, uncapped islands is close to the corresponding value in bulk, whereas it is reduced by ~20% in presence of a Si cap layer. This result can be understood by taking into account the change of the boundary condition imposed to the Ge lattice, which is constrained to match that of the silicon matrix.

- When the method is applied to the case of Ge dots capped with Si layers of different thicknesses we observe a transition from a strictly biaxial stress situation for uncapped dots to a status of quasihydrostatic strain for cap-layer thicknesses larger than a critical value of the order of the dot height.

To explain this behaviour we developed a simple elastic model which takes into account the effects of the wetting layer WL and dot capping on the dot residual strain. We consider three contributions to the coefficient $d\omega_S/dP$. The obvious one is from the external hydrostatic pressure and the other two arise from changes in the built-in strain of the QDs indirectly induced by the applied pressure due to the different compressibility, i.e., bulk modulus of the dot and surrounding material. From the latter contributions one corresponds to the biaxial deformation caused by the wetting layer and the other comes from the recompression of the dots during capping. The conclusion is that there is an abrupt transition from a strictly biaxial stress situation of uncapped dots to a fully hydrostatic isotropic three-

---

[3] Diamond Anvil Cell

dimensional compression state of the dots for cap layers thicker than a certain critical value.

CORE RESEARCH ARTICLES

Article n: 5

Authors: A. Bernardi, J. S. Reparaz, A. R. Goñi, M. I. Alonso, and M. Garriga

Title: Raman scattering of capped and uncapped carbon-induced Ge dots under hydrostatic pressure

Journal: Physica Status Solidi B

Doi: 10.1002/pssb.200672543

Article n: 6

Authors: J. S. Reparaz, A. Bernardi, A. R. Goñi, P. D. Lacharmoise, M. I. Alonso, M. Garriga, J. Novák, and I. Vávra

Title: Phonon pressure coefficient as a probe of the strain status of self-assembled quantum dots

Journal: Applied Physics Letters

Doi: 10.1063/1.2773958

Article n: 7

Authors: J. S. Reparaz, A. Bernardi, A. R. Goñi, M. I. Alonso, and M. Garriga

Title: Polarized Raman study of self-assembled Ge/Si dots under hydrostatic pressure

Journal: Physica Status Solidi B

Doi: 10.1002/pssb.200880529

physica status solidi b

phys. stat. sol. (b) **244**, No. 1, 76–81 (2007) / **DOI** 10.1002/pssb.200672543

Raman scattering of capped and uncapped carbon-induced Ge dots under hydrostatic pressure

A. Bernardi[*], **J. S. Reparaz**, **A. R. Goñi**[**], **M. I. Alonso**, and **M. Garriga**

Institut de Ciència de Materials de Barcelona-CSIC, Esfera UAB, 08193 Bellaterra, Spain

Received 25 July 2006, accepted 8 August 2006
Published online 8 December 2006

PACS 62.50.+p, 63.22.+m, 78.30.Am, 78.67.Bf, 81.07.Ta

We compare results from Raman scattering for both capped and uncapped Ge quantum dots under hydrostatic pressure. The behavior of lattice vibrations and electronic transitions of the quantum dots are affected by the presence or absence of a cap layer. The pressure coefficient obtained for the Ge mode of relaxed, uncapped islands is close to the corresponding value in bulk, whereas it is reduced by ~20% in presence of a Si cap layer. This result can be understood by taking into account the change of the boundary condition imposed to the Ge lattice, which is constrained to match that of the silicon matrix. Measurements of the capped sample exhibit a resonant enhancement which is not appreciable for the uncapped dots. We relate this effect to the different lifetime of electronic states.

© 2007 WILEY-VCH Verlag GmbH & Co. KGaA, Weinheim

1 Introduction

Self-assembled Ge quantum dots (QDs) on Si(001) might, in the future, be considered as a candidate for optoelectronic applications by controlling the built-in strain which, in turn, allows to tailor the optical properties of nanostructures [1]. Raman scattering represents a powerful diagnostic tool to gather information on composition and strain in thin films and quantum dots. Moreover, due to the different compressibility of Si and Ge, experiments under hydrostatic pressure [2, 3] can also be used to tune the strain induced by the silicon matrix on the embedded Ge dots and, as a result, a shift of their interband electronic transitions can be obtained [4, 5]. Previous works on Ge dots under pressure focused on samples capped with thick layers (~200 nm) and reported pressure coefficients ($d\omega/dP$) for the optical Ge mode systematically lower than the value measured for the bulk material (3.9 cm^{-1}/GPa) [6–8]. Such discrepancy is discussed accounting for the different elastic properties of Ge and the surrounding silicon host matrix [9].

In this work, we investigated the case of uncapped quantum dots and we demonstrate that if the compression acting at the substrate/island interface (at the dot basis) is not affecting substantially the whole volume of the island, then the measured pressure coefficient tends to the value of bulk Ge. On the contrary, a really thin (10 nm) Si cap-layer is enough to achieve an important reduction (by ~20%) of the pressure coefficient, in analogy with data of the literature obtained for much thicker cap layers. Moreover, the presence of a thin cap layer enables the resonant enhancement of Raman scattering intensity to be observed, when an interband electronic transition of the Ge QDs is brought into resonance with the laser line by applying pressure. This effect is otherwise not detectable in uncapped samples due to a reduced lifetime of electronic states.

[*] Corresponding author: e-mail: abernardi@icmab.es, Fax: +34 93 580 57 29
[**] ICREA Research Professor

© 2007 WILEY-VCH Verlag GmbH & Co. KGaA, Weinheim

2 Experimental details

Samples were grown by solid-source molecular beam epitaxy according to the following procedure: after oxide desorption at 900 °C and 50 nm-thick Si buffer layer deposition, a ~4 Å thick Ge wetting layer was grown before depositing 0.1 monolayers (MLs) of carbon. This surface modification allows for the control of shape and density (~3×10^9 cm^{-2}) of islands in the next growth step, when ~6 Å of Ge are deposited at 500 °C. The resulting topography consists of dome-shaped dots 10–15 nm high [10]. For the capped sample, a 10 nm thick Si layer was subsequently grown at low temperature (300 °C) in order to avoid silicon intermixing and to preserve the island shape.

The Raman spectra were collected with a LabRam HR800 system in backscattering geometry at room temperature using different lines from an argon-ion laser. Measurements under pressure were carried out using the diamond anvil cell (DAC) technique. A 4:1 mixture of methanol and ethanol was employed as the pressure-transmitting medium. Pressure was monitored *in situ* by the shift of the ruby R1 line [12]. The samples loaded in the DAC were previously thinned to about 30 microns by mechanical polishing.

3 Results and discussion

3.1 Vibrational modes

Figure 1 shows Raman spectra measured at various pressures up to ~7 GPa in the capped sample. The Raman signal close to ~300 cm^{-1} is ascribed to the Ge–Ge phonon mode of the Ge dots. We note that these spectra were measured in crossed polarization $z(x, y)\bar{z}$, where x, y, and z are the [100], [010], and [001] crystallographic directions of the Si substrate, in order to suppress the second-order Raman signal of the transverse acoustical phonons of the Si substrate, which would interfere with the Ge dot mode. The very strong signal at ~520 cm^{-1} is attributed to the optical phonon of the Si substrate. Both modes shift to higher frequencies with increasing pressure and their intensities change due to resonance effects. The intensity decrease of the substrate mode is related to the shift of the E_1 electronic transition of Si to higher energies with increasing pressure.

The overall intensity of the spectra in the uncapped sample is much lower than for the capped one and no polarization analysis was made. However, the Ge–Ge mode and second order Si-2TA signal that almost overlap each other at $P = 0$ can be resolved under pressure, since they shift in opposite directions [7]. The frequency shift of the strong Si substrate signal at ~520 cm^{-1} can be used as internal wavenumber calibration of the spectra. The Raman shifts measured as a function of pressure are plotted in Fig. 2. A linear fit to the data gives the pressure coefficient $d\omega/dP = (3.9 \pm 0.1)$ cm^{-1}/GPa and the phonon frequency at

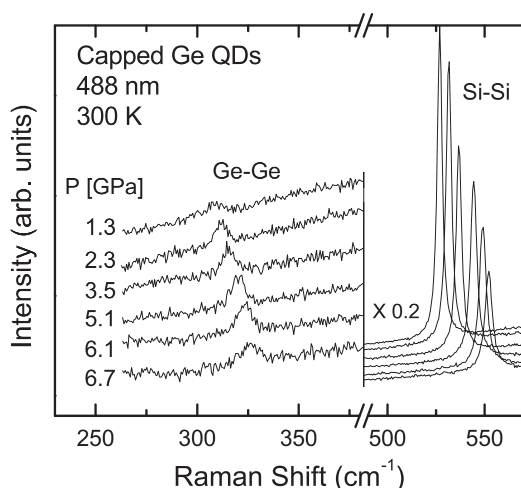

Fig. 1 Raman spectra of the capped QDs measured at different pressures. The peak at ~300 cm^{-1} (ambient pressure value) corresponds to the Ge–Ge phonon, whereas the very strong signal at ~520 cm^{-1} comes from the Si substrate.

 © 2007 WILEY-VCH Verlag GmbH & Co. KGaA, Weinheim

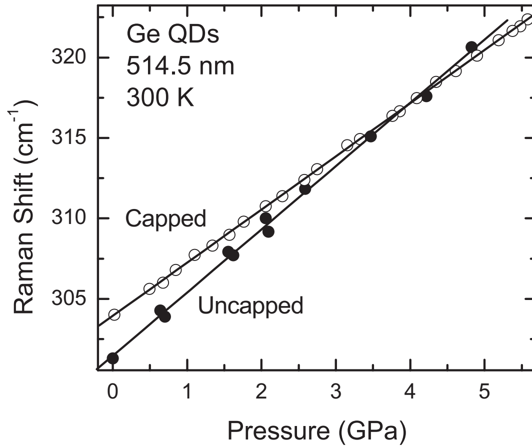

Fig. 2 Position of the Raman peaks observed in the two samples as a function of pressure. Open (closed) circles are results of the capped (uncapped) sample. Solid lines correspond to least-squares fits to the experimental data using a linear function.

zero pressure $\omega_0 = 301.5 \pm 0.2\ \text{cm}^{-1}$ for the uncapped sample, and $\text{d}\omega/\text{d}P = 3.30 \pm 0.02\ \text{cm}^{-1}/\text{GPa}$ and $\omega_0 = 303.94 \pm 0.04\ \text{cm}^{-1}$ for the capped sample. The values of ω_0 are different due to an increase in built-in strain for the capped QDs with respect to the relaxed, uncapped ones.

The pressure coefficient obtained for the uncapped sample is in very good agreement with the expected Ge bulk value. However, for the sample capped with 10 nm of Si we obtain instead a lower coefficient which is closer to the values reported for dots overgrown with much thicker Si cap-layers [7] or in superlattices [8].

The carbon-induced Ge dots under investigation are Ge rich (>90%) dome-shaped islands [10, 11], whose enhanced aspect-ratio leads to an efficient relaxation of the strain originating at the island/substrate interface due to the lattice mismatch between Ge and Si (~4%). Raman scattering spectroscopy gives information on the average Ge content and mean strain of the islands. In particular, the Ge–Ge mode is likely to steam mainly from the Ge-rich core of the islands, where holes are better confined. We thus expect that only a small contribution corresponds to the volume of material close and elastically coupled to the silicon substrate, for example, the wetting layer.

The different pressure coefficients obtained for samples with and without cap layer can be explained if we consider the boundary conditions applicable for each case. In general, the strain induced on the dot by applying external pressure can be decomposed in two terms:

$$\varepsilon(P) = \varepsilon^{\text{hydro}}(P) + \varepsilon^{\text{matrix}}(P)\,, \tag{1}$$

where the first term is the pure hydrostatic part of the Ge dot described by the Murnaghan equation of state (B_0^{Ge} is the bulk modulus of Ge)

$$\varepsilon^{\text{hydro}}(P) = \frac{a^{\text{Ge}}(P) - a_0^{\text{Ge}}}{a_0^{\text{Ge}}} = 1 + \left(\frac{B_0'}{B_0^{\text{Ge}}}P + 1\right)^{-\frac{1}{3B_0'}} \cong -\frac{P}{3B_0^{\text{Ge}}} + \dots \tag{2}$$

When the dot is constrained into a host material the additional term accounts for the strain originating from the different compressibility of the dot and matrix material. It depends on the boundary condition which we express in terms of a parameter $0 < \varphi < 1$ to describe the degree of relaxation of the dot according to

$$\begin{aligned}\varepsilon^{\text{matrix}}(P) &= \frac{a^{\text{QD}}(P) - a^{\text{Ge}}(P)}{a_0^{\text{Ge}}} \\ &= \frac{[a^{\text{Si}}(P) + \varphi(a^{\text{Ge}}(P) - a^{\text{Si}}(P))] - a^{\text{Ge}}(P)}{a_0^{\text{Ge}}} \qquad \begin{cases} \varphi = 0, & a^{\text{QD}} = a^{\text{Si}} \\ \varphi = 1, & a^{\text{QD}} = a^{\text{Ge}}\,. \end{cases}\end{aligned} \tag{3}$$

© 2007 WILEY-VCH Verlag GmbH & Co. KGaA, Weinheim

Combining Eqs. (1)–(3) we can obtain a general expression for the expected Raman frequency shift under pressure, with a constant term representing the shift due to the built-in strain (at applied pressure $P = 0$) and a linear term on P, whose slope is the pressure coefficient of the phonon mode (here $\tilde{K}_{ij}$ are the phonon deformation potentials for Ge):

$$\Delta\omega = \frac{\omega_0}{2}\left(\tilde{K}_{11} + 2\tilde{K}_{12}\right)\varepsilon(P) \approx \frac{\omega_0}{2}\left(\tilde{K}_{11} + 2\tilde{K}_{12}\right)\left[(1-\varphi)\,\frac{a_0^{\mathrm{Si}} - a_0^{\mathrm{Ge}}}{a_0^{\mathrm{Ge}}}\right] - \frac{\omega_0}{6}\left(\tilde{K}_{11} + 2\tilde{K}_{12}\right)\left[\frac{1}{B_0^{\mathrm{Si}}} + \varphi\left(\frac{1}{B_0^{\mathrm{Ge}}} - \frac{1}{B_0^{\mathrm{Si}}}\right)\right]P\,. \quad (4)$$

If we consider the sample with uncapped QDs and we assume that due to strain relaxation the average lattice parameter in the dot is $a^{\mathrm{QD}} \approx a^{\mathrm{Ge}}$ (corresponding to the case $\varphi \approx 1$), then there is no built-in strain and the pressure coefficient is given by the pure hydrostatic term, dependent on the bulk modulus of Ge. When a cap layer is present, the dot is compressed to adjust its lattice parameter to that of the host material, i.e. $a^{\mathrm{QD}} \approx a^{\mathrm{Si}}$ (if the dot is fully compressed then $\varphi \approx 0$). In this second case, as deduced from Eq. (4), only the bulk value of silicon enters in the calculation of the pressure coefficient and a constant frequency shift is arising from the built-in strain. From Eq. (4) follows that $(\mathrm{d}\omega/\mathrm{d}P)^{\mathrm{capped}}/(\mathrm{d}\omega/\mathrm{d}P)^{\mathrm{uncapped}} = B_0^{\mathrm{Ge}}/B_0^{\mathrm{Si}} = 0.77$, in good agreement with the experimental value (0.84).

3.2 Electronic states

The influence of pressure on the E_1 and $E_1 + \Delta_1$ electronic transitions of the QDs can be studied by resonant Raman measurements [13, 14]. When the energy of the exciting laser is close to that of the optical transitions, the resonance curve can be tuned by pressure. In our experiments we were able to measure a resonant enhancement of the Ge–Ge Raman phonon only on the sample with cap layer. The Raman intensity on the uncapped sample was rather low and remained constant within noise. This fact seems contradictory because these electronic transitions were measured by ellipsometry on the uncapped sample at $E_1 = 2.23$ eV and $E_1 + \Delta_1 = 2.43$ eV and are in the suitable spectral range. According to these energies, the QDs have an average composition $x = 0.92$ [10]. The Ge transition energies on the capped sample cannot be fitted clearly due to absorption by the Si cap, nevertheless, the QD composition should not be altered by the low T capping process. In order to understand the different resonance behavior with/without cap layer, we have modeled the shape and relative intensity of the two resonance curves by considering the expression of the Raman polarizability near the two-dimensional critical points E_1 and $E_1 + \Delta_1$ [15]:

$$|a|^2 \propto \left|\frac{d_{1,0}^5}{4\sqrt{2}}\,\frac{d(\chi^{E_1} + \chi^{E_1+\Delta_1})}{\mathrm{d}E_1} - d_{3,0}^5\left(\frac{\chi^{E_1} - \chi^{E_1+\Delta_1}}{\Delta_1}\right)\right|^2,$$
$$\chi^{E_j} = A_j\,\mathrm{e}^{i\phi_j}\,\frac{E_j^2}{E^2}\ln\left[1 - \left(\frac{E}{E_j - i\Gamma_j}\right)^2\right], \quad (5)$$

where χ^{E_j} is the electronic susceptibility and the critical-point parameters are the amplitude A_j, the width Γ_j and the phase ϕ_j. The latter are obtained from analysis of ellipsometric spectra. The pressure-tuned resonance curve is obtained at fixed laser energy $E = E_{\mathrm{L}} = 2.541$ eV. To introduce the dependence on pressure we take into account that both gaps shift with the same pressure coefficient α, that is, $E_j(P) = E_j(0) + \alpha P$. In this way, the pressure coefficient α can be evaluated from measurements using only one laser line.

The results for the resonant enhancement of the Ge-mode intensity for the capped sample are plotted in Fig. 3. Raman intensities are normalized relative to the maximum intensity at resonance and are given in arbitrary units. We fit the shape of the curve as a function of pressure having α as fit parameter. The

 © 2007 WILEY-VCH Verlag GmbH & Co. KGaA, Weinheim

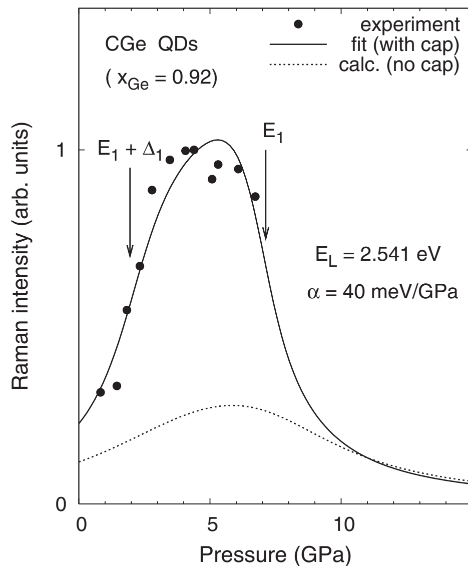

Fig. 3 Resonant Raman intensities of the Ge–Ge mode as a function of pressure for the capped dot sample (symbols). The solid (dotted) line is the calculated resonance curve for the capped (uncapped) dots, as explained in the text. Arrows indicate the pressure values for which the laser of energy E_L coincides with the corresponding optical transition.

actual transition energies are calculated from the known composition $x = 0.92$ and with a best-fit built-in biaxial strain $\varepsilon_{\|} = -0.6\%$. The rest of the needed quantities are taken from literature values for Ge [15]. In particular, the broadening of the gaps are taken as those of bulk Ge. For the uncapped sample, the broadening obtained from ellipsometry is about a factor of two larger. If we just calculate the resonance curve expected for the uncapped sample with larger broadening, the overall Raman intensity drops considerably, as shown in Fig. 3 by the dotted curve.

The value of $\alpha = 40 \pm 5$ meV/GPa obtained from the fit is similar to previous measurements in capped samples, reduced with respect to bulk Ge in the same way as the phonon pressure coefficient. It is likely that α in the uncapped sample should be closer to the bulk value but, unfortunately, it was not possible to be evaluated.

4 Conclusions

In this work we compared Raman scattering from Ge QDs under hydrostatic pressure when the dots are uncapped versus the situation where they are covered with a Si cap layer. We demonstrated that if the dots are not embedded in the Si matrix, then the measured pressure coefficient tends to the value of bulk Ge. On the contrary, just a very thin 10 nm Si cap layer is sufficient to reduce the coefficient by ~20% to values similar as previously obtained in literature for much thicker cap layers.

We considered the different boundary conditions to explain these two experimental situations, namely we dealt with the limiting cases of fully relaxed uncapped dots (highest $d\omega/dP$) and fully compressed capped dots (lowest $d\omega/dP$). Nevertheless, Eq. (4) also holds for a much more complex and generalized scenario, where an intermediate situation can be accounted for. Depending on the shape (aspect ratio) and on the size of the dots the degree of relaxation (φ) is expected to vary considerably and the DAC technique for the determination of pressure coefficients turns out to be a powerful diagnostic tool for studying the mechanisms of relaxation in self-assembled nanostructures.

Moreover, we observed that in uncapped dots no significant resonant enhancement of Raman scattering intensity can be observed, an effect clearly seen in presence of a thin cap layer. The increased lifetime (smaller broadening) of electronic states in capped samples is considered as a plausible explanation for this observation.

Acknowledgments We thank the spanish Ministerio de Educación y Ciencia for support through MAT2003-00738 and an FPI fellowship (A.B.). J.S.R. acknowledges an Alßan fellowship.

© 2007 WILEY-VCH Verlag GmbH & Co. KGaA, Weinheim

References

[1] J. Stangl, V. Holy, and G. Bauer, Rev. Mod. Phys. **76**, 725 (2004).
[2] Z. Sui, H. H. Burke, and I. P. Herman, Phys. Rev. B **48**, 2162 (1993).
[3] Z. Sui, I. P. Herman, and J. Bevk, Appl. Phys. Lett. **58**, 2351 (1991).
[4] Z. X. Liu, O. G. Schmidt, U. D. Venkateswaran, K. Eberl, and K. Syassen, Semicond. Sci. Technol. **15**, 155 (2000).
[5] K. L. Teo, S. H. Kwok, P. Y. Yu, and S. Guha, Phys. Rev. B **62**, 1584 (2000).
[6] M. Seon, M. Holtz, T.-R. Park, O. Brafman, and J. C. Bean, Phys. Rev. B **58**, 4779 (1998).
[7] K. L. Teo, L. Qin, Z. X. Shen, and O. G. Schmidt, Appl. Phys. Lett. **80**, 2919 (2002).
[8] L. Qin, K. L. Teo, Z. X. Shen, C. S. Peng, and J. M. Zhou, Phys. Rev. B **64**, 075312 (2001).
[9] L. Liu, K. L. Teo, Z. X. Shen, J. S. Sun, E. H. Ong, A. V. Kolobov, and Y. Maeda, Phys. Rev. B **69**, 125333 (2004).
[10] A. Bernardi, J. O. Ossó, M. I. Alonso, A. R. Goñi, and M. Garriga, Nanotechnology **17**, 2602 (2006).
[11] A. Bernardi, M. I. Alonso, A. R. Goñi, J. O. Ossó, and M. Garriga, Appl. Phys. Lett. **89**, 101921 (2006).
[12] H. K. Mao, J. Xu, and P. M. Bell, J. Geophy. Res. **91**, 4673 (1986).
[13] D. Bougeard, P. H. Tan, M. Sabathil, P. Vogl, G. Abstreiter, and K. Brunner, Physica E **21**, 312 (2004).
[14] A. B. Talochkin, S. A. Teys, and S. P. Suprun, Phys. Rev. B **72**, 115416 (2005).
[15] M. I. Alonso and M. Cardona, Phys. Rev. B **37**, 10107 (1988).

© 2007 WILEY-VCH Verlag GmbH & Co. KGaA, Weinheim

Phonon pressure coefficient as a probe of the strain status of self-assembled quantum dots

J. S. Reparaz,[a] A. Bernardi, A. R. Goñi, P. D. Lacharmoise, M. I. Alonso, and M. Garriga
Institut de Ciència de Materials de Barcelona-CSIC, Esfera UAB, 08193 Bellaterra, Spain

J. Novák and I. Vávra
Institute of Electrical Engineering, Slovak Academy of Sciences, 841 04 Bratislava, Slovakia

(Received 11 May 2007; accepted 31 July 2007; published online 23 August 2007)

The built-in strain in self-assembled quantum dots has large impact on their physical properties, but both its average value and degree of anisotropy are often unknown. The authors demonstrate that the pressure coefficient of optical phonons might be used as probe for the strain status of the dots. This method was applied to the case of Ge dots capped with Si layers of different thicknesses. The authors observe a transition from a strictly biaxial stress situation for uncapped dots to a status of quasihydrostatic strain for cap-layer thicknesses larger than a critical value of the order of the dot height. © *2007 American Institute of Physics*. [DOI: 10.1063/1.2773958]

Self-assembled quantum dots (QDs) are fundamental building blocks in optoelectronics nowadays[1] for their electronic, optical, and transport properties can be tailored by controlling dot parameters such as size, shape, and composition.[2] Another key parameter which is inherent to self-assembled growth and which has large influence on the optoelectronic properties of the dots is the residual built-in strain. Unfortunately, the strain status of the dots in the ready device is usually unknown. In this respect, Raman scattering has been demonstrated to be a powerful tool for measuring strain in compound semiconductor microstructures.[3] For the most frequent case of Raman measurements in backscattering geometry from the (001) surface, the strain is directly determined from the frequency shift of the Raman-allowed *singlet* component of the optical phonons according to[4,5] $\omega_s(x,\varepsilon)=\omega_0+b_s\varepsilon_\parallel$, where x is the alloy composition, $\varepsilon_\parallel$ is the in-plane strain, and b_s is the so-called strain-shift coefficient given by

$$b_s=\omega_0(-\tilde{K}_{11}\alpha/2+\tilde{K}_{12}). \qquad (1)$$

Here, ω_0 is the frequency of the unstrained phonon mode, $\tilde{K}_{ij}$ are the dimensionless phonon deformation potentials, as defined in Ref. 3, and $\varepsilon_\perp=-\alpha\varepsilon_\parallel$ is the relation between in-plane strain and that in the growth direction.

Equation (1) was deduced for the case of a strictly biaxial stress like that in quantum wells, for which $\alpha=2C_{12}/C_{11}\approx 1$, where C_{ij} are the elastic constants of the material. It also holds for a purely hydrostatic strain just by setting $\alpha=-1$, because in this case all three strain components along the principal axes are the same. In the general case of dealing with a mixed stress tensor containing a hydrostatic and a biaxial component, one might, in principle, still be using Eq. (1) but with an unknown value of the parameter α lying between ± 1. Such is too often the situation for self-assembled QDs depending on the aspect ratio and cap-layer thickness. Thus, it is not surprising to find in the literature a wide spread of values for the strain-shift coefficient b_s. For Ge/Si thin films and/or QDs, for instance, b_s ranges from about -400 to -800 cm^{-1}.[5–12] The conclusion is that in order to obtain sound quantitative results from Raman scattering for the residual strain in QD systems, it is crucial to know the strain situation, i.e., which is the pertinent value for α.

In this letter, we show that the pressure coefficient of the longitudinal optical phonon $(d\omega_s/dP)$ can be regarded as a probe of the strain status of quantum dots. The main reason for using the pressure derivative of the phonon frequency instead of the frequency itself is that the former is to a very good approximation only sensitive to the strain distribution rather than QD composition, size, or even the presence of dislocations. For that purpose we have studied systematically the hydrostatic pressure coefficient of the optical phonon of a series of carbon-induced Ge dots capped with a layer of Si with different thicknesses ranging from 0 to 200 nm. With increasing cap-layer thickness we observe a steep decrease of the phonon-pressure coefficient followed by saturation. Based on the results of a simple elastic model which accounts for the pressure dependence of the phonon frequency, we interpret this behavior as indication of a transition from a purely biaxial stress situation for uncapped dots to a status of quasihydrostatic compression for dots embedded in the Si matrix.

Samples were grown by molecular beam epitaxy on Si(001) substrates according to the following sequence: after deposition of a 100-nm-thick Si buffer layer, a 4.8 Å thick Ge wetting layer was grown before depositing 0.1 ML of carbon to control the shape and density of the QDs.[13–15] In the next step, 15 Å of Ge were grown at 500 °C leading to dot formation. Finally, the Ge QDs were capped with either 0, 3, 10, 50, or 200 nm of Si also at 500 °C. The reference sample without cap layer was used to determine the dot shape and density using atomic force microscopy (AFM). As shown in Figs. 1(a) and 1(b), the average dot height is about $h=14$ nm, the base length is $b=120$ nm, and the areal density is about 40 dots/μm^2. In Fig. 1(c), we show a representative transmission electron microscopy (TEM) image of a Ge dot. The cap layer can be easily identified, as it copies the QD shape.

Raman spectra were collected with a LabRam HR800 system in backscattering geometry at room temperature using the 514.5 nm line of an Ar$^+$ laser. Raman peak positions are determined with an error of less than 0.5 cm^{-1}. Measurements under pressure were carried out using the diamond

[a]Electronic mail: sebareparaz@hotmail.com

This article is copyrighted as indicated in the article. Reuse of AIP content is subject to the terms at: http://scitation.aip.org/termsconditions. Downloaded to IP: 158.109.18.157 On: Thu, 08 Oct 2015 12:16:40

 © 2007 American Institute of Physics

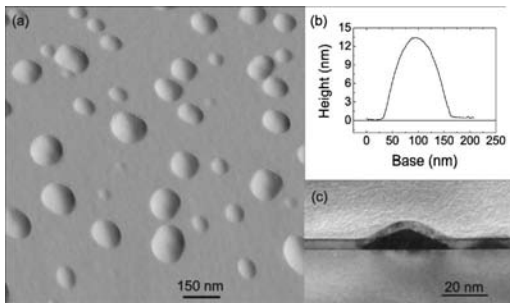

FIG. 1. (a) Topographic image by AFM of the uncapped sample and (b) line scan across a representative carbon-induced Ge quantum dot. (c) TEM image of the sample with 10-nm-thick cap layer showing one Ge dot in cross section.

anvil cell (DAC) technique. A 4:1 mixture of methanol and ethanol was employed as the pressure-transmitting medium. Pressure was monitored *in situ* by the shift of the Si longitudinal optical phonon, which was previously calibrated using the pressure shift of the ruby R1 line.[16] Samples loaded into the DAC were previously thinned to about 30 μm by mechanical polishing.

Figure 2 displays the dependence on hydrostatic pressure of the frequency of the Raman peak corresponding to the Ge optical phonon for five samples with cap-layer thickness, as indicated in the legend. We show only data in the pressure range up to 5 GPa, in which the pressure dependence of ω_s is well described by a straight line. The solid lines in Fig. 2 represent the results of least-squares fits to the data points using a linear relation.[17] The fit results are listed in Table I. The phonon pressure coefficient $(d\omega_s/dP)$ obtained from the fitted slopes exhibits a clear decreasing trend with increasing cap-layer thickness.

In Fig. 3 we have plotted the tabulated values of the phonon pressure coefficient as a function of cap-layer thickness. A fast exponential reduction of $d\omega_s/dP$ is observed for thicker Si caps. Preliminary results on smaller Ge QDs were published elsewhere.[18] To explain this behavior we developed a simple elastic model which takes into account the effects of the wetting layer (WL) and dot capping on the dot residual strain. We consider three contributions to the coefficient $d\omega_s/dP$. The obvious one is from the external hydrostatic pressure and the two arise from changes in the built-in strain of the QDs indirectly induced by the applied pressure due to the different compressibilities, i.e., bulk modulus of

TABLE I. Coefficients describing the pressure dependence of the Raman-allowed optical phonon of Ge dots capped with a Si layer of different thicknesses t obtained from fits of a linear expression $\omega_s=\omega_0+(d\omega_s/dP)\cdot P$ to the experimental data. Error bars are indicated in parenthesis.

Cap (nm)	ω_0 (cm^{-1})	$d\omega_s/dP$ (cm^{-1}/GPa)
0	301.4(1)	3.72(4)
3	302.4(2)	3.54(3)
10	304.2(2)	3.29(3)
50	305.2(2)	3.16(3)
200	304.7(2)	3.20(3)

the dot and surrounding material which we labelled hereafter B and A, respectively. From the latter contributions one corresponds to the biaxial deformation caused by the wetting layer and the other comes from the recompression of the dots during capping.

For hydrostatic pressures up to a few gigapascals, the reduction in relative volume is proportional to the applied pressure, $\Delta V/V \approx -P/B_0$, where B_0 is the bulk modulus. The corresponding contribution to the phonon pressure coefficient is simply given by

$$\frac{d\omega_s^{(P)}}{dP} = -\frac{a}{B_0^B}, \quad \text{with } a = \frac{\omega_0}{6}(\tilde{K}_{11}+2\tilde{K}_{12}), \tag{2}$$

the hydrostatic phonon deformation potential.[3] For $B\equiv$Ge is $-a/B_0^{\rm Ge} \approx 4$ cm^{-1}/GPa,[19] which constitutes an upper bound for the phonon pressure coefficient of the dots.

Although the residual QD strain is not known *a priori*, the way it varies by applying hydrostatic pressure due to the different elastic properties of the dot and surrounding material is readily estimated as $d\varepsilon_\parallel/dP=1/3(1/B_0^B-(1/B_0^A))$. In the present case, we have A$\equiv$Si with $B_0^{\rm Si}=98$ GPa and $B\equiv$Ge with $B_0^{\rm Ge}=75$ GPa.[20] Let us first consider the case of uncapped dots, for which there is a strictly biaxial stress situation due to the constraint of isomorphism to the Si substrate. Since such stress is transduced to the dot through the wetting layer, we call it the WL contribution. The dot, however, relaxes its strain by expanding laterally, as it grows in height h. Thus, the measured blueshift of the QD phonon would be smaller by a phenomenological factor φ than is mandatory after Eq. (1). This factor is expected to depend on aspect ratio and WL composition but not on pressure. Hence, the contribution of the biaxial stress to the phonon pressure coefficient can be written as

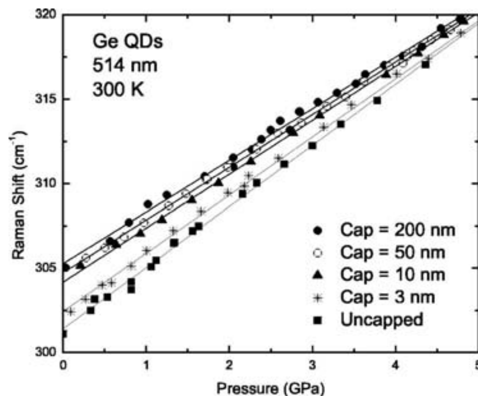

FIG. 2. Dependence on pressure of the frequency of the Ge longitudinal optical phonon mode for five samples with cap layer thicknesses of 0, 3, 10, 50, and 200 nm. Solid lines are results of least-squares fits to the data points using linear relations.

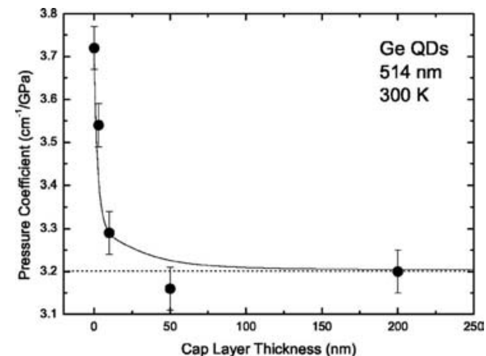

FIG. 3. Phonon pressure coefficient of Ge optical mode of the dots vs cap layer thickness as obtained from the slopes of the fits in Fig. 2. The solid curve represents the result of a fit to the data points using Eqs. (2), (3), and (5) with λ as adjustable parameter.

This article is copyrighted as indicated in the article. Reuse of AIP content is subject to the terms at: http://scitation.aip.org/termsconditions. Downloaded to IP: 158.109.18.157 On: Thu, 08 Oct 2015 12:16:40

$$\frac{d\omega_s^{(\mathrm{WL})}}{dP} = \varphi b_s \frac{d\varepsilon_\parallel}{dP} = \frac{\varphi b_s}{3}\left(\frac{1}{B_0^B} - \frac{1}{B_0^A}\right). \tag{3}$$

The effect of capping the dots with a layer of thickness t is twofold: On the one hand, the cap layer produces a hydrostatic recompression of the dots and, on the other hand, the expansion in the growth direction due to the biaxial compression induced by the WL is gradually suppressed with increasing t. The latter supposes for the parameter φ a phenomenological dependence on t, $\varphi=\varphi_0 e^{-t/\lambda}$, with λ a critical cap-layer thickness. The amount of recompression caused by capping is a function of the ratio of the cap layer volume V_c to the volume of the dot V_d, in order to minimize the total elastic energy of the dot/cap system. Inspired by TEM pictures like that of Fig. 1(c) we consider for the calculation of the elastic energy a dot shape of a half revolution ellipsoid with an aspect ratio $f=b/h$ surrounded by a Si layer of thickness t $(g=t/h)$. The minimum energy is attained for a dot strain of

$$\varepsilon_d = \frac{\varepsilon_\parallel}{1+(V_d/V_c)(B_0^B/B_0^A)}, \quad \frac{V_d}{V_c} = \frac{f^2}{(f+g)^2}\frac{(1+g)^2}{(1+g)^3-1}. \tag{4}$$

Considering this strain as hydrostatic, it yields for the contribution of the cap layer to the phonon pressure coefficient the term

$$\frac{d\omega_s^{(\mathrm{cap})}}{dP} = \frac{a}{1+(V_d/V_c)(B_0^B/B_0^A)}\left(\frac{1}{B_0^B} - \frac{1}{B_0^A}\right). \tag{5}$$

The solid line in Fig. 3 is the result of a least-squares fit to the experimental data of $d\omega_s/dP$ using the function which consists of the three terms given by Eqs. (2), (3), and (5). Here, λ is the only adjustable parameter, since φ_0 is determined by comparing the value of $d\omega_s/dP$ for the uncapped dots to that of bulk Ge. In spite of the crudeness of the model, we obtain a good description of the behavior of the phonon pressure coefficient with cap-layer thickness for $\lambda=8$ nm. Even more important is the fact that the model provides further insight into the strain status of self-assembled dots, leading to a deeper understanding of the high pressure results. For example, the meaning of the saturation value of the pressure coefficient is the following: When $t\to\infty$, $\varphi\to 0$ and $V_d/V_c\to 0$ too. The term $d\omega_s/dP^{(\mathrm{WL})}$ vanishes and the other two yield $d\omega_s/dP=-a/B_0^A \approx 3.2\ \mathrm{cm}^{-1}/\mathrm{GPa}$ $(A\equiv\mathrm{Si})$, which is the pressure coefficient calculated with the hydrostatic deformation potential of Ge but using the bulk modulus of the Si matrix. In fact, a similar pressure coefficient has been reported by Teo *et al.* for a sample with Ge QDs capped with 200 nm of Si.[21] This led us to the conclusion that there is an abrupt transition from a strictly biaxial stress situation of uncapped dots to a fully hydrostatic (isotropic) three-dimensional compression state of the dots for cap layers thicker than the critical value λ (8 nm in the present case). We emphasize that this result is independent of the model; the latter is helpful to understand the underlying physics.

Obviously, λ depends on f. For very flat dots one expects $\lambda\to\infty$, thus, the dots, capped or uncapped, are always in a state of biaxial compression like the wetting layer. In fact, Raman measurements from the cleaved edge of a QD sample containing very flat dots $(h\approx 2$ nm) exhibit a clear singlet-doublet splitting,[6,8] which is evidence of biaxial strain. On the contrary, our sample with a 200-nm-thick cap layer does not display any splitting, being indicative of a hydrostatic (isotropic) compression of the Ge dots.

The practical importance of this work is to provide a means to infer the proper strain situation which applies for a given quantum dot structure, independent of the material system. Our pressure experiments indicate that for QDs with heights larger than about 5 nm or with steep facets like dome-shaped dots, if the cap layer is of the order of the dot height or above, then to consider a quasihydrostatic strain status is appropriate. On the contrary, for very flat or uncapped dots their deformation is better accounted for using a biaxial stress tensor. This would allow for the proper use of Eq. (1) with the correct value of the parameter α for the determination of the mean dot strain by Raman scattering.

One of the authors (J.S.R.) acknowledges financial support from the AlBan fellowship Program. Another author (A.B.) acknowledges an FPI fellowship and P.D.L. an I3P-CSIC grant. Another author (A.R.G.) is an ICREA Research Professor. This work was supported in part by the Spanish Ministerio de Educación y Ciencia through grant MAT2006-02680.

[1] *Nano-Optoelectronics*, edited by M. Grundmann (Springer, Berlin, 2002), pp. 299–428.
[2] J. Stangl, V. Holý, and G. Bauer, Rev. Mod. Phys. **76**, 725 (2004).
[3] E. Anastassakis and M. Cardona, Semicond. Semimetals **55**, 117 (1998) and references therein.
[4] F. Cerdeira, A. Pinczuk, L. C. Bean, B. Batlogg, and B. A. Wilson, Appl. Phys. Lett. **45**, 1138 (1984).
[5] M. Stoehr, D. Aubel, S. Juillaguet, J. L. Bischoff, L. Kubler, D. Bolmont, F. Hamdani, B. Fraisse, and R. Fourcade, Phys. Rev. B **53**, 6923 (1996).
[6] P. H. Tan, K. Brunner, D. Bougeard, and G. Abstreiter, Phys. Rev. B **68**, 125302 (2003).
[7] K. L. Teo, L. Qin, Z. X. Shen, and O. G. Schmidt, Appl. Phys. Lett. **80**, 2919 (2002).
[8] P. H. Tan, D. Bougeard, G. Abstreiter, and K. Brunner, J. Appl. Phys. **98**, 113517 (2005).
[9] A. V. Baranov, A. V. Fedorov, T. S. Perova, R. A. Moore, S. Solosin, V. Yam, D. Bouchier, and V. Le Thanh, J. Appl. Phys. **96**, 2857 (2004).
[10] A. V. Baranov, A. V. Fedorov, T. S. Perova, R. A. Moore, V. Yam, D. Bouchier, V. Le Thanh, and K. Berwick, Phys. Rev. B **73**, 075322 (2006).
[11] M. Ya. Valakh, V. O. Yukhymchuk, V. M. Dzhagan, O. S. Lytvyn, A. G. Milekhin, A. I. Nikiforov, O. P. Pchelyakov, F. Alsina, and J. Pascual, Nanotechnology **16**, 1464 (2005).
[12] V. A. Volodin, M. D. Efremov, A. S. Deryabin, and L. V. Sokolov, Semiconductors **40**, 1314 (2006).
[13] A. Bernardi, M. I. Alonso, A. R. Goñi, J. O. Ossó, and M. Garriga, Appl. Phys. Lett. **89**, 101921 (2006).
[14] A. Bernardi, J. O. Ossó, M. I. Alonso, A. R. Goñi, and M. Garriga, Nanotechnology **17**, 2602 (2006).
[15] A. Bernardi, M. I. Alonso, A. R. Goñi, J. O. Ossó, and M. Garriga, Surf. Sci. **601**, 2783 (2007).
[16] H. K. Mao, J. Xu, and P. M. Bell, J. Geophys. Res. **91**, 4673 (1986).
[17] At ambient pressure the frequency of the second-order Raman feature associated to scattering by two transverse acoustic phonons of Si (2TA) is similar to that of the Ge–Ge mode. Nevertheless, for our dots the Ge peak is about ten times more intense than the 2TA feature, thus, having no influence on the determination of the pressure coefficient of the Ge mode. Moreover, both peaks shift with pressure in opposite directions, leading to an increased peak separation with pressure.
[18] A. Bernardi, J. S. Reparaz, A. R. Goñi, M. I. Alonso, and M. Garriga, Phys. Status Solidi B **244**, 76 (2007).
[19] C. Ulrich, E. Anastassakis, K. Syassen, A. Debernardi, and M. Cardona, Phys. Rev. Lett. **78**, 1283 (1997).
[20] *Numerical Data and Functional Relationships in Science and Technology*, Landolt-Börnstein, New Series Vol. 17, edited by O. Madelung, H. Weiss, and M. Schulz (Springer, Heidelberg, 1982), Sec. 2, p. 64 and p. 107.
[21] K. L. Teo, L. Qin, I. M. Noordin, G. Karunasiri, Z. X. Shen, O. G. Schmidt, K. Eberl, and H. J. Queisser, Phys. Rev. B **63**, 121306 (2001).

This article is copyrighted as indicated in the article. Reuse of AIP content is subject to the terms at: http://scitation.aip.org/termsconditions. Downloaded to IP: 158.109.18.157 On: Thu, 08 Oct 2015 12:16:40

Phys. Status Solidi B **246**, No. 3, 482–485 (2009) / **DOI** 10.1002/pssb.200880529

physica status solidi pss b
www.pss-b.com
basic solid state physics

Polarized Raman study of self-assembled Ge/Si dots under hydrostatic pressure

J. S. Reparaz*, A. Bernardi, A. R. Goñi, M. I. Alonso, and M. Garriga**

Institut de Ciència de Materials de Barcelona (ICMAB), CSIC, Esfera UAB, 08193 Bellaterra, Spain

Received 16 June 2008, accepted 13 August 2008
Published online 12 December 2008

PACS 07.35.+k, 62.50.–p, 63.22.–m, 68.65.Hb, 78.30.Am, 78.67.Hc

* Corresponding author: e-mail sebareparaz@hotmail.com
** ICREA Research Professor

We have studied the correlation between the morphology of Si-capped Ge islands grown on Si substrates and their vibrational properties as measured by Raman scattering at ambient and under high hydrostatic pressure. For this study we have grown by molecular beam epitaxy a sample that exhibits a size distribution with two distinct island types having different aspect ratios called pyramids and domes. In accordance, Raman spectra show a double-peak structure at the frequencies of the Ge–Ge vibrational mode (~300 cm^{-1}) as well as for the Si–Ge mode (around 400 cm^{-1}). Pairwise, different selection rules have been found for these modes depending upon the Raman polarization configurations, suggesting a correlation between both Ge dot sizes and the double peak structure in the Raman spectra. Finally, a different strain status of the dots was observed by studying the pressure coefficient of the Ge–Ge phonon mode, resulting in a value of 3.3 and 3.6 cm^{-1}/GPa for pyramids and domes, respectively. The main conclusion of our work is that the double-peak structure observed in Raman spectra is indicative of a bimodal dot size distribution in contrast with what is proposed in previous work within the so-called *core-shell model* [M. Y. Valakh et al., Nanotechnol. **16**, 1464 (2005)].

© 2009 WILEY-VCH Verlag GmbH & Co. KGaA, Weinheim

1 Introduction Quantum dot (QD) systems have been widely studied during the last decade due to their potential applications in the optoelectronic industry [1, 2]. In particular, Ge/Si dots have attracted much attention due to their possible integration with the Si based technology. Different dot morphologies such as pyramids, domes, and super domes were systematically grown and studied due to their distinct physical properties [3 5]. High pressure measurements as well as Raman scattering have proved to be powerful tools in strain and compositional characterization of these systems, as is shown in recent work [6 8]. Nevertheless, in several cases a confusing situation is found in literature concerning the assignment of certain quantum dot vibrational modes such as the Ge Ge and Si Ge optical phonons. A double peak structure at the frequencies of the Ge Ge as well as the Si Ge vibrations was in some cases observed [7, 9], leading to the so called *core-shell model* as a possible interpretation [9]. Within this model a single dot is divided in two regions, a core surrounded by a shell, each of which is considered responsible for one peak of the observed double peak structure. This model is in clear contrast with the results presented by Bernardi et al. [7], where the doublet is suggested to originate form dots of different morphology.

In this work we intend to clarify this situation by showing that, in fact, the doublets originate from dots with different aspect ratio and strain status. By combining polarized Raman scattering with high pressure measurements we have investigated a specially designed sample which contains a bimodal distribution of dots (domes and pyramids). We have found that the doublets of both, the Ge Ge and Si Ge vibrational modes, exhibit *pairwise* different Raman polarization selection rules. Moreover, each peak of the Ge Ge doublet displays a slightly different dependence on hydrostatic pressure. Results from a previous high pressure study [6] tell us that this is indicative of a different strain status for pair. Our findings led us to the conclusion that each pair Ge Ge and Si Ge Raman peaks arises from different QDs, in contrast with the proposed *core-shell model* in which the doublets are explained as arising from dots with a single morphology (pyramids).

2 Experiments Samples were grown by molecular beam epitaxy on Si(001) substrates according to the fol

© 2009 WILEY-VCH Verlag GmbH & Co. KGaA, Weinheim

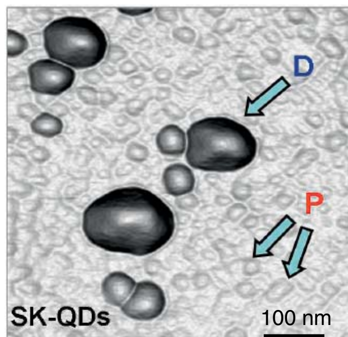

Figure 1 (online colour at: www.pss-b.com) Topographic images of uncapped Ge/Si QDs. The grey scale indicates surface inclination (darker colour islands have steeper facets and higher aspect ratio). Labels refer to pyramids (P) and domes (D).

lowing sequence: After oxide desorption at 900 C and 100 nm thick Si buffer layer deposition, the substrate tem perature was set to 500 C. In the next step, 12 ML of Ge were grown leading to dot formation in the standard Stran ski Krastanow (SK) growth mode. Finally, part of the sample was capped with a 10 nm thick Si layer in order to avoid oxidation of the dots. The cap layer was deposited at low temperature (300 C) in order not to significantly alter the shape and composition of the dots. Growth was moni tored in situ by reflection high energy electron diffraction (RHEED). The uncapped region was used to study the sample topography using atomic force microscopy (AFM), as shown in Fig. 1, where the grey scale stands for facet inclination (steeper facets correspond to darker colour). Dots with different aspect ratio, named as pyramids (P) and domes (D) in the figure, were found to be of approxi mately 10 nm and 20 nm in height with aspect ratios of 0.1 and 0.2, respectively.

Raman spectra were collected with a LabRam HR800 system equipped with confocal microscope in backscat tering geometry at room temperature using the 514.5 nm line of an Ar ion laser. Light was focused onto the sample with a spot size of about 1 μm and a laser power of 4 mW. Polarized measurements were performed in $z(x,y)z$ and $z(x',y')z$, where x, y, z are the [100], [010] and [001] crystallographic directions, and x', y' are axes rotated by 45 with respect to x, y ones. Measurements under pressure were carried out using the diamond anvil cell (DAC) tech nique. A 4:1 mixture of methanol and ethanol was em ployed as the pressure transmitting medium. Pressure was monitored in situ by the shift of the Si longitudinal optical phonon, which was previously calibrated using the pres sure shift of the ruby R1 line [10]. Samples loaded into the DAC were previously thinned to about 30 μm by mechani cal polishing.

3 Results and discussion Figure 2 shows the Raman spectra of the capped sample for two different polarization configurations. The $z(x,y)z$ configuration (upper spec trum) exhibits four peaks distributed in two spectral re

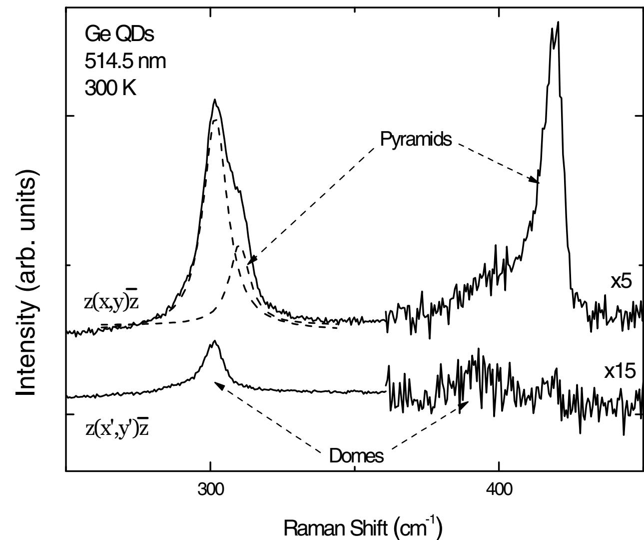

Figure 2 Raman spectra of the QDs sample using two different polarization configurations: $-z(x,y)z$ (upper), and $-z(x',y')z$ (lower). The spectra in the region of the Si–Ge mode are multiplied by the given factors. Dashed lines represent the deconvolution of the spectral line shape using Gaussians.

gions around 300 cm^{-1} and 400 cm^{-1}. The Raman peaks of the first and second region are attributed to Ge Ge and Si Ge vibrational modes of the quantum dots, respectively [11]. The observation of Si Ge phonons is a consequence of a process of interdiffusion during growth. The over whelming signal of the Si substrate is not shown in Fig. 2 for the sake of clarity in the discussion of the QD features. Since for all the cases we have used crossed polarization configurations, the signal from the second order Raman scattering by acoustic phonons of Si substrate is widely suppressed in the spectra. The line shape analysis of the spectra was performed using four Gaussians. The dashed lines in Fig. 2 are an example of the deconvolution of the 300 cm^{-1} feature into two contributions. A preliminary as signment of the four peaks pairwise to domes and pyra mids, as indicated in Fig. 2, is possible by considering the peak positions. A comparative study of the properties of conventional and carbon induced self assembled Ge QDs before and after capping [7] shows that domes are better able to relax strain elastically and exhibit less Si interdiffu sion after capping than pyramids. Hence, the correspond ing Raman features are expected to be blueshifted for pyra mids with respect to domes.

For cubic materials the Raman selection rules state that in backscattering from the (001) crystal surface the longi tudinal optical zone centre phonon is allowed in the $z(x,y)z$ but forbidden in the $z(x',y')z$ polarization con figuration, as can be found elsewhere [12]. As illustrated in Fig. 2, when the $z(x',y')z$ polarization configuration is ap plied the peaks at 310 cm^{-1} and 420 cm^{-1} vanish with an extinction ratio of about 1:100. in contrast, the peaks at 300 cm^{-1} and 390 cm^{-1} decrease in signal only by a 1:5 ratio.

© 2009 WILEY-VCH Verlag GmbH & Co. KGaA, Weinheim

The behaviour of these double peak structures with polarization provides a clue to understand their origin. Elastic strain relaxation by formation of domes is much more efficient than for pyramids. As a result, the parent cubic lattice is much more distorted within a dome. Besides, only pyramids are easily recompressed by the cap layer, remaining pseudomorphic to the substrate [13]. It is then expected that pyramids follow better the polarization selection rules than domes, since the cubic/tetragonal symmetry is locally distorted by strain within the domes, leading to the observed relaxation of the Raman selection rules. It follows that the pair of peaks at 300/390 cm^{-1} most likely arises from the domes, whereas the pair at 310/420 cm^{-1} originates from the pyramids.

We rule out that this depolarization effect arises from refraction of the incident light entering the sample, which is slightly deviated from normal incidence due to the fact that the surface of the sample is not flat, particularly above the larger islands, i.e., domes. For this purpose we have grown a sample with similar domes but a much thicker cap layer of approximately 300 nm. In this case the sample surface is completely flat, thus, no deviation of the incident beam can occur. However, we obtained a similar depolarization in this case too, implying that the observed effect is intrinsic to the domes.

As previously shown [14], the QD strain status can a be also studied by applying hydrostatic pressure and measuring the pressure coefficient of the Ge Ge mode arising from both types of dots. In Fig. 3 we show three representative spectra for different pressures. As clearly observed, with increasing pressure the separation between both Ge Ge peaks (domes and pyramids) decreases. In order to obtain the pressure coefficient of each dot ensemble type, we have restricted ourselves to the range between 0 GPa and 2 GPa where the pressure dependence of the phonon frequency is essentially linear. In the inset to Fig. 3 we display the obtained results to determine the pressure coefficients. The points represent the position of the maximum of the Ge Ge peak for the domes and pyramids and the straight line is a linear fit to the experimental data. Unfortunately, it was not possible to obtain the pressure coefficients of the Si Ge modes because inside the DAC the signal was too low to distinguish these peaks (see Fig. 3). In addition, it should be pointed out that the pressure experiments were performed in strict backscattering configuration, so that the strong Raman signal from the diamond at 1332 cm^{-1} affects more the measurement of the Si Ge than the Ge Ge mode.

The obtained linear pressure coefficients of the Ge Ge mode are 3.30(20) cm^{-1}/GPa and 3.60(5) cm^{-1}/GPa for pyramids and domes, respectively. Numbers in parentheses represent error bars. Although these values are quite similar, the difference is beyond experimental uncertainty. As shown by Reparaz et al. [14] the pressure coefficient of dots decreases in magnitude as the dot to cap layer volume ratio decreases. Since the cap layer is the same for all dots in our sample, we expect that pyramids which are much

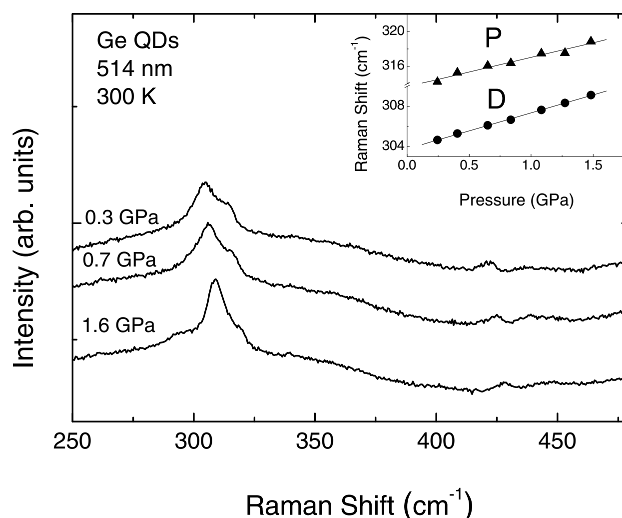

Figure 3 (online colour at: www.pss-b.com) Pressure coefficient determination for the Ge–Ge mode for pyramids and domes. Inset: The points indicate the position of the measured peaks and the solid line is a linear fit of the data.

smaller than domes have a lower pressure coefficient. Hence, the pressure results confirm the assignment of the Raman peaks already made based on the polarization behaviour.

Our observations are not compatible with the interpretation of the double peak structures as arising from the same QD ensemble but from different regions of the same dot, as proposed by Valakh et al. [9], within the so called *core shell* model. In this model it is considered that every QD consists of two distinct regions; a Ge rich core and an outer intermixed shell, giving rise to two peaks in the Raman spectra. The lower frequency Ge Ge component is ascribed to the intermixed shell together with the most prominent Si Ge peak at higher frequency. Our measurements demonstrate, however, that these peaks display different polarization behaviour, invalidating the assignment to the dot shell. Moreover, the same pressure coefficient is expected for core and shell region of the same dot because at high Ge contents the pressure coefficient is independent of composition [8].

4 Summary

We have combined polarized Raman spectroscopy with high pressure measurements to establish the origin of the double peak structures at the frequencies of the Ge Ge and Si Ge modes very often observed in self assembled Ge/Si dot samples. We have shown that the lower frequency peaks and the higher frequency ones of the Ge Ge and Si Ge doublets are coupled to each other and that each of these pairs can be attributed to different dot types, domes and pyramids, indicating the existence of a bimodal size distribution. Our results are relevant for the interpretation of Raman spectra of quantum dot samples in general since they are valid for *any* material system besides Si/Ge.

© 2009 WILEY-VCH Verlag GmbH & Co. KGaA, Weinheim

Acknowledgements J.S.R. acknowledges financial support from the AlBan fellowship Program. A.B. acknowledges an FPI fellowship. This work was supported in part by the Spanish Ministerio de Educación y Ciencia through grant MAT2006-02680. Measurements were performed at the Nanotechnology Laboratory of MATGAS 2000 A.I.E.

References

[1] J. Faist, F. Capasso, D. L. Sivco, C. Sirtori, A. L. Hutchinson, and A. Y. Cho, Science **264**, 553 (1994).
[2] B. F. Levine, J. Appl. Phys. **74**, R1 (1993).
[3] Y. W. Mo, D. E. Savage, B. S. Swartzentruber, and M. G. Lagally, Phys. Rev. Lett. **65**, 1020 (1990).
[4] G. Medeiros-Ribeiro, A. M. Bratkovski, T. I. Kamins, D. A. A. Ohlberg, and R. S. Williams, Science **279**, 353 (1998).
[5] M. Stoffel, A. Rastelli, J. Stangl, T. Merdzhanova, G. Bauer, and O. G. Schmidt, Phys. Rev. B **75**, 113307 (2007).
[6] J. S. Reparaz, A. Bernardi, A. R. Goñi, M. I. Alonso, and M. Garriga, Appl. Phys. Lett. **91**, 081914 (2007).
[7] A. Bernardi, M. I. Alonso, J. S. Reparaz, A. R. Goñi, P. D. Lacharmoise, J. O. Ossó, and M. Garriga, Nanotechnology **18**, 475401 (2007).
[8] J. S. Reparaz, A. Bernardi, A. R. Goñi, M. I. Alonso, and M. Garriga, Appl. Phys. Lett. **92**, 081909 (2008).
[9] M. Y. Valakh, V. Yukhymchuk, V. M. Dzhagan, O. S. Lytvyn, A. G. Milekhin, A. I. Nikiforov, O. P. Pchelyakov, F. Alsina, and J. Pascual, Nanotechnology **16**, 1464 (2005).
[10] H. K. Mao, J. Xu, and P. M. Bell, J. Geophys. Res. **91**, 4673 (1986).
[11] M. I. Alonso and K. Winer, Phys. Rev. B **39**, 10056 (1989).
[12] K. Mizoguchi and S. Nakashima, J. Appl. Phys. **65**, 2583 (1989).
[13] B. V. Kamenev, H. Grebel, L. Tsybeskov, T. I. Kamins, R. S. Williams, J. M. Baribeau, and D. J. Lockwood, Appl. Phys. Lett. **83**, 5035 (2003).
[14] J. S. Reparaz, A. Bernardi, A. R. Goñi, M. I. Alonso, and M. Garriga, Appl. Phys. Lett. **91**, 081914 (2007).

© 2009 WILEY-VCH Verlag GmbH & Co. KGaA, Weinheim

2.2.2 SiGe alloys: measurement of phonon strain-shift coefficients

For the spectroscopic determination of strain one needs to know the so-called strain shift coefficient, defined as the ratio of the phonon frequency shift over the strain that induces the shift: $b_s = \Delta\omega/\Delta\epsilon$. For the most frequent case of Raman measurements in backscattering geometry from the (001) surface, the strain is directly determined from the frequency shift of the Raman-allowed *singlet* component of the optical phonons using the expression for the strain shift coefficient given by:

$$b_s = \omega_0 \left(-\widetilde{K}_{11} \cdot \frac{\alpha}{2} + \widetilde{K}_{12}\right)$$

Here, ω_0 is the frequency of the unstrained phonon mode, $\widetilde{K}_{ij}$ are the dimensionless phonon deformation potentials, and $\epsilon_{\perp} = -\alpha\, \epsilon_{\parallel}$ represents the relation between the strain in growth direction and in the growth plane.

A series of samples containing a strained $Si_{1-x}Ge_x$ alloy layer was grown by molecular beam epitaxy on Si(001) substrates at a temperature of 400 °C. The growth sequence consists of deposition of a 100-nm-thick Si buffer layer, followed by the SiGe alloy layer with thickness below critical to ensure pseudomorphism and, finally, a 300 nm-thick Si cap layer. A thick cap layer is crucial to avoid elastic strain relaxation of the SiGe layer after cleavage for micro-Raman measurements from the cleaved edge. The nominal thicknesses of the alloy layers with a Ge concentration x = 0.73, 0.55, 0.38, and 0.26 were 7, 10, 7, and 15 nm, respectively. For the lowest Ge content of 0.10, a multilayer SiGe/Si structure with a total alloy thickness of 200 nm was deposited to increase the Raman signal without exceeding the critical thickness. The strain and composition of the alloys were determined by x-ray reciprocal space mapping along the (224) diffraction direction using the relationship between lattice constant and composition given in the literature. All alloys showed good pseudomorphic growth onto Si. Raman spectra were collected in backscattering geometry at room temperature using the 514.5 nm line of an Ar+ laser. Raman peak positions were determined with an error of less than 0.5 cm^{-1}. Special care was taken to keep laser power as low as possible to avoid laser heating and the consequent but spurious redshift of the Raman peaks, mainly when exciting at the cleaved edge. A laser power density of 1.5 kW/cm^2 turned out to be adequate. Measurements under pressure were carried out using the diamond anvil cell DAC technique. A 4:1 mixture of methanol and ethanol was employed as the pressure-transmitting medium. Pressure was monitored *in situ* by the shift of the Si longitudinal optical phonon.

The threefold degeneracy of the optical phonon modes at the Brillouin-zone centre is lifted at the alloy layer due to the tetragonal distortion of the lattice caused by the biaxial stress induced by its lattice mismatch to Si. The zone-centre phonons split into a singlet (s, vibrations in growth direction) and a doublet (d, in-plane vibrations component) which are apparent in Raman spectra with different linearly polarized light configurations owing to the following selection rules: the singlet component is observed in backscattering from the growth direction,

whereas the doublet component appears in spectra measured in backscattering from the cleaved edge.

By measuring the hydrostatic strain-induced shift of the phonon frequencies and the singlet-doublet splitting, we obtain the phonon deformation potentials for the different alloys.

- The resulting deformation potentials for all SiGe alloy modes are essentially constant, exhibiting a slight tendency to decrease ($\widetilde{K}_{11}$) or increase ($\widetilde{K}_{12}$) in absolute value with increasing Ge content.

- The main conclusion is that the strain shift coefficients of the Ge–Ge and Si–Si modes, to a good approximation, depend only slightly on Ge composition (x) following the phenomenological expression $b_s=b_0+b_4(x-1)^4$. The strain shift coefficient of the Si–Ge mode is just the arithmetic average of the coefficients of the other two modes. The results are of great practical importance since they provide accurate values for the strain shift coefficient of the optical phonons of $Si_{1-x}Ge_x$ alloys to be used for the proper determination of the strain status of SiGe nanostructures by Raman scattering.

COMPLEMENTARY ARTICLES

Article n: 8

Authors: J. S. Reparaz, A. Bernardi, A. R. Goñi, M. I. Alonso, and M. Garriga

Title: Composition dependence of the phonon strain shift coefficients of SiGe alloys revisited

Journal: Applied Physics Letters

Doi: 10.1063/1.2884526

Article n: 9

Authors: J. S. Reparaz, A. R. Goñi, A. Bernardi, M. I. Alonso, and M. Garriga

Title: Measurement of phonon pressure coefficients for a precise determination of deformation potentials in SiGe alloys

Journal: Physica Status Solidi B

Doi: 10.1002/pssb.200880531

Composition dependence of the phonon strain shift coefficients of SiGe alloys revisited

J. S. Reparaz,[a] A. Bernardi, A. R. Goñi, M. I. Alonso, and M. Garriga
Institut de Ciència de Materials de Barcelona-CSIC, Esfera UAB, 08193 Bellaterra, Spain

(Received 21 November 2007; accepted 31 January 2008; published online 26 February 2008)

By combining Raman scattering from the cleaved edge and under hydrostatic pressure, we have accurately determined the tetragonal phonon deformation potentials of strained $Si_{1-x}Ge_x$ alloys in the entire compositional range for the Ge-like, Si-like, and mixed Si–Ge optical modes. A known biaxial strain is induced on thin alloy layers by pseudomorphic epitaxial growth on silicon and subsequent capping. We also determine the strain shift coefficient of the three modes, which are essentially independent of Ge content between 0.4 and 1. This is key information for an effective use of Raman scattering as strain-characterization tool in SiGe nanostructures. © *2008 American Institute of Physics*. [DOI: 10.1063/1.2884526]

A precise knowledge of the phonon deformation potentials (DPs), i.e., the derivative of the optical phonon frequency with respect to an elastic deformation of the lattice, is crucial for an effective use of Raman scattering as powerful strain-characterization tool in compound semiconductor microstructures.[1] In particular, for the SiGe material system, there is a great deal of discrepancy between different literature sources about the exact values of the DPs mainly for intermediate Ge concentrations.[2–7] There might be many reasons for such differences (up to a factor of 2) such as strain relaxation effects for epitaxial layers exceeding the critical thickness,[3] the use of polycrystalline samples,[4] or, as pointed out in Ref. 5, due to large uncertainties in the determination of the phonon frequency for the unstrained alloy as compared with literature data obtained for bulk materials.[8,9] Such disappointing state-of-the-art is surprising in view of the technological importance of strained SiGe/Si heterostructures and the great potential of Raman scattering to measure built-in strain in nanostructured materials such as superlattices,[2] self-assembled quantum dots,[10–13] and complementary metal-oxide semiconductor devices.[14]

In practice, for the spectroscopical determination of strain one needs to know the so-called strain shift coefficient, defined as the ratio of the phonon frequency shift over the strain that induces the shift: $b_s=\Delta\omega/\Delta\varepsilon$. For the most frequent case of Raman measurements in backscattering geometry from the (001) surface, the strain is directly determined from the frequency shift of the Raman-allowed *singlet* component of the optical phonons using the expression for the strain shift coefficient given by[2,6]

$$b_s=\omega_0(-\tilde{K}_{11}\cdot\alpha/2+\tilde{K}_{12}). \tag{1}$$

Here, ω_0 is the frequency of the unstrained phonon mode, $\tilde{K}_{ij}$ are the dimensionless phonon deformation potentials, as defined in Ref. 1, and $\varepsilon_\perp=-\alpha\varepsilon_\parallel$ represents the relation between the strain in growth direction and in-plane strain. For the case of a strictly bisotropic stress like in epitaxially grown pseudomorphic layers holds $\alpha=2C_{12}/C_{11}$, where C_{ij} are the elastic constants of the material. A confusing situation is found in the literature for the accepted values of the strain shift coefficient of the optical phonons in $Si_{1-x}Ge_x$ alloys:[2–7] For intermediate Ge concentrations in the range of $0.3\leqslant x\leqslant 0.8$, the values of b_s for the Ge–Ge and the Si–Si mode are twice as large and about 50% higher than for the pure materials, respectively. This is not only counterintuitive but recently appeared theoretical evidence[15] for b_s being fairly constant over the whole concentration range, holding this for the three optical modes of the SiGe alloy.

In order to clarify this inconsistency, we have grown a set of five strained epitaxial SiGe layers on Si with Ge concentrations between 0.1 and 0.75 and measured the shift and splitting of the optical phonons caused by the strain due to the lattice mismatch between alloy and substrate. From these measurements and that of the pressure coefficient of the singlet, we were able to accurately determine two phonon deformation potential constants, $\tilde{K}_{11}$ and $\tilde{K}_{12}$, as a function of alloy composition. We obtained for the strain shift coefficient of the Ge–Ge, Si–Ge, and Si–Si alloy modes the same flat dependence on Ge content from pure Ge down to $x\sim 0.4$, followed by a slight increase for lower concentrations. Our results are in good qualitative agreement with the calculations of Ref. 15, based on a modified Keating model.

A series of samples containing a strained $Si_{1-x}Ge_x$ alloy layer was grown by molecular beam epitaxy on Si(001) substrates at a temperature of 400 °C.[16] The growth sequence consists of deposition of a 100-nm-thick Si buffer layer, followed by the SiGe alloy layer with thickness below critical to ensure pseudomorphism and, finally, a 300 nm-thick Si cap layer. A thick cap layer is crucial to avoid elastic strain relaxation of the SiGe layer after cleavage for micro-Raman measurements from the cleaved edge. The nominal thicknesses of the alloy layers with a Ge concentration $x=0.73$, 0.55, 0.38, and 0.26 were 7, 10, 7, and 15 nm, respectively. For these layer thicknesses, we estimate an upper bound of 0.2 cm^{-1} for the frequency shift due to phonon-confinement effects,[17] which is negligible compared to other error sources. For the lowest Ge content of 0.10, a multilayer SiGe/Si structure with a total alloy thickness of 200 nm was deposited to increase the Raman signal without exceeding the critical thickness. The strain and composition of the alloys were determined by x-ray reciprocal space mapping along the (224) diffraction direction and for the lattice constant dependence on composition, we used the relation given elsewhere.[18,19] All alloys showed good pseudomorphic growth to Si.

[a]Electronic mail: sebareparaz@hotmail.com.

This article is copyrighted as indicated in the article. Reuse of AIP content is subject to the terms at: http://scitation.aip.org/termsconditions. Downloaded to IP: 158.109.18.157 On: Thu, 08 Oct 2015 12:15:28

 © 2008 American Institute of Physics

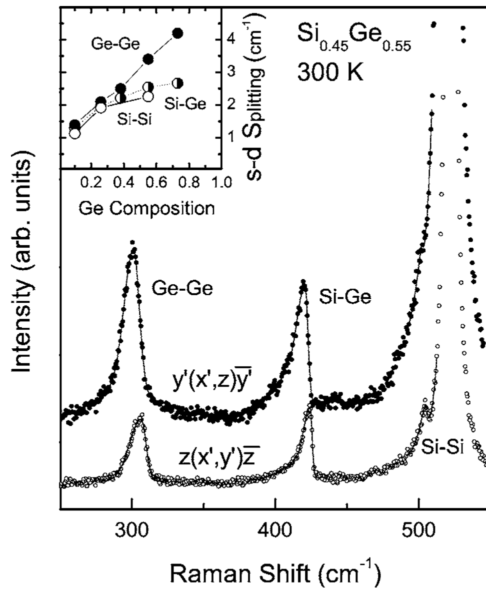

FIG. 1. Representative Raman spectra of a strained alloy layer with Ge content $x=0.55$ measured at room temperature in different scattering configurations with crossed linearly polarized light. Peak assignment to the optical modes of the alloy is indicated. Solid lines represent the results of least-squares fits to the spectra using asymmetric Gaussians. The inset shows the values of the singlet-doublet splitting for the three optical alloy modes as a function of Ge concentration.

Raman spectra were collected in backscattering geometry at room temperature using the 514.5 nm line of an Ar^+ laser. Raman peak positions are determined with an error of less than 0.5 cm^{-1}. Special care was taken to keep laser power as low as possible to avoid laser heating and the consequent but spurious redshift of the Raman peaks, mainly when exciting at the cleaved edge. A laser power density of 1.5 kW/cm^2 turned out to be adequate. Measurements under pressure were carried out using the diamond anvil cell (DAC) technique. A 4:1 mixture of methanol and ethanol was employed as the pressure-transmitting medium. Pressure was monitored *in situ* by the shift of the Si longitudinal optical phonon. Samples with similar alloy composition but without cap layer were grown for the Raman experiments under pressure. Samples loaded into the DAC were previously thinned to about 30 μm by mechanical polishing.

The threefold degeneracy of the optical phonon modes at the Brillouin-zone center is lifted at the alloy layer due to the tetragonal distortion of the lattice caused by the bisotropic stress induced by its lattice mismatch to Si. The zone-center phonons split into a singlet (s, vibrations in growth direction) and a doublet (d, in-plane vibrations) component which are apparent in Raman spectra with different linearly polarized light configurations owing to the following selection rules: the singlet component is observed in backscattering from the growth direction using the geometry $z(xy)\bar{z}$, whereas, the doublet component appears in spectra measured in backscattering from the cleaved edge $x'(zy')\bar{x}'$, where x, y, z, x', and y' are the [100], [010], [001], [110], and [$\bar{1}$10] crystallographic directions, respectively. Figure 1 shows two representative spectra of the alloy with 0.55 Ge content. Geometries with crossed linear polarization were chosen on purpose in order to suppress contributions from second-order Raman processes by acoustic phonons in Si, which would have hampered the precise determination of the peak position mainly for the Ge–Ge mode. The position of all Raman peaks was determined by a conventional least-squares fitting procedure using asymmetric Gaussians for the alloy modes and a Lorentzian for the Raman peak of the Si layers. The frequency splitting between peaks measured using both scattering geometries is indicative of a tetragonal strain in the alloy layer. Splitting values of the three alloy modes are plotted as a function of alloy composition in the inset of Fig. 1. The Ge–Ge mode splitting increases linearly with Ge concentration, whereas, for the other modes, the increase of the splitting is sublinear.

The hydrostatic strain-induced shift of the phonon frequencies and the singlet-doublet splitting, which are linear on the strain $\Delta\varepsilon=(a_{\mathrm{Si}}-a_0(x))/a_0(x)$ given by the lattice mismatch, can be written in terms of the adimensional phonon deformation potentials as[1,20]

$$\frac{\omega_s+2\omega_d}{3\omega_0}=1+\frac{2-\alpha}{6}(\tilde{K}_{11}+2\tilde{K}_{12})\Delta\varepsilon, \quad (2)$$

$$\frac{\omega_s-\omega_d}{\omega_0}=-\frac{1+\alpha}{2}(\tilde{K}_{11}-\tilde{K}_{12})\Delta\varepsilon. \quad (3)$$

Using these equations, one should be able to determine the phonon DPs of the alloys from the measured frequencies of the singlet and doublet components. This method, however, presents a major drawback which concerns large uncertainties derived from the estimation of the unstrained frequency ω_0 from literature data.[5,8] As an alternative, we propose to get rid of ω_0 by division of Eq. (2) by Eq. (3), adding a third equation which corresponds to the hydrostatic pressure coefficient of the singlet frequency. For that purpose, we have performed Raman measurements using the DAC for every concentration. The logarithmic derivative of the phonon frequency over pressure is readily calculated as:[13]

$$6\frac{d\ln\omega_s}{dP}=-\frac{\tilde{K}_{11}+2\tilde{K}_{12}}{B_0^{\mathrm{SiGe}}}+(2\tilde{K}_{12}-\alpha\tilde{K}_{11})\left(\frac{1}{B_0^{\mathrm{SiGe}}}-\frac{1}{B_0^{\mathrm{Si}}}\right), \quad (4)$$

where B_0 is the bulk modulus of the corresponding material. For the alloys, B_0 was obtained by linear interpolation between the values of the pure elements. The second term in Eq. (4) represents the correction to the phonon pressure coefficient due to the different elastic properties of alloy and Si substrate, which tends to reduce the lattice mismatch strain with increasing pressure. This correction amounts up to 15% for high Ge concentrations, hence, it has to be taken into account for an accurate determination of the phonon DPs. The key point is that ω_0 does not appear explicitly in Eq. (4).

We obtain a system of two linear equations with two unknowns, which is easily solved to obtain the phonon deformation potentials $\tilde{K}_{11}$ and $\tilde{K}_{12}$ plotted in Fig. 2 as a function of Ge concentration for the three optical modes of the SiGe alloy. The values corresponding to the pure materials are the ones tabulated in Ref. 1, but for Ge, they were increased in absolute value by 13.5% in order to account for the correct Grüneisen parameter $\gamma=(\tilde{K}_{11}+2\tilde{K}_{12})/6$ obtained from hydrostatic pressure experiments.[21] As already performed for GaAs (Ref. 22) and Si,[23] such a correction is necessary because of a systematic underestimation of the applied stress due to surface strain relaxation in the uniaxial-stress Raman experiments performed with a laser energy above the band gap of the material. Despite the relatively large error bars for Si rich alloys, the overall picture that

This article is copyrighted as indicated in the article. Reuse of AIP content is subject to the terms at: http://scitation.aip.org/termsconditions. Downloaded to IP: 158.109.18.157 On: Thu, 08 Oct 2015 12:15:28

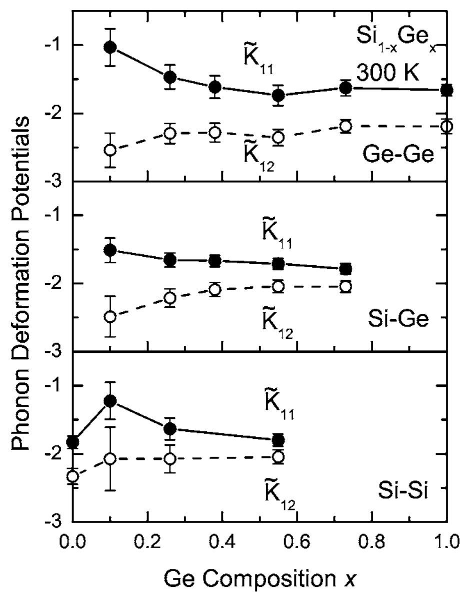

FIG. 2. Dependence on Ge concentration of the phonon deformation potentials $\tilde{K}_{11}$ and $\tilde{K}_{12}$ of the Ge–Ge, Si–Ge, and Si–Si optical modes for the SiGe material system. Solid lines are guides for the eyes.

comes out of Fig. 2 is that both deformation potentials for all SiGe alloy modes are essentially constant, exhibiting $\tilde{K}_{11}$ and $\tilde{K}_{12}$, a slight tendency to decrease or increase in absolute value with decreasing Ge content, respectively.

Using Eq. (2) and the values for the DPs of Fig. 2, one can calculate ω_0, and hence, the strain shift coefficient b_s for all phonon modes of the alloy. The resulting values are plotted in Fig. 3 as a function of the composition of the SiGe alloy. The curves represent the results of a least-squares fit to the experimental data using for all modes the same phenomenological expression given by $b_s=b_4(x-1)^4+b_0$, where x is the Ge content and b_4 and b_0 are adjustable parameters. Interestingly, $b_4=-190(15)$ cm^{-1} has a common value for all three optical modes, whereas, b_0 are $-460(20)$ cm^{-1}, $-555(15)$ cm^{-1}, and $-650(20)$ cm^{-1} for the Ge–Ge, Si–Ge, and Si–Si phonon mode, respectively. Numbers in parenthesis are the corresponding error bars. These values are in good agreement with the ones obtained by Volodin *et al.*[9] for high Ge content.

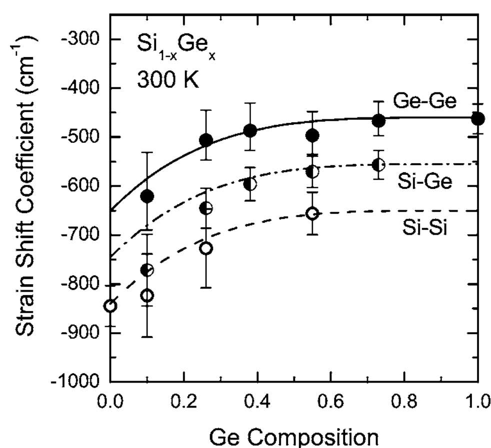

FIG. 3. Phonon strain shift coefficient b_s of the Ge–Ge, Si–Ge, and Si–Si optical modes of $Si_{1-x}Ge_x$ alloys as a function of composition. The curves represent the results of a fit to the data points using the same phenomenological polynomial function.

A comparison between our b_s values and the collection of data in Fig. 3 of Ref. 15 suggests a much better agreement with the calculations within the modified Keating model, which predict constant strain shift coefficients. This settles the issue about the discrepancies between the different experimental and theoretical reports of the literature. The main conclusion is that the strain shift coefficients of the Ge–Ge and Si–Si modes, to a good approximation, depend only slightly on composition. The strain shift coefficient of the Si–Ge mode is just the arithmetic average of the coefficients of the other two modes. Thus, the results of Fig. 3 are of great practical importance for they provide accurate values for the strain shift coefficient of the optical phonons of $Si_{1-x}Ge_x$ alloys to be used for the proper determination of the strain status of SiGe nanostructures by Raman scattering.

A.R.G. is an ICREA Research Professor. We are grateful to A. Crespi, X. Martí, J. Rius, and J. Santiso for x-ray diffraction measurements. J.S.R. acknowledges an AlBan fellowship, A.B. a FPI fellowship and PDL an I3P-CSIC grant. This work was supported by the Spanish Ministerio de Educación y Ciencia through Grant No. MAT2006-02680. Measurements were performed at MATGAS 2000 A.I.E.

[1]E. Anastassakis and M. Cardona, Semicond. Semimetals **55**, 117 (1998).
[2]F. Cerdeira, A. Pinczuk, J. C. Bean, B. Batlogg, and B. A. Wilson, Appl. Phys. Lett. **45**, 1138 (1984).
[3]D. J. Lockwood and J.-M. Baribeau, Phys. Rev. B **45**, 8565 (1992).
[4]Z. Sui, H. H. Burke, and I. P. Herman, Phys. Rev. B **48**, 2162 (1993).
[5]J. C. Tsang, P. M. Mooney, F. Dacol, and J. O. Chu, J. Appl. Phys. **75**, 8098 (1994).
[6]M. Stoehr, D. Aubel, S. Juillaguet, J. L. Bischoff, L. Kubler, D. Bolmont, F. Hamdani, B. Fraisse, and R. Fourcade, Phys. Rev. B **53**, 6923 (1996).
[7]S. Nakashima, T. Mitani, M. Ninomiya, and K. Matsumoto, J. Appl. Phys. **99**, 053512 (2006).
[8]M. I. Alonso and K. Winer, Phys. Rev. B **39**, 10056 (1989).
[9]V. A. Volodin, M. D. Efremov, A. S. Derya, and L. V. Sokolov, Semiconductors **45**, 1314 (2006).
[10]K. L. Teo, L. Qin, Z. X. Shen, and O. G. Schmidt, Appl. Phys. Lett. **80**, 2919 (2002).
[11]A. Bernardi, M. I. Alonso, J. S. Reparaz, A. R. Goñi, P. D. Lacharmoise, J. O. Ossó, and M. Garriga, Nanotechnology **18**, 475401 (2007).
[12]P. H. Tan, D. Bougeard, G. Abstreiter, and K. Brunner, J. Appl. Phys. **98**, 113517 (2005).
[13]J. S. Reparaz, A. Bernardi, A. R. Goñi, P. D. Lacharmoise, M. I. Alonso, M. Garriga, J. Novák, and I. Vávra, Appl. Phys. Lett. **91**, 081914 (2007).
[14]J. Schmidt, G. Vogg, F. Bensch, S. Kreuzer, P. Ramm, S. Zollner, R. Liu, and P. Wennekers, Mater. Sci. Semicond. Process. **8**, 267 (2005).
[15]F. Pezzoli, E. Grilli, M. Guzzi, S. Sanguinetti, D. Chrastina, G. Isella, H. von Känel, E. Wintersberger, J. Stangl, and G. Bauer, Mater. Sci. Semicond. Process. **9**, 541 (2006).
[16]D. D. Perovic, B. Bahierathan, H. Lafontaine, D. C. Houghton, and D. W. McComb, Physica A **239**, 11 (1997).
[17]E. B. Gorokhov, V. A. Volodin, D. V. Marin, D. A. Orekhov, A. G. Cherkov, A. K. Gutakovskii, V. A. Shvets, A. G. Borisov, and M. D. Efremov, Semiconductors **39**, 1168 (2005).
[18]J. P. Dismukes, L. Ekstrom, and R. J. Paff, J. Phys. Chem. **68**, 3021 (1964).
[19]R. Lange, K. E. Junge, S. Zollner, S. S. Iyer, A. P. Powell, and K. Eberl, J. Appl. Phys. **80**, 4578 (1996).
[20]G. L. Bir and G. E. Pikus, *Symmetry and Strain-Induced Effects in Semiconductors* (Halsted, New York, 1974).
[21]C. Ulrich, E. Anastassakis, K. Syassen, A. Debernardi, and M. Cardona, Phys. Rev. Lett. **78**, 1283 (1997).
[22]P. Wickbold, E. Anastassakis, R. Sauer, and M. Cardona, Phys. Rev. B **35**, 1362 (1987).
[23]E. Anastassakis, A. Cantarero, and M. Cardona, Phys. Rev. B **41**, 7529 (1990).

This article is copyrighted as indicated in the article. Reuse of AIP content is subject to the terms at: http://scitation.aip.org/termsconditions. Downloaded to IP: 158.109.18.157 On: Thu, 08 Oct 2015 12:15:28

Phys. Status Solidi B **246**, No. 3, 548–552 (2009) / **DOI** 10.1002/pssb.200880531

physica status solidi b
www.pss-b.com
basic solid state physics

Measurement of phonon pressure coefficients for a precise determination of deformation potentials in SiGe alloys

J. S. Reparaz, A. R. Goñi*, A. Bernardi, M. I. Alonso, and M. Garriga

Institut de Ciència de Materials de Barcelona-CSIC, Esfera UAB, 08193 Bellaterra, Spain

Received 16 June 2008, revised 23 September 2008, accepted 7 October 2008
Published online 12 December 2008

PACS 62.50.–p, 63.50.Gh, 78.30.Am

* Corresponding author: e-mail goni@icmab.es, Phone: +34-93-5801853, Fax: +34-93-5805729

For an effective use of Raman scattering as strain characterization tool in SiGe nanostructures a precise knowledge of the phonon deformation potentials (DPs) is strictly necessary. The optical phonon DPs can be determined by means of Raman scattering measurements from the cleaved edge of a biaxially strained SiGe alloy layer grown pseudomorphically on silicon and subsequently capped. Due to uncertainties in the literature values of the unstrained phonon frequencies it turns out that the desired degree of accuracy is only attained by complementing the Raman measurements from the edge with that of the hydrostatic pressure coefficient of the optical phonons. For that purpose we have grown by molecular beam epitaxy up to seven partially strained $Si_{1-x}Ge_x$ alloys on Si spanning the entire compositional range and measured the dependence on hydrostatic pressure of the frequency of the Ge-like, Si-like and mixed Si–Ge optical modes. After correcting for the pressure dependent biaxial stress induced by the Si substrate on the alloy layer and taking into account the dependence on alloy composition of the bulk modulus we obtain a fairly constant value of the Grüneisen parameter around 1.0 for all three optical modes in the whole range of Ge contents. We also determined the strain shift coefficients for the three modes, which are essentially independent of Ge content between 0.4 and 1. Our results are in very good agreement with recentcalculations of the SiGe phonon deformation potentials using a modified Keating model, which settles the longstanding issue about the large discrepancies between results from different experiments.

© 2009 WILEY-VCH Verlag GmbH & Co. KGaA, Weinheim

1 Introduction Raman scattering has demonstrated to be a powerful strain-characterization tool in compound semiconductor microstructures [1]. The accuracy of such a determination, though, depends much on the precise knowledge of the phonon deformation potentials (DPs), i.e., the derivative of the optical phonon frequency with respect to an elastic deformation of the lattice. In this respect, the situation found in the literature for the SiGe material system is particularly disappointing. There is a great deal of discrepancy between different sources about the values of the DPs mainly for intermediate Ge concentrations [2–7]. As pointed out in Ref. [5] the most probable reason for such differences arises from the fact that the actual value of the phonon frequency for the *unstrained* alloy is obtained from the literature data for bulk materials [8, 9] although it appears to be sample dependent. In a recent paper [10], however, we demonstrate that it is possible to circumvent the problem posed by the exact knowledge of ω_0, the unstrained frequency of any particular phonon mode, by using its hydrostatic pressure coefficient as an additional input parameter. In this way, we were able to complement information about shifts and splitting of the phonon modes measured from the cleaved edge in samples containing strained SiGe alloy layers of different compositions to obtain a linear system of two equations with two unknowns, which is solved for a precise determination of the dimensionless phonon deformation potential constants, $\tilde{K}_{11}$ and $\tilde{K}_{12}$, as defined in Ref. [1]. Needless to say that ω_0 does not appear explicitly in these equations.

In this work we present the results on the hydrostatic pressure coefficient of the three optical modes of SiGe alloys in the entire range of compositions used for the precise determination of the DPs reported in Ref. [10]. For that purpose we have grown a set of seven thick, partially

WILEY InterScience® DISCOVER SOMETHING GREAT

© 2009 WILEY-VCH Verlag GmbH & Co. KGaA, Weinheim

Original Paper

strained epitaxial SiGe layers on Si with Ge concentrations between 0.1 and 1.0 and used the diamond- anvil cell technique to measure the pressure-induced shift of the optical phonons by Raman scattering. We found that the Grüneisen parameter (the logarithmic derivative of the frequency with respect to volume) for all three phonon modes is close to 1.0, being independent of the Ge content. In this way and using the results of Ref. [10], we obtained for the Ge–Ge, Si–Ge and Si–Si alloy modes the value of the so-called strain shift coefficient, defined as the ratio of the phonon frequency shift over the strain that induces that shift, as a function of alloy composition. Our results are in good qualitative agreement with recent calculations based on a modified Keating model [11].

2 Experimental A series of samples containing a thick, partially relaxed $Si_{1-x}Ge_x$ alloy layer with $x = 0.19$, 0.26, 0.39, 0.47, 0.55, 0.74 and 1.00 was grown by molecular beam epitaxy on Si(001) substrates at a temperature of 400 °C. The growth sequence consists of deposition of a 100 nm thick Si buffer layer followed by the SiGe alloy layer with thickness ranging between 100 nm and 500 nm. Such large values which are in most cases beyond the critical thickness for the given Ge content [12] were necessary to attain reasonable signal-to-noise ratios for Raman scattering inside the pressure cell. Thus, partial or even total strain relaxation of the SiGe layers is unavoidable, mainly for the higher Ge concentrations. Nevertheless, we point out that within the linear approximation (constant bulk modulus independent of pressure) the amount of strain relaxation is irrelevant for the determination of the pressure coefficient of the phonon frequency. We performed, however, the correction due to the presence of the Si substrate which has a different bulk modulus than the alloy layer grown pseudomorphically on top. Finally, the composition of the alloys was determined by X-ray reciprocal space mapping along the (224) diffraction direction.

Raman spectra were collected with a LabRam HR800 system equipped with a large working distance microscope objective in backscattering geometry at room temperature using the 514.5 nm line of an Ar^+ laser. Raman peak positions are determined with an error of less than 0.5 cm^{-1}. A laser power density of 1.5 kW/cm^2 turned out to be adequate to avoid laser heating and the consequent but spurious redshift of the Raman peaks. Measurements under pressure were carried out using the diamond anvil cell (DAC) technique. A 4:1 mixture of methanol and ethanol was employed as the pressure-transmitting medium. Pressure was monitored *in situ* by the shift of the Si longitudinal optical phonon, which was previously calibrated using the pressure shift of the ruby R1 line [13]. Samples loaded into the DAC were previously thinned to about 30 µm by mechanical polishing.

3 Results and discussion The three-fold degeneracy of the optical phonon modes at the Brillouin-zone center is lifted at the alloy layer due to the tetragonal distortion of the lattice caused by the bisotropic stress induced by its lattice mismatch to Si. The zone-center phonons split into a singlet (*s*, vibrations in growth direction) and a doublet (*d*, in-plane vibrations) component. For the case of Raman measurements in backscattering geometry from the (001) surface the shift of the frequency ω_s of the Raman-allowed *singlet* component of the optical phonons is linear on the strain $\Delta\varepsilon = (a_{Si} - a_0(x))/a_0(x)$ given by the lattice mismatch according to

$$\omega_s = \omega_0 + b_s \cdot \Delta\varepsilon\,. \tag{1}$$

The expression for the strain shift coefficient as a function of the DPs is given by [2, 6]

$$b_s = \omega_0 \cdot (\;\tilde{K}_{11} \cdot \alpha/2 + \tilde{K}_{12})\,. \tag{2}$$

For the case of a strictly *bisotropic* stress like in epitaxially grown pseudomorphic layers holds $\alpha = 2C_{12}/C_{11}$, where C_{ij} are the elastic constants of the material.

In addition, the frequency shift induced by the external hydrostatic pressure in the diamond anvil cell can be also written in terms of the phonon deformation potentials as [1, 14]

$$\omega_s = \omega_0 \cdot \;\; 1 + \frac{\gamma P}{B_0^{SiGe}} \;\;, \tag{3}$$

$$\gamma = -\frac{\tilde{K}_{11} + 2\tilde{K}_{12}}{6}\,, \tag{4}$$

where γ is the mode Grüneisen parameter. By adding the contributions from Eqs. (1) and (3) one readily obtains for the logarithmic derivative of the phonon frequency over pressure following expression [15]

$$\frac{d\ln\omega_s}{dP} = \frac{\gamma}{B_0^{SiGe}} + \frac{b_s}{3\omega_0} \cdot \;\; \frac{1}{B_0^{SiGe}} \quad \frac{1}{B_0^{Si}} \;\; . \tag{5}$$

The second term in Eq. (5) represents the correction to the phonon pressure coefficient due to the different elastic properties of alloy and Si substrate, which tends to reduce the lattice mismatch strain with increasing pressure. This correction amounts up to 15% for high Ge concentrations, hence, it has to be taken into account for an accurate determination of the Grüneisen parameters.

Figure 1 shows two representative spectra of the alloy with a Ge content of 0.47 measured at pressures of 0.9 GPa and 3.8 GPa. The assignment of the optical modes corresponding to the Ge–Ge, Si–Ge and one of the Si–Si alloy vibrations is indicated [8]. To increase the signal-to-noise ratio in the DAC detection is not polarized. Thus, it is not possible to suppress contributions from second-order Raman processes by acoustic phonons in the Si substrate. This gives rise to the features around 300 cm^{-1} and 450 cm^{-1}, which sometimes might interfere with the precise determination of the peak position mainly for the Ge–Ge mode [16]. The position of all Raman peaks was determined by a conventional least-squares fitting procedure using asym-

 © 2009 WILEY-VCH Verlag GmbH & Co. KGaA, Weinheim

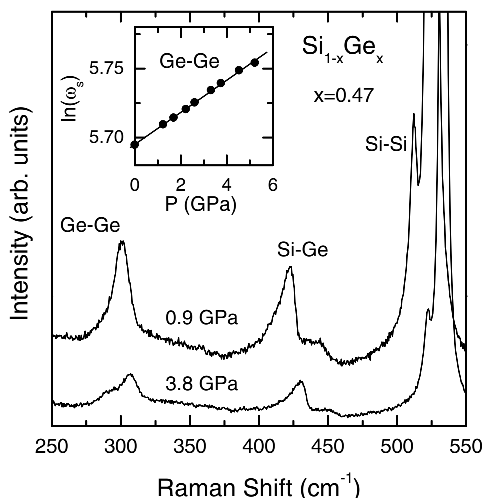

Figure 1 Two representative Raman spectra of an alloy layer with Ge content $x = 0.47$ measured at hydrostatic pressures of 0.9 GPa and 3.8 GPa. Peak assignment to the optical modes of the alloy is indicated. The inset shows, as an example, the values of the logarithm of the frequency for the Ge–Ge optical alloy mode as a function of pressure. The straight line represents a least-squares fit through the data points.

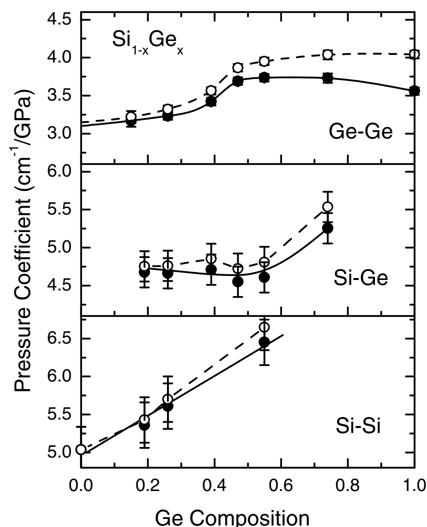

Figure 2 (closed symbols) Dependence on Ge concentration of the phonon linear pressure coefficient of the Ge–Ge, Si–Ge, and Si–Si optical modes for the SiGe material system. Open circles correspond to the values of the pressure coefficient after correction for the effect of the biaxial stress caused by the Si substrate. Solid lines are guides to the eye.

metric Gaussians for the Ge–Ge and Si–Ge alloy modes and a Lorentzian for the Si–Si ones. All alloy modes shift to higher frequencies with increasing pressure. As an example, we plot in the inset to Fig. 1 the logarithm of the Ge–Ge mode frequency as a function of pressure. A great advantage of this representation is that in the pressure range up to 5 GPa $\ln(\omega_s)$ exhibits for all optical modes a totally linear dependence on pressure irrespective of alloy composition. Thus, the slope $d \ln \omega_s/dP$ fully characterizes the pressure behavior of the phonon modes. In contrast, a parabolic dependence is very often encountered within the conventional practice of plotting frequency against pressure, which leads to different results for the linear pressure coefficient depending on the criteria used to account for the curvature.

Using the slopes determined from linear fits to the $\ln(\omega_s)$-vs.-P data points and the frequency values for zero pressure we obtained the linear pressure coefficients of the optical phonons of the alloys plotted in Fig. 2 (closed symbols) as a function of Ge content. The solid curves are guides to the eye. These data were used to complement the Raman measurements from the cleaved edge of fully stressed alloy layers for the precise determination of the phonon deformation potentials $\tilde{K}_{11}$ and $\tilde{K}_{12}$, as previously reported in Ref. [10]. With this knowledge of the DPs we make use of Eq. (5) to calculate the correction to the linear pressure coefficient due to the pressure-induced changes in the biaxial strain caused by the Si substrate. The resulting coefficients, which are plotted in Fig. 2 as open circles, correspond to the values that would be obtained for the *bulk* alloy material, i.e. for free-standing alloy samples. As pointed out before, the higher the Ge concentration, the larger is the correction due to the significant difference in bulk modulus between alloy and Si substrate. We emphasize that whereas for the Ge–Ge and Si–Ge modes at intermediate Ge concentrations the pressure coefficients obtained in Ref. [4] are about 30% larger than ours, we find very good agreement with the results of calculations within a modified Keating model [11]. We believe that in the former case the discrepancy is likely due to the polycrystalline character of the samples employed in Ref. [4].

The mode Grüneisen parameters γ are thus extracted from the corrected values of the linear pressure coefficients using Eq. (5). For the alloys the bulk modulus B_0 was obtained by linear interpolation between the ones of the pure elements [17]. Figure 3 shows the resulting γ values of the optical phonon modes of the alloys for the whole range of compositions. A striking result concerns the fact that the Grüneisen parameters of all three modes are almost constant and very similar in absolute value, being its average equal to 1.00 ± 0.05. This is in clear contrast with several literature sources, where γ values as large as 1.3 to 1.4 are reported for intermediate Ge concentrations [4, 6]. Furthermore, a constant γ implies that the observed variation of the phonon pressure coefficient with alloy composition (see Fig. 2) is due only to a change in bulk modulus. This is actually very intuitive since the Grüneisen parameters of the pure materials differ only by 5%, thus, no appreciable dependence on composition is to be expected.

Due to its practical importance it is very instructive to compare our results for the strain shift coefficient b_s for all phonon modes of the alloy with the available literature data. b_s is readily obtained from the values for the DPs of Ref. [10] using Eq. (2). Results are plotted in Fig. 4 (full data points) as a function of composition. The dot-dashed

© 2009 WILEY-VCH Verlag GmbH & Co. KGaA, Weinheim

Phys. Status Solidi B **246**, No. 3 (2009)

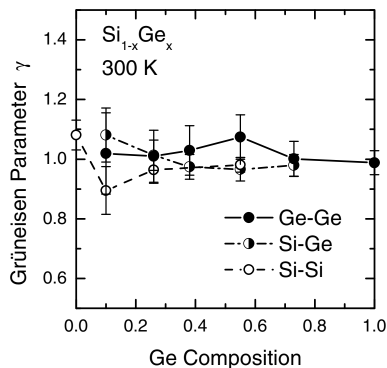

Figure 3 Mode Grüneisen parameter γ of the Ge–Ge (full circles), Si–Ge (half-filled circles) and Si–Si (open circles) optical phonons of $Si_{1-x}Ge_x$ alloys as a function of composition.

curves represent the results of a least-squares fit to the experimental data using for all modes the same phenomenological expression given by

$$b_s = b_4 \cdot (x \quad 1)^4 + b_0 ,$$

where x is the Ge content and b_4, b_0 are adjustable parameters. Interestingly, $b_4 = -190(15)\ \text{cm}^{-1}$ has a common value for all three optical modes, whereas b_0 is $-460(20)\ \text{cm}^{-1}$, $-555(15)\ \text{cm}^{-1}$ and $-650(20)\ \text{cm}^{-1}$ for the Ge–Ge, Si–Ge and Si–Si phonon mode, respectively. Numbers in parentheses are the corresponding error bars.

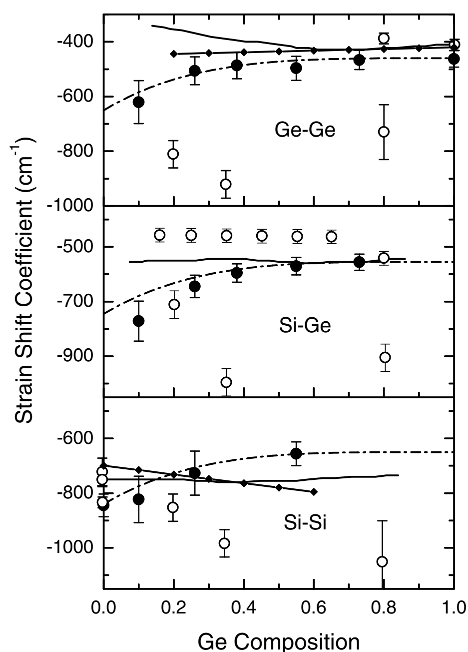

Figure 4 Phonon strain shift coefficient b_s of the Ge–Ge, Si–Ge and Si–Si optical modes of $Si_{1-x}Ge_x$ alloys as a function of composition. Closed symbols and dashed-dotted curves represent our results [10], open circles correspond to the experimental results of Refs. [2, 7, 11, 18, 19] and solid curves are the results of the Keating-model calculations [11]. The solid straight lines with the small diamonds represent the experimental results of Ref. [9].

Until very recently, a confusing situation was found in the literature for the accepted values of the phonon strain shift coefficients in $Si_{1-x}Ge_x$ alloys [2–7]. As illustrated in Fig. 4, for intermediate Ge concentrations in the range $0.3 \le x \le 0.8$ the values of b_s are 50% to 100% higher than for the pure materials, respectively. This is not only counterintuitive but recently appeared theoretical evidence [11] for b_s being nearly constant over the whole concentration range, holding this for the three optical modes of the SiGe alloy. In fact, our data are in fairly good agreement with these calculations within the modified Keating model. The agreement is also good with the b_s values of the Ge–Ge mode obtained by Volodin et al. [9] for high Ge content (solid straight line with small diamonds in Fig. 4). Although we cannot point to a unique and clear reason for the large discrepancies observed among the different experimental and theoretical results, we suggest that one mayor source of error in the determination of the phonon deformation potentials is the precise knowledge of the *unstrained* frequency ω_0 which is typically taken from literature data but appears to be strongly sample dependent. We circumvent this problem by making use of the phonon pressure coefficient, hence, being able to obtain accurate values for the phonon strain-shift coefficient.

4 Conclusions

The measurements of the linear pressure coefficient for the optical phonon modes in the entire compositional range of SiGe alloys were crucial for the precise determination of the corresponding strain shift coefficients. In this way, we have settled the issue about the discrepancies between the different experimental and theoretical values for b_s. Hence, these results are of great practical relevance for they provide accurate strain shift coefficients for the optical phonon modes to be used for the proper determination of the strain status of SiGe nanostructures by Raman scattering.

Acknowledgements A.R.G. is an ICREA Research Professor. We are grateful to A. Crespi, X. Martí, J. Rius and J. Santiso for X-ray diffraction measurements. J.S.R. acknowledges financial support from the AlBan fellowship Program. A.B. acknowledges an FPI fellowship. This work was supported in part by the Spanish Ministerio de Educación y Ciencia through grant MAT2006-02680. Measurements were performed at the Nanotechnology Laboratory of MATGAS 2000 A.I.E.

References

[1] E. Anastassakis and M. Cardona, Semicond. Semimet. **55**, 117 (1998), and references therein.
[2] F. Cerdeira, A. Pinczuk, J. C. Bean, B. Batlogg, and B. A. Wilson, Appl. Phys. Lett. **45**, 1138 (1984).
[3] D. J. Lockwood and J. M. Baribeau, Phys. Rev. B **45**, 8565 (1992).
[4] Z. Sui, H. H. Burke, and I. P. Herman, Phys. Rev. B **48**, 2162 (1993).
[5] J. C. Tsang, P. M. Mooney, F. Dacol, and J. O. Chu, J. Appl. Phys. **75**, 8098 (1994).

 © 2009 WILEY-VCH Verlag GmbH & Co. KGaA, Weinheim

[6] M. Stoehr, D. Aubel, S. Juillaguet, J. L. Bischoff, L. Kubler, D. Bolmont, F. Hamdani, B. Fraisse, and R. Fourcade, Phys. Rev. B **53**, 6923 (1996).
[7] S. Nakashima, T. Mitani, M. Ninomiya, and K. Matsumoto, J. Appl. Phys. **99**, 053512 (2006).
[8] M. I. Alonso and K. Winer, Phys. Rev. B **39**, 10056 (1989).
[9] V. A. Volodin, M. D. Efremov, A. S. Derya, and L. V. Sokolov, Semiconductors **45**, 1314 (2006).
[10] J. S. Reparaz, A. Bernardi, A. R. Goñi, M. I. Alonso, and M. Garriga, Appl. Phys. Lett. **92**, 081909 (2008).
[11] F. Pezzoli, E. Grilli, M. Guzzi, S. Sanguinetti, D. Chrastina, G. Isella, H. von Känel, E. Wintersberger, J. Stangl, and G. Bauer, Mater. Sci. Semicond. Process. **9**, 541 (2006).
[12] D. D. Perovic', B. Bahierathan, H. Lafontaine, D. C. Houghton, and D. W. McComb, Physica A **239**, 11 (1997).
[13] H. K. Mao, J. Xu, and P. M. Bell, J. Geophy. Res. **91**, 4673 (1986).
[14] G. L. Bir and G. E. Pikus, Symmetry and Strain-induced Effects in Semiconductors (Halsted Press, New York, 1974).
[15] J. S. Reparaz, A. Bernardi, A. R. Goñi, P. D. Lacharmoise, M. I. Alonso, M. Garriga, J. Novák, and I. Vávra, Appl. Phys. Lett. **91**, 081914 (2007).
[16] The second-order acoustic-phonon feature of the Si substrate exhibits a *negative* pressure coefficient, thus, it shifts in opposite direction as the Ge–Ge Raman mode with increasing pressure. As a consequence, the precise determination of the Ge–Ge peak position is impaired by the former only in a narrow pressure range around 1 GPa (see inset of Fig. 1, for instance).
[17] Numerical Data and Functional Relationships in Science and Technolog, Landolt-Börnstein, New Series Vol. 17, edited by O. Madelung, H. Weiss, and M. Schulz (Springer, Heidelberg, 1982), Section 2, pp. 64 and 107.
[18] J. Schmidt, G. Vogg, F. Bensch, S. Kreuzer, P. Ramm, S. Zollner, R. Liu, and P. Wennekers, Mater. Sci. Semicond. Process. **8**, 267 (2005).
[19] K. Brunner, EMIS Datarev., 115 (1999).

© 2009 WILEY-VCH Verlag GmbH & Co. KGaA, Weinheim

2.2.3 Multilayers of Ge quantum dots

Self-assembled dot multilayers usually exhibit long-range ordering across the multiple layers. Such a coherent dot growth is driven by the strain field surrounding a dot, hence producing a vertical alignment of the dots from one layer to the next. Only sufficiently large Si spacers between dot layers are able to erase this strain memory, suppressing any interlayer correlation. Here, we are particularly interested in the possibility of designing quantum-dot multiple-layer structures with uncorrelated dots independent of the Si spacer thickness by adding C to the system. Since C is roughly speaking about 50% smaller than Si, the deposition of a submonolayer of C on the nucleation surface for the Ge-dot growth induces locally strong strain fields upon C incorporation. These inhomogeneities drastically reduce the mobility of the oncoming Ge atoms, which neutralizes any seeding effect for QD nucleation due to the presence of a dot in the underlying layer.

We designed two multiple-layer structures grown by solid-source molecular beam epitaxy on the same Si(001) wafer under identical conditions, except for the way C was used to influence the dot nucleation in each heterostructure. A different C-deposition sequence was readily achieved by shuttering half of the wafer area in certain C evaporation steps. The layer structure consists of an eightfold stack of self-assembled Ge dots separated by a 20 nm thick Si spacer. This thickness ensures that in the absence of C, the Ge dots are vertically correlated. The first period was identical in the two samples: a 4 Å thick Ge wetting layer was grown before depositing 0.1 monolayer of carbon to control the shape and density of the quantum dots. In the next step, 7 Å of Ge was deposited for the dots to nucleate, which was capped with the 20 nm thick Si spacer, completing the period. Adopting this procedure, a typical dot shape of 6 nm height and 40 nm base size with a density of about 40 dots/μm^2 is obtained. The remaining seven periods were grown using the shutter to cover half wafer during C deposition. In this way, we obtain two samples with similar dot parameters such as size and density but in the region where no C is present, an almost perfect vertical correlation is expected, whereas in the area with C deposited in each period, such correlation should be totally destroyed. The vertical arrangement of the Ge dots in each case was further confirmed by transmission electron microscopy.

We employed Raman scattering to probe the effect of disorder in the vertical alignment of Ge quantum dots of the multilayered structure. For stacks with perfect dot correlation in the growth direction, the interaction of acoustic phonons with the ensemble of electronic states confined to the dots gives rise to well defined Raman interferences.

- From the position of the interference maxima and the relative intensities, it is possible to extract by simulation of the Raman spectra important structural parameters of the dot stacks such as the spacer-layer thickness and average dot height.

- It was also confirmed that such Raman interferences blur almost completely by total loss of coherence between dots of subsequent layers. In our work, a strong piling disorder was introduced by means of C deposition prior to the QD growth in each layer.

- The resulting spectra exhibit a smooth envelope in the form of a broad band, with maximum position and width related to the mean dot size. In this way, acoustic-phonon Raman scattering provides us with a powerful analytical, fast, and non-invasive tool for the characterization of the structural properties of QD multilayers.

- Using carbon as a route to engineer the fabrication of uncorrelated Ge QDSLs is also an effective strategy to obtain a twofold decrease in thermal conductivity, as compared to ordered structures with the same spacer thickness.

COMPLEMENTARY ARTICLES

Article n: 10

Authors: P. D. Lacharmoise, A. Bernardi, A. R. Goñi, M. I. Alonso, M. Garriga, N. D. Lanzillotti-Kimura, and A. Fainstein

Title: Raman scattering interferences as a probe of vertical coherence in multilayers of carbon-induced Ge quantum dots

Journal: Physical Review B

Doi: 10.1103/PhysRevB.76.155311

Article n: 11

Authors: J. Alvarez-Quintana, X. Alvarez, J. Rodriguez-Viejo, D. Jou, P. D. Lacharmoise, A. Bernardi, A. R. Goñi, and M. I. Alonso

Title: Cross-plane thermal conductivity reduction of vertically uncorrelated Ge/Si quantum dot superlattices

Journal: Applied Physics Letters

Doi: 10.1063/1.2957038

Raman scattering interferences as a probe of vertical coherence in multilayers of carbon-induced Ge quantum dots

P. D. Lacharmoise,* A. Bernardi, A. R. Goñi, M. I. Alonso, and M. Garriga
Institut de Ciència de Materials de Barcelona-CSIC, Esfera UAB, 08193 Bellaterra, Spain

N. D. Lanzillotti-Kimura and A. Fainstein
Centro Atómico Bariloche-Instituto Balseiro, CNEA, San Carlos de Bariloche, 8400 Río Negro, Argentina
(Received 25 June 2007; revised manuscript received 2 August 2007; published 16 October 2007)

We have probed the effect of disorder in the vertical alignment of Ge quantum dots of a multilayered structure by means of Raman scattering. Despite of using a thin Si spacer of 20 nm between dot layers, the coherent piling up of Ge dots one on top of the other is fully suppressed by the deposition of a submonolayer of carbon prior to the dot growth in each layer. For stacks with perfect dot correlation in the growth direction, the interaction of acoustic phonons with the ensemble of electronic states confined to the dots gives rise to well defined Raman interferences. The interference contrast almost vanishes when carbon is introduced on the dot-nucleation surfaces. Instead, a strong and decreasing background is observed at small Raman shifts. These drastic changes in the Raman spectra of dot multilayers with and without C are very well reproduced by simulations based on the interference model of Cazayous *et al.* [Phys. Rev. B **62**, 7243 (2000)].

DOI: 10.1103/PhysRevB.76.155311 PACS number(s): 78.30.−j, 78.67.Pt, 63.20.Kr, 81.07.Ta

I. INTRODUCTION

Self-assembled Ge quantum dots (QDs) attracted a lot of attention in recent years because of their great potential as building blocks in semiconductor nanodevices, which are compatible with Si-based technology. In particular, Ge-dot multiple-layer structures have been widely studied for their promising engineering possibilities, for example, in thermoelectric applications and even optoelectronics.[1–4] To achieve materials with improved thermoelectric properties, a precise control of the morphology and the spatial distribution of the quantum dots is required. For the Si/Ge material system, a possible pathway consists in the deposition of a small amount of carbon, which is known to induce drastic changes in the dot formation mechanism.[5–8] In this way, one has a handle not only on the dot morphology but also on its density and, what is of crucial importance for our work, on the vertical correlation of the dots among different layers. The latter is because self-assembled dot multilayers exhibit long-range ordering across the multiple layers. For a review on the possible arrangements of QDs in stacks, we refer to the work of Stangl *et al.* and references therein.[9] Such a coherent dot growth is driven by the strain field surrounding a dot that propagates, hence producing a vertical alignment of the dots from one layer to the next.[10,11] Only sufficiently large Si spacers between dot layers are able to erase this strain memory, suppressing any interlayer correlation. Here, we are particularly interested in the possibility of designing quantum-dot multiple-layer structures with uncorrelated dots independent of the Si spacer thickness by adding C to the system. Since C is roughly speaking about 50% smaller than Si, the deposition of a submonolayer of C on the nucleation surface for the Ge-dot growth induces locally strong strain fields upon C incorporation. These inhomogeneities drastically reduce the mobility of the oncoming Ge atoms, which neutralizes any seeding effect for QD nucleation due to the presence of a dot in the underlying layer.[6]

In order to address the vertical coherence in C-induced Ge-dot multilayers, we performed Raman scattering experiments in the acoustic-phonon region. The photoelastic model has been typically used to describe the inelastic light scattering by acoustic phonons in superlattices.[12,13] A correct description of both the photoelastic and the acoustic modulation is necessary in order to properly outline the features in Raman spectra of multilayered systems.[14] Variations of this model were developed for the case of resonant and out-of-resonance Raman scattering. Whereas an assignment of a photoelastic constant to each material of the superlattice is enough to describe systems out of resonance, the electron-phonon interaction and thus the distribution of electronic states must be taken into account explicitly in the resonant case. Ruf *et al.* addressed this problem when studying the effects of thickness fluctuations in quantum wells, giving a microscopic description of the photoelastic Raman-scattering mechanism by considering the interaction between acoustic phonons and confined electronic states explicitly.[15–17] The importance of finite sample effects and a precise calculation of the phonon modes in superlattices and quasiperiodical systems were discussed in subsequent works.[18–21] The concept of Raman interferences by acoustic-phonon scattering, however, was introduced by Giehler *et al.*[22] Finally, Cazayous *et al.* clearly demonstrated how acoustic phonons can interact with the ensemble of electronic confined states in multiple layers of dots, thus giving rise to pronounced Raman scattering interferences.[23–27] Within this model, the Raman intensity results from a real interference of the inelastically scattered photons by acoustic phonons in processes mediated by electrons confined to different quantum dots. Hence, the spatial arrangement of the quantum dots might play a crucial role. In fact, as discussed in previous works,[23–27] we show here both experimentally and theoretically that making use of the sensitivity of Raman scattering to the spatial ordering of quantum dots in multilayered systems, we are able to unravel the strong randomization in-

 ©2007 The American Physical Society

duced by C deposition on QD nucleation, which cares less about the strain field extending from layer to layer.

II. EXPERIMENTAL DETAILS AND SPECTRA

We designed two multiple-layer structures grown by solid-source molecular beam epitaxy on the same Si(001) wafer under identical conditions, except for the way C was used to influence the dot nucleation in each heterostructure. A different C-deposition sequence was readily achieved by shuttering half of the wafer area in certain C evaporation steps. First, a 100 nm thick Si buffer layer was deposited. Then, the temperature was set to 500 °C to proceed with the layer structure. It consists of an eightfold stack of self-assembled Ge dots separated by a 20 nm thick Si spacer. This thickness ensures that in the absence of C, the Ge dots are vertically correlated. The first period was identical in the two samples: a 4 Å thick Ge wetting layer was grown before depositing 0.1 monolayer of carbon to control the shape and density of the quantum dots.[7,8] In the next step, 7 Å of Ge was deposited for the dots to nucleate, which was capped with the 20 nm thick Si spacer, completing the period. Adopting this procedure, a typical dot shape of ~6 nm height and ~40 nm base size with a density of about 40 dots/μm^2 is obtained.[7,8] The remaining seven periods were grown using the shutter to cover half wafer during C deposition. In this way, we obtain two samples with similar dot parameters such as size and density but in the region where no C is present, an almost perfect vertical correlation is expected, whereas in the area with C deposited in each period, such correlation should be totally destroyed.[6] Hereafter, we will refer to the multilayers as "without C" and "with C," respectively. The vertical arrangement of the Ge dots in each case was further confirmed by transmission electron microscopy.

Raman spectra were collected at room temperature with a Jobin-Yvon T64000 triple spectrometer in subtractive mode. The spectral resolution was about 2 cm^{-1}. The scattering configuration was close to the backscattering geometry. We used the lines of an Ar-Kr laser ranging from 2.18 eV (red) to 2.54 eV (blue) for excitation. Figure 1 shows measured Raman spectra of both multilayers with and without C for different laser lines with photon energies around that of the E_1 interband transition of the Ge quantum dots. Due to the large energy width of the resonance curve for this transition,[28] resonance conditions are easily fulfilled for the whole dot ensemble. The spectra of the two samples are qualitatively different, revealing the drastic effect of C deposition on the vertical alignment of the dots. The Raman spectrum of the multilayer without C displays a clear interference pattern, whereas the one with C shows a decaying signal slightly modulated when exciting at 2.54 eV. For the multilayer without C, the maximum interference contrast is attained for blue excitation at 2.5 eV, slowly decreasing as one moves away from the resonance to completely disappear at around 1.91 eV. A similar resonant behavior is observed for the intensity of the decaying signal in the spectra of the multilayer with C.

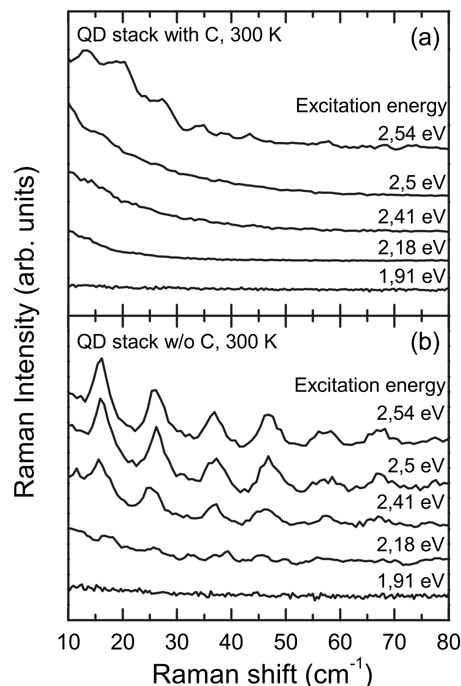

FIG. 1. Raman spectra in the acoustic-phonon region of Ge quantum-dot multilayers (a) with and (b) without carbon deposition prior to the dot nucleation measured at room temperature with different laser excitation energies.

III. ANALYSIS

A. Raman interference model

We simulated Raman spectra of our QD stack samples using the three-dimensional model proposed by Cazayous *et al.*[23–25] The analysis of the Raman spectra in many studies of periodic heterostructures was performed on the basis of the photoelastic model and the folding of the phonon dispersion curve due to the superimposed periodicity of the structure.[29–31] However, the validity of this model for finite, low-dimensional systems such as quantum-dot multilayers is arguable. First of all, the Brillouin minizone formation would strictly require an infinite periodical modulation of the acoustical impedance, which is not the case in many studied multiple-layer structures with low number of periods. The finite size of the dots, for instance, is also neglected in such calculations. Moreover, a strictly two-dimensional photoelastic model is completely unable to describe the spatial coherence of the dots from layer to layer. Thus, this kind of simulations would never meet the requirements to distinguish between vertically aligned and randomly distributed dots, as shown below to be the case in Raman scattering experiments.

In the model of Raman interferences, the energy of the measured peaks is only related to the fact of having a constructive interference between photons scattered by acoustic phonons, which interact with the three-dimensional ensemble of electronic states confined to the dots. The interference model takes explicitly into account the effect of electronic confinement since its spectral envelope in the Raman spectrum, i.e., the intensity modulation of the interference peaks,

is determined by the Fourier transform of the electronic wave function and its spatial extension. In our simulations, the quantum dots are treated as identical quantum disks with $\varphi_{n,l_p}(z)$ and $\Psi_{m,l_p}(\vec{r})$ denoting the electronic wave function in the growth direction and the in-plane component, respectively, for confined states with subindices (n,m). The symbols l_p and p denote the layer index and the dot index within that layer, respectively. The lack of translation invariance breaks the wave-vector conservation rules and, therefore, all acoustic phonons may scatter in the Raman process. Considering the deformation potential as the main electron-phonon interaction mechanism between an acoustic phonon with wave vector q and displacement field u_q and the ensemble of electronic states, the Raman intensity is proportional to[16,17,24]

$$I_R \propto \left| \sum_{p,l_p} \vec{q}\cdot\vec{u}_q \int \Psi^*_{m,l_p}(\vec{r}) e^{i(\Delta\vec{k}_\parallel - \vec{q}_\parallel)\cdot\vec{r}} \Psi_{\check{m},l_p}(\vec{r}) d^2r \times \int \varphi^*_{n,l_p}(z) e^{i(\Delta k_z - q_z)\cdot z} \varphi_{\check{n},l_p}(z) dz \right|^2, \quad (1)$$

where Δk_z ($\Delta k_\parallel$) is the difference between the incident and scattered photon wave vector in the growth (in-plane) direction. Identical dots hold that $\varphi_{n,l_p}(z)=\varphi(z-z_p)$ and $\Psi_{m,l_p}(\vec{r}) = \psi(\vec{r}-\vec{r}_p)$ where z_p and $\vec{r}_p$ are the spatial coordinates of the dot with index p. Hence, Eq. (1) can be simplified to

$$I_R \propto \overbrace{\left| \int \Psi^*(\vec{r})\Psi(\vec{r}) e^{-i\vec{q}_\parallel\cdot\vec{r}} d^2r \int \varphi^*(z)\varphi(z) e^{-iq_z z} dz \right|^2}^{F} \times \underbrace{\left| \sum_{p,l_p} u_{q,l_p} e^{-i(q_z-\Delta k_z)z_{l_p}} e^{-i(\vec{q}_\parallel - \Delta\vec{k}_\parallel)\cdot\vec{r}_{l_p,p}} \right|^2}_{S} \quad (2)$$

where F and S are the form and structure factor, respectively. F depends only on the electronic confinement within the dots and determines the spectral envelope, whereas S represents the interference pattern coming from the interaction of the extended phonon with the dot ensemble. Periodical oscillations of the Raman signal coming from S are expected if the dot layers are regularly spaced, being the oscillation period inversely proportional to the spacer thickness. A random number generator algorithm is used to determine the in-plane positions of the quantum dots in the first layer of the structure. The obtained in-plane dot distribution is repeated for the subsequent layers in the case of ordered multilayers. On the contrary, a random in-plane distribution for each layer is considered in the case of disordered structures. In order to have sufficient statistics in the calculation, each Raman spectrum is simulated by summing over 200 different configurations.

B. Results and discussion

Figure 2 shows two series of simulated spectra in the case of a sample with vertically correlated dots. All the QD multilayers consist in a stack of eight periods. An effective refractive index of 4.4 and a laser energy of 2.54 eV were used in the calculations. In the first series, the dot parameters are fixed and only the spacer thickness varies. From the form factor in Eq. (2), we infer that the degree of confinement in a specific direction determines the weight of the contribution from phonons traveling in that direction. Since the dot height is about seven times smaller than the base diameter, we are mainly dealing with plane waves with in-plane wave vectors close to zero. In the calculations, we consider for the sake of simplicity that the phonon displacements $u_q(z)$ are solely a function of z. Hence, to a good approximation, the physical picture is that of two counterpropagating plane waves with crystal momentum $\pm q_z$ and sound velocity V_{eff} traveling simultaneously. The condition to obtain a maximum in the interference pattern is $q_z \pm \Delta k_z = 2\pi n/L$, where L and n are the spacer thickness and an integer, respectively. Doublets of order n with a fixed energy separation of $2\Delta k_z V_{eff}$ are expected. In the upper part of Fig. 2, the dotted lines indicate the shift of the doublets of orders 1 and 2. The separation between different doublets diminishes as the spacer thickness increases. Since the shift of the peaks is proportional to n, contributions from doublets with different n can merge to form new doublets, as is the case of the spectrum for $L = 20$ nm.

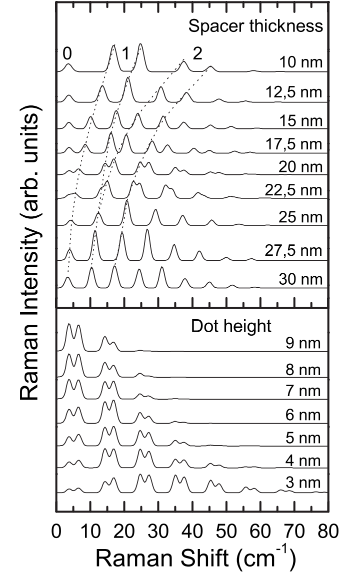

FIG. 2. Series of simulated Raman spectra of an ordered Ge-dot multilayer as a function of the spacer thickness (top panel) and the dot dimensions (bottom panel). The former dots of 4 nm height and 27 nm base size were considered. In the latter case, a fixed spacer thickness equal to 20 nm and an aspect ratio of 0.15 were used.

In the lower panel of Fig. 2, we display the simulated Raman spectra of multilayers with a Si spacer of 20 nm but where the height and the base diameter of the dots were varied at a fixed aspect ratio. We note that the width of the spectral envelope which modulates the intensity of the interference peaks increases with decreasing dot size, i.e., for stronger confinement of the electronic states. The model is not only clearly sensitive to the spatial distribution of the

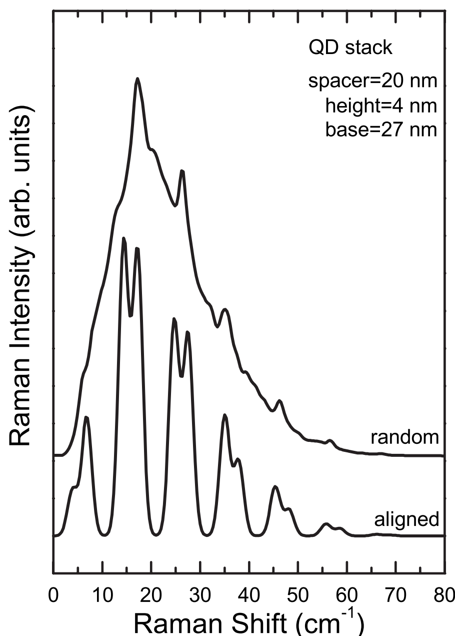

FIG. 3. Simulated Raman spectra of two Ge-dot multilayer structures both with the same parameters but differing only in the spatial correlation of the dots in the growth direction. The lower and upper curves were calculated with vertically correlated (aligned) and uncorrelated (random) dots, respectively.

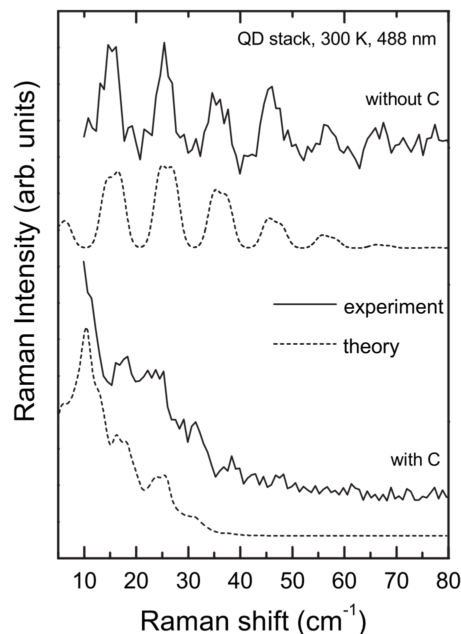

FIG. 4. (Solid curves) Measured Raman spectra of Ge-dot multiple-layer samples with and without carbon. The dashed curves represent the corresponding spectra simulated using the Raman interference model (see text for details).

dots but also to the extent of the electronic wave functions.

Figure 3 displays two spectra calculated for the same multilayer consisting in QD stacks of eight periods, which differ only in the vertical ordering of the dots, as described before. The upper one has randomly distributed dots within the first dot layer but exactly the same dot pattern is repeated in the subsequent layers, leading so to perfect stacking in the growth direction. The spectrum exhibits high-contrast interferences. The lower spectrum corresponds to the case of randomly distributed dots in every layer without interlayer correlation. The interferences blur almost completely, giving a continuum contribution modulated by the form factor envelope. Nevertheless, faint interference peaks on top of the envelope remain visible even for the disordered dot distribution. These effects are thus expected to show up in resonant Raman spectra in the acoustic-phonon region, allowing us to study the spatial correlation of dots in multilayered systems.

For comparison, both measured and calculated Raman spectra of the samples with and without C are plotted together in Fig. 4. In order to avoid the background signal coming from Rayleigh scattering, a reference spectrum measured on a Si wafer has been subtracted from the experimental spectra. The stray light coming from the laser made impossible to work below 8 cm^{-1} in backscattering geometry because of the surface roughness of the samples. For the simulations, we considered a density of 40 dots/μm^2 and we summed over many dot distributions to prevent finite-size effects of the ensemble. We also performed a convolution using a Gaussian with a width of 2 cm^{-1} in order to account for the experimental line broadening. The calculations are in very good agreement with the experiment, as far as the peak positions and relative intensities are concerned. However, the most compelling evidence that C deposition effectively suppresses the vertical coherence of the dot growth is the striking similarity of the measured and simulated Raman spectra of the stack with C.

The spectrum of the multilayer without C displays clear periodic oscillations coming from the constructive interferences between dot layers. The oscillation period is well accounted for by the simulation, when performed with a spacer thickness of 20 nm. This is in excellent agreement with the nominal growth parameters. The interference contrast is a clear indicator of the spatial correlation between dots in the z direction. In randomly distributed dot stacks, the interferences vanish. This is again well demonstrated by the spectrum of the C-induced Ge dot multilayer, where the deposition of C in each layer has erased the strain memory responsible for a coherent growth of the dots from layer to layer. The simulation with a random distribution across the stack also reproduces the spectral features in this case. We note a slight modulation interference coming from the structure factor contribution on top of an exponential decaying signal. A closer inspection to the structure factor of Eq. (2) reveals that the interferences appear when the contribution from the dots add up coherently. This is determined by the phase which is given by

$$(q_z - \Delta k_z) z_{l_p} + (\vec{q}_{\parallel} - \Delta\vec{k}_{\parallel}) \cdot \vec{r}_{l_p,p}. \qquad (3)$$

Both terms in Eq. (3) are independent. The former leads always to interferences since the QD stacks exhibit good periodicity in the z direction regardless of the existence or loss of interlayer correlations due to the introduction of C. The interference blurring comes from the second term

$\vec{q}_{\parallel}\cdot\vec{r}_{l_p,p}$, which introduces a dephasing if the dots are not aligned in the growth direction. The $\vec{q}_{\parallel}$ that participate in the scattering process are defined by the lateral extension of the dot. Since the diameter of the dot is about 60 times the lattice constant of the material, the $\vec{q}_{\parallel}$ that contribute the most are close to zero. Thus, the values of the dephasing term are large enough to blur the interferences but not completely, as observed also in the experimental spectra.

It is important to notice that although a 20 nm thick spacer has been chosen for our samples, the disordering effect of C should be effective for even thinner spacers. Vertically uncorrelated Ge-dot stacks with such thinner spacers would be impossible to achieve with conventional self-assembled dot growth. Unfortunately, it was not possible to study intermediate cases between aligned and randomly distributed dots in the z direction because of the drastic effect that very small amounts of C have on the dot-nucleation mechanism.

We now turn to the discussion of the spectral envelope. As we mentioned before, this envelope depends on the form factor F, which is determined by the electronic density associated with the confined dot states, i.e., it depends on dot dimensions. The envelope for the multilayer without C is well reproduced by the simulations considering dots with 4 nm height and 27 nm base size. In contrast, slightly bigger dots with a height of 6 nm and a base length of 40 nm account better for the envelope in the case of the C-induced quantum dots. This is actually closely related to the QD-growth mechanism itself, which is different in both cases. When carbon is deposited, the nucleation of the Ge dots proceeds immediately, leading to an effective reduction of the critical thickness for the Stranski-Krastanow growth mode.[5–8] If no C is deposited, part of the Ge coverage is used to achieve that critical thickness; hence, the resulting dots are smaller in size compared to those grown using C deposition. As illustrated by the calculated Raman spectra of Fig. 2 (lower panel), the position of the envelope maximum shifts to larger Raman shifts for smaller dot sizes. Such shift is extremely sensitive to changes as small as 1 nm in the height of the dots, which is the dimension leading to the strongest confinement.

IV. CONCLUSIONS

In summary, the multiple-peak structure observed in the spectra of Raman scattering by acoustic phonons of Ge QD stacks with ordered dots along the growth direction is well explained within the model of Raman interferences. From the position of the interference maxima and the relative intensities, it is possible to extract by simulation of the Raman spectra important structural parameters of the dot stacks such as the spacer-layer thickness and average dot height. It was also confirmed that such Raman interferences blur almost completely by total loss of coherence between dots of subsequent layers. In our work, a strong piling disorder was introduced by means of C deposition prior to the QD growth in each layer. The resulting spectra exhibit a smooth envelope in the form of a broad band, with maximum position and width related to the mean dot size. In this way, acoustic-phonon Raman scattering provides us with a powerful analytical, fast, and noninvasive tool for the characterization of the structural properties of QD multilayers for specific applications in SiGe-based thermoelectrical nanodevices.

ACKNOWLEDGMENTS

P.D.L. thanks Groenen and Huntzinger for very fruitful discussions. P.D.L. acknowledges an I3P-CSIC grant and A.B. acknowledges support from FPI program. A.R.G. is supported by ICREA. This work was supported in part by the Spanish Ministerio de Educación y Ciencia through Grant No. MAT2006-02680.

*placharmoise@icmab.es

[1] J. L. Liu, A. Khitun, K. L. Wang, W. L. Liu, G. Chen, Q. H. Xie, and S. G. Thomas, Phys. Rev. B **67**, 165333 (2003).
[2] Y. Bao, W. L. Liu, M. Shamsa, K. Alim, A. A. Balandin, and J. L. Liu, J. Electrochem. Soc. **152**, G432 (2005).
[3] A. A. Shklyaev and M. Ichikawa, Appl. Phys. Lett. **80**, 1432 (2002).
[4] O. G. Schmidt, K. Eberl, and J. Auerswald, J. Lumin. **80**, 491 (1998).
[5] Y. Wakayama, L. V. Sokolov, N. Zakharov, R. Werner, and U. Gösele, Appl. Surf. Sci. **216**, 419 (2003).
[6] O. G. Schmidt, S. Schieker, K. Eberl, O. Kienzle, and F. Ernst, Appl. Phys. Lett. **73**, 659 (1998).
[7] A. Bernardi, M. I. Alonso, A. R. Goñi, J. O. Ossó, and M. Garriga, Appl. Phys. Lett. **89**, 101921 (2006).
[8] A. Bernardi, J. O. Ossó, M. I. Alonso, A. R. Goñi, and M. Garriga, Nanotechnology **17**, 2602 (2006).
[9] J. Stangl, V. Holý, and G. Bauer, Rev. Mod. Phys. **76**, 725 (2004).
[10] Q. Xie, A. Madhukar, P. Chen, and N. P. Kobayashi, Phys. Rev. Lett. **75**, 2542 (1995).
[11] G. S. Solomon, J. A. Trezza, A. F. Marshall, and J. S. Harris, Phys. Rev. Lett. **76**, 952 (1996).
[12] C. Colvard, T. A. Gant, M. V. Klein, R. Merlin, R. Fischer, H. Morkoc, and A. C. Gossard, Phys. Rev. B **31**, 2080 (1985).
[13] D. J. Lockwood, M. W. C. Dharma-wardana, J. M. Baribeau, and D. C. Houghton, Phys. Rev. B **35**, 2243 (1987).
[14] B. Jusserand and M. Cardona, in *Light Scattering in Solids V*, edited by M. Cardona and G. Guntherodt (Springer, Heidelberg, 1989), p. 49.
[15] T. Ruf, V. I. Belitsky, J. Spitzer, V. F. Sapega, M. Cardona, and K. Ploog, Phys. Rev. Lett. **71**, 3035 (1993).
[16] T. Ruf, J. Spitzer, V. F. Sapega, V. I. Belitsky, M. Cardona, and K. Ploog, Phys. Rev. B **50**, 1792 (1994).
[17] V. I. Belitsky, T. Ruf, J. Spitzer, and M. Cardona, Phys. Rev. B **49**, 8263 (1994).
[18] P. X. Zhang, D. J. Lockwood, and J. M. Baribeau, Can. J. Phys. **70**, 843 (1992).

[19] A. Mlayah, R. Grac, G. Armelles, R. Carles, A. Zwick, and F. Briones, Phys. Rev. Lett. **78**, 4119 (1997).
[20] M. Trigo, A. Fainstein, B. Jusserand, and V. Thierry-Mieg, Phys. Rev. B **66**, 125311 (2002).
[21] P. Lacharmoise, A. Fainstein, B. Jusserand, and V. Thierry-Mieg, Appl. Phys. Lett. **84**, 3274 (2004).
[22] M. Giehler, T. Ruf, M. Cardona, and K. Ploog, Phys. Rev. B **55**, 7124 (1997).
[23] M. Cazayous, J. R. Huntzinger, J. Groenen, A. Mlayah, S. Christiansen, H. P. Strunk, O. G. Schmidt, and K. Eberl, Phys. Rev. B **62**, 7243 (2000).
[24] M. Cazayous, J. Groenen, J. R. Huntzinger, A. Mlayah, and O. G. Schmidt, Phys. Rev. B **64**, 033306 (2001).
[25] M. Cazayous, J. Groenen, A. Zwick, A. Mlayah, R. Carles, J. L. Bischoff, and D. Dentel, Phys. Rev. B **66**, 195320 (2002).
[26] M. Cazayous, J. Groenen, J. Brault, A. Gendry, U. Denker, and O. G. Schmidt, Physica E (Amsterdam) **17**, 533 (2003).
[27] M. Cazayous, J. Groenen, J. R. Huntzinger, A. Mlayah, U. Denker, and O. G. Schmidt, Mater. Sci. Eng., B **88**, 173 (2002).
[28] A. Bernardi, J. S. Reparaz, A. R. Goñi, M. I. Alonso, and M. Garriga, Phys. Status Solidi B **244**, 76 (2007).
[29] C. Colvard, R. Merlin, M. V. Klein, and A. C. Gossard, Phys. Rev. Lett. **45**, 298 (1980).
[30] B. Jusserand, F. Alexandre, J. Dubard, and D. Paquet, Phys. Rev. B **33**, 2897 (1986).
[31] P. V. Santos, L. Ley, J. Mebert, and O. Koblinger, Phys. Rev. B **36**, 4858 (1987).

Cross-plane thermal conductivity reduction of vertically uncorrelated Ge/Si quantum dot superlattices

J. Alvarez-Quintana,[1] X. Alvarez,[1] J. Rodriguez-Viejo,[1,a)] D. Jou,[1] P. D. Lacharmoise,[2] A. Bernardi,[2] A. R. Goñi,[2] and M. I. Alonso[2]
[1]*Departament de Física, Universitat Autònoma de Barcelona, 08193 Bellaterra, Spain*
[2]*Institut de Ciència de Materials de Barcelona-CSIC, Esfera UAB, 08193 Bellaterra, Spain*

(Received 17 January 2008; accepted 20 June 2008; published online 9 July 2008)

A drastic reduction in temperature dependent cross-plane thermal conductivity $\kappa_\perp$ occurs in Ge quantum dot superlattices (QDSLs), depending on the vertical correlation between dots. Measurements show at least a twofold decrease of $\kappa_\perp$ in uncorrelated dot structures as compared to structures with the same Si spacer of 20 nm but good vertical dot alignment. The observed impact of disorder on the conductivity provides an alternative route to reduce the thermal conductivity of QDSLs. The results of this work have implications for the development of highly efficient thermoelectric materials and on-chip nanocooling devices. © *2008 American Institute of Physics*.
[DOI: 10.1063/1.2957038]

SiGe nanostructures are very promising for thermoelectric cooling of microelectronic devices and high-temperature thermoelectric power generation. The thermal conductivity κ is significantly reduced in superlattices[1–5] (SLs) and quantum dot SLs (QDSLs).[6–10] Previous studies by Lee *et al.* on short period 3–7 nm Si/Ge SLs unveiled a decrease of $\kappa_\perp$ with decreasing SL period.[1] A minimum value of about 3 W/mK was measured at 300 K. For larger periods, $L > 13$ nm, they unexpectedly observed a decrease of $\kappa_\perp$ which was attributed to the existence of extended defects. On the contrary, Borca-Tasciuc *et al.*[2] measured symmetrically strained $Si_{0.5}Ge_{0.5}$ SLs with periods of 4–14 nm without observing a clear dependence of $\kappa_\perp$ on the SL period. Huxtable *et al.*[3] have shown the influence of the acoustic interface mismatch (AIM) in the thermal conductivity of $Si/Si_{0.7}Ge_{0.3}$ and $Si_{0.84}Ge_{0.16}/Si_{0.76}Ge_{0.24}$ SLs. Further nanostructuring and phonon confinement may result in enhanced figures of merit and therefore Ge QDSLs have also been analyzed by a number of authors.[6–10] Liu *et al.*[6,7] measured $\kappa_\perp$ in Ge QDSLs with Ge content from 7% to 20% and a Si spacer of 20 nm. They reported values as low as 6.2 W/mK for samples grown at 500 °C with an average composition of $Si_{0.93}Ge_{0.07}$ and dot surface coverage about 10%. Bao *et al.*[8] and Shamsa *et al.*[9] analyzed QDSLs grown by molecular beam epitaxy (MBE) at 550 °C with average Ge concentrations from 6% to 9% and a Si spacer of 20 nm and found values between 8–12 W/mK at 300 K. More recently, Lee and Venkatasubramanian[10] measured $\kappa_\perp$ in QDSLs grown by metal organic chemical vapor deposition at 750 °C and concluded that low values of $\kappa_\perp$ can be attained either by using low SL periods or by increasing the dot coverage. They reported values between 2–2.7 W/mK at short periods of 4 nm and areal densities around 20%.

All these studies deal with vertically correlated QDSLs. The vertical correlation between Ge dots can be modified by a proper selection of the spacer layer thickness. A larger thickness results in a lower correlation function. However, there is a serious drawback of this approach to increase the figure of merit in thermoelectric materials, since the electrical conductivity is expected to diminish with increasing Si spacer width. To circumvent this situation, one can use a seed layer of C to counteract stress memory between layers. Several authors[11–13] have shown that adding submonolayer amounts of C drastically affects the dot-nucleation mechanism, which can be successfully employed to grow uncorrelated nanostructures without an additional increase of the Si spacer.

In this letter, we report on the temperature-dependent thermal conductivity measured on Ge QDSLs grown simultaneously on the same Si wafer, which differ only in the degree of vertical correlation of the dots. We observe a decrease of the cross-plane conductivity for the uncorrelated samples in excess of a factor of 2. We interpret such a drastic impact of disorder on $\kappa_\perp$ by using a theoretical approach based on a modification of the Fourier transport equation.

Samples were grown by solid-source MBE on Si (001) substrates as described elsewhere.[13] By shuttering half of the wafer area in each deposition, it was possible to grow two multilayer structures on each Si wafer. In the area with C only in the seed layer, there is perfect vertical dot correlation between layers, whereas in the area with C deposited in each layer the correlation is almost completely suppressed. The growth temperature was fixed at 500 °C and the Si spacer at 20 nm for both samples. Table I shows the main parameters of sample 52. The vertical arrangement of the Ge dots in each case was confirmed by transmission electron microscopy and Raman scattering.[14] The cross-plane thermal conductivity was measured with the differential 3ω method in the temperature range 77–300 K.[15] A thin film of 10 nm Ti/100 nm Pt is deposited onto a 200 nm thick SiO_2 insulating layer previously grown on both the sample surface and

TABLE I. Main characteristics of the MBE samples.

Sample	Period	Ge layer thickness (A)	Si layer thickness (nm)	Dot height, diameter (nm)	dot density (cm^{-2})
52 Corr	8	7	20	4, 30	5×10^9
52 Unc	8	7	20	7, 40	5×10^9

[a)]Author to whom correspondence should be addressed. Electronic mail: javier.rodriguez@uab.es.

This article is copyrighted as indicated in the article. Reuse of AIP content is subject to the terms at: http://scitation.aip.org/termsconditions. Downloaded to IP: 158.109.18.157 On: Thu, 08 Oct 2015 12:23:41

 © 2008 American Institute of Physics

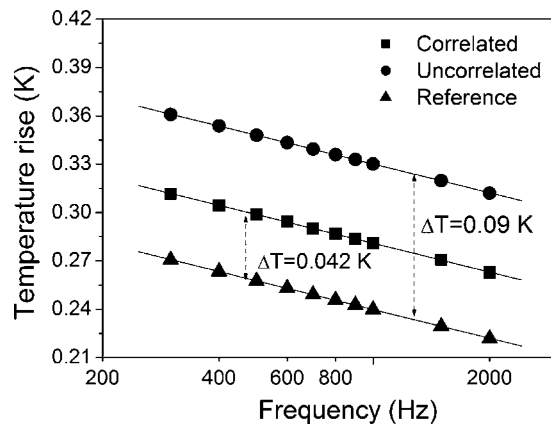

FIG. 1. Temperature rise as a function of modulated frequency at 300 K for the correlated and uncorrelated 160 nm Ge QDSL and the reference sample.

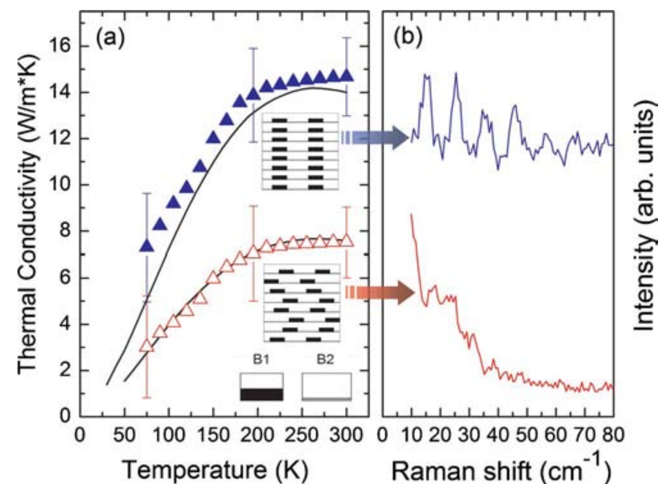

FIG. 2. (Color online) (a) Measured thermal conductivity as a function of temperature for sample 52 with vertically aligned dots (solid blue symbols) and without vertical correlation (open red symbols). Also shown are results of calculations using the extended Fourier heat transport equation (solid line). The inset shows sketches of the QDSL nanostructures with and without vertical correlation. Black squares represent the Ge dots, whereas gray regions correspond to the Ge wetting layer. White regions represent the Si spacer. (b) Measured Raman spectra (Ref. 14) of the corresponding samples in (a).

the Si wafer used as reference. The thin film heater defined by photolithography and lift-off is 1 mm long $\times$ 15 μm wide. The thermal contribution of the SiO_2/Si is measured independently and subtracted from the measurements on the $SiO_2/QDSL/Si$ stack. The heater-width-to-film thickness and the film/substrate thermal conductivity ratios are 75 and about 0.05–0.1 at 300 K, respectively. Based on these values the heat spreading in the parallel direction of the film is very small, thus, the cross-plane thermal conductivity of the film calculated from the one-dimensional steady-state heat conduction model would be within 5% close to the true value for the film.[16] Figure 1 illustrates the temperature rises in the correlated and uncorrelated QDSLs and the reference sample as a function of the modulation frequency. The input power was 35 mW at 300 K. The temperature drop across the uncorrelated film is constant at 0.090 K over a wide frequency interval. The thermal conductivity values derived for the undoped Si substrate and the 200 nm SiO_2 film yield 150 W/mK and 1.36 W/mK at 300 K, respectively, which closely agree with literature values.[15,17,18]

Figure 2(a) shows the thermal conductivity as a function of temperature for sample 52 which is representative of a series of Ge QDSLs, being this particular one also studied by Raman scattering. The equivalent Ge fraction of the QDSL is estimated to be 3%. The thermal conductivity of an undoped $Si_{0.97}Ge_{0.03}$ alloy at 300 K is about 17 W/mK,[19] slightly above the value measured for the correlated sample, 14.5 W/mK. This value can be qualitatively compared to results of Refs. 8 and 9 which obtained 12 W/mK at 300 K for a QDSL of overall composition $Si_{0.94}Ge_{0.06}$ grown by MBE at 550 °C. However, in general it is slightly larger than previously published data for QDSLs.[6–10] The Ge content and the total surface coverage of the dots in our QDSLs (see Table I) are below those reported in earlier studies rendering difficult a direct comparison. If we extrapolate data from Lee *et al.*[10] to 4%–5% coverage and 20 nm Si period, a value about 20 W/mK may be inferred. The lower value that we obtain may be due to the lower growth temperature which favors a high Ge content within the dot and therefore increases the AIM of the SL. At low temperatures, the cross-plane thermal conductivity increases monotonically with temperature remaining then at a relatively constant value between 200 and 300 K. This behavior is in frank contrast to that of bulk Si which exhibits maximum conductivity at 40 K but decreases to a value of ~150 W/mK at 300 K. The striking result of this work is the further reduction of the room-temperature thermal conductivity by a factor in excess of 2, which is attained just by destroying the vertical correlation between dots. In this respect, it is very instructive to compare the results of thermal transport with those from Raman scattering. As illustrated in Fig. 2(b), in QDSL structures, there is a close relationship between the magnitude of the thermal conductivity and the spectral features of light scattering by acoustic phonons.[14] For the multilayer sample with perfect dot correlation in the growth direction, the interaction of the acoustic phonons with the ensemble of electronic states confined to the dots gives rise to well-defined Raman interferences. The interference contrast almost vanishes when carbon is introduced on the dot-nucleation surfaces in each layer. Instead, a strong and decreasing background is observed at small Raman shifts [bottom spectrum in Fig. 2(b)]. These drastic changes in the Raman spectra of dot multilayers with and without carbon are directly related to the existence or lack of vertical correlation between Ge dots, as confirmed by calculations within the Raman interference model reported in Ref. 14.

To understand the observed thermal conductivity reduction, we compute $\kappa_\perp$ by an approach based on an extension of the Fourier heat transfer equation that yields an analytical expression for the thermal conductivity of nanosystems of given size,[20]

$$\kappa_{\mathrm{Si,Ge}} = \frac{\kappa_0 L^2}{2\pi^2 \ell^2}\left[\sqrt{1+4\left(\frac{\pi \ell}{L}\right)^2}-1\right], \tag{1}$$

where κ_0 is the material bulk thermal conductivity, ℓ is the mean phonon free path,[21] and L is the size of the system in the direction of propagation. The ordered (disordered) sample is formed by QDs which are vertically correlated (uncorrelated), as schematically illustrated in the inset to Fig. 2(a). Using an average dot base diameter of 30–40 nm and dot densities about 5×10^9 cm^{-2} (see Table I), the surface fraction covered with dots f_{dots}, in the eight-period stacks of

This article is copyrighted as indicated in the article. Reuse of AIP content is subject to the terms at: http://scitation.aip.org/termsconditions. Downloaded to IP: 158.109.18.157 On: Thu, 08 Oct 2015 12:23:41

the (un)correlated samples amounts 0.5 and 0.05, respectively. The effective thermal conductivity is written as the weighted sum of two parallel thermal processes,

$$\kappa_{\perp} = f_{\text{dots}} \cdot \kappa_{B1} + (1 - f_{\text{dots}})\kappa_{B2}, \quad (2)$$

where κ_{B1} represents the thermal conductivity contribution due to the presence of QD (region B1) and κ_{B2} is the thermal conductivity contribution in the regions without Ge dots (region B2). κ_{B2} is the dominant thermal path in the correlated sample. To model $\kappa_{\perp}$ we use the two elementary building blocks of Fig. 2(a). Block 1 is formed by a dot of height L_d and a silicon spacer of width L_{s1}. The resistance is given by the sum of four series resistors, i.e., the resistance of the dot r_d, the resistance of the spacer r_{s1}, and two interface thermal resistances r_i (Kapitza resistances), due to the difference of acoustic properties and interface quality at the dot/matrix interface. The resistance of the block is not dependent on the height of the dot due to the linearity of Eq. (1) in the low size regime. Therefore, the variation of the Ge dot height plays a minor role on the effective thermal conductivity compared to disorder. Block 2 is mainly composed of Si, with a width $L_{s2}=L_{s1}+L_w$. and the resistance is the sum of the resistance of the silicon spacer r_{s2} and the interface thermal resistance imposed by the wetting layer r_w. In all cases, the thermal conductivity is readily obtained by substituting the lengths and mean free paths in Eq. (1). We use Eq. (2) to calculate the $\kappa_{\perp}$ across the sample [solid lines in Fig. 2(a)]. The thermal boundary resistances (TBRs) at 300 K that provide a good fit are $r_i=3\times10^{-8}$ m^2 K/W and $r_w=2.5\times10^{-11}$ m^2 W/K for the dot/matrix interface and the wetting layer, respectively. We have assumed that the temperature dependence of the TBR follows predictions of the diffusive mismatch model (DMM).[22] The value obtained at 300 K for the dot/matrix resistance is of the same order of magnitude as previously reported for other systems[23,24] and larger by an order of magnitude to the value of 3×10^{-9} W/m^2 K derived from DMM at 300 K. However, the value associated with the thermal resistance of the wetting layer is significantly smaller probably due to phonon tunneling effects across it.

Despite its simplicity, the agreement between the model based on Eqs. (1) and (2) and the experimental data reinforces the concept that the reduction of thermal conductivity between correlated and uncorrelated samples is entirely due to the strong randomization of the dot spatial distribution induced by the presence of C in every layer. It is expected that lower thermal conductivities could be attained by doping and by reducing the Si spacer thickness which leads to an effective increase of the number of interfaces per unit length in the growth direction. Therefore, we anticipate that a combination of a short period with a random stacking of the dots in the vertical direction may lead to Ge QDSLs with even smaller values of $\kappa_{\perp}$, which in combination with a high electron mobility Si-rich nanostructures may lead to unprecedentedly large figures of merit.

In conclusion, we have shown that at room-temperature uncorrelated Ge QDSLs with a thin Si spacer of 20 nm exhibit at least a twofold decrease in thermal conductivity, as compared to ordered structures with the same spacer thickness. A model that incorporates the microstructure of the sample shows very satisfactory agreement with the experiment. This work provides an alternative route to reduce the cross-plane thermal conductivity. Thus, our results are important for the development of a different strategy to attain improved figures of merit for thermoelectric applications of nanostructured materials based on stacks of Si/Ge QDs.

We thank J. O. Ossó and M. Garriga for help with sample growth and characterization. J.A.Q. thanks Conacyt Mexico for fellowship and P.D.L. acknowledges an I3P-CSIC grant. This work was supported in part by the Spanish Ministerio de Educación y Ciencia through Grant Nos. MAT2006-02680, MAT2007-61521, and FIS2006-12296-C02-01 and by Direcció General de Recerca of the Generalitat of Catalonia through Grants Nos. 2005SGR00201 and 2005SGR00087. A.R.G. is an ICREA Research Professor. Measurements were performed at the Nanotechnology Lab of MATGAS 2000 A.I.E.

[1] S. M. Lee, D. Cahill, and R. Venkatasubramanian, Appl. Phys. Lett. **70**, 2957 (1997).
[2] T. Borca-Tasciuc, W. Lu, J. Liu, T. Zeng, D. W. Song, C. D. Moore, G. Chen, K. L. Wang, M. S. Goorsky, T. Radetic, R. Gronsky, T. Koga, and M. S. Dresselhaus, Superlattices Microstruct. **28**, 199 (2000).
[3] S. T. Huxtable, A. R. Abramson, C.-L. Tien, A. Majumdar, C. LaBounty, X. Fan, G. Zeng, J. E. Bowers, A. Shakouri, and E. T. Croke, Appl. Phys. Lett. **80**, 1737 (2002).
[4] X. Lu and J. Chu, J. Appl. Phys. **101**, 114323 (2007).
[5] A. A. Kiselev, K. W. Kim, and M. A. Stroscio, Phys. Rev. B **62**, 6896 (2000).
[6] J. L. Liu, A. Khitun, K. L. Wang, W. L. Liu, G. Chen, Q. H. Xie, and S. G. Thomas, Phys. Rev. B **67**, 165333 (2003).
[7] J. L. Liu, A. Khitun, K. L. Wang, T. Borca-Tasciuc, W. L. Liu, G. Chen, and D. P. Yu, J. Cryst. Growth **227**, 1111 (2001).
[8] Y. Bao, W. L. Liu, M. Shamsa, K. Alim, A. A. Balandin, and J. L. Liu, J. Electrochem. Soc. **152**, G432 (2005).
[9] M. Shamsa, W. Liu, A. Balandin, and J. Liu, Appl. Phys. Lett. **87**, 202105 (2005).
[10] M. L. Lee and R. Venkatasubramanian, Appl. Phys. Lett. **92**, 053112 (2008).
[11] O. G. Schmidt and K. Eberl, Appl. Phys. Lett. **73**, 2790 (1998).
[12] O. Leifeld, A. Beyer, E. Muller, K. Kern, and D. Grutzmacher, Mater. Sci. Eng., B **74**, 222 (2000).
[13] A. Bernardi, M. I. Alonso, A. R. Goñi, J. O. Ossó, and M. Garriga, Appl. Phys. Lett. **89**, 101921 (2006).
[14] P. D. Lacharmoise, A. Bernardi, A. R. Goñi, M. I. Alonso, M. Garriga, N. D. Lanzillotti-Kimura, and A. Fainstein, Phys. Rev. B **76**, 155311 (2007).
[15] D. G. Cahill and S. M. Lee, J. Appl. Phys. **81**, 2590 (1997).
[16] T. Borca-Tasciuc, A. R. Kumar, and G. Chen, Rev. Sci. Instrum. **72**, 2139 (2001).
[17] D. G. Cahill and S. M. Lee, J. Appl. Phys. **81**, 2590 (1996).
[18] J. Alvarez-Quintana and J. Rodriguez-Viejo, Sens. Actuators, A **142**, 232 (2008).
[19] J. P. Dismukes, L. Ekstrom, E. F. Steigmeier, I. Kudman, and D. S. Beers, J. Appl. Phys. **35**, 2899 (1964).
[20] X. Alvarez and D. Jou, Appl. Phys. Lett. **90**, 083109 (2007).
[21] C. Dames and G. Chen, J. Appl. Phys. **95**, 682 (2004).
[22] E. T. Swartz and R. O. Pohl, Rev. Mod. Phys. **61**, 605 (1989).
[23] R. J. Stoner and H. Maris, Phys. Rev. B **48**, 16373 (1993).
[24] Y. Ezzahri, S. Grauby, S. Dilhaire, J. M. Rampnoux, and W. Claeys, J. Appl. Phys. **101**, 013705 (2007).

This article is copyrighted as indicated in the article. Reuse of AIP content is subject to the terms at: http://scitation.aip.org/termsconditions. Downloaded to IP: 158.109.18.157 On: Thu, 08 Oct 2015 12:23:41

2.2.4 Ge nanostructures via PLD nanostencilling

So far we showed results related with the study of the growth dynamics in self-assembling of QDs by molecular beam epitaxy (MBE). We explored different scenarios, from the effect of the pre-deposition of carbon (2.1.1), to the growth on strained SiGe layers (2.1.2) or the fabrication of a multistack of quantum dots (1.1.1). An alternative technique to grow high-quality epitaxial Ge nanostructures is the pulsed laser deposition (PLD). In particular we investigated an unconventional patterning approach based on direct, selective PLD of materials through solid-state nanostencils, i.e. masks with hexagonal arrays of circular apertures opened in freestanding, low-stress SiN membranes.

These miniature shadow masks were mechanically clamped onto the Si(100) substrate and the substrate-stencil assembly mounted in front of a rotating Ge solid target. Ge deposition was performed in high vacuum (~10^{-5} mbar), using a KrF excimer laser (λ= 248 nm), at a repetition rate of 10 Hz and laser fluence on the target of 4 J/cm^2. The substrate temperature was set at 600 °C.

With increasing Ge thickness, the shapes of the obtained structures evolve from the flat "two-dimensional (2D)-mound" to three-dimensional (3D) nanocrystalline agglomerations (10–100 nm in lateral size) formed on top of these mounds, undergoing further a transition to a "coffee-bean-like" grained structure, and finally coalescing into single nanocrystals, as shown my SEM/AFM topographic imaging.

Micro-Raman spectroscopy was used to provide a structural characterization of the Ge clusters. The spectral position and shape of the Ge–Ge phonon mode reveals that the Ge clusters are crystalline, and the absence of the Si–Ge phonon band around 400 cm^{-1} clearly indicates that there is no Si intermixing.

- Spectra recorded after the initial stages of growth exhibit a blueshifted Ge–Ge phonon frequency 303 cm^{-1} attributed to compressive strain ($\varepsilon<-1\%$) at the island-substrate interface. The strain is progressively relieved for taller clusters i.e., higher Ge coverage whose phonon frequency approaches the value expected for bulk Ge 300.8 cm^{-1}. The presence of built-in strain suggests that the Ge nanostructures match the Si substrate lattice. In fact, they retain the substrate crystallographic orientation, as confirmed by the phonon selection rules in polarized Raman measurements.

- The 2D mounds are reminiscent of the thin WL, which normally precedes islanding in classical SK growth. AFM topographies indicate that the 2D mounds grow to a maximum height of 6–7 nm, roughly ten times thicker than the critical value for a conventional Ge WL. The anomalous critical thickness for the onset of 3D nucleation can be explained by invoking the finite size of the deposited areas: the 2D mounds, acting as a WL, relieve strain at their periphery, delaying the strain-induced 3D nucleation of structures.

- The dots that initially nucleate on top of the 2D mounds are round shaped and their aspect ratios defined as the dot's height divided by the square root of the base area range from 0.16 to 0.20. These dots are reminiscent of the dome-shaped islands observed in Ge / Si(001) heteroepitaxy.

- With increasing coverage, we observe a shape transition from rounded to "coffee-bean" dots. At this stage of growth, we detect both coalescence of grains and the formation of a depletion region at the centre of the underlying 2D mounds, where we expect higher elastic compression.

- Finally, at higher Ge coverage above 1000 ablation pulses, the depletion region disappears and is replaced by a single rounded cluster.

CORE RESEARCH ARTICLE

Article n: 12

Authors: C. V. Cojocaru, A. Bernardi, J. S. Reparaz, M. I. Alonso, J. M. MacLeod, C. Harnagea, and F. Rosei

Title: Site-controlled growth of Ge nanostructures on Si(100) via pulsed laser deposition nanostenciling

Journal: Applied Physics Letters

Doi: 10.1063/1.2783473

Site-controlled growth of Ge nanostructures on Si(100) via pulsed laser deposition nanostenciling

C. V. Cojocaru
INRS—Énergie, Matériaux et Télécommunications, Université du Québec, 1650 Boul. Lionel-Boulet, Varennes, Quebec J3X 1S2, Canada

A. Bernardi, J. S. Reparaz, and M. I. Alonso
Institut de Ciència de Materials de Barcelona-CSIC, Esfera UAB, 08193 Bellaterra, Spain

J. M. MacLeod, C. Harnagea, and F. Rosei[a)]
INRS—Énergie, Matériaux et Télécommunications, Université du Québec, 1650 Boul. Lionel-Boulet, Varennes, Quebec J3X 1S2, Canada

(Received 12 July 2007; accepted 20 August 2007; published online 14 September 2007)

The authors combine nanostenciling and pulsed laser deposition to pattern germanium (Ge) nanostructures into desired architectures. They have analyzed the evolution of the Ge morphology with coverage. Following the formation of a wetting layer within each area defined by the stencil's apertures, Ge growth becomes three dimensional and the size and number of Ge nanocrystals evolve with coverage. Micro-Raman spectroscopy shows that the deposits are crystalline and epitaxial. This approach is promising for the parallel patterning of semiconductor nanostructures for optoelectronic applications. © *2007 American Institute of Physics*. [DOI: 10.1063/1.2783473]

The growth of germanium (Ge) thin films and structures on silicon (Si) surfaces has been the subject of extensive study due to the prospective device applications[1,2] and the fundamental research importance vis-à-vis the understanding of growth processes.[3–7] In the quest to expand integrated silicon technology, in particular, to applications in optoelectronics, Ge/Si nanoheterostructures[8] with engineered band structures have come under intense investigation as important candidates for light-emitting quantum dot (QD) based devices.

Abundant research efforts have been dedicated to the exploration of "dotlike" structures obtained via the Stranski-Krastanov (SK) growth mode, which comprises the formation of a wetting layer (WL) followed by three-dimensional island ("dot") formation that relaxes the strain induced by the 4.2% lattice mismatch between Ge and Si. To control the size, shape, and density, but mostly the spatial positioning of Ge dots, many strategies including combinations of lithography-based (top down) and spontaneous self-organization approaches (bottom up) have been pursued.[9–14] Much work has focused on the assisted organization of Ge dots grown on prepatterned Si or SiO_2 substrates either by chemical vapor deposition[15,16] (CVD) or molecular beam epitaxy (MBE).[17–19]

While CVD and MBE have been extensively used, pulsed laser deposition (PLD) emerged just recently[20] as a versatile tool to study the structural[21] and functional[22] properties of self-assembled Ge QDs on silicon substrates. A well-established technique developed mainly to grow high-quality epitaxial films of complex materials,[23] PLD offers additionally the possibility of fine tuning and controlling deposition parameters rather easily in the case of elemental materials. We previously investigated a promising unconventional patterning approach based on direct, selective PLD of functional materials at *room temperature* through solid-state, reusable nanostencils. This strategy leads to the organization of nanostructures without any pre patterning or complementary invasive process prior applied to the substrates.[24]

In this letter we describe the patterning of Ge/Si semiconductor heterostructures via PLD nanostenciling at *high temperature* (600 °C). The intent of this approach is twofold: first, to investigate the kinetic processes of PLD of Ge nanodots and ultimately to compare it with more studied processes such as MBE or CVD, and, second, to demonstrate a flexible approach to gain control over the positioning of ordered arrays of nanostructures with potential applications in device engineering.

To achieve precise positioning of Ge on Si(100), we used nanostencils with hexagonal arrays of circular apertures opened in freestanding, low-stress SiN membranes.[25] These miniature shadow masks were mechanically clamped onto the substrate and the substrate-stencil assembly mounted in front of a rotating Ge solid target (99% purity) [Fig. 1(a)]. Prior to deposition, Si(100) substrates (*n* type, Sb doped resistivity of 0.015 Ω cm) were cleaned in ultrasound solvent baths. The native oxide layer was chemically removed in a 5% HF solution. Ge deposition was performed in high vacuum ($\sim 10^{-5}$ mbar), using a GSI Lumonics KrF excimer laser ($\lambda = 248$ nm, $\tau = 15.4$ ns) at a repetition rate of 10 Hz and laser fluence on the target of 4 J/cm^2. The substrate temperature was set at 600 °C and the same stencil was used in consecutive depositions.[26]

Swift fabrication of ordered arrays of Ge structures was achieved in a single deposition step [Fig. 1(b)]. In the initial stages of growth (up to 250 laser ablation pulses) ordered arrays of Ge structures are formed as flat circular mounds, 350 nm in diameter and with a 700 nm periodicity [Fig. 1(c)], i.e., the replica of the design defined by the sieve's apertures. In Fig. 2, scanning electron microscopy (SEM) micrographs for four samples illustrate the patterned Ge islands obtained on Si(100) by varying the number of laser pulses between 250 and 1500 with an estimated rate of ~0.28 Å/pulse. SEM micrographs show that with increasing Ge thickness, the shapes of the obtained structures evolve

a)Electronic mail: rosei@emt.inrs.ca

This article is copyrighted as indicated in the article. Reuse of AIP content is subject to the terms at: http://scitation.aip.org/termsconditions. Downloaded to IP: 158.109.18.157 On: Thu, 08 Oct 2015 12:16:08

 © 2007 American Institute of Physics

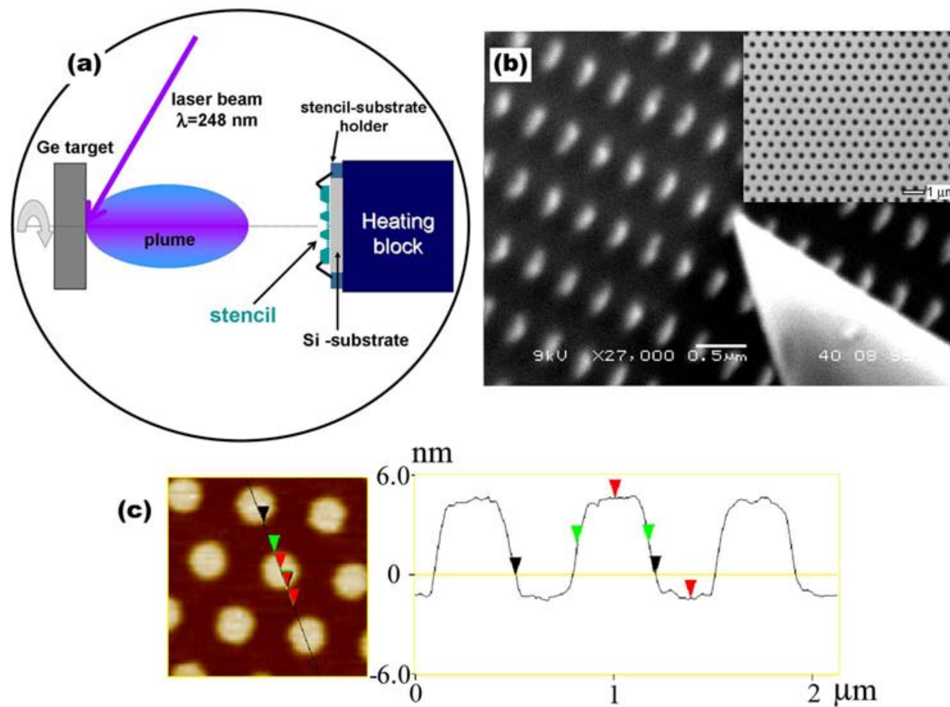

FIG. 1. (Color online) Experimental setup used for stencil deposition and further characterization of Ge ordered arrays: (a) schematic drawing of the PLD-based Ge direct patterning process achieved at high temperature through SiN stencils attached to the Si(100) substrates; (b) SEM micrograph showing an AFM tip scanning across the Ge patterned area in a JEOL-4500 UHV AFM-STM-SEM microscope. The inset shows a detail of a perforated freestanding SiN membrane built in the stencil chip; (c) AFM topography and Ge mound height profile obtained for 250 pulses deposited at 600 °C using a stencil with the architecture shown in the inset (b).

from the flat "two-dimensional (2D)-mound" type [Fig. 2(a)] to three-dimensional (3D) nanocrystalline agglomerations (10–100 nm in lateral size) formed on top of these mounds [Fig. 2(b)], undergoing further a transition to a "coffee-bean-like" grained structure [Fig. 2(c)], and finally coalescing into single nanocrystals [Fig. 2(d)]. Atomic force microscopy (AFM) and SEM images from Figs. 1 and 2 show that all islands are perfectly separated and well defined. The lateral extent of the deposits is always restricted to the range of the aperture areas defined in the stencil.

Micro-Raman spectroscopy was used to provide a structural characterization of the Ge clusters. The optical measurements were carried out by probing the patterned area with the 514.5 nm line of an Ar^+ ion laser focused with a spot size of about 1 μm, i.e., each Raman spectrum (Fig. 3) is collected from the region of two to three apertures. The spectral position and shape of the Ge–Ge phonon mode reveal that the Ge clusters are crystalline, and the absence of the Si–Ge phonon band around $\sim$400 cm^{-1} (inset in Fig. 3) clearly indicates that there is no Si intermixing. Further, the Ge–Ge phonon peak becomes more intense with increased

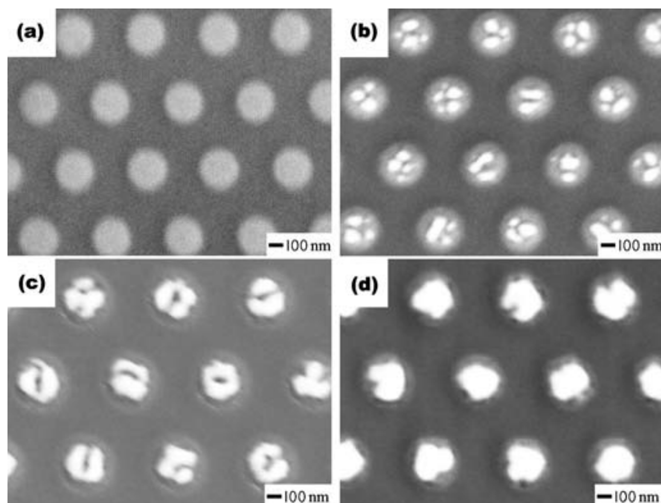

FIG. 2. Coverage dependence of Ge morphology: SEM micrographs showing ordered Ge nanostructures replicated on Si(100) by PLD at 600 °C, for (a) 250, (b) 750, (c) 1250, and (d) 1500 laser pulses with a fluence of 4 J/cm2, for a target-substrate distance of 6.5 cm.

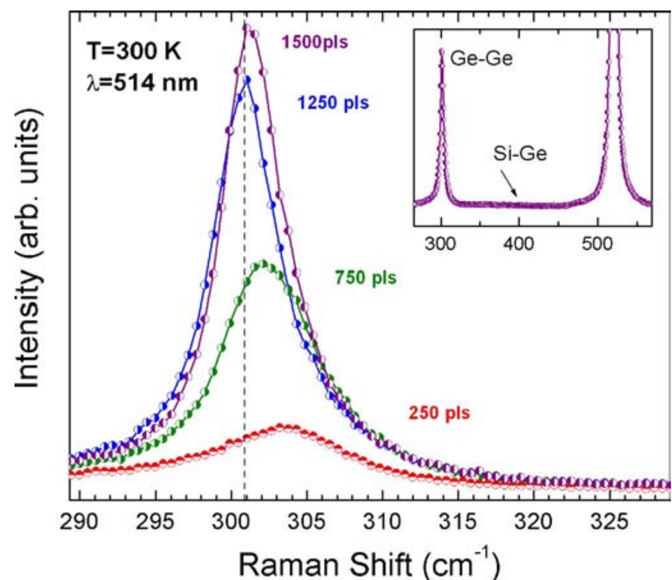

FIG. 3. (Color online) Raman spectra acquired by probing the Ge patterned areas with the 514.5 nm line of an Ar+ ion laser. The absence of the Si–Ge phonon band around ~400 cm^{-1} (see inset) indicates no trace of Si intermixing.

This article is copyrighted as indicated in the article. Reuse of AIP content is subject to the terms at: http://scitation.aip.org/termsconditions. Downloaded to IP: 158.109.18.157 On: Thu, 08 Oct 2015 12:16:08

Ge coverage. Spectra recorded after the initial stages of growth exhibit a blueshifted Ge–Ge phonon frequency ($\sim$303 cm^{-1}) attributed to compressive strain ($\varepsilon < -1\%$) at the island-substrate interface.[27] The strain is progressively relieved for taller clusters (i.e., higher Ge coverage) whose phonon frequency approaches the value expected for bulk Ge (300.8 cm^{-1}). The presence of built-in strain suggests that the Ge nanostructures match the Si substrate lattice. In fact, they retain the substrate crystallographic orientation, as confirmed by the phonon selection rules in polarized Raman measurements (not shown here).

The 2D mounds are reminiscent of the thin WL which normally precedes islanding in classical SK growth. AFM topographies indicate that the 2D mounds grow to a maximum height of 6–7 nm, roughly ten times thicker than the critical value for a conventional Ge WL.[28] The anomalous critical thickness for the onset of 3D nucleation can be explained by invoking the finite size of the deposited areas: the 2D mounds, acting as a WL, relieve strain at their periphery, delaying the strain-induced 3D nucleation of structures. Similar phenomenology was discussed in the case of self-assembling of Ge on lithography-patterned windows opened in ultrathin silicon oxide layers.[29]

The dots that initially nucleate on top of the 2D mounds [Fig. 2(b)] are round shaped and their aspect ratios (defined as the dot's height divided by the square root of the base area) range from $\sim$0.16 to $\sim$0.20. These dots are reminiscent of the dome-shaped islands observed in Ge/Si(001) heteroepitaxy.[30] The average aspect ratio of the dots increases with coverage to allow for more efficient strain relaxation. Above 500 pulses, we observe a shape transition from rounded to "coffee-bean" dots [Fig. 2(c)]. At this stage of growth, we detect both coalescence of grains and the formation of a depletion region at the center of the underlying 2D mounds, where we expect higher elastic compression. Finally, at higher Ge coverage (above 1000 ablation pulses), the depletion region disappears and is replaced by a single rounded cluster.

The number of Ge dots is of the order of tens per aperture for the samples deposited from 250 up to 500 pulses. For samples deposited up to 1000 pulses, the dots are larger and less numerous [e.g., three to five dots/aperture as shown in Fig. 2(b)]. This implies a feasible control over the number of dots per nominal location and thus their density in the whole patterned area.[31]

In summary, we showed that combining nanostenciling with PLD provides a flexible approach to grow and pattern crystalline Ge/Si nanostructures. The location of the Ge clusters is entirely controlled by the pattern of the nanostencil, and the density and physical dimensions of the dots can be further adjusted by varying the deposition parameters. The morphological evolution of the structures with coverage follows a modified Stranski-Krastanov growth mode due to the finite size of the WL in each aperture location. Raman spectroscopy indicates that the nanostructures are crystalline Ge and that they follow the substrate's crystallographic orientation. In future work we will establish a correlation between the deposition parameters such as laser fluence, substrate orientation and temperature, and the Ge dots' density per deposited site.

The authors acknowledge financial support from the Canada Foundation for Innovation, and NSERC of Canada. F.R. is grateful to FQRNT and the Canada Research Chairs program for salary support. A.B. acknowledges a FPI fellowship. J.S.R. acknowledges financial support from the AlBan fellowship Program. This work was supported in part by the Spanish Ministerio de Educación y Ciencia through Grant No. MAT2006-02680.

[1] J. Konle, H. Presting, H. Kibbel, K. Thonke, and R. Sauer, Solid-State Electron. **45**, 1921 (2001).
[2] D. L. Harame, S. J. Koester, G. Freeman, P. Cottrel, K. Rim, G. Dehlinger, D. Ahlgren, J. S. Dunn, D. Greenberg, A. Joseph, F. Anderson, J.-S. Rieh, S. A. S. T. Onge, D. Coolbaugh, V. Ramachandran, J. D. Cressler, and S. Subbanna, Appl. Surf. Sci. **224**, 9 (2004).
[3] D. J. Eaglesham and M. Cerullo, Phys. Rev. Lett. **64**, 1943 (1990).
[4] G. Medeiros-Ribeiro, A. M. Bratkovski, T. I. Kamins, D. A. A. Ohlberg, and R. S. Williams, Science **279**, 353 (1998).
[5] F. M. Ross, J. Tersoff, and R. M. Tromp, Phys. Rev. Lett. **80**, 984 (1998).
[6] J. Stangl, V. Holý, and G. Bauer, Rev. Mod. Phys. **76**, 725 (2004).
[7] F. Ratto, G. Costantini, A. Rastelli, O. G. Schmidt, K. Kern, and F. Rosei, J. Exp. Nanosci. **1**, 279 (2006).
[8] J. M. Baribeau, X. Wu, N. L. Rowell, and D. J. Lockwood, J. Phys.: Condens. Matter **18**, R139 (2006).
[9] J. R. Heath, R. S. Williams, J. J. Shiang, S. J. Wind, J. Chu, C. D'Emic, W. Chen, C. L. Stanis, and J. J. Bucchignano, J. Phys. Chem. **100**, 3144 (1996).
[10] T. I. Kamins and R. S. Williams, Appl. Phys. Lett. **71**, 1201 (1997).
[11] E. S. Kim, N. Usami, and Y. Shiraki, Appl. Phys. Lett. **72**, 1617 (1998).
[12] G. Capellini, M. de Seta, C. Spinella, and F. Evangelisti, Appl. Phys. Lett. **82**, 1772 (2003).
[13] A. Karmous, A. Cuenat, A. Ronda, I. Berbezier, S. Atha, and R. Hull, Appl. Phys. Lett. **85**, 6401 (2004).
[14] A. Bernardi, M. I. Alonso, A. R. Goñi, J. O. Ossó, and M. Garriga, Appl. Phys. Lett. **89**, 101921 (2006).
[15] T. I. Kamins, D. A. A. Ohlberg, R. S. Williams, W. Zhang, and S. Y. Chou, Appl. Phys. Lett. **74**, 1773 (1999).
[16] L. Vescan, Mater. Sci. Eng., A **302**, 6 (2001).
[17] O. G. Schmidt, N. Y. Jin-Phillipp, C. Lange, U. Denker, K. Eberl, R. Schreiner, H. Grabeldinger, and H. Schweizer, Appl. Phys. Lett. **77**, 4139 (2000).
[18] G. Jin, J. L. Liu, and K. L. Wang, Appl. Phys. Lett. **76**, 3591 (2000).
[19] Z. Zhong, A. Halilovic, M. Muhlberger, F. Schäffler, and G. Bauer, J. Appl. Phys. **93**, 6258 (2003).
[20] B. Shin, J. P. Leonard, J. W. McCamy, and M. J. Aziz, Appl. Phys. Lett. **87**, 181916 (2005).
[21] M. S. Hegazy and H. E. Elsayed-Ali, J. Appl. Phys. **99**, 054308 (2006).
[22] X. Ma, Z. Yan, B. Yuan, and B. Li, Nanotechnology **16**, 832 (2005).
[23] D. B. Chrisey and G. K. Hubler, *Pulsed Laser Deposition of Thin Films* (Wiley, New York, 1994).
[24] C. V. Cojocaru, C. Harnagea, A. Pignolet, and F. Rosei, IEEE Trans. Nanotechnol. **5**, 470 (2006).
[25] The stencil chip has 14 freestanding membranes, 2 mm in length and 100 μm in width; nominal diameter of the circular apertures is 350 nm and the pitch 700 nm; stencils fabricated at Aquamarijn Filtration, The Netherlands.
[26] Samples were prepared with various Ge thicknesses (coverages). In PLD, the deposited film thickness is controlled by varying the number of laser pulses for a certain target-substrate distance provided that desorption from the substrate is negligible.
[27] A. Bernardi, J. O. Ossó, M. I. Alonso, A. R. Goñi, and M. Garriga, Nanotechnology **17**, 2602 (2006).
[28] Typically 0.4–0.6-nm-thick for Ge on Si(001); Y.-W. Mo, D. E. Savage, B. S. Swartzentruber, and M. G. Lagally, Phys. Rev. Lett. **65**, 1020 (1990).
[29] L. Vescan, T. Stoica, B. Holländer, A. Nassiopoulou, A. Olzierski, I. Raptis, and E. Sutter, Appl. Phys. Lett. **82**, 3517 (2003).
[30] A. Rastelli, M. Stoffel, J. Tersoff, G. S. Kar, and O. G. Schmidt, Phys. Rev. Lett. **95**, 026103 (2005).
[31] For any given set of deposition parameters, the sizes of the dots are fairly narrowly distributed. Their density can be further tuned by using stencils with smaller or larger apertures and varying PLD parameters.

This article is copyrighted as indicated in the article. Reuse of AIP content is subject to the terms at: http://scitation.aip.org/termsconditions. Downloaded to IP: 158.109.18.157 On: Thu, 08 Oct 2015 12:16:08

COMPLEMENTARY ARTICLE

Article n: 13

Authors: J. M. MacLeod, C. V. Cojocaru, F. Ratto, C. Harnagea, A. Bernardi, M. I. Alonso and F. Rosei

Title: Modified Stranski–Krastanov growth in Ge/Si heterostructures via nanostenciled pulsed laser deposition

Journal: Nanotechnology

Doi: 10.1088/0957-4484/23/6/065603

Nanotechnology **23** (2012) 065603 (9pp) doi:10.1088/0957-4484/23/6/065603

Modified Stranski–Krastanov growth in Ge/Si heterostructures via nanostenciled pulsed laser deposition

J M MacLeod[1], C V Cojocaru[1,5], F Ratto[2], C Harnagea[1], A Bernardi[3], M I Alonso[3] and F Rosei[1,4]

[1] INRS, Énergie, Matériaux et Télécommunications, Université du Québec, 1650 Boulevard Lionel-Boulet, Varennes, QC, J3X 1S2, Canada
[2] IFAC-CNR Institute of Applied Physics, via Madonna del Piano 10, I-50019 Sesto Fiorentino, Italy
[3] Institut de Ciència de Materials de Barcelona, ICMAB-CSIC, Esfera UAB, E-08193 Bellaterra, Spain
[4] Centre for Self-Assembled Chemical Structures, McGill University, 801 Sherbrooke st. West Montreal, Quebec, H3A 2K6, Canada

E-mail: rosei@emt.inrs.ca

Received 23 September 2011, in final form 8 December 2011
Published 17 January 2012
Online at stacks.iop.org/Nano/23/065603

Abstract
The combination of nanostenciling with pulsed laser deposition (PLD) provides a flexible, fast approach for patterning the growth of Ge on Si. Within each stencilled site, the morphological evolution of the Ge structures with deposition follows a modified Stranski–Krastanov (SK) growth mode. By systematically varying the PLD parameters (laser repetition rate and number of pulses) on two different substrate orientations (111 and 100), we have observed corresponding changes in growth morphology, strain and elemental composition using scanning electron microscopy, atomic force microscopy and μ-Raman spectroscopy. The growth behaviour is well predicted within a classical SK scheme, although the Si(100) growth exhibits significant relaxation and ripening with increasing coverage. Other novel aspects of the growth include the increased thickness of the wetting layer and the kinetic control of Si/Ge intermixing via the PLD repetition rate.

S Online supplementary data available from stacks.iop.org/Nano/23/065603/mmedia

(Some figures may appear in colour only in the online journal)

1. Introduction

Despite advances in organic electronics and other novel approaches, group IV semiconductors continue to constitute the foundation of modern microelectronics. The controlled positioning of nanoscale semiconductor structures is of paramount importance to their continued use, leading to extensive studies of the self-directed formation of dot-like structures via the Stranski–Krastanov (SK) growth mode [1–4]. The possibility for novel optoelectronic devices arises with the miniaturization of device components down to the nanometre length scale, including quantum dots for single-electron transistors, light-emitting diodes, quantum cellular automata, etc. In this context, the SK self-assembly of Ge/Si dots in epitaxially grown germanium overlayers on silicon has attracted interest due to its bottom-up parallel profile. Various features of the morphological evolution of this system have been explored in detail, including studies of the influence of kinetics versus thermodynamics [5–8] and the influence of intermixing (alloying) on growth phenomena [9–13]. Ordering and strict spatial registration of structures is essential for electronic applications, but in most cases SK islands exhibit poor lateral ordering since island nucleation is statistical in nature [14].

The growth of high-quality crystalline arrays of semiconductor nanostructures, homogeneously shaped and sized, and precisely registered on the substrate of choice, is

[5] Present address: NRC Industrial Materials Institute, 75 de Mortagne Boulevard, Boucherville, QC, J4B 6Y4, Canada.

 © 2012 IOP Publishing Ltd Printed in the UK &the USA

an intricate problem that has not been satisfactorily addressed via self-assembly alone, although efforts have capitalized on the influence of strain fields on the island nucleation or the kinetics of the growth process [15–25]. To some extent, order can be imposed on the SK growth process through the use of patterned substrates. Vicinal surfaces [26–28] and cleaved samples (cleaved edge overgrowth) [29] have been used to control nucleation. Extensive work has also been done using top-down techniques to pre-pattern surfaces for SK growth. Templates for growth have included mesas [19, 20] and holes [30, 31]. This hybrid combination of top-down pre-patterning and bottom-up SK growth provides an efficient methodology for the controlled positioning of semiconductor nanostructures. Among its drawbacks, however, is the invasiveness and increased processing time associated with the pre-patterning step, which rapidly rise with the desired precision and may reduce the potential for scale-up, such as in the case of electron or ion beam lithography [14].

In this paper we describe an alternative hybrid top-down/bottom-up approach for controlling deposition via nanostenciling, a method which selectively deposits Ge directly onto sites of predefined geometry and spacing without the need for pre-patterning the surface. Pulsed laser deposition (PLD) of Ge onto both Si(001) and (111) substrates results in the confinement of 3D island growth within predefined locations on the surface [32]. Herein, we describe a systematic study of the nanostenciled Ge/Si system. We find that the PLD-deposited Ge structures are confined exclusively to the stencil region and that the Ge nanostructures exhibit very little silicon intermixing.

2. Experimental details

A schematic of the experimental geometry is shown in figure 1. PLD was performed in vacuum ($\approx 10^{-5}$ mbar), using a GSI Lumonics KrF excimer laser unit ($\lambda = 248$ nm, $\tau = 15.4$ ns pulse FWHM) and a rotating solid Ge target (99.9% purity). Ge was deposited through the stencil onto either Si(100) (n-type, Sb-doped, resistivity of 0.015 Ω cm) or Si(111) (n-type, As-doped, 0.001–0.005 Ω cm). Prior to deposition, substrates were degreased and cleaned in ultrasonic solvent baths. To passivate the (100) surface, the native oxide layer was chemically removed in an aqueous HF (5%) solution, after which the samples were rinsed in deionized water and rapidly mounted in the chamber. On the Si(111) samples, a modified Shiraki cleaning method (H_2SO_4: $H_2O_2 = 4:1$ by volume) was applied prior to oxide stripping in a 5% HF solution.

Ge deposition was performed with a laser fluence of 4 J cm^{-2} and a repetition rate of either 1 or 10 Hz. The size of the laser spot on the Ge target had an average lateral dimension of 2 mm. The substrate temperature was set at 600 °C, as measured with a K-type thermocouple on the heating block supporting the stencil–substrate assembly. The amount of material deposited by PLD can be easily controlled by varying the number of laser pulses for a certain target–substrate distance. The nominal deposition rate for all samples was $\approx$0.28 Å/pulse, based on atomic force microscopy (AFM) measurement of the wetting layer thickness for samples near the critical thickness for 3D island growth (see supporting information, available at stacks.iop.org/Nano/23/065603/mmedia).

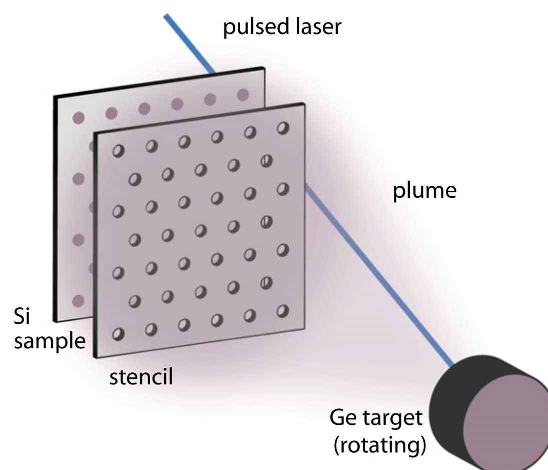

Figure 1. Simplified sketch of the sample geometry, showing the Ge target, the stencil and the Si sample.

The stencil[6] comprised a hexagonal pattern of circular apertures 350 nm in diameter with a pitch of 700 nm. The hexagonal pattern is contained in trenches 2 mm $\times$ 100 μm with an aspect ratio of approximately 4:1 (depth/width), housed in a silicon support frame. This geometry results in a thickness gradient on the structures patterned within the 100 μm wide stripe, i.e. lower-coverage structures were formed towards each edge of the patterned stripe area due to shadowing effects [33]. All data presented in this paper reflect the growth characteristics at the centre of the patterned stripe, where these shadowing effects are negligible.

The actual size of the sites patterned onto the silicon surface is dictated by the geometry of the experiment, and depends strongly on the spacing between the stencil and the sample [34]. The gap between the stencil and sample should be as small as possible, but this spacing can vary due to substrate or stencil irregularities, particulates or distortion of the stencil. In these experiments, the sample and stencil were both carefully cleaned prior to use, the stencil was held as firmly as possible against the sample and the resulting separation was inferred from the size of the stencilled features. The spacing between the substrate and the sample was not directly measured.

The same stencil was used in consecutive depositions for various numbers of ablation pulses. With repeated use, the accumulation of Ge on the stencil caused a reduction in aperture size. After ten successive depositions, corresponding to a total deposited thickness of about 300 nm, the lateral size of the deposited sites was reduced by $\approx$10%. The deposited Ge could be removed by dipping the stencil in warm hydrogen peroxide (H_2O_2) and subsequently rinsing in water. In trials using a similar stencil with smaller openings, we were able to produce a pattern of 96 nm germanium circles on the silicon

[6] Stencils fabricated at Aquamarijn Filtration (The Netherlands).

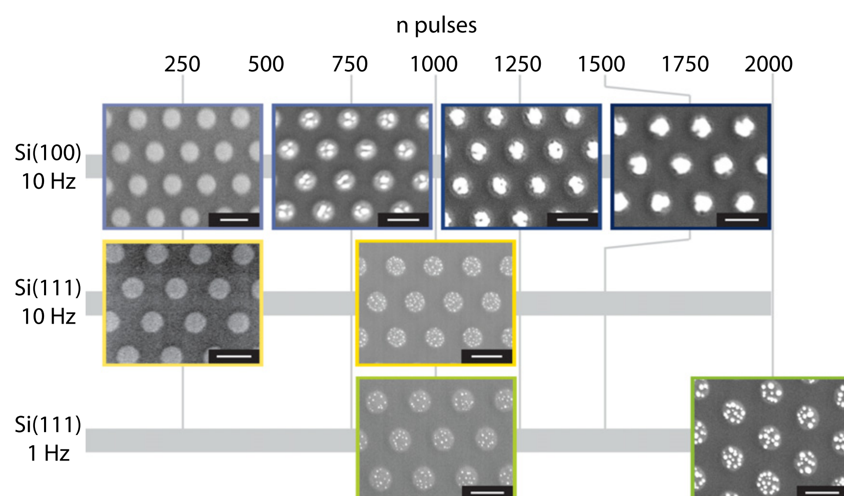

Figure 2. SEM images of patterned Ge structures formed at 600 °C via PLD through a nanostencil. Samples were fabricated on Si(100) and (111) with different numbers of PLD pulses, n, and a laser repetition rate of 10 Hz, and on Si(111) at a laser repetition rate of 1 Hz. A 500 nm scale bar is indicated in white in the lower right corner of each image.

surface using stencil openings of 85 nm diameter. However, these small openings were extremely prone to clogging, making the type of variable-coverage study described here untenable [33].

Structural characterization of the patterned Ge islands was performed via contact-mode AFM, using a Veeco Nanoprobe equipped with a general purpose cantilever (Si_3N_4, tip apex radius 20 nm) and scanning electron microscopy (SEM), using a JEOL JSM-6300F. SEM and AFM images were calibrated via the 700 nm pitch of the stencilled sites. Further information was obtained from micro-Raman spectroscopy, a surface-sensitive technique particularly suitable to extract information about elemental composition and strain inside group IV semiconductor nanostructures [35, 36]. The Raman measurements were carried out at room temperature by probing the patterned area with the 514.5 nm line of an Ar^+ ion laser focused with a spot size of about 1 μm, i.e. each spectrum is collected from a few stencil sites.

3. Results

To systematically investigate the growth processes of stencilled Ge on Si, a number of samples were prepared under different conditions. Figure 2 shows SEM images obtained from each of the samples.

At low Ge coverage, smooth 2D mounds are formed on both Si(100) and (111). The SEM images in figure 2 illustrate this growth at 250 laser ablation pulses (equivalent deposited thickness ≈7 nm). AFM measurements indicate typical thicknesses for the smooth wetting layer of 6–7 nm on the (100) surface and 3–5 nm on the (111) surface. The substrate region between the stencil sites remains flat and uniform.

Beyond the critical (wetting layer) thickness, growth proceeds through the formation of three-dimensional islands. The morphology of these islands is markedly different between the Si(100) and (111) surfaces: whereas each stencil site on Si(100) hosts a small number of large islands that gradually coalesce with increasing Ge coverage, the islands on (111) are smaller and remain discrete to at least 2000 laser pulses, corresponding to a nominal thickness of 56 nm. AFM measurements (not shown) do not reveal well-defined faceting on the 3D islands on either substrate but indicate that the maximum height of the islands increases with coverage. The maximum island height, measured from the wetting layer, increases from 32 ± 4 nm at 750 pulses to 53 ± 4 nm at 1250 pulses on Si(100), and from 20 ± 4 nm at 1000 pulses to 42 ± 5 nm at 2000 pulses on Si(111) (1 Hz). Variation in the laser repetition rate was also found to affect the island growth. For the structures grown on Si(111), 1000 pulses at 1 Hz (figure 2) produced fewer larger dots than in the counterpart sample prepared at 10 Hz.

Statistical analysis of the SEM images confirms these qualitative trends, as shown in figure 3. On Si(100) the distribution in the number of dots per site shows an average of ≈3, with a standard deviation of ≈1, for 750 pulses. The mean number of islands converges towards unity with increasing coverage of Ge. Conversely, the statistics for the 1 Hz samples on (111) show less sensitivity to coverage. The distributions have means of ≈11, for both 1000 and 2000 pulses, with the standard deviation slightly increasing from 2.1 to 2.5, respectively. The distribution for the sample grown at 10 Hz has a higher mean number of islands, ≈24, with a relatively small standard deviation of 2.2.

The corresponding major axis lengths for the 3D islands are shown in figure 4. The samples prepared on Si(100) have much larger islands than the samples prepared on Si(111). The (100) islands sizes are broadly distributed after 750 pulses, with an average size of 115 nm, and a standard deviation of 49 nm. Increasing the Ge coverage to 1250 pulses increases the average island size to 315 nm, with the distribution narrowing to a standard deviation of 40 nm. Finally, at 1500 pulses, the island size converges towards 274 nm, with a

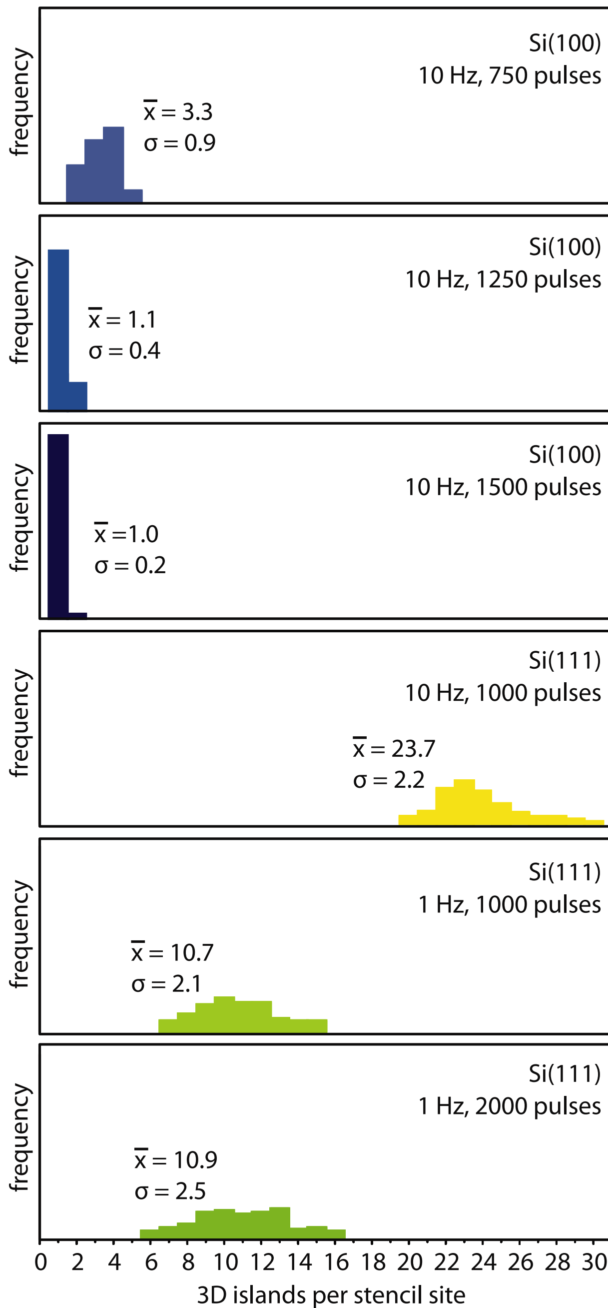

Figure 3. Number of 3D islands per stencil site for samples similar to those shown in figure 2. The mean and standard deviation for each of the normalized distributions is shown in the figure.

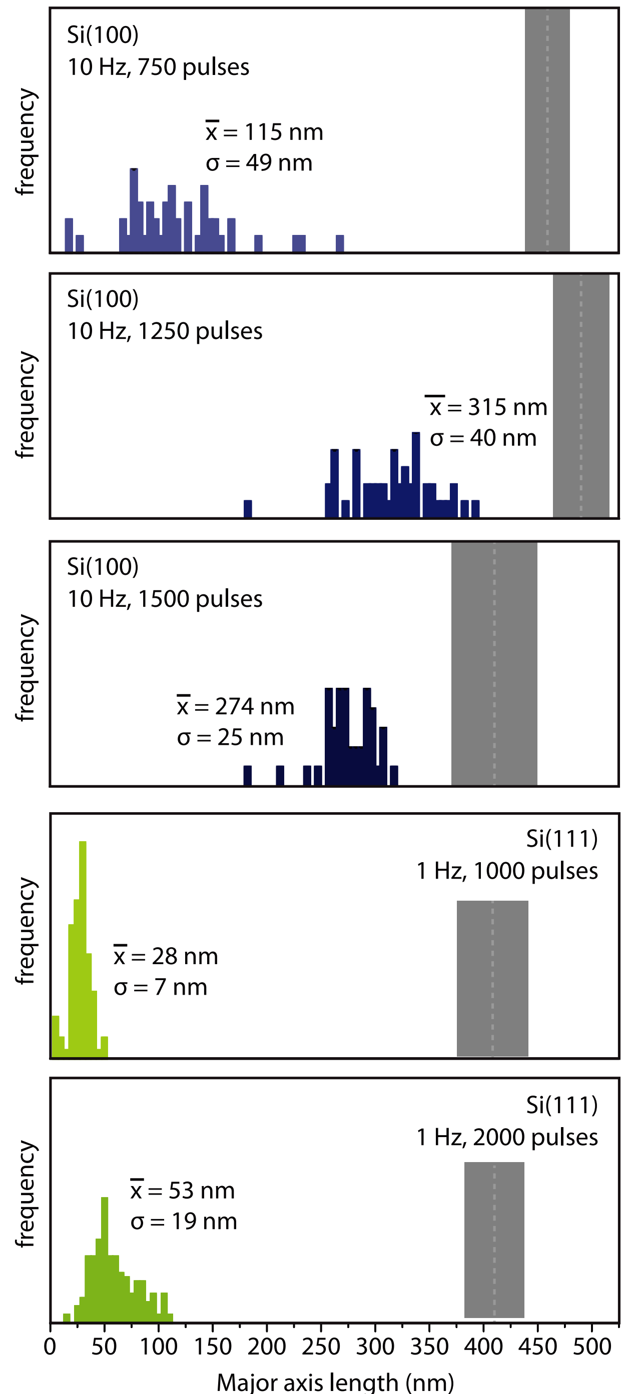

Figure 4. Major axis length distributions of 3D islands for samples similar to those shown in figure 2. The mean and standard deviation for each of the normalized distributions is shown in the figure. The dashed lines indicate the average diameter of the stencilled sites for each sample.

standard deviation of 25 nm. The increase in lateral size with coverage is less pronounced on the Si(111) substrate. In going from 1000 to 2000 pulses, the mean size increases from 28 nm to 53 nm, accompanied by a broadening of the size distribution.

The average diameters for the stencilled sites are also shown in figure 4. The site size varied from ≈410 nm for the samples grown on Si(111) at 1 Hz, as well as the 1500 pulse Si(100) sample, to 490 nm for the 1250 pulse, Si(100) sample.

The μ-Raman spectra are shown in figure 5. The spectra are consistent with those expected for Si/Ge hybrid structures [37], and we assign the dominant phonon peaks accordingly: Ge–Ge at ≈300 cm^{-1}, Si–Si at 520 cm^{-1} and Ge–Si at ≈400 cm^{-1}. The spectra from the samples grown on Si(100) do not contain a Si–Ge peak, indicating no detectable intermixing. On these samples, the Ge–Ge peak shifts down in frequency as the number of pulses increases, consistent with a progressive relaxation of strain with increasing coverage. Notable features of the spectra obtained from Si(111) include the presence of a Ge–Si peak for the samples prepared at 1 Hz,

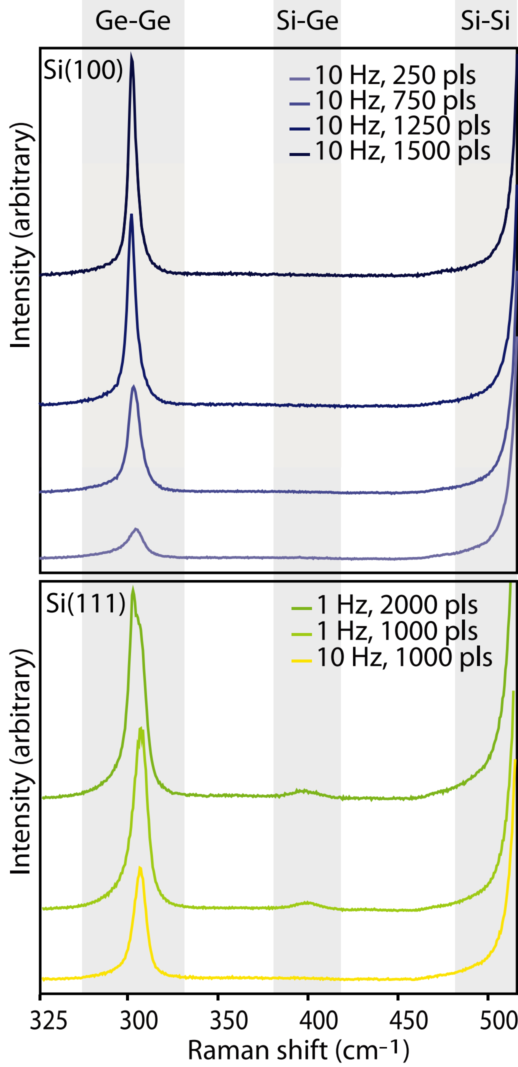

Figure 5. μ-Raman spectra for Ge patterned onto Si(100) (top) and Si(111) (bottom). The approximate locations of the Ge–Ge, Ge–Si and Si–Si peaks are identified with grey shading. The traces have been offset from one another for clarity.

indicating Si–Ge intermixing, and the separation of the Ge–Ge peak into two components, which is particularly marked in the 2000-pulse sample. As in the case of the Si(100) samples, no intermixing is detected in the sample prepared at 10 Hz.

The phonon peaks in figure 5 were fitted with Lorentzian functions, and the spectral positions obtained for the Ge–Ge and Si–Ge peaks (in cm^{-1}) were used to calculate the composition (x) of the $\mathrm{Si}_{1-x}\mathrm{Ge}_x$ alloy and the in-plane strain ($\epsilon_\parallel$) by applying the empirical relations from [36]:

$$\omega_{\mathrm{Ge-Ge}} = 284 + 5x + 12x^2 + b_{\mathrm{Ge-Ge}}\epsilon_\parallel \quad (1)$$

$$\omega_{\mathrm{Si-Ge}} = 400 + 29x - 95x^2 + 213x^3 - 170x^4 + b_{\mathrm{Si-Ge}}\epsilon_\parallel. \quad (2)$$

For samples grown on Si(100) we used the values of the phonon strain-shift coefficients $b_{\mathrm{Ge-Ge}}(100) \approx -460\ \mathrm{cm}^{-1}$ and $b_{\mathrm{Si-Ge}}(100) \approx -555\ \mathrm{cm}^{-1}$, determined by Reparaz *et al* [38]. For samples grown on Si(111) the biaxial strain splits

Table 1. In-plane strain ($\epsilon_\parallel$) and composition (x) of the $\mathrm{Si}_{1-x}\mathrm{Ge}_x$ alloy extracted from μ-Raman data.

Sample	$\omega_{\mathrm{Ge-Ge}}$ (cm^{-1})	$\omega_{\mathrm{Si-Ge}}$ (cm^{-1})	$\epsilon_\parallel$	x
Si(100)				
10 Hz, 250 pulses	302.7	—	−0.4% ± 0.2%	1
10 Hz, 750 pulses	302.4	—	−0.3% ± 0.2%	1
10 Hz, 1250 pulses	301.0	—	0% ± 0.2%	1
10 Hz, 1500 pulses	301.4	—	−0.1% ± 0.2%	1
Si(111)				
1 Hz, 1000 pulses	304.7	396.4	−1.2% ± 0.2%	0.93 ± 0.2
1 Hz, 2000 pulses	300.9	—	0	1
	305.7	395.5	−1.4% ± 0.2%	0.94 ± 0.2
10 Hz, 1000 pulses	304.4	—	−0.7% ± 0.2	1

the triply degenerated LO–TO optical phonon branches into two components: a singlet LO and a doublet TO branch. We calculated the phonon strain-shift coefficients for these modes as explained in [39] using the phonon deformation potentials p and q from [38]. The two different notations are related by $\widetilde{K}_{11} = p/\omega_0^2$, $\widetilde{K}_{12} = q/\omega_0^2$. The component $\widetilde{K}_{44} = r/\omega_0^2$ was taken to be that of Ge for the Ge–Ge mode and the average of the Si and Ge values for the Si–Ge mode [38]. The resulting strain-shift coefficients are $b_{\mathrm{Ge-Ge}}(111, d) \approx -668\ \mathrm{cm}^{-1}$, $b_{\mathrm{Ge-Ge}}(111, s) \approx -152\ \mathrm{cm}^{-1}$, $b_{\mathrm{Si-Ge}}(111, d) \approx -835\ \mathrm{cm}^{-1}$ and $b_{\mathrm{Si-Ge}}(111, s) \approx -307\ \mathrm{cm}^{-1}$, where d and s stand for doublet and singlet, respectively. Although one of the samples on Si(111) showed a double peak, cf figure 5, this splitting is not attributed to these two components. In fact, in the experiments we could not resolve the singlet because the observed peak positions were almost insensitive to polarization. Therefore, the Raman modes that we observe on the Si(111) samples must correspond to the more intense doublet TO modes only [39]. Using the strain-shift coefficients given above we obtained the composition and strain values as tabulated in table 1.

4. Discussion

4.1. Stencilling as a methodology

The circular profile of the deposited regions of Ge directly reproduces the shape of the apertures in the stencil. This fidelity may be linked to a combination of effects: (i) a strong confinement of the PLD-generated Ge flux, (ii) limited diffusion across the substrate (see below) and (iii) enhanced corner diffusion, observed to take place when highly energetic species arrive at the substrate [40], which promotes circular structures. The confinement of the Ge flux is further indicated by the lack of observable structures on the substrate between the stencil sites. This is seen to occur despite the fact that typical Ge diffusion lengths [41] on clean Si at 600 °C should range from $\approx 2 \times 10^2$ nm (Si(111), 250 pulses) to as much as $\approx 2 \times 10^4$ nm (Si(100), 1750 pulses). The lack of island growth

between the stencil sites may be due to inhibition of either diffusion or nucleation in these regions, which could occur due to the presence of an oxide layer, as has been observed, for example, in nanostructured oxide patterns [42]. We note that under ultrahigh vacuum conditions, where oxide formation is negligible, Sn and Ag are observed to diffuse hundreds of nanometres from similar stencil sites on Si(100) [34]. In our experiments, the presence of O_2 in the relatively high chamber background pressure leads to the dynamic development of the oxide at high temperature, which appears to passivate the regions of the Si substrate between the aperture sites against Ge growth. This effect is suppressed within the stencil sites by the direct flux of energetic Ge impinging on the surface.

For all samples, the size of the patterned regions on the substrate was larger than the 350 nm opening in the stencil. This spreading is a geometrical consequence of the experimental geometry, and for our fixed source–sample spacing, depends on two variables: the size of the source, i.e. the size of the laser spot on the target and the spacing between the stencil and the sample (see supporting information, available at stacks.iop.org/Nano/23/065603/mmedia). Taking the average laser spot size of 2 mm, the corresponding sample–substrate spacings were estimated to be between 1.8 and 4.2 μm, although it is not obvious whether the variation in the size of the patterned sites is solely due to differences in the stencil positioning, or whether fluctuation in the laser spot size also contributed.

4.2. Growth mechanisms

Wetting layer. The stencilled growth of Ge on Si can be described as a modified Stranski–Krastanov process. In conventional SK growth, typically observed critical values are 2–3 atomic bilayers (0.63–0.95 nm) for Ge on Si(111) [43] or 3–5 monolayers (0.4–0.68 nm) for Ge on Si(001) [44]. Our observed values are about five times larger for the (111) surface and about ten times larger for the (100) surface. These anomalously high critical thickness for the onset of 3D nucleation can be explained by invoking the small size of the deposited areas. The discrete sites may benefit from mechanisms for lateral strain relief at their periphery, thus delaying the strain-induced 3D nucleation of islands [45]. The fact that we see a thicker wetting layer on (100), as opposed to (111), may indicate that dislocation nucleation is more facile on the (100)-oriented stencil sites.

Island nucleation and growth. In traditional SK growth of Ge on Si, the nucleation of the 3D islands occurs nearly simultaneously across the substrate [46]. Nucleation is a statistical process which requires a critical density of mobile atoms. In turn the density of mobile atoms results from the competition of deposition and capture from the growing islands. Therefore nucleation ends when the separation between the islands becomes a fraction of the diffusion length of the mobile atoms, with the exact value depending on factors such as the deposition rate, diffusivity and critical size of stable nuclei [14]. After nucleation, the islands continue to grow at constant density at least until ripening begins.

Consistent with this picture, the histograms in figure 3 show that, at 1 Hz, the density of 3D islands per site has nearly identical values for 1000 and 2000 pulses. Evaluation of the size distribution for the same samples (figure 4) shows a fairly narrow distribution in the case of the sample prepared for 1000 pulses with a mean value of 28 nm, whereas a mean value of 53 nm (major length) and a broader distribution is found for the islands grown at 2000 pulses. This broader size distribution at 2000 pulses is not an immediate consequence of growth kinetics, and may point to the onset of Ostwald ripening. The increase in average size with deposition is clearly associated with SK growth at constant island density. However, the increase of island width occurs significantly faster than expected for expansion occurring exclusively from the deposited material (i.e. the size does not scale as expected with the number of pulses beyond the wetting layer), suggesting the possibility of additional material sources for island growth, such as from the erosion of the wetting layer [47, 48].

The higher density of islands for the same substrate at a PLD repetition rate of 10 Hz is clearly associated with a higher incidence of nucleation, which results from the higher supply of mobile atoms at constant diffusivity feeding their density. The increased deposition rate also has a direct impact on the nucleation density. As shown in figure 3, for samples prepared on Si(111) at 1000 pulses, a laser repetition rate of 1 Hz produces roughly half the density of dots produced at a rate of 10 Hz. This is consistent with the power law increase in nuclei density with deposition rate, which occurs as a general consequence of SK kinetics [49–52].

The nucleation behaviour on the Si(100) surface is markedly different, as shown by the small number of islands on the 750-pulse sample. This decreased nucleation density may be due to an enhanced diffusion and possibly a larger critical size for the stable nuclei under the specific conditions imposed by nanostenciling. Contrary to the Si(111) samples, which do not show a marked change in island density with coverage, islands on the (100) samples are observed to ripen and coalesce with increasing coverage, finally converging to a single island per stencil site at 1500 pulses. This is also consistent with increased diffusivity, and may also be influenced by the nearly complete strain relaxation (see below for further discussion).

Island crystallinity, composition and strain. The Raman data for these samples provide more insight into the mechanisms underlying the observed morphologies. The spectral shape and position of the Ge–Ge phonon mode (figure 5) indicates that all patterned structures are crystalline. The blueshifting of the peak away from the bulk value at around 301 cm^{-1} indicates the presence of compressive strain, a hallmark of Ge/Si epitaxial growth. Another important feature of the recorded spectra is the Si–Ge peak, observed for the samples prepared at 1 Hz, which implies Si–Ge intermixing. Table 1 tabulates the calculated intermixing and strain based on the locations of these peaks. The 1000-pulse sample has $x = 0.93 \pm 0.2$ and is compressively strained by $-1.2 \pm 0.2\%$. The 2000-pulse peak contains two components. The

low-frequency component indicates slightly less intermixing ($x = 0.94 \pm 0.2$) than the 1000-pulse sample, as well as a slight increase in strain ($-1.4 \pm 0.2\%$). However, most of the intensity in the Ge–Ge peak for the 2000-pulse sample is contributed by an unstrained, pure Ge component[7]. The emergence of this component may be due to the rearrangement of the strained islands indicated at 1000 pulses, e.g. due to the nucleation of misfit dislocations above a critical island size and/or a feature of the additional material deposited onto the islands, which may or may not maintain the epitaxial relationship to the substrate.

The unusually large thickness of the wetting layer in these experiments precludes some of the conventional mechanisms for the relaxation of Ge dots on Si, which rely on the sourcing of Si from the substrate [53], so the relaxation of these islands must depend heavily on the formation of dislocations. It is also interesting to note that, using traditional growth methodologies, it can be difficult to produce Ge-rich structures in Ge/Si growth, since energetics favour the intermixing of Si into Ge (but not vice versa) [54]. Hence, this growth methodology provides access to a stoichiometric regime not normally achieved.

The Si–Ge peak is absent from the Raman spectra for all the samples prepared on (111) at 10 Hz, suggesting that the Si–Ge intermixing is kinetically suppressed. This is confirmed through the lack of intermixing observed for the Si(100) samples, all of which were prepared at 10 Hz.

According to table 1, an almost complete relaxation of the misfit strain occurs for the samples grown on Si(100). This relaxation plays a critical role in the growth and ripening of the islands and enables large lateral sizes and coalescence, with the structure evolving to a single island per site on the samples grown at 1500 pulses. Interestingly the coalescence of these islands is accompanied by some anomalous behaviour, with the mean length decreasing and the misfit strain increasing slightly in going from 1250 to 1500 pulses. Together, these changes indicate ripening, which smooths asperities that may have contributed to the size and very efficient strain relief for the 1250-pulse sample. The lateral width of the wetting layer correspondingly decreases between the 1250- and 1500-pulse samples, further suggesting that these large, ripened islands are directly size-constrained according to the diameter of the patterned sites.

5. Conclusions and outlook

The stencilled PLD growth of Ge on Si provides new opportunities for controlling the growth of nanoscale group IV structures. The stencil used in this study produced a pattern of circular structures, each ≈15–40% larger than the 350 nm stencil openings. Since this spreading depends on both the evaporation source size and the distance between the stencil and the sample, it can presumably be minimized by reducing the size of the laser spot on the PLD target, while at the same time taking care to ensure good sample–stencil contact.

Within each stencil site, the growth process is largely consistent with SK growth, and begins with the formation of a thick wetting layer. The layer thickness was slightly larger for (100) samples than (111), suggesting that strain relief via dislocation formation occurs more easily on the former. The completion of the wetting layer is followed by the nucleation of three-dimensional islands. On Si(111), the island density is found to be higher for a 10 Hz PLD repetition rate than for a 1 Hz rate, and the density does not change with coverage, as expected within the SK regime. On Si(100), the initial nucleation density is much lower than on (111), and the evolution of growth with coverage is strongly dominated by coalescence and ripening. For the highest-coverage samples studied, the final structure evolved to a single island, the size of which appeared to be directly related to the size of the stencilled site. The μ-Raman measurements indicate that the structures on Si(100) are nearly fully relaxed, whereas more strain is present in all of the samples on (111).

This approach produces novel growth characteristics when compared to its conventional counterparts. The anomalously thick wetting layer may suppress Si intermixing into the 3D islands and the PLD repetition rate can further be adjusted to suppress intermixing. The oxide-covered substrate regions between the stencil sites did not exhibit any Ge accumulation, providing for excellent fidelity in the transfer of the stencil pattern. These factors could make this method attractive for the production of Si–Ge islands with a Ge-rich stoichiometry, which provides a counterpoint to other patterning methods that promote silicon intermixing [55].

[7] This interpretation rests on the association of the observed Si–Ge peak with the higher-frequency component of the Ge–Ge peak and the assumption that the lower-frequency Ge–Ge component is not associated with any intermixing. Although the frequency of the corresponding singlet would be 300.7 cm^{-1}, both the high intensity of the observed peak and the absence of a split Si–Ge peak reinforce the given interpretation.

Acknowledgments

The authors acknowledge financial support from the Canada Foundation for Innovation, and NSERC of Canada. FR is grateful to FQRNT and the Canada Research Chairs programme for salary support. AB acknowledges an FPI fellowship. JM was supported by an NSERC postdoctoral fellowship. This work was supported in part by the Spanish Ministry of Science and Innovation (MICINN) through grant MAT2009-09480. We thank Josh Lipton-Duffin for his assistance with the composition and strain calculations.

References

[1] Eaglesham D J and Cerullo M 1990 Dislocation-free Stranski–Krastanov growth of Ge on Si(100) *Phys. Rev. Lett.* **64** 1943–6

[2] Mo Y W, Savage D E, Swartzentruber B S and Lagally M G 1990 Kinetic pathway in Stranski–Krastanov growth of Ge on Si(001) *Phys. Rev. Lett.* **65** 1020–3

[3] Leonard D, Krishnamurthy M, Reaves C M, Denbaars S P and Petroff P M 1993 Direct formation of quantum-sized dots from uniform coherent islands of InGaAs on GaAs-surfaces *Appl. Phys. Lett.* **63** 3203–5

[4] Stangl J, Holy V and Bauer G 2004 Structural properties of self-organized semiconductor nanostructures *Rev. Mod. Phys.* **76** 725–83

[5] Williams R S, Medeiros-Ribeiro G, Kamins T I and Ohlberg D A A 1999 Chemical thermodynamics of the size and shape of strained Ge nanocrystals grown of Si(001) *Acc. Chem. Res.* **32** 425–33
[6] Medeiros-Ribeiro G, Bratkovski A M, Kamins T I, Ohlberg D A A and Williams R S 1998 Shape transition of germanium nanocrystals on a silicon (001) surface from pyramids to domes *Science* **279** 353–5
[7] Ross F M, Tersoff J and Tromp R M 1998 Coarsening of self-assembled Ge quantum dots on Si(001) *Phys. Rev. Lett.* **80** 984–7
[8] Rosei F and Rosei R 2002 Atomic description of elementary surface processes: diffusion and dynamics *Surf. Sci.* **500** 395–413
[9] Boscherini F, Capellini G, Di Gaspare L, Rosei F, Motta N and Mobilio S 2000 Ge–Si intermixing in Ge quantum dots on Si(001) and Si(111) *Appl. Phys. Lett.* **76** 682–4
[10] Boscherini F, Capellini G, Di Gaspare L, De Seta M, Rosei F, Sgarlata A, Motta N and Mobilio S 2000 Ge–Si intermixing in Ge quantum dots on Si *Thin Solid Films* **380** 173–5
[11] Ratto F, Rosei F, Locatelli A, Cherifi S, Fontana S, Heun S, Szkutnik P D, Sgarlata A, De Crescenzi M and Motta N 2004 Composition of Ge(Si) islands in the growth of Ge on Si(111) *Appl. Phys. Lett.* **84** 4526–8
[12] Ratto F, Costantini G, Rastelli A, Schmidt O G, Kern K and Rosei F 2006 Alloying of self-organized semiconductor 3D islands *J. Exp. Nanosci.* **1** 279–305
[13] MacLeod J M, Lipton-Duffin J A, Lanke U, Urquhart S G and Rosei F 2009 Shape transition in very large germanium islands on Si(111) *Appl. Phys. Lett.* **94** 103109
[14] Ratto F and Rosei F 2010 Order and disorder in the heteroepitaxy of semiconductor nanostructures *Mater. Sci. Eng.* R **70** 243–64
[15] Kamins T I and Williams R S 1997 Lithographic positioning of self-assembled Ge islands on Si(001) *Appl. Phys. Lett.* **71** 1201–3
[16] Kamins T I, Ohlberg D A A, Williams R S, Zhang W and Chou S Y 1999 Positioning of self-assembled, single-crystal, germanium islands by silicon nanoimprinting *Appl. Phys. Lett.* **74** 1773–5
[17] Vescan L 2001 SiGe nanostructures by selective epitaxy and self-assembling *Mater. Sci. Eng.* A **302** 6–13
[18] Kim E S, Usami N and Shiraki Y 1998 Control of Ge dots in dimension and position by selective epitaxial growth and their optical properties *Appl. Phys. Lett.* **72** 1617–9
[19] Jin G, Liu J L, Thomas S G, Luo Y H, Wang K L and Nguyen B Y 1999 Controlled arrangement of self-organized Ge islands on patterned Si(001) substrates *Appl. Phys. Lett.* **75** 2752–4
[20] Jin G, Liu J L and Wang K L 2000 Regimented placement of self-assembled Ge dots on selectively grown Si mesas *Appl. Phys. Lett.* **76** 3591–3
[21] Zhong Z Y, Halilovic A, Muhlberger M, Schaffler F and Bauer G 2003 Positioning of self-assembled Ge islands on stripe-patterned Si(001) substrates *J. Appl. Phys.* **93** 6258–64
[22] Schmidt O G, Jin-Phillipp N Y, Lange C, Denker U, Eberl K, Schreiner R, Grabeldinger H and Schweizer H 2000 Long-range ordered lines of self-assembled Ge islands on a flat Si(001) surface *Appl. Phys. Lett.* **77** 4139–41
[23] Vescan L 2002 Ge nanostructures grown by self-assembly; influence of substrate orientation *J. Phys.: Condens. Matter* **14** 8235–52
[24] Karmous A, Cuenat A, Ronda A, Berbezier I, Atha S and Hull R 2004 Ge dot organization on Si substrates patterned by focused ion beam *Appl. Phys. Lett.* **85** 6401–3
[25] Bernardi A, Alonso M I, Goni A R, Osso J O and Garriga M 2006 Density control on self-assembling of Ge islands using carbon-alloyed strained SiGe layers *Appl. Phys. Lett.* **89** 101921
[26] Ogino T, Hibino H and Homma Y 1997 Step arrangement design and nanostructure self-organization on Si surfaces *Appl. Surf. Sci.* **117** 642–51
[27] Zhu J H, Brunner K and Abstreiter G 1998 Two-dimensional ordering of self-assembled Ge islands on vicinal Si(001) surfaces with regular ripples *Appl. Phys. Lett.* **73** 620–2
[28] Sakamoto K, Matsuhata H, Tanner M O, Wang D W and Wang K L 1998 Alignment of Ge three-dimensional islands on faceted Si(001) surfaces *Thin Solid Films* **321** 55–9
[29] Arai J, Usami N, Ota K, Shiraki Y, Ohga A and Hattori T 1997 Precise control of island formation using overgrowth technique on cleaved edges of strained multiple quantum wells *Appl. Phys. Lett.* **70** 2981–3
[30] Zhong Z, Schmidt O G and Bauer G 2005 Increase of island density via formation of secondary ordered islands on pit-patterned Si(001) substrates *Appl. Phys. Lett.* **87** 133111
[31] Chen G, Lichtenberger H, Bauer G, Jantsch W and Schaeffler F 2006 Initial stage of the two-dimensional to three-dimensional transition of a strained SiGe layer on a pit-patterned Si(001) template *Phys. Rev.* B **74** 035302
[32] Cojocaru C V, Bernardi A, Reparaz J S, Alonso M I, MacLeod J M, Harnagea C and Rosei F 2007 Site-controlled growth of Ge nanostructures on Si(100) via pulsed laser deposition nanostenciling *Appl. Phys. Lett.* **91** 113112
[33] Cojocaru C V 2007 Controlled growth and positioning of functional materials by unconventional nanoscale patterning *PhD Thesis* Université du Québec INRS-EMT
[34] Linklater A and Nogami J 2008 Defining nanoscale metal features on an atomically clean silicon surface with a stencil *Nanotechnology* **19** 285302
[35] Bernardi A, Osso J O, Alonso M I, Goni A R and Garriga M 2006 Influence of Si interdiffusion on carbon-induced growth of Ge quantum dots: a strategy for tuning island density *Nanotechnology* **17** 2602–8
[36] Alonso M I, de la Calle M, Osso J O, Garriga M and Goni A R 2005 Strain and composition profiles of self-assembled Ge/Si(001) islands *J. Appl. Phys.* **98** 033530
[37] Jain S C and Hayes W 1991 Structure, properties and applications of Ge_xSi_{1-x} strained layers and superlattices *Semicond. Sci. Technol.* **6** 547–76
[38] Reparaz J S, Bernardi A, Goni A R, Alonso M I and Garriga M 2008 Composition dependence of the phonon strain shift coefficients of SiGe alloys revisited *Appl. Phys. Lett.* **92** 081909
[39] Mermoux M, Crisci A, Baillet F, Destefanis V, Rouchon D, Papon A M and Hartmann J M 2010 Strain in epitaxial Si/SiGe graded buffer structures grown on Si(100), Si(110), and Si(111) optically evaluated by polarized Raman spectroscopy and imaging *J. Appl. Phys.* **107** 013512
[40] Amar J G 1999 Mechanisms of mound coarsening in unstable epitaxial growth *Phys. Rev.* B **60** 11317–20
[41] Dolbak A E and Olshanetsky B Z 2006 Ge diffusion on Si surfaces *Cent. Euro. J. Phys.* **4** 310–7
[42] Robinson J T, Ratto F, Moutanabbir O, Heun S, Locatelli A, Mentes T O, Aballe L and Dubon O D 2007 Gold-catalyzed oxide nanopatterns for the directed assembly of Ge island arrays on Si *Nano Lett.* **7** 2655–9
[43] Voigtlander B 2001 Fundamental processes in Si/Si and Ge/Si epitaxy studied by scanning tunneling microscopy during growth *Surf. Sci. Rep.* **43** 127
[44] Brehm M *et al* 2009 Key role of the wetting layer in revealing the hidden path of Ge/Si(001) Stranski–Krastanov growth onset *Phys. Rev.* B **80** 205321
[45] Kukta R V 2010 Mechanics of quantum-dot self-organization by epitaxial growth on small areas *J. Appl. Mech. Trans. ASME* **77** 041001

[46] Shklyaev A A, Shibata M and Ichikawa M 1998 Ge islands on Si(111) at coverages near the transition from two-dimensional to three-dimensional growth *Surf. Sci.* **416** 192–9
[47] Joyce P B, Krzyzewski T J, Bell G R, Joyce B A and Jones T S 1998 Composition of InAs quantum dots on GaAs(001): direct evidence for (In, Ga) As alloying *Phys. Rev.* B **58** 15981–4
[48] Patella F, Arciprete F, Fanfoni M, Sessi V, Balzarotti A and Placidi E 2005 Reflection high energy electron diffraction observation of surface mass transport at the two- to three-dimensional growth transition of InAs on GaAs(001) *Appl. Phys. Lett.* **87** 252101
[49] Venables J A, Derrien J and Janssen A P 1980 Direct observation of the nucleation and growth modes of Ag/Si(111) *Surf. Sci.* **95** 411–30
[50] Venables J A, Spiller G D T and Hanbucken M 1984 Nucleation and growth of thin films *Rep. Prog. Phys.* **47** 399
[51] Sullivan J S, Evans H, Savage D E, Wilson M R and Lagally M G 1999 Mechanisms determining three-dimensional SiGe island density on Si(001) *J. Electron. Mater.* **28** 426–31
[52] Capellini G, De Seta M and Evangelisti F 2003 Ge/Si(100) islands: Growth dynamics versus growth rate *J. Appl. Phys.* **93** 291–5
[53] Smith D J, Chandrasekhar D, Chaparro S A, Crozier P A, Drucker J, Floyd M, McCartney M R and Zhang Y 2003 Microstructural evolution of Ge/Si(100) nanoscale islands *J. Cryst. Growth* **259** 232–44
[54] Schorer R, Friess E, Eberl K and Abstreiter G 1991 Structural stability of short-period Si/Ge superlattices studied with Raman-spectroscopy *Phys. Rev.* B **44** 1772–81
[55] Chen G, Vastola G, Zhang J J, Sanduijav B, Springholz G, Jantsch W and Schaeffler F 2011 Enhanced intermixing in Ge nanoprisms on groove-patterned Si(1110) substrates *Appl. Phys. Lett.* **98** 023104

2.2.5 Optical characterization of Ge nanocrystals

A promising way to synthesize Ge nanocrystals within a SiO_2 matrix film is by high-temperature annealing of SiO_2/a-Ge/SiO_2 trilayer structures. The ability to obtain a suitable distribution of nanocrystals with a specific size relies on a deep knowledge of the kinetics and thermodynamics involved in the nucleation and growth process. Scanning nanocalorimetric characterization at temperatures up to 1300 K was used to obtain results on ultrafast heating of a trilayer structure formed by a 3-nm amorphous Ge (a-Ge) layer sandwiched between 10 nm SiO_2 thin films.

Within this collaboration the author of the thesis performed structural characterization by micro- Raman spectroscopy.

- The micro-Raman spectrum of the as-deposited sample shows a broad peak centred near 270 cm^{-1}, which corresponds to a-Ge.

- After heating to 800 K, the Raman spectrum remains as for a-Ge, however, the low-frequency shoulder at 220 cm^{-1} disappears. Comparing this result with the apparent heat capacity data, we can associate this change with the broad exothermic peak of the a-Ge which corresponds to an irreversible structure relaxation of the a-Ge, characteristic of non-equilibrium amorphous phases. After the rapid heating to 955 K the Ge layer remains amorphous. No changes were observed in the Raman spectra, which agrees with the monotonic behaviour of the first calorimetric scan between 803 and 955K.

- Heating to 1010 K, slightly above the onset of the endothermic calorimetric peak of the first scan, induces some changes in the structure of the film and the micro-Raman indicates now a partially nanocrystalline/amorphous structure. The Raman spectrum exhibits a sharp peak at 296 cm^{-1}, associated to the optical Raman mode of crystallized Ge on top of the broad band of a-Ge.

- The shift of the Ge peak frequency with respect to the value for bulk c-Ge (301 cm^{-1}), might be due to confinement effects in the Ge nanocrystals. By inspection of the phonon dispersion in Ge we infer that a shift of 5 cm^{-1} corresponds to an average nanocrystal size of at most 10 nm.

- The absence of a Si–Ge phonon mode reflects no interdiffusion nor mixing in spite of the high temperatures.

COMPLEMENTARY ARTICLES

Article n: 14

Authors: M. I. Alonso, M. Garriga, A. Bernardi, A. R. Goñi, A. F. Lopeandia, G. Garcia, J. Rodríguez-Viejo and J. L. Lábár

Title: Ellipsometric measurements of quantum confinement effects on higher interband transitions of Ge nanocrystals

Journal: Physica Status Solidi A

Doi: 10.1002/pssa.200777851

Article n: 15

Authors: A.F. Lopeandía, E. Leon-Gutierrez, G. Garcia, F. Pi, A. Bernardi, A.R. Goñi, M.I. Alonso, J. Rodríguez-Viejo

Title: Nanocalorimetric high-temperature characterization of ultrathin films of a-Ge

Journal: Materials Science in Semiconductor Processing

Doi: 10.1016/j.mssp.2006.08.078

phys. stat. sol. (a) **205**, No. 4, 888–891 (2008) / **DOI** 10.1002/pssa.200777851

physica status solidi a
www.pss-a.com
applications and materials science

Ellipsometric measurements of quantum confinement effects on higher interband transitions of Ge nanocrystals

M. I. Alonso*[,1], M. Garriga[1], A. Bernardi[1], A. R. Goñi[,1], A. F. Lopeandia[2], G. Garcia[2], J. Rodríguez-Viejo[2], and J. L. Lábár[3]**

[1] Institut de Ciència de Materials de Barcelona, CSIC, Esfera UAB, 08193 Bellaterra, Spain
[2] Departament de Física, Universitat Autònoma de Barcelona, 08193 Bellaterra, Spain
[3] Research Institute for Technical Physics and Materials Science, P.O. Box 49, 1525 Budapest 114, Hungary

Received 28 June 2007, revised 20 November 2007, accepted 21 November 2007
Published online 20 March 2008

PACS 68.60.Dv, 73.63.Bd, 78.20.Ci, 78.67.Bf, 81.05.Cy, 81.07.Bc

* Corresponding author: e-mail isabel.alonso@icmab.es, Phone: +34-93-5801853, Fax: +34-93-5805729
** ICREA Research Professor

We studied the dielectric functions of Ge nanocrystals obtained by crystallization of amorphous Ge thin films embedded in SiO_2. Partial crystallization of films was induced by thermal annealing. Crystalline regions gave rise to clear spectral features due to interband transitions whose critical point parameters correlated with the initial a-Ge thickness. These changes were clearly attributed to quantum confinement effects.

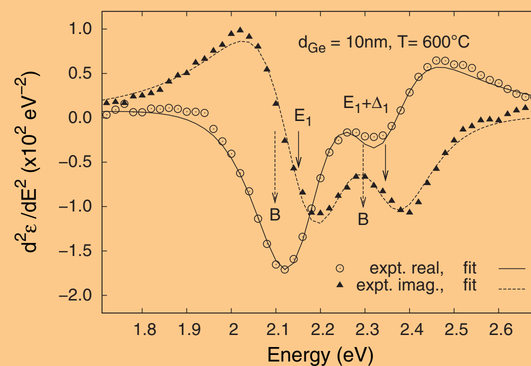

Second derivative of dielectric function spectra and their fit showing the blueshift in E_1 and $E_1 + \Delta_1$ transitions. Energies obtained in bulk Ge are labeled "B" and given for reference.

© 2008 WILEY-VCH Verlag GmbH & Co. KGaA, Weinheim

1 Introduction Considerable attention is continuously devoted to the study of the optical and electronic properties of semiconductor quantum dots. Growing interest in Ge nanostructures is mainly due to their promising applications in advanced electronic devices. In particular, possible application of Ge nanocrystals in optoelectronics is based on quantum size effects on the optical gap and on the photoluminescence [1, 2]. Quantum size effects on higher interband transitions are in general less studied, although this is a subject of fundamental interest. In this work we have used spectroscopic ellipsometry to measure the dielectric functions of Ge nanocrystals and to study the quantum confinement effects in the optical response.

2 Experimental

2.1 Samples The samples were obtained by annealing of structures where a-Ge was sandwiched between SiO_2 layers to minimize heterogeneous nucleation at the interfaces. The complete structures were SiO_2(cap)/a-Ge/SiO_2(buffer)/Si(substrate), all sequentially deposited by e-beam evaporation on a 4″ Si wafer. Several a-Ge film thicknesses between 2 nm and 50 nm were obtained with help of a sliding shutter. To study the crystallization after different heating treatments, the wafer was cut and each piece was annealed in vacuum only once. The setpoint temperatures were reached in 80 s and samples kept hot during 30 min.

WILEY InterScience DISCOVER SOMETHING GREAT

© 2008 WILEY-VCH Verlag GmbH & Co. KGaA, Weinheim

2.2 Ellipsometric measurements Measurements were done at room temperature using a rotating polarizer ellipsometer in the spectral range from 0.7 eV to 5 eV. The ellipsometric spectra were analyzed with a 5-phase (ambient/SiO_2/film: unknown/SiO_2/Si substrate) multilayer model. To obtain all layer thicknesses for every sample, the dielectric functions of the Si substrate and of the SiO_2 were fixed to reference values [3, 4]. The Ge films were treated as unknowns and their dielectric functions were parameterized using splines as previously described [5]. This general parameterization is very useful to fit layer thicknesses in the same way for all samples, without having to introduce different explicit models for the Ge layers. Although oxide thicknesses were similar in all samples, around 15 nm (cap layers) and 100 nm (buffer layers), these parameters were allowed to vary in each particular case. From this analysis it was clear that different tan Ψ and cos Δ spectra obtained for different annealing temperatures were almost exclussively due to changes in the dielectric functions of the Ge films. These changes indicated that, for increasing annealing temperature the as-deposited amorphous layers gave rise to an amorphous Ge matrix with Ge crystallites, and eventually a fully crystallized Ge film. Figure 1 shows the dielectric function obtained from a fit for one sample with a 10 nm thick Ge layer that was annealed at 600 °C. Using as reference the spectra of a-Ge and of crystallized nc-Ge deduced in totally amorphous and totally crystallized samples, we evaluated volume fractions (±5%) of amorphous and crystallized material by applying the Bruggeman effective medium approximation [6]. Conversely, using these volume fractions and the effective dielectric functions fitted in every case, it is possible to calculate the contribution from the crystalline fraction, as shown in Fig. 1. This spectrum shows representative features obtained in this study for many samples. First, the dielectric function shows lower values compared to bulk Ge, both in the real and imaginary part [7–10]. Also, the E_2 critical point is apparently weaker than the E_1. Finally, in the thinnest Ge films, we obtain an increased absorption near 0.8 eV.

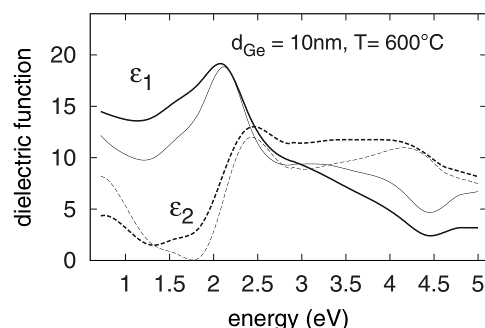

Figure 1 Dielectric function fitted with splines for a 10 nm thick Ge layer after annealing at 600 °C. Thick lines are the fitted effective dielectric functions. Thin lines indicate the dielectric function of the crystalline fraction, determined to be 60% in volume.

In order to accurately determine the energies of interband transitions in the Ge layers, we used the layer thicknesses obtained from the above described analysis, and calculated point-by-point dielectric function spectra by numerical inversion. They basically coincided with the spline but contained more detail, although some portions of the spectra were very noisy. Then we numerically built the second derivative and fitted the observed critical point (CP) parameters [11] by using analytic lineshapes. We chose direct-space rather than reciprocal-space analysis [12] because the former is more reliable in the case of two close CPs, like spin-orbit split counterparts. The best resolved transitions in these samples were in general the E_1 and $E_1 + \Delta_1$ interband transitions, as shown in the Title figure for the same sample of Fig. 1. All spectra were well described by 2D lineshapes, which are suitable for a bulk-like Ge band structure [11].

3 Results and discussion We show representative results of critical point parameters for two series of samples with 50 nm and 10 nm thick Ge layers. We focus on the spectral regions of E_1 and E_2 transitions. The E_0' CP was too broad and noisy and could not be reliably fitted.

3.1 E_1 transitions Figure 2 shows the energies and linewidths obtained for E_1 and $E_1 + \Delta_1$ interband transitions in the investigated samples. Comparing the obtained behavior as a function of annealing temperature for 50 nm thick and 10 nm thick Ge films we observe larger blueshifts with respect to bulk Ge for the thinner films. However, the splitting Δ_1 is approximately constant for all samples, and it coincides with that of bulk Ge. This is con-

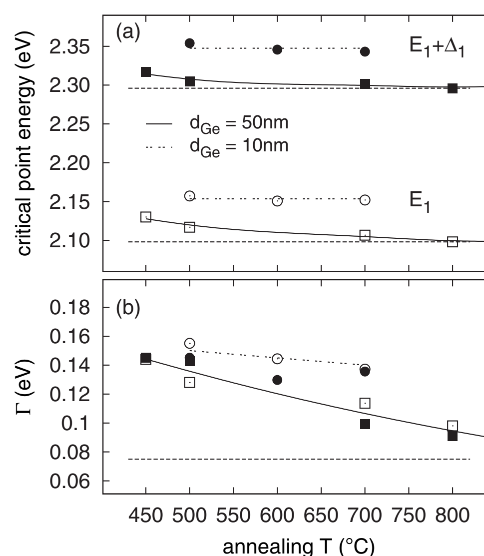

Figure 2 Transition energies (a) and linewidths (b) for the E_1 and $E_1 + \Delta_1$ critical points as a function of annealing temperature. Symbols display fitted values and curves are guides to the eye. Horizontal dashed lines provide reference values for bulk crystalline Ge.

© 2008 WILEY-VCH Verlag GmbH & Co. KGaA, Weinheim

sistent with results from X-ray diffraction and from Raman scattering indicating that the Ge crystallites are free from strain, and also not intermixed with Si. Therefore, the blueshifts are attributed to quantum confinement effects [13], as it was previously reported using resonant Raman scattering in similar systems [14, 15]. Therefore, we relate a larger blueshift to a smaller crystallite size. According to this and the results of Fig. 2 the crystallite sizes in the 50 nm thick samples increase for increasing annealing temperatures, tending to bulk values. On the contrary, in the 10 nm thick films, sizes are roughly constant with temperature and smaller than in 50 nm thick films. At the same time, the crystallized volume fraction in the 10 nm thick films remains constant as well, whereas it increases with temperature in 50 nm thick films. A simple $1/R^2$ dependence [14–16] allows to estimate these sizes. We obtain particle radii R around 7 nm for the three 10 nm thick Ge films of Fig. 2. In the 50 nm thick films, radii increase from 8.3 nm to more than 15.3 nm, which is the estimated E_1 exciton size. The binding energy of this exciton in the model is estimated to be 25 meV, which is the value of kT at room temperature. The calculated sizes are obviously an approximation, but the order of magnitude is consistent with the film thicknesses. All results together suggest that crystallites can only grow to a size which is roughly equal to the initial layer thickness. This mechanism was proposed by Williams et al. [17]. The increased broadening of the transitions is roughly correlated with the confinement energy, that is, it probably indicates a reduced lifetime [18], although a contribution due to crystallite size inhomogeneity cannot be excluded.

3.2 E_2 transitions The spectral region of E_2 transitions is more difficult to analyze, especially for smaller film thicknesses, where an increased broadening of these transitions is observed and consequently more noise into the second derivative spectra is introduced. In Fig. 3 we have plotted the well-resolved results for the 50 nm thick films annealed at different temperatures. A numerical derivative with its fit is shown in Fig. 3(a), and the evolution with temperature of energies and linewidths is shown in Fig. 3(b) and (c), respectively. We observe that E_2 energies also exhibit a small blueshift, but the main effect is an increased broadening. The critical point amplitude is similar for all samples, but due to the large linewidth, the E_2 transitions appear weaker than in bulk Ge, as mentioned in Section 2.2.

3.3 Samples annealed at 900 °C The raw ellipsometric spectra of samples annealed at 900 °C were for all thicknesses qualitatively different from those previously discussed. It was not possible to understand such spectra based on the effective medium approximation using known spectra of a-Ge and of crystallized nc-Ge from other samples. Applying the multilayer model and spline parameterization of the Ge layer, different fits were possible and in general gave very large film thicknesses and very low values of the dielectric functions. We used cross section transmission electron microscopy (TEM) as complementary tool to investigate the structural changes occurring at 900 °C, as shown in Fig. 4(a) in the case of a 6 nm thick layer. At this temperature the Ge films dewet and form islands much thicker than the initial a-Ge thickness, creating a mixed layer with SiO_2 and also voids. In this case, extracted from the TEM images, we used a thickness of 30 nm for the Ge-containing layer and found the imaginary part of the dielectric function of Fig. 4(b). We do not attempt to extract the contribution of the Ge islands, because the void fraction cannot be evaluated from the images. However, the observed electronic transitions are associ-

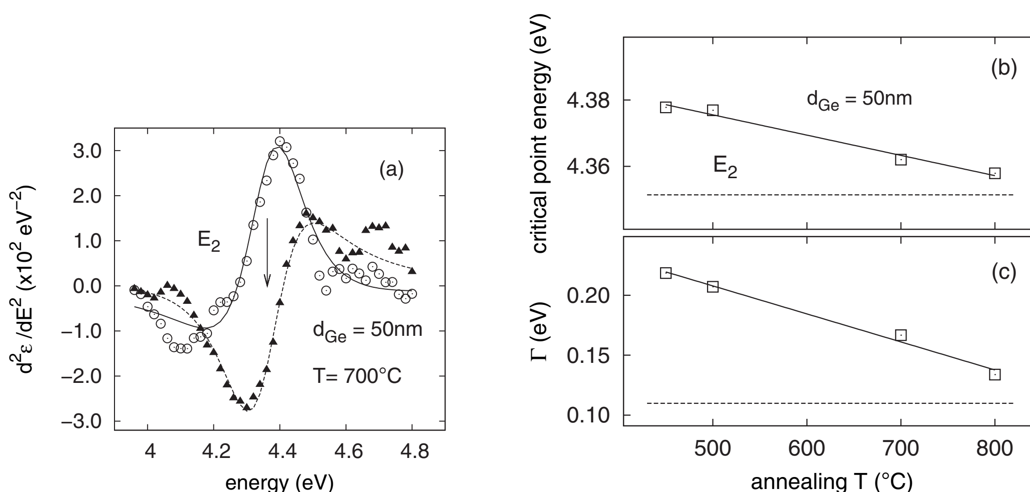

Figure 3 (a) Second derivative of the dielectric function obtained for the 50 nm thick film annealed at 700 °C. Points are experimental values and lines are fitted using 2D lineshapes. The arrow marks the E_2 interband transition energy obtained from fit. (b), (c) Energies and linewidths fitted for 50 nm thick films annealed at different temperatures. Symbols display fitted values, lines are guides to the eye. Horizontal dashed lines provide reference values for bulk crystalline Ge.

© 2008 WILEY-VCH Verlag GmbH & Co. KGaA, Weinheim

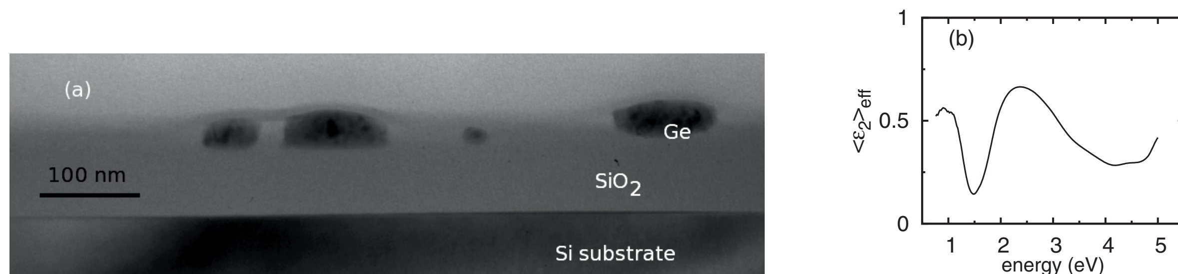

Figure 4 (a) Transmission electron microscopy cross sectional view of the sample with originally 6 nm thick a-Ge layer after annealing at 900 °C. (b) Imaginary part of the effective dielectric function fitted for the Ge-containing layer of this sample.

ated to the Ge islands. Comparing with Fig. 1 there are some similarities, like the increased absorption around 1 eV and the loss of spectral strength around 4 eV. This very low value of $\langle \varepsilon_2 \rangle$ for the E_2 CP is partially due to the effects of mixing with SiO_2 and voids and the large expected broadening. There are other causes that we cannot quantify, among them the dispersion of crystallite sizes.

4 Conclusion The investigation of a-Ge thin films embedded in SiO_2 by spectroscopic ellipsometry allowed us to follow the crystallization onset and progress as a function of annealing temperature. The effective dielectric function spectra that were obtained for the different layers annealed below 900 °C could be described by Bruggeman mixtures of amorphous and crystalline material. However, the spectra of nanocrystalline Ge displayed changes with respect to bulk Ge that were ascribed to size effects. In particular, the interband transitions E_1, $E_1 + \Delta_1$, and E_2 exhibited blueshifts and broadenings attributed to quantum confinement. Spectra of samples annealed at 900 °C could not be interpreted in the same way as those for lower temperatures. Complementary structural study by transmission electron microscopy showed that those films contained isolated nanocrystals within the SiO_2 matrix.

Acknowledgements We are grateful to Dr. F. Pi and Dr. P. Godignon for help in preparing the samples. We acknowledge financial support from the Spanish Ministerio de Educación y Ciencia through MAT2004-04761 and MAT2006-02680 as well as a FPI fellowship (A.B.).

References

[1] Y. Kanemitsu, K. Masuda, M. Yamamoto, K. Kajiyama, and T. Kushida, J. Lumin. **87–89**, 457 (2000).
[2] G. Nesher, L. Kronik, and J. R. Chelikowsky, Phys. Rev. B **71**, 035344 (2005).
[3] D. E. Aspnes and A. A. Studna, Phys. Rev. B **27**, 985 (1983).
[4] H. R. Philipp, Handbook of Optical Constants of Solids (Academic Press, New York, 1985), p. 749.
[5] M. Garriga, M. I. Alonso, and C. Domínguez, phys. stat. sol. (b) **215**, 247 (1999).
[6] D. E. Aspnes, Thin Solid Films **89**, 249 (1982).
[7] P. Tognini, L. C. Andreani, M. Geddo, A. Stella, P. Cheyssac, R. Kofman, and A. Migliori, Phys. Rev. B **53**, 6992 (1996).
[8] P. W. Li, D. M. T. Kuo, W. M. Liao, and M. J. Tsai, Jpn. J. Appl. Phys. Part 1 **43**, 7788 (2004).
[9] M. M. Giangregorio, M. Losurdo, M. Ambrico, P. Capezzuto, G. Bruno, and L. Tapfer, J. Appl. Phys. **99**, 063511 (2006).
[10] M. Mansour, A. En Naciri, L. Johann, S. Duguay, J. Grob, M. Stchakovsky, and C. Eypert, J. Phys. Chem. Solids **67**, 1291 (2006).
[11] L. Viña, S. Logothetidis, and M. Cardona, Phys. Rev. B **30**, 1979 (1984).
[12] S. D. Yoo and D. E. Aspnes, J. Appl. Phys. **89**(12), 8183 (2001).
[13] H. C. Weissker, J. Furthmüller, and F. Bechstedt, Phys. Rev. B **65**, 155328 (2002).
[14] K. L. Teo, S. H. Kwok, P. Y. Yu, and S. Guha, Phys. Rev. B **62**, 1584 (2000).
[15] I. E. Tyschenko, A. B. Talochkin, A. G. Cherkov, K. S. Zhuravlev, and R. A. Yankov, Solid State Commun. **129**, 63 (2004).
[16] M. I. Alonso, M. Garriga, A. Bernardi, A. R. Goñi, A. F. Lopeandia, G. Garcia, J. Rodríguez-Viejo, and J. L. Lábár, Thin Solid Films, in press (2008). DOI: 10.1016/j.tsf.2008.01.003.
[17] G. V. M. Williams, A. Bittar, and H. J. Trodahl, J. Appl. Phys. **67**, 1874 (1990).
[18] H. C. Weissker, J. Furthmüller, and F. Bechstedt, Phys. Rev. B **69**, 115310 (2004).

 © 2008 WILEY-VCH Verlag GmbH & Co. KGaA, Weinheim

Available online at www.sciencedirect.com
ScienceDirect
ELSEVIER
Materials Science in Semiconductor Processing 9 (2006) 806–811
MATERIALS SCIENCE IN SEMICONDUCTOR PROCESSING

Nanocalorimetric high-temperature characterization of ultrathin films of a-Ge

A.F. Lopeandía[a], E. Leon-Gutierrez[a], G. Garcia[a], F. Pi[a], A. Bernardi[b], A.R. Goñi[b], M.I. Alonso[b], J. Rodríguez-Viejo[a,*]

[a]Departament Física, Universidad Autónoma de Barcelona, 08193 Bellaterra, Spain
[b]Institut de Ciència de Materials de Barcelona, CSIC, Esfera UAB, 08193 Bellaterra, Spain

Available online 3 November 2006

Abstract

The crystallization temperature of ultrathin films of a-Ge sandwiched between SiO_2 layers increases with decreasing thickness and also with the heating rate. Based on this premise we used ultrafast heating to probe the amorphous-to-liquid transition in ultrathin films of amorphous Ge. Upon cooling, the melt solidifies into nanocrystalline Ge. We show that sensitive nanocalorimetric measurements can provide kinetic and thermodynamic information involved during the amorphous-to-liquid- and nanocrystalline-to-liquid-phase transitions in the Ge system. A 3-nm a-Ge ultrathin layer is condensed from an e-beam evaporator under high vacuum conditions onto the 180 nm thick free-standing SiN_x membranes of the calorimeters that form the calorimetric cells. The a-Ge film is sandwiched between a-SiO_2 layers to minimize heterogeneous nucleation at the interfaces. Nanocalorimetric measurements are carried out in-situ inside the e-beam setup. The apparent heat capacity (Cp) of the a-Ge layers is extracted measuring the power released to the sample at fast heating rates (10^4–10^5 K/s), in the temperature range from 350 to 1200 K.
© 2006 Published by Elsevier Ltd.

Keywords: Nanocalorimetry; Ge thin films; Melting

1. Introduction

Ge nanocrystals embedded in SiO_2 have attracted a strong interest in the scientific community due to their potential applications in optoelectronics, because of its light-emitting properties, and in high-speed and low-power logic and memory devices [1,2]. A promising way to synthesize Ge nanocrystals within a SiO_2 matrix film is by high-temperature annealing of SiO_2/a-Ge/SiO_2 trilayer structures [3]. The ability to obtain a suitable distribution of nanocrystals with a specific size relies on a deep knowledge of the kinetics and thermodynamics involved in the nucleation and growth process. A suitable technique to characterize these properties during and after the synthesis process is Calorimetry. However, few data regarding crystallization and melting behavior for Ge thin films [3,4] or nanocrystals [1] can be found in the literature. The main difficulty to such measurements is related to sensitivity limitations of conventional differential scanning calorimetry (DSC) on measuring small samples. The development of Silicon micromachining techniques associated to the silicon technology has enabled the scaling down of

*Corresponding author.
E-mail address: javirod@vega.uab.es (J. Rodríguez-Viejo).

1369-8001/$ - see front matter © 2006 Published by Elsevier Ltd.
doi:10.1016/j.mssp.2006.08.078

membrane-based nanocalorimeters able to measure small samples, ranging from pg to ng, with a high sensitivity [5,6].

In the present work we show the use of a scanning nanocalorimeter at temperatures up to 1300 K and report preliminary results on ultrafast heating of a trilayer structure formed by a 3-nm a-Ge layer sandwiched between 10 nm SiO_2 thin films. Structural characterization was performed by micro-Raman spectroscopy.

2. Experimental

2.1. Microreactor fabrication

Nanocalorimeters were fabricated at the clean room of the *Instituto de Microelectrónica de Barcelona* (IMB-CNM) using standard microfabrication technologies. Details of the microfabrication procedure are reported in detail elsewhere [7]. To achieve high-temperature stability a 150 nm Al_2O_3 protective layer was grown on top of the 100 nm Pt/10 nm Ti heater and sensor. Membrane shape and dimensions and heater design were optimized to achieve good electrical and mechanical stability preventing heater damage and buckling formation in all the measuring range up to 1300 K. Over these temperatures, some degradation appears due to electromigration and agglomeration [8].

2.2. Experimental procedure for nanocalorimetric measurements

Fig. 1 shows a schematic cross-section (A) and a 3D view (B) of the nanocalorimeter and its four-point measuring configuration. The calorimetric cell is heated by Joule effect introducing a constant pulse of current (I) through the metallic heater. The power and its average temperature are obtained from a simultaneous 4-point measurement of the voltage drop ($V(t)$) while the current is flowing. The temperature is determined using the coefficient of resistance which is measured in a previous calibration. The specific U-shaped design of the heater enables measurements from slow heating rates (few K/s) in power compensation [9] to ultrafast heating rates ($>10^4$ K/s) [6-7]. Using current pulses in the range of $\sim$10 mA, the calorimetric cell increases its temperature at heating rates of 5×10^4 K/s, around 50 times faster than typical cooling rates at temperatures below 700 K. Therefore at such temperatures the nanocalorimeter behaves quasi-adiabatically and the heat capacities for each calorimetric cell can be obtained from

$$Cp(T(t)) = \frac{P(t)}{\beta(t)},$$

where P is the power introduced in the calorimetric cell and β is the heating rate. At higher temperatures, heat losses should be taken into account in order to determine the heat capacity of the sample, since the above expression is transformed into

$$Cp(T(t)) = \frac{1}{\beta(t)}(P(t) - P_{\mathrm{Loss}}),$$

where P_{loss} refers to the power lost by heat conduction through the membrane and thermal radiation. Under the assumption that the temperature profile during heating and cooling are identical, one can estimate the thermal resistance and emissivity of the nanocalorimeter by means of the characteristic $T(t)$ cooling curve. The percentage of power losses at high temperatures is large, however, a differential measurement between two nearly identical calorimetric cells, one with sample (sample calorimetric cell, SCC) and the second one acting as

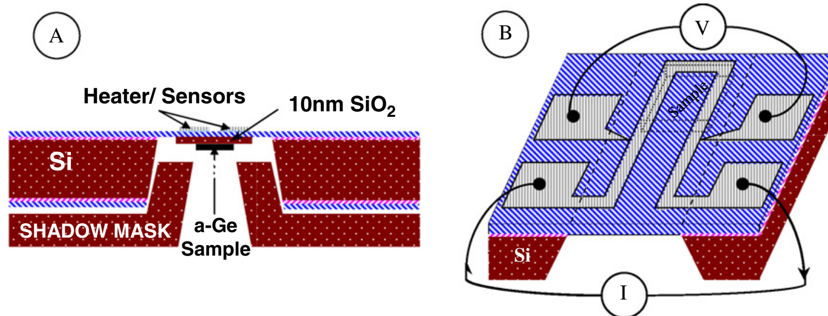

Fig. 1. Schematics of the nanocalorimeter. (A) Cross section of the nanocalorimeter. The microfabricated shadow mask limits the deposition area to the sensing area, below the heater/sensors. (B) 3D view of the nanocalorimeter.

a reference (reference calorimetric cell, RCC), decreases its contribution and improves the accuracy of the measurement [10]. The main limitation to perform accurate high-temperature nanocalorimetry relies on the assumption that heat losses are similar in both calorimetric cells. We use a Si microfabricated shadow mask (Fig. 1) to deposit only in the sensing area of the cell. Therefore, if the conductivity of the sample does not change significantly, the thermal resistance between the membrane and the silicon frame can be considered the same for both cells. The treatment of the radiative losses is more difficult to handle. Whereas emissivity measurements at each temperature may be required for a precise determination of the sample heat capacity, the growth of a top SiO_2 capping layer is used to minimize the difference between both calorimetric cells.

2.3. Nanocalorimetry experiments

A nanocalorimetric twin system was mounted inside the HV e-beam evaporator chamber of the Thin-Film Laboratory at UAB. The device was placed in a custom-built pogopin probe designed to contact the electrical pads and to align the Si-microfabricated shadow mask. Two independent shutters give the possibility to make a selective deposition on the different calorimetric cells, see Fig. 2. We follow the general procedure described by Allen et al. [10]. Once the system is aligned and under high vacuum, typically 5×10^{-2} Pa, 1000 consecutive heating ramps are carried out until 1250 K with the same current values that will be used in the subsequent experiments. A current of 13 mA was chosen to attain heating rates of 5×10^{4} K/s. This procedure guarantees the thermal stability in the measuring range and also cleans the membrane from organic contamination. A buffer thin film SiO_2 with a nominal thickness of 10 nm was evaporated onto both membranes; the mass evaporated is measured by a previously calibrated crystal quartz monitor (CQM). The SiO_2 layer is deposited to inhibit the heterogeneous nucleation of Ge at the interface [1,4]. After the first deposition of SiO_2, 500 high temperature scans are performed and averaged to extract the calorimetric baseline. The baseline gives the initial difference in heat capacities between both calorimetric cells, SCC and RCC. Afterwards, a shutter is positioned to block the RCC, and the 3 nm a-Ge layer is evaporated from a pure Ge pellet onto the SCC. The temperature of the CCS during deposition was around 300 K, and the growth rate was 0.1 nm/s. Finally, a capping layer of 10 nm of SiO_2 was deposited on top of both CC covering the a-Ge sample.

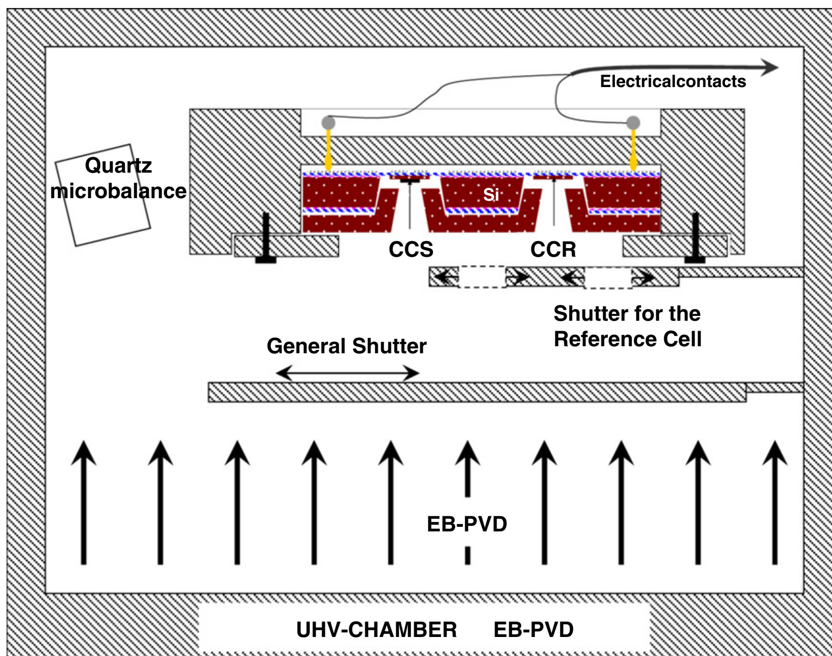

Fig. 2. Experimetal setup used for growth of the SiO_2/a-Ge/SiO_2 trilayers and the nanocalorimetric measurements.

2.4. Raman spectroscopy

Raman spectroscopy was carried out in back-scattering geometry with a high-resolution LabRam HR800 spectrometer, using the 514.5 nm line of an Ar-ion laser for excitation. The beam was focused onto the sample with a spot size of about 1 μm and a laser power of 2 mW.

3. Results and discussion

The structure of the as-deposited Ge thin film was confirmed to be fully amorphous by plane-view transmission electron microscopy (TEM) images and selected area electron diffraction (SAED) patterns. EDX nanoanalysis with a spot size of 5 nm confirmed the continuity of the as-deposited film.

Fifty consecutive nanocalorimetric scans were performed from room temperature up to 1200 K on a sample of SiO_2/a-Ge/SiO_2 with a nominal Ge thickness of 3 nm. Three of the calorimetric traces obtained are shown in Fig. 3. It is important to highlight that these curves correspond to single scans from which the averaged baseline contribution is subtracted. The first scan shows a one-time irreversible broad peak on the low-temperature region (see inset) and a large endothermic peak centered at 1080 K while after the second scan a reversible reaction at slightly higher temperatures is shown to be highly reproducible. The elevated increase in heat capacity at the higher end may be due to uncorrected heat losses and it is being the object of further analysis. In order to identify the nature of the reactions involved in these scans, a sample of a-Ge sandwiched between 10 nm of SiO_2 was grown on top of another nanocalorimeter. Fig. 4 shows a systematic study of the sample structure performed by micro-Raman spectroscopy after rapid heating, 5×10^4 K/s, within the nanocalorimeter up to different temperatures. The micro-Raman spectrum of the as-deposited sample shows a broad peak centered near 270 cm^{-1} which corresponds to a-Ge [11]. After heating to 803 K, the Raman spectrum remains as for a-Ge, however, the low-frequency shoulder at 220 cm^{-1} disappears. Comparing this result with the apparent heat capacity data, we can associate this change with the broad exothermic peak of the a-Ge which corresponds to an irreversible structure relaxation of the a-Ge, characteristic of non-equilibrium amorphous phases [12]. After the rapid heating to 955 K the Ge layer remains amorphous. No changes were observed in the Raman spectra which agrees with the monotonic behavior of the first calorimetric scan between 803 and 955 K. Heating to 1013 K, slightly above the onset of the endothermic calorimetric peak of the first scan, induces some

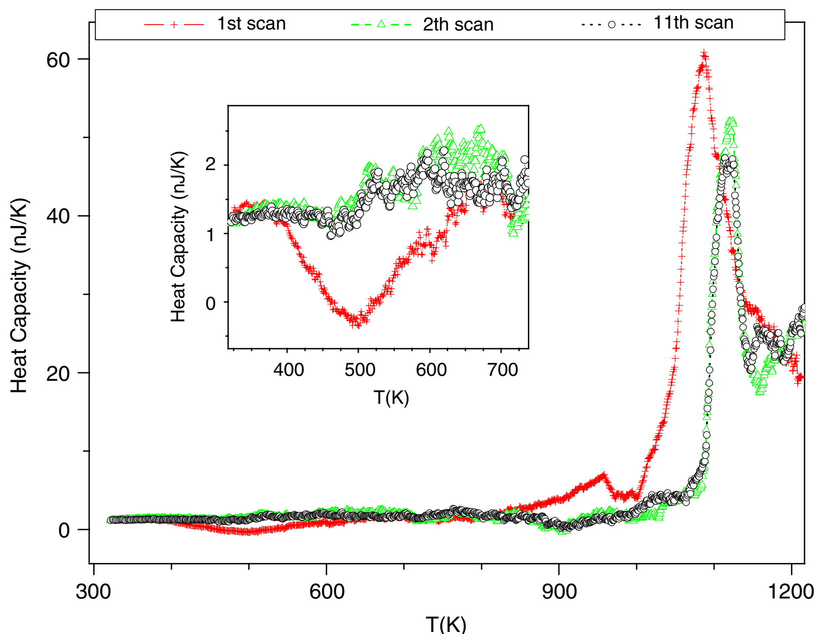

Fig. 3. Apparent heat capacity vs. temperature for the 3-nm a-Ge thin film sandwiched between two films of 10-nm thick SiO_2.

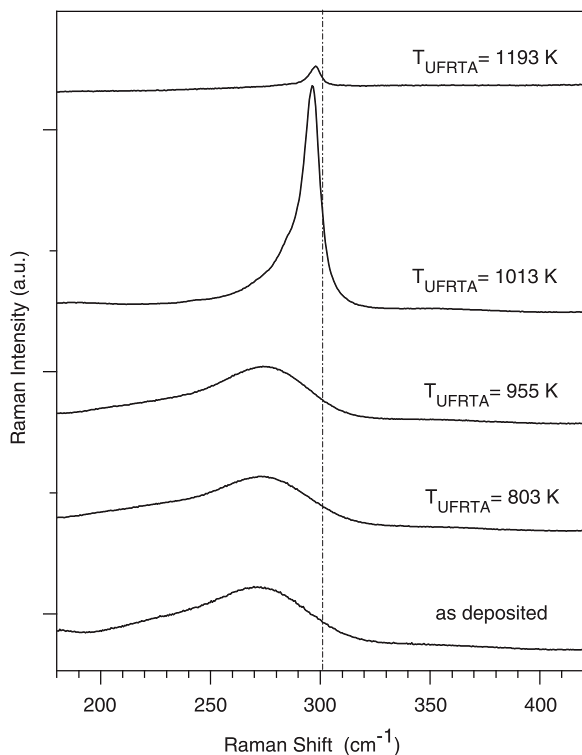

Fig. 4. Raman spectra of a SiO_2/a-Ge/SiO_2 trilayer after rapid heating to different temperatures. The structure of the Ge phonon mode is representative of the crystalline state of the Ge layer. The spectra are vertically shifted for clarity. The vertical line corresponds to phonons frequency for bulk crystalline Ge.

changes in the structure of the film and the micro-Raman indicates now a partially nanocrystalline/amorphous structure. The Raman spectrum exhibits a sharp peak at $296\,cm^{-1}$ associated to the optical Raman mode of crystallized Ge on top of the broad band of a-Ge. The shift of the Ge peak frequency with respect to the value for bulk c-Ge ($301\,cm^{-1}$), might be due to confinement effects in the Ge nanocrystals. By inspection of the phonon dispersion in Ge we infer that a shift of $\sim 5\,cm^{-1}$ corresponds to an average nanocrystal size of at most 10 nm. The absence of a Si–Ge phonon mode reflects no interdiffusion and mixing in spite of the high temperatures. The above findings support the idea that the endothermic peak of the first calorimetric scan is due to an amorphous-to-liquid transition because crystallization is hindered upon heating by the fast heating rates and the small thickness of the layer. The onset of melting is around 1000 K, close to the value predicted from the intersection of the liquid and amorphous free-energy curves, which gives a value of 970 K. Since Ge changes from a fourfold coordinated structure in the solid state to a 12-fold metallic structure in the liquid the transition of amorphous-to-liquid is first-order in nature and should be observed by an abrupt change of the heat capacity. During cooling, due to the lower cooling rate, solidification occurs and the previously small melted fraction transforms into nanocrystalline Ge. Heating to higher temperatures, 1193 K, results in complete melting of the a-Ge layer. The micro-Raman spectrum after cooling back shows only the contribution from crystalline Ge which is again formed upon solidification of the melt. Comparing the two last spectra, we observe a clear reduction in the intensity of the fully crystallized Ge peak as well as a shift towards the bulk frequency, indicating a smaller confinement in the last one. The peak intensity is resonantly enhanced in the nanocrystals due to E_1-like electronic transitions close to the exciting laser energy. In bulk Ge the enhancement occurs at lower energy, $\sim 2.2\,eV$ which is consistent with the loss of resonance in the highest heated sample. AFM imaging of the sample after a first complete scan to 1200 K shows the formation of nanoislands with an average height around 12 nm. The other two calorimetric traces in Fig. 3 show the melting of nanocrystalline Ge, formed after melting of the amorphous material and nanocrystallization on cooling. The onset for melting of a nanocrystalline Ge layer with a nominal thickness of 3 nm Ge is 1090 K. This value is 125 K lower than the melting temperature for bulk crystalline Ge, 1210 K. More experiments with nanocrystals of different sizes are needed since the depression seems to be smaller than expected from size-dependent effects [13]. This behavior could be attributed to the high Hamaker constant of Ge which may facilitate superheating of the nanocrystals above the expected melting temperature. Further corrections of the heat losses during the melting transition are necessary to extract reliable values of the transition enthalpy.

4. Conclusions

We have performed nanocalorimetric measurements on a 3-nm a-Ge sandwiched between 10 nm SiO_2 layers. In the first scan, the calorimetric curve shows the structure relaxation of the a-Ge and the amorphous-to-liquid melting transition with an onset temperature close to 1000 K. During cooling to room temperature solidification results in the nanocrystallization of the sample and in the

second and subsequent scans the calorimetric curve shows the crystalline-to-liquid transition of the nc-Ge structure. The onset for melting of nc-Ge occurs at 1090 K, 125 K below the bulk melting temperature.

Acknowledgments

We thank Dr. F.J. Muñoz from the IMB-CNM for his collaboration in the microfabrication of the calorimeters. We also would like to thank fruitful discussions with Dr. K. Zekentes from FORTH about Ge growth. We acknowledge financial support from projects MAT2004-04761 and 2005SGR00201 granted by MEC and Generalitat de Catalunya, respectively. AFL and AB acknowledge financial support through fellowships from MEC. ARG is an ICREA Research Professor.

References

[1] Kolobov AV, Wei SQ, Yan WS, Oyanagi H, Maeda Y, Tanaka K. Phys Rev B 2003;67:195214.
[2] Das K, NandaGoswami M, Mahapatra R, Kar GS, Dhar A, Acharya HN, et al. Appl Phys Lett 2003;84:8.
[3] Choi WK, Ng V, Swee VSL, Ong CS, Yu Rusli MB, Yoon SF. Scr Mater 2001;44:1873.
[4] Zacharias M, Streitenberger P. Phys Rev B 2000;62:12.
[5] Denlinger DW, Abarra EN, Allen K, Rooney PW, Messer MT, Watson SK, et al. Rev Sci Instrum 1994;65:946.
[6] Lai SL, Ramanath G, Allen LH, Infante P, Ma Z. Appl Phys Lett 1995;67(9):28.
[7] Lopeandía AF, Rodríguez-Viejo J, Chacón M, Clavaguera-Mora MT, Muñoz FJ. J Micromech Microeng 2006;16:1.
[8] Firebaugh SL, Jensen KF, Schmidt MA. J Microelectromech Syst 1998;7:128.
[9] Lopeandía AF, Cerdó Ll, Clavaguera-Mora MT, Arana LR, Jensen KF, Rodríguez-Viejo J. Rev Sci Instrum 2005;76:065104.
[10] Efremov M, Olson E, Zhang M, Lai S, Schiettakatte F, Zhang Z, et al. Thermochim Acta 2004;412:13.
[11] Kumar S, Trodahl HJ. J Appl Phys 1991;70:3088.
[12] Donovan EP, Spaepen F, Turnbull D, Poate JM, Jacobson DC. J Appl Phys 1985;57:1785.
[13] Jiang Q, Yang CC, Li JC. Mater Lett 2002;56:1019.

2.3 Rolled-up semiconductor microtubes

Self-assembling of 3D islands is just one of the possible pathways for strain relaxation when a multilayer of pseudomorphic materials is grown. Strain-engineered nanoscale materials can be used to fabricate quite a variety of different nanometer-sized objects with special properties and a big potential for application in micro-devices.

Strain-driven engineering is a bottom-up approach to obtain objects whose positions and dimensions depend critically on the design and elastic properties of the starting semiconductor multilayer structures.
Rolled-up nanotubes, for example, can be obtained from strained heterostructures after releasing the multilayer structure from the substrate by selective etching. The basic idea behind the strain-driven engineering is that strained thin films tend to acquire a different equilibrium shape in order to minimize their elastic energy.

Apart from micro- and nanotubes, it is also possible to take advantage of the built-in strain in semiconductor epitaxial layers to build up self-standing microhinges bending until reaching an equilibrium position with a controlled radius of curvature. These flexible hinges are the building blocks for a method of fabrication, denominated *micro-origami*, which can be used to prepare a number of smart integrated devices such as micro-mirrors, microstages, and others with a wide range of applications in microelectronics, optoelectronics, and biology. Production of future micro-optoelectromechanical systems (MOEMSs) in which the built-in strain is expected to change their electronic band structure as well as their optical properties, will certainly require adequate control over the fabrication process by being able to tailor the strain in the device. Then, it is desirable to count on a fast, noninvasive, and spatially resolved characterization technique such as micro-Raman scattering, which allows for the determination of the strain in the ready device.

Light can be used to characterize these materials but, on the other end, photons can be employed as the core principle to unveil properties of the environment where the microtube device is exposed, converting this functional material in a sensor. By nature a microtube acts like a fantastic capillary for microfluidic applications and, if we combine light probing with fluidics, we obtain a prototype of an opto-fluidic device. The “rolled-up nanotech” is an excellent candidate for designing cheap and reliable optofluidic systems. The strain gradient stored inside a thin layer can be conveniently exploited to cause spontaneous curling of a thin film into a microtube by a simple single-step underetching procedure. The microtube acts both as a waveguide with light confined in the tube walls, and as a ringlike resonator with optical resonant modes sensitive to the fluid flowing inside of the microdevice. The fabrication process can be relatively cheap and scalable with an intelligent strategy for positioning and integration of the optofluidic components. Therefore, there is a big potential of monolithically integrating an optofluidic function into mainstream Si technology to build a Lab-on-a-chip.

2.3.1 Probing strain in microtubes by micro-Raman spectroscopy

We showed how Raman spectroscopy can be used as a sensitive diagnostic tool to obtain a postprocessing feedback on strain engineering for further design optimization applied to the case of InGaAs/GaAs microtubes. Starting from an elastic model of the actual microtubes produced by the "*micro-origami* method" we derived analytical expressions for the relevant components of the strain tensor in cylindrical coordinates, which are then used to calculate the expected frequency shifts of the optical phonons of the constituent materials.
In particular we obtain the expressions for the radial (ϵ_{rr}) and hydrostatic (ϵ_{hydro}) strain components at the surface of the microtube which are directly related to the phonon frequency shift which we expect to measure by Raman scattering (LO mode):

$$\epsilon_{rr} = \frac{2}{\left(\nu - \frac{1}{\nu}\right)\widetilde{K}_{12} + \widetilde{K}_{11}} \frac{\Delta\omega_{LO}}{\omega_0}$$

$$\epsilon_{hydro} = \frac{2\nu - 1}{\nu} \epsilon_{rr}$$

To fabricate the microtubes a multilayered structure was grown by molecular-beam epitaxy on a GaAs (001) substrate. The structure consists of 80 nm of sacrificial layer $Al_{0.52}Ga_{0.48}As$/AlAs, a strained layer of $In_{0.19}Ga_{0.81}As$ (each sample has a different thickness), and a GaAs top layer (55 nm). Once defined narrow trenches along the [001] direction using photolithography, the sacrificial layer was selectively etched with HF: as a consequence, the freestanding multilayer rolls up like a carpet to minimize elastic energy.

Raman spectra were collected at room temperature using a Jobin-Yvon T6400 Raman spectrometer and with different lines of an Ar^+ laser as excitation source. The size of the laser spot was 2 μm, and the laser power on the sample was about 2 mW. Measurements were performed in backscattering geometry with crossed polarization (to select the LO phonon mode) by focusing the laser beam on different regions of the samples: on the tubes and on the as-grown regions nearby.

- When the laser is focused onto the microtube the outer layer of material is the strained $In_{0.19}Ga_{0.81}As$ thin film. For this reason an interchange of intensity is observed between peaks corresponding to the LO phonons of InGaAs and GaAs, if we compare with the spectra collected from the as-grown areas.

- The peak attributed to the $In_{0.19}Ga_{0.81}As$ LO phonon is shifted from the expected mode frequency for this alloy composition. This shift is obviously due to the residual strain of the bent layer.

- Microtubes with different radii of curvature are also characterized by a different strain field inside the bilayer constituting the tube wall and consequently they exhibit a different phonon frequency shift.

- The values obtained for the hydrostatic and radial strain components are clearly correlated with the radius of curvature of the microtubes. We observe a striking crossover from compressive to tensile strain (hydrostatic component) of the thin InGaAs layer, when the radius decreases from 4.5 to less than 3.0 μm.

- The values of strain obtained by Raman match quite well with the predictions of the elastic model describing the strain status of the microtubes. Results point to strain relaxation along the tube axis for the samples with thicker layers of InGaAs.

To gather further information about the strain not only at the surface of the tube but also at different depths within the tube wall, we have investigated nanostructures consisting of microtubes fabricated by rolling-up InGaAs/AlGaAs/GaAs(QW)/AlGaAs/GaAs multilayers. The GaAs quantum wells (QW) are buried at known depths inside the tube wall. By comparison of the experimental results with calculations of the strain tensor components within an elastic model for stratified media we gained insight into the way the multilayer material deforms while it takes its final shape of a tube. Notice that from Raman analysis it is possible to obtain the hydrostatic and radial strain components without knowing the strain component along the tube axis (ϵ_z). In contrast, some assumption on this last value (due to strain relaxation along the tube axis, for example) is needed to estimate the tangential (ϵ_θ) strain component.

- Raman spectra collected from the microtubes are characterized by strong peaks at ~290 cm^{-1} and ~390 cm^{-1} ascribed to GaAs-like and AlAs-like longitudinal optical (LO) phonon modes, respectively. Both peaks are shifted from the expected bulk values due to the strain stored in the wall of the tube. Raman scattering from the 7 nm thick InGaAs layer becomes detectable in the tube spectrum because this thin strained layer is directly at the tube surface instead of being buried like in the as-grown region.

- Taking into account the penetration depth in InGaAs and GaAs for the 488 nm laser light (20–80 nm) and considering the exponential decay of light intensity inside the tube wall, we estimate that the measured phonon positions come from the volume of material closer to the tube external surface, whereas scattering from deeper layers would give smaller contributions forming an asymmetric shoulder not affecting the peak maxima. In contrast, the $Al_{0.7}Ga_{0.3}As$ alloy has a much smaller absorption coefficient and so we assume that its peak position accounts for the average strain in the whole layer sandwiched between the InGaAs film and the GaAs QW.

- With the assumption that the highly compressed InGaAs layer tends to expand along the tube axis while the tube rolls up, the predictions of the elastic model match very well the experimental data points obtained by Raman analysis for the radial and hydrostatic strain components.

- Comparative measurements in a second sample consisting of a multilayer structure with the same stressor layer (7 nm of InGaAs) but a thicker GaAs/AlGaAs layer on top are compatible with the assumption that no strain relaxation takes place along the tube axis. This experimental observation is consistent with the fact that, at fixed InGaAs thickness, if the tube wall is thick enough the thin strained layer is forced to adjust its lattice parameter to the rest of the structure.

2.3.2 Lab-in-a-tube: on-chip integration of an optical ring resonator for biochemical sensing

Once demonstrated the possibility to fabricate microtubes with bottom up techniques, with easy positioning by lithography and availability of non-invasive optical techniques to characterize them, we developed a prototype of an optofluidic device integrated on a silicon chip.

The microtube has intrinsic capillary properties that make it a perfect candidate as a microfluidic channel and, at the same time, the tube wall acts as a waveguide and a ringlike resonator with characteristic whispering gallery modes (WGMs). The mechanism is similar to other optical ring resonators based on microspheres, microdisks, or micron-sized glass capillaries, but the great advantage is that rolled-up microtubes are easily integrated monolithically on a chip.

In this work, we test the possibility to build a nanostructured refractometer by inserting an aqueous sugar solution into the microtube. The shifts of resonant mode peak positions are analyzed and compared to results from numerical simulations.

The samples were processed from a 20-nm-thick Si layer strained on top of a plastically relaxed Ge sacrificial buffer layer grown on Si(001) substrates at 300 °C by molecular beam epitaxy. Subsequently, a 25-nm-thick SiO_x layer was thermally evaporated onto the strained Si layer. Deep trenches into the Ge buffer were defined, and the layers were released from the substrate by selectively etching the Ge sacrificial layer with H_2O_2. After the formation of rolled-up micro- tubes by the downward bending of the Si layers, the sample was annealed at 850 °C for 30 min to induce the formation of Si nanoclusters in the SiO_x layer, creating an optically active medium inside the tube wall. The resulting structure consists of a tube with 2–3 μm diameter.

The optical response of this rolled-up Si/SiO_x microresonator was studied by microphotoluminescence (μ-PL) spectroscopy, using a frequency-doubled Nd:YVO4 laser with emission wavelength of 532 nm as excitation source and

collecting the emission band (600–1000 nm) associated with the Si nano-clusters embedded within the tube wall. Integrated PL intensity maps were obtained by scanning the laser over the microtube with submicron steps, employing a two-axes microstage activated by dc motors.

In order to test the potential application as an ultra compact blood-glucose sensor, the microtube was filled with an aqueous solution of sugar by placing one open extremity of the tube in contact with a droplet deposited onto the substrate by a glass capillary.

By mapping the PL emission of the fluid-filled microtube it is possible to reveal spatial regions with two distinctive spectral fingerprints: portions of tube filled with air and portions filled with sugar solution. Spectra reveal peaks corresponding to the resonant modes of the resonator and these peak positions can be accurately reproduced by a finite-difference time-domain (FDTD) simulation. For a microtube filled with sugar solution, the evanescent wave penetrates more pronouncedly into the inner part of the tube and the WGMs redshift compared to the air-filled microtube.

- Keeping the simulation parameters fixed we varied the index of refraction of the liquid, extracting a value of sensitivity of ~62 nm/RIU (Refractive Index Unit) comparable with other existing refractometers which have bigger channel cross section. This means that the microtube resonator requires the minimum liquid volume, allowing for analysis of femtoliter fluid droplets.

- Taking into account the experimentally observed linewidth (~6 nm), we estimated a detection limit of ~ 0.05 RIU. By engineering the tube walls there is margin for improvement of the performance of the microtube optical resonator.

CORE RESEARCH ARTICLES

Article n: 16

Authors: A. Bernardi, A. R. Goñi, M. I. Alonso, F. Alsina, H. Scheel, P. O. Vaccaro, and N. Saito

Title: Probing residual strain in In Ga As/Ga As micro-origami tubes by micro-Raman spectroscopy

Journal: Journal of Applied Physics

Doi: 10.1063/1.2183353

Article n: 17

Authors: A. Bernardi, P. D. Lacharmoise, A. R. Goñi, M. I. Alonso, P. O. Vaccaro, and N. Saito

Title: Strain profile of the wall of semiconductor microtubes: A micro-Raman study

Journal: Physica Status Solidi B

Doi: 10.1002/pssb.200672547

Article n: 18

Authors: A. Bernardi, S. Kiravittaya, A. Rastelli, R. Songmuang, D. J. Thurmer, M. Benyoucef, and O. G. Schmidt

Title: On-chip Si / SiO x microtube refractometer

Journal: Applied Physics Letters

Doi: 10.1063/1.2978239

Probing residual strain in InGaAs/GaAs micro-origami tubes by micro-Raman spectroscopy

A. Bernardi,[a] A. R. Goñi,[b] and M. I. Alonso
Institut de Ciència de Materials de Barcelona, CSIC, Esfera UAB, 08193 Bellaterra, Spain

F. Alsina
Departament de Física, Universitat Autònoma de Barcelona, 08193 Bellaterra, Spain

H. Scheel
Institut für Festkörperphysik, Technische Universität Berlin, Hardenbergstrasse 36, 10623 Berlin, Germany

P. O. Vaccaro and N. Saito
Department of Photonics, ATR Wave Engineering Laboratories, 2-2-2 Hikaridai, Keihanna Science City, Kyoto 619-0288, Japan

(Received 5 April 2005; accepted 8 February 2006; published online 24 March 2006)

We have experimentally investigated nanostructures consisting of free-standing microtubes with diameters in the micrometer range fabricated by rolling-up InGaAs/GaAs bilayers grown by molecular-beam epitaxy on a GaAs substrate. The formation of the microtubes is powered by the built-in strain in the InGaAs layer and they develop after releasing the bilayer structure from the substrate by selective etching. Through micro-Raman spectroscopy we were able to detect the residual strain of the microtube, which results in a frequency shift of phonon modes measured on the tube as compared with reference unstrained material. We developed a simple elastic model to describe the measured phonon frequency shifts, from which we estimate the strain status of the microtube. Results demonstrate the power of Raman spectroscopy as a diagnostic tool for engineering of strain-driven self-positioning microelectromechanical systems. © *2006 American Institute of Physics*. [DOI: 10.1063/1.2183353]

I. INTRODUCTION

An emerging class of three dimensional micro- and nanometer-sized objects can be fabricated by strain-driven engineering, a bottom-up approach to obtain objects whose positions and dimensions depend critically on the design and elastic properties of the starting semiconductor multilayer structures. Rolled-up nanotubes, for example, can be obtained from strained heterostructures after releasing the multilayer structure from the substrate by selective etching.[1] The basic idea behind the strain-driven engineering is that strained thin films tend to acquire a different equilibrium shape in order to minimize their elastic energy. Apart from micro- and nanotubes it is also possible to take advantage of the built-in strain in semiconductor epitaxial layers to build up self-standing microhinges bending until reaching an equilibrium position with a controlled radius of curvature.[2] These flexible hinges are the building blocks for a method of fabrication, denominated *micro-origami*, which can be used to prepare a number of smart integrated devices such as micromirrors, microstages,[3,4] and others with a wide range of applications in microelectronics, optoelectronics, and biology.[5,6] Production of future microoptoelectromechanical systems (MOEMSs) in which the built-in strain is expected to change their electronic band structure as well as their optical properties,[7] will certainly require adequate control over the fabrication process by being able to tailor the strain in the device.

In this respect, it is desirable to count on a fast, noninvasive, and spatially resolved characterization technique such as micro-Raman scattering, which allows for the determination of the strain in the ready device and for comparison with modeling results. It is well known that the presence of strain lowers the symmetry of the crystalline semiconductor, such that the optical phonons split and shift in frequency, as compared with the unstrained material. Micro-Raman (μ-Raman) scattering is a particularly suitable method to probe these phonon-frequency shifts with large spatial resolution up to 1 μm, thus, to map the magnitude of strain in micrometer-sized objects, such as self-rolled microtubes (MTs).

In this work we show how μ-Raman spectroscopy can be used as a sensitive diagnostic tool to obtain a postprocessing feedback on strain engineering for further design optimization applied to the case of InGaAs/GaAs microtubes. Starting from an elastic model of the actual microtubes produced by the origami method we derive analytical expressions for the relevant components of the strain tensor in cylindrical coordinates, which are then used to calculate the expected frequency shifts of the optical phonons of the constituent materials. The strain is then mapped out over the device by measuring vibrational spectra with a μ-Raman setup.

II. THEORY

A. Elastic model for a free-standing microtube

The origami method for fabricating micro- and nanotubes is based on the epitaxial growth of a bilayer of differ-

[a]Author to whom correspondence should be addressed; electronic mail: abernardi@icmab.es; URL: http://www.icmab.es/lpo/
[b]Also at ICREA.

[This article is copyrighted as indicated in the article. Reuse of AIP content is subject to the terms at: http://scitation.aip.org/termsconditions. Downloaded to] IP: 158.109.18.157 On: Thu, 08 Oct 2015 12:18:49

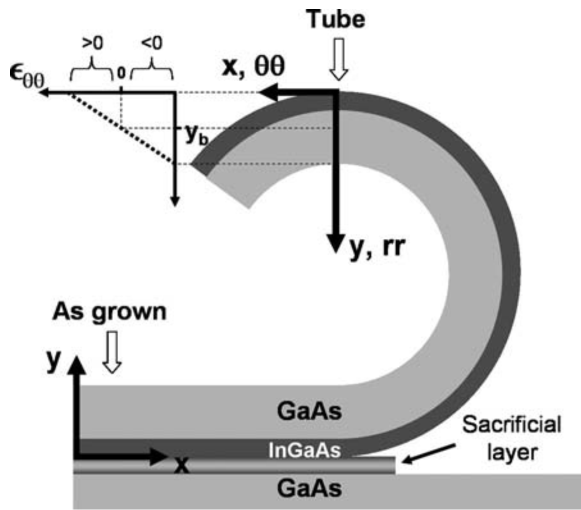

FIG. 1. Schematic representation of the cross section of a microtube fabricated by self-rolling of a strained bilayer. The definition of the coordinate axes and a diagram with the circumferential strain distribution are indicated. The coordinate denoted as y_b corresponds to the position of the zero-strain surface within the tube. The labels "Tube" and "As grown" refer to the regions where the laser beam will be focused to collect Raman spectra.

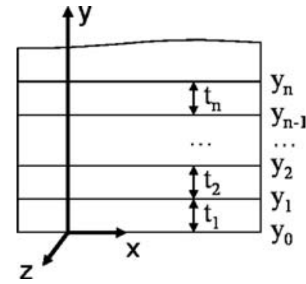

FIG. 2. Generalized multilayer strained structure for microtube or microhinge fabrication.

ent materials with a built-in misfit strain. As the strained film is detached from the substrate, the interatomic forces in the compressed and stretched layers tend to accommodate the strain by changing interatomic distances. These forces in the two layers are oppositely directed and produce a momentum of force that acts to bend the planar double-layer film giving form to a self-rolled microtube (see Fig. 1). Once the equilibrium shape is reached, the material constituting the wall of the tube is characterized by a residual strain. If we consider the circumferential (in plane, $\epsilon_{\Theta\Theta}$) component of strain, the material at the external surface of the tube is tensily strained, as depicted in Fig. 1. Inside the tube wall the distribution of strain changes from tensile ($\epsilon_{\Theta\Theta}>0$) to compressive ($\epsilon_{\Theta\Theta}<0$), crossing a portion of unstrained material represented by a cylinder with radial coordinate y_b, according to the reference frame depicted in Fig. 1.

The diameter can be roughly estimated knowing the overall thickness, the misfit strain, and the thickness ratio of the two layers by using an analytical elastic model proposed by Tsui and Clyne.[8] This is though an approximated formulation which turns to be inadequate for a precise quantitative description of diameter scalability.[9] A much more accurate curvature estimation, which can also be generalized to multilayer structures, has been recently developed.[10] The key point is that here one takes into account the displacement constraint present in all tubes fabricated by micro-origami, namely, that the multilayer strip bends and rolls up into a tube but always keeping one end rigidly attached to the planar part of the as-grown sample, as schematically shown in Fig. 1. This model predicts fairly precisely the radius of curvature of a tube or hinge starting from any strained multilayer consisting of n layers, as depicted in Fig. 2. Each layer has a thickness t_i $(i=1,2,\ldots,n)$ and is characterized by its Young modulus (E_i), Poisson ratio (ν_i), and initial strain (ϵ_i^0). Interfaces between layers are located at the positions defined by the coordinates y_i $(y_0=0$ and $y_i=y_{i-1}+t_i$ for $i=1,\ldots,n)$.

The radius of curvature of a rolled-up microtube is then given by the expression

$$R=\frac{2\sum_{i=1}^{n}[E_i/(1-\nu_i^2)]t_i[y_i^2+y_iy_{i-1}+y_{i-1}^2-3y_b(y_i+y_{i-1}-y_b)]}{3\sum_{i=1}^{n}[E_i/(1-\nu_i^2)]t_i(y_i+y_{i-1}-2y_b)[c-(1+\nu_i)\epsilon_i^0]}, \tag{1}$$

where the parameter c represents the uniform strain component corresponding to the situation after the multilayer has been released from the substrate, and y_b is the location of the surface inside the multilayer, where the bending strain component is zero (see Fig. 1). They are calculated according to

$$c=\frac{\sum_{i=1}^{n}[E_i/(1-\nu_i^2)]t_i(1+\nu_i)\epsilon_i^0}{\sum_{i=1}^{n}[E_i/(1-\nu_i^2)]t_i}, \tag{2}$$

$$y_b=\frac{\sum_{i=1}^{n}[E_i/(1-\nu_i^2)]t_i(y_i+y_{i-1})}{\sum_{i=1}^{n}[E_i/(1-\nu_i^2)]t_i}. \tag{3}$$

Based on this simple elastic model for a rolled-up tube,[10] we were able to derive expressions for the three diagonal components of the strain tensor. The off-diagonal components which vanish for a free-standing closed tube are assumed here to be negligibly small. This seems to be a good approximation, as far as the strain effects on the phonon frequencies are concerned (see below), provided that the ra-

[This article is copyrighted as indicated in the article. Reuse of AIP content is subject to the terms at: http://scitation.aip.org/termsconditions. Downloaded to] IP: 158.109.18.157 On: Thu, 08 Oct 2015 12:18:49

dius of curvature is large compared with the wall thickness of the tube.[11] The resulting strain distribution inside the tube wall is a linear function of the y coordinate (see coordinate axes definition in Fig. 1) as given by

$$\epsilon_{\Theta\Theta} = c + \frac{y - y_b}{R}. \quad (4)$$

The radial component of strain is calculated using Hooke's law and by considering that along the direction of the tube axis z the strain is given by the lattice mismatch

$$\epsilon_{rr} = \frac{1}{E}[\sigma_{rr} - \nu(\sigma_{\Theta\Theta} + \sigma_{zz})] = \frac{\nu}{1-\nu}\left[-\left(c + \frac{y - y_b}{R}\right) - \epsilon^0\right], \quad (5)$$

$$\epsilon_{zz} = \epsilon^0. \quad (6)$$

The sum of the three diagonal components of strain gives the hydrostatic strain status of the material $\epsilon_{\mathrm{hydro}} = (\epsilon_{\Theta\Theta} + \epsilon_{rr} + \epsilon_{zz})$, being $\epsilon_{\mathrm{hydro}}$ positive (negative) for an expansion (compression) of the lattice.

B. Strain-induced phonon frequency shift in a microtube

The residual strain field of a self-rolled microtube affects the frequencies of the optical phonon modes of the crystal lattice, which can be measured by Raman scattering.[12–14] The mode frequencies in the presence of strain can be obtained in a perturbative way by diagonalizing the contribution to the dynamical matrix due to the deformation. The threefold degeneracy of the optical phonons at the Brillouin-zone center of a material with a zinc blende structure is lifted, when it bends into the shape of a tube. For small curvatures, i.e., when the tube radius is many orders of magnitude larger than the wall thickness (as in our case), the three frequencies of the LO-phonon modes can be obtained from the following secular equation:[12,15]

$$\begin{vmatrix} K_{11}\epsilon_{\Theta\Theta} + K_{12}(\epsilon_{rr} + \epsilon_{zz}) - \lambda & 2K_{44}\epsilon_{\Theta r} & 2K_{44}\epsilon_{\Theta z} \\ 2K_{44}\epsilon_{\Theta r} & K_{11}\epsilon_{rr} + K_{12}(\epsilon_{zz} + \epsilon_{\Theta\Theta}) - \lambda & 2K_{44}\epsilon_{rz} \\ 2K_{44}\epsilon_{\Theta z} & 2K_{44}\epsilon_{rz} & K_{11}\epsilon_{zz} + K_{12}(\epsilon_{\Theta\Theta} + \epsilon_{rr}) - \lambda \end{vmatrix} = 0 \quad (7)$$

with

$$\lambda = \omega^2 - \omega_0^2 \approx 2\omega_0 \Delta\omega, \quad (8)$$

where ω_0 is the unstrained phonon frequency. Crossed nondiagonal terms of the secular determinant, in first approximation, can be neglected since for a small curvature the distorted lattice structure can be locally modeled with a tetragonal cell.

Due to the selection rules for backscattering from the (010) surface, only LO phonons with atomic displacements along the radial direction are active in depolarized Raman spectra with incident (scattered) linear polarization parallel (perpendicular) to the tube axis [by fabrication all tubes are oriented along the [001] direction]. From Eq. (7) the eigenvalue for the LO phonon in radial direction is given by

$$\lambda = K_{11}\epsilon_{rr} + K_{12}(\epsilon_{zz} + \epsilon_{\Theta\Theta}). \quad (9)$$

Rearranging Eqs. (7)–(9), and inserting the normalized dimensionless deformation potentials[13,14] $\tilde{K}_{ij} = K_{ij}/\omega^2$, we obtain the following expression for the frequency shift of the corresponding LO mode:

$$\Delta\omega_{\mathrm{LO}} = \frac{\omega_0}{2}[\tilde{K}_{11}\epsilon_{rr} + \tilde{K}_{12}(\epsilon_{zz} + \epsilon_{\Theta\Theta})]. \quad (10)$$

Equation (10) can be rearranged to put in evidence the contribution of the hydrostatic (first term) and biaxial components (second term) of the strain:

$$\Delta\omega_{\mathrm{LO}} = \frac{\omega_0}{6}(\tilde{K}_{11} + 2\tilde{K}_{12})(\epsilon_{\Theta\Theta} + \epsilon_{rr} + \epsilon_{zz}) + \frac{\omega_0}{6}(\tilde{K}_{11} - \tilde{K}_{12}) \times (2\epsilon_{rr} - \epsilon_{\Theta\Theta} + \epsilon_{zz}). \quad (11)$$

By inserting in Eq. (10) the explicit expressions for the strain components from Eqs. (4)–(6) we obtain

$$\Delta\omega_{\mathrm{LO}} = \frac{\omega_0}{2}\left(\frac{\nu - 1}{\nu}\tilde{K}_{12} + \tilde{K}_{11}\right)\epsilon_{rr}. \quad (12)$$

Finally, by rearranging Eq. (12) we obtain the expressions for the radial and hydrostatic strain components at the external surface of the microtube which are directly related to the phonon frequency shift measured by Raman scattering,

$$\epsilon_{rr} = \frac{2}{((\nu - 1/\nu)\tilde{K}_{12} + \tilde{K}_{11})}\frac{\Delta\omega_{\mathrm{LO}}}{\omega_0}, \quad (13)$$

$$\epsilon_{\mathrm{hydro}} = \frac{2\nu - 1}{\nu}\epsilon_{rr}. \quad (14)$$

We point out that the insight about the strain status gained from the experiment refers to the actual volume of material that is contributing to the Raman scattering signal. That means that the estimation of the strain using Eqs. (13) and (14) corresponds to an average value which, in principle, should depend on the penetration depth of light. Nevertheless, for each layer, the InGaAs and the GaAs one, the dominant contribution to the intensity of the Raman spectra comes

[This article is copyrighted as indicated in the article. Reuse of AIP content is subject to the terms at: http://scitation.aip.org/termsconditions. Downloaded to] IP: 158.109.18.157 On: Thu, 08 Oct 2015 12:18:49

TABLE I. Description of sample parameters (thickness of the InGaAs layer and tube radius) and summary of relevant results (phonon frequency shift and hydrostatic and radial strain components).

Sample	t_{InGaAs} (nm)	$\|R^{calc}\|$ (μm)	$\|R^{exp}\|$ (μm)	$\Delta\omega$ (cm^{-1})	ϵ_{rr}	ϵ_{hydro}
A	7	5.9	4.6	2.1	0.3%	−0.5%
B	14	3.9	2.9	−1.2	−0.2%	0.3%
C	28	3.4	2.7	−1.8	−0.3%	0.4%

from the outer shell of material a few nanometer thick, owing to the strong absorption of visible light in the semiconductors. The strain distribution inside the tube wall would lead to a broadening and slight asymmetry of the Raman peaks, but the position of the maximum (which defines the frequency shift) is still being mainly determined by outer layers, from which the average strain is extracted.

III. EXPERIMENT

A multilayered structure was grown by molecular-beam epitaxy (MBE) on a GaAs (010)-oriented substrate. Starting from the substrate, the structure consists of a GaAs buffer layer (200 nm), an $Al_{0.52}Ga_{0.48}As/AlAs$ (×100 0.4/0.4 nm) digital alloy (80 nm), an $In_{0.19}Ga_{0.81}As$ strained layer, and a GaAs top layer (55 nm), as shown schematically in Fig. 1. The structure has been doped with Si for a better quality of the scanning electron micrographs (SEMs). Three structures (samples A, B, and C) were prepared with different thicknesses of the $In_{0.19}Ga_{0.81}As$ layer (7, 14, and 28 nm) but with the remaining parameters unchanged. Microtubes which are characterized by different radii of curvature were fabricated starting from samples A, B, and C by defining narrow trenches along the [001] direction using photolithography and a nonselective etchant, followed by etching of the AlGaAs/AlAs sacrificial layer with diluted HF, according to the experimental procedure developed by Vaccaro *et al.*[2] The radii of the microtubes were measured by SEM, finding good agreement with the predictions of the elastic model [Eq. (1)]. Measured and calculated values of the radii are listed in Table I.

Raman spectra were collected at room temperature using a Jobin-Yvon T6400 μ-Raman spectrometer and with different lines of an Ar^+ laser as excitation source. The size of the laser spot was 2 μm, and the laser power on the sample was about 2 mW. Measurements were performed in backscattering geometry with $y(z,x)\bar{y}$ polarization by focusing the laser beam in different regions of the samples (on the tubes and in the as-grown regions nearby, for example, as indicated in Fig. 1). Laser plasma lines provided precise internal calibration. Different measurements were recorded moving the samples with a translation stage along and/or across a microtube in steps of at least 1 μm.

IV. RESULTS AND DISCUSSION

Measurements collected on the microtubes contain remarkably different spectral features as compared to that observable in the surrounding as-grown regions, where the material remains undetached from the substrate. An example is shown in Fig. 3. The main peaks in all spectra are assigned to longitudinal optical (LO) phonon modes of the different materials constituting the heterostructure, in agreement with the selection rules for backscattering geometry in crossed polarization $y(z,x)\bar{y}$. In the as-grown regions, the main peak at 292 cm^{-1} comes from the top GaAs layer, whereas the modes arising from the buried thin $In_{0.19}Ga_{0.81}As$ layer fall inside the broad feature between 260 and 285 cm^{-1}. For the as-grown regions this broad spectral feature also contains signal from the GaAs-like TO phonons activated by disorder[16] (alloying and doping) as well as a contribution stemming from the lower branch of the coupled LO-phonon-plasmon mode of the doped layers. Clear signal coming from the AlGaAs sacrificial layer is apparent as a peak at ≃400 cm^{-1}. When the laser is focused onto the microtube the outer layer of material is now the strained $In_{0.19}Ga_{0.81}As$ thin film. For this reason an interchange of intensity is observed between peaks corresponding to the LO phonons of InGaAs and GaAs. The Raman scattering from the buried GaAs layer at the inner side of the tube is now recognizable only as a shoulder to the main peak which corresponds to the "GaAs-like" LO phonon of the InGaAs alloy, which exhibits two-mode behavior[16] (see Fig. 3). Of course, the signal from the absent sacrificial layer is not detectable anymore.

The most remarkable feature in the spectra collected from the microtubes is that the peak attributed to the $In_{0.19}Ga_{0.81}As$ LO phonon is shifted from the expected mode frequency for this alloy composition. This shift is obviously due to the residual strain of the bent layer, as given by Eqs. (10)–(12). Microtubes with different radii of curvature are also characterized by a different strain field inside the bilayer constituting the tube wall and consequently they exhibit a

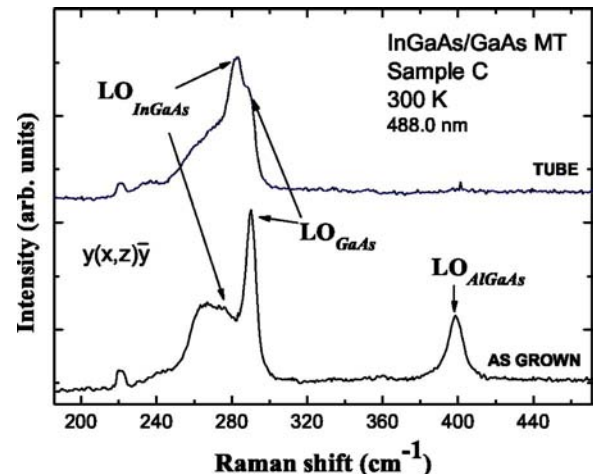

FIG. 3. Representative Raman spectra collected from the tube and from the nearby as-grown region in backscattering geometry at room temperature. Mode assignment is indicated.

[This article is copyrighted as indicated in the article. Reuse of AIP content is subject to the terms at: http://scitation.aip.org/termsconditions. Downloaded to] IP: 158.109.18.157 On: Thu, 08 Oct 2015 12:18:49

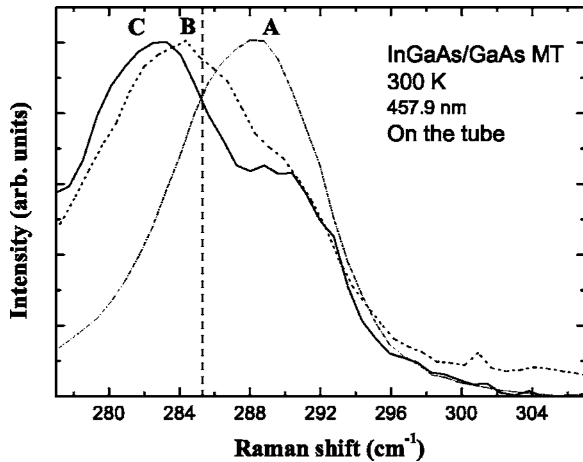

FIG. 4. Raman spectra of microtubes with different radius of curvature (samples A, B, and C). The main peak is assigned to the $In_{0.19}Ga_{0.81}As$ LO phonon, whereas the high-energy shoulder corresponds to the GaAs LO-phonon mode. The vertical dashed line indicates the reference phonon frequency for the unstrained material.

different phonon frequency shift. This small shift from sample to sample can be better appreciated in Fig. 4, where we have plotted one Raman spectrum for each sample but only in the spectral region of the main peak. We notice that the smaller the curvature radius (sample C), the larger is the observed redshift of the InGaAs LO phonon.

To gain a general overview of the strain state of the tubes for each sample, a systematic study has been performed on the three samples by collecting spectra from different positions along the microtubes and from different tubes on the same sample, using also different laser wavelengths. Results are summarized in Fig. 5, where each point corresponds to the average value taken from the different measurements; the dispersion of the data due to either experimental errors or sample inhomogeneity is represented by the error bars. The frequency of the LO phonon displays a clear correlation with the radius of curvature of the microtube. The literature values

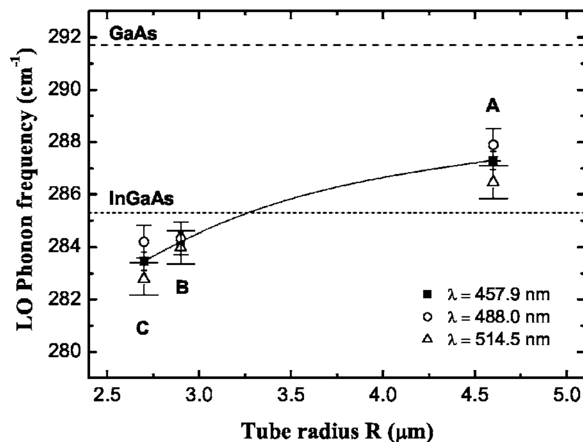

FIG. 5. Frequencies of the Raman peak assigned to the $In_{0.19}Ga_{0.81}As$ LO phonon mode from spectra collected on the three samples (refer to labels A, B, and C) at room temperature and with different laser wavelengths. Data are plotted vs the tube radius measured by SEM and the line connecting points is a guide to the eye. The dashed horizontal lines represent the literature values of the LO phonons of unstrained $In_{0.19}Ga_{0.81}As$ and GaAs (see Ref. 16).

for unstrained $In_{0.19}Ga_{0.81}As$ and GaAs[16] used as reference to evaluate the frequency shifts are indicated in the figure by horizontal dashed lines. Thus, sample A is characterized by a blueshift of the LO InGaAs phonon frequency corresponding to a compressive hydrostatic strain of the lattice, whereas for samples B and C, on the contrary, the redshift gives experimental evidence of tensile strain.

Apart from strain, laser heating could also induce a frequency shift.[17] Therefore, in order to test this effect, we have measured Raman spectra using increasing laser powers on the sample without noticing any change of the position or shape of the peaks. We concluded that heating of the samples in our case can be ruled out as cause of the observed phonon frequency shift. This result, however, is in contrast to what was reported recently for thin InAs/GaAs nanotubes.[18] Possibly the discrepancy is due to the much smaller dimensions of the InAs/GaAs tubes and the better heat conductivity of our samples as a consequence of the Si doping.

In order to check the effect of the penetration depth of the laser light, Raman spectra were collected using three different wavelengths (457.9, 488.0, and 514.5 nm), as illustrated in Fig. 5 with different symbols. In the energy range of ($\simeq$2.5 eV) the absorption coefficient of the InGaAs alloy is $(1-5)\times 10^5$ cm^{-1}, corresponding to a penetration depth of about 80–20 nm. However, within experimental uncertainty there is no evidence of any trend for the shifts or linewidths as a function of laser wavelength. As mentioned above, this is a consequence of the exponential decay of the laser intensity into the material due to absorption. Hence, we assume that the information obtained from the position of the maximum of the LO peak corresponds to an outer shell and is not substantially affected by the strain distribution of the inner layers.

We now proceed with the quantitative analysis of the Raman data of Fig. 5 to evaluate the residual strain of the microtubes. For that purpose we take $\Delta\omega_{LO}$ as the difference between the average value of LO-phonon frequency for each sample and the reference value for the unstrained $In_{0.19}Ga_{0.81}As$ alloy[16] and calculate the strain components using Eqs. (13) and (14). The phonon deformation potentials for the InGaAs alloy have been calculated by interpolation of literature data.[19] The results for the radial and hydrostatic strain components at the outer surface of the different microtubes are shown in Table I.

The values obtained for the hydrostatic and radial strain components are also shown in Fig. 6 as a function of the curvature radius. Even though the error bars for the strain components are large (from propagation of errors we estimate a standard deviation of $\simeq \pm 0.2\%$), our results show a clear correlation between the radius of curvature of the microtube and its residual strain. Moreover, we observe a striking crossover from compressive to tensile strain (hydrostatic or volume component) of the thin InGaAs layer, when the radius decreases from 4.5 to less than 3.0 μm.

Since the elastic model appears to be able to give quite accurate estimates of the radius of curvature of the microtubes (see Table I, where calculated values are compared to the ones measured by SEM), it is also instructive to compare the predictions of the model about the strain status of the

[This article is copyrighted as indicated in the article. Reuse of AIP content is subject to the terms at: http://scitation.aip.org/termsconditions. Downloaded to] IP: 158.109.18.157 On: Thu, 08 Oct 2015 12:18:49

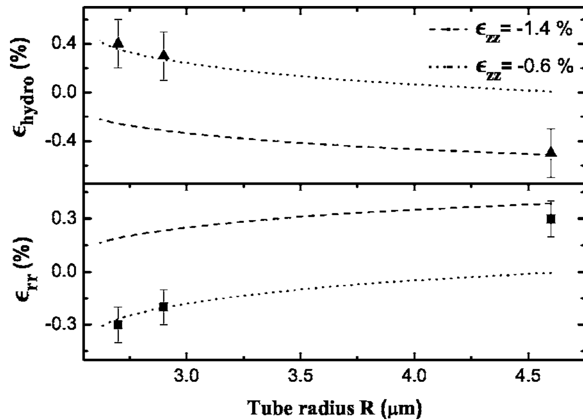

FIG. 6. Residual strain components (hydrostatic and radial) at the surface of the InGaAs layer versus microtube radius. Symbols represent data obtained from the Raman measurement, whereas lines correspond to calculations using the elastic model assuming different strain relaxations along the tube direction z.

material with the numbers obtained by μ-Raman. The results of the calculations are represented by the dashed and dotted curves in Fig. 6. Assuming that along the tube-axis direction the strain equals the lattice mismatch between $In_{0.19}Ga_{0.81}As$ and GaAs [see Eq. (6)], the predictions of the model correspond to the dashed lines of Fig. 6. In this case, the model fits nicely to the experimental data obtained for the bigger microtubes of sample A, the one characterized by having a thickness of the $In_{0.19}Ga_{0.81}As$ layer below the critical value for this composition. On the contrary, for the microtubes of smaller radius of curvature (samples B and C) the elastic model can only reproduce the experimental results (dotted line in Fig. 6) by considering that a strain relaxation from the nominal lattice misfit of $\simeq -0.014$ to a value of $\epsilon_z^{\mathrm{InGaAs}} \simeq -0.006$ has occurred. For thicker InGaAs layers strain is likely to relax either by generation of dislocations during epitaxial growth or simply because the microtube can expand along its length. The boundary condition of having the tube lattice matched to the GaAs substrate along the contact line might not be strong enough to prevent relaxation of the $\epsilon_{zz} < \epsilon_0$ component, when the thickness of the InGaAs stress-driving layer starts to be comparable with half of the tube wall.

V. CONCLUSIONS

In summary, we have demonstrated that micro-Raman spectroscopy is a useful tool to obtain detailed information about the local strain in microsized objects such as self-rolled microtubes. Starting from the accurate description of the elastic properties of micro-origami tubes with proper boundary conditions, a simple model has been developed to correlate the frequency shifts of the phonon modes measured by Raman with the components of the strain tensor. This model can, in principle, be applied to other micro-objects based on strain engineering (for example, microhinges in MOEMS). In the case of semiconductor microtubes, we have obtained experimental evidence that the residual hydrostatic strain in the outer part of the tube wall changes from compressive to tensile with decreasing radius of curvature, in good agreement with our calculations based on an elastic model. Thanks to this observation the fabrication of self-rolled micro- and nanotubes appears to be a smart solution for storing intense strain fields in materials without applying any external stress.

ACKNOWLEDGMENTS

We thank J. Pascual and C. Thomsen for helpful discussions. We acknowledge financial support from the Dirección General de Investigación from Spain under Project No. MAT2003-00738 and an FPI fellowship from the Spanish Ministry of Education and Science. One of the authors (A. B.) is also grateful to the Aldo Gini foundation for supporting the mobility of young researchers.

[1]V. Prinz, V. Seleznev, A. Gutakovsky, A. Chehovskiy, V. Preobrazhenskii, M. Putyato, and T. Gavrilova, Physica E (Amsterdam) **6**, 828 (2000).
[2]P. O. Vaccaro, K. Kubota, and T. Aida, Appl. Phys. Lett. **78**, 2852 (2001).
[3]A. Vorob'ev, P. O. Vaccaro, K. Kubota, S. Saravanan, and T. Aida, J. Appl. Phys. **42**, 4024 (2003).
[4]J. M. Z. Ocampo *et al.*, Microelectron. Eng. **73–74**, 429 (2004).
[5]V. Y. Prinz, Physica E (Amsterdam) **24**, 54 (2004).
[6]A. V. Prinz and V. Y. Prinz, Surf. Sci. **532–535**, 911 (2003).
[7]N. Ohtani, K. Kishimoto, K. Kubota, S. Saravanan, Y. Sato, S. Nashima, P. Vaccaro, T. Aida, and M. Hosoda, Physica E (Amsterdam) **21**, 732 (2004).
[8]Y. C. Tsui and T. W. Clyne, Thin Solid Films **306**, 23 (1997).
[9]C. Deneke, C. Müller, N. Y. Jin-Phillipp, and O. G. Schmidt, Semicond. Sci. Technol. **17**, 1278 (2002).
[10]G. P. Nikishkov, J. Appl. Phys. **94**, 5333 (2003).
[11]C. Thomsen, S. Reich, H. Jantoljak, I. Loa, K. Syassen, M. Burghard, G. S. Duesberg, and S. Roth, Appl. Phys. A: Mater. Sci. Process. **69**, 309 (1999).
[12]F. Cerdeira, C. J. Buchenauer, F. H. Pollak, and M. Cardona, Phys. Rev. B **5**, 580 (1972).
[13]P. Wickboldt, E. Anastassakis, R. Sauer, and M. Cardona, Phys. Rev. B **35**, 1362 (1987).
[14]E. Anastassakis, J. Appl. Phys. **81**, 3046 (1997).
[15]S. Reich, H. Jantoljak, and C. Thomsen, Phys. Rev. B **61**, R13389 (2000).
[16]J. Groenen, R. Carles, G. Landa, C. Guerret-Piecourt, C. Fontaine, and M. Gendry, Phys. Rev. B **58**, 10452 (1998).
[17]P. Puech, G. Landa, R. Carles, and C. Fontaine, J. Appl. Phys. **82**, 4493 (1997).
[18]C. Deneke, N.-Y. Jin-Phillipp, I. Loa, and O. G. Schmidt, Appl. Phys. Lett. **84**, 4475 (2004).
[19]S. Reich, A. R. Goñi, C. Thomsen, F. Heinrichsdorff, A. Krost, and D. Bimberg, Phys. Status Solidi B **215**, 419 (1999).

[This article is copyrighted as indicated in the article. Reuse of AIP content is subject to the terms at: http://scitation.aip.org/termsconditions. Downloaded to] IP: 158.109.18.157 On: Thu, 08 Oct 2015 12:18:49

physica status solidi b

phys. stat. sol. (b) **244**, No. 1, 380–385 (2007) / **DOI** 10.1002/pssb.200672547

Strain profile of the wall of semiconductor microtubes: A micro-Raman study

A. Bernardi[*, 1], **P. D. Lacharmoise**[1], **A. R. Goñi**[**, 1], **M. I. Alonso**[1], **P. O. Vaccaro**[2], and **N. Saito**[2]

[1] Institut de Ciència de Materials de Barcelona-CSIC, Esfera UAB, 08193 Bellaterra, Spain
[2] Department of Photonics, ATR Wave Engineering Laboratories, 2-2-2 Hikaridai, Keihanna Science City, Kyoto 619-0288, Japan

Received 4 July 2006, revised 1 September 2006, accepted 1 September 2006
Published online 8 December 2006

PACS 78.30.Fs, 81.05.Ea, 85.85.+j

We have investigated three-dimensional nanostructures consisting of microtubes fabricated by rolling-up III–V semiconductor multilayers. Through micro-Raman spectroscopy we were able to derive the depth profile of residual strain in the microtubes by monitoring the phonon shifts experienced by different layers buried inside the tube wall. By this procedure we were able to obtain the strain components at different depths moving from the outer to the inner surface of the tube wall. We compared them with the strain distribution calculated by elastic modeling, gaining insight into the strain relaxation processes that produce the final local nanostructure of semiconductor microtubes.

© 2007 WILEY-VCH Verlag GmbH & Co. KGaA, Weinheim

1 Introduction

Nowadays a new class of three-dimensional (3D) micro/nanostructures can be fabricated by strain-driven engineering, a bottom-up approach to obtain complex 3D objects extremely challenging from the point of view of fundamental research as well as potential applications in optoelectronics [1] and nanomechanics [2]. The basic concept is that pseudomorphically strained thin films, once released from the substrate by selective etching, tend to acquire a new equilibrium shape in order to minimize their elastic energy. This technique has been employed to fabricate microtubes in the shape of rolled-up carpets [3, 4] or curved hinges as building blocks for a method, so called “micro-origami” [5], to prepare smart integrated micro-electromechanical systems (MEMS) such as micro-mirrors or micro-stages. We recently demonstrated [6] that, by developing a simple model that correlates the phonon frequency shifts with the components of the strain tensor, Raman spectroscopy is an adequate tool to map out the residual strain in III–V microtubes. In the meantime, a very similar approach was applied to freestanding microtubes obtained from SiGe/Si bilayers [7]. Apart from Raman scattering, insight into the crystalline structure and strain distribution in microtubes was gained from transmission-electron microscopy (TEM) [7], photoluminescence [8, 9] and X-ray microdiffraction [10]. The advantage of Raman scattering is that it is a fast, sensitive and non-destructive diagnostic technique to study this type of nanostructures. In particular, we showed that with our experimental setup there is no need to separate the microtube from the substrate, as it was necessary for other Raman and TEM works [7, 11], thus avoiding alteration of the tube structure of ready devices.

[*] Corresponding author: e-mail: abernardi@icmab.es, Fax: +34 93 580 57 29
[**] ICREA Research Professor

WILEY InterScience® DISCOVER SOMETHING GREAT

© 2007 WILEY-VCH Verlag GmbH & Co. KGaA, Weinheim

In this work, we have investigated nanostructures consisting of microtubes fabricated by rolling-up InGaAs/GaAs/AlGaAs multilayers. By monitoring the strain-induced phonon shifts corresponding to the different layers conforming the tube wall with high spatial resolution we were able to evaluate the residual strain at various depths within the wall of the microtubes. By comparison of the experimental results with calculations of the strain tensor components within an elastic model for stratified media we gained insight into the way the multilayer material deforms while it takes its final shape of a tube.

2 Experimental details

Two types of multilayers were grown by molecular-beam-epitaxy (MBE) on a GaAs substrate. The structure of the first sample contains a GaAs single quantum well, thus in the following, we refer to it as the SQW tube. Starting from the substrate, it consists of a GaAs buffer layer (200 nm), an $Al_{0.52}Ga_{0.48}As$/AlAs digital alloy (80 nm), an $In_{0.19}Ga_{0.81}As$ strained layer (7 nm) and a top layer (32 nm) lattice matched to the substrate containing the GaAs single quantum well. The GaAs SQW is 2.3 nm thick and is sandwiched by two $Al_{0.7}Ga_{0.3}As$ barrier layers with 10 nm thickness. The structure is terminated by a GaAs cap layer (10 nm). A similar sample but containing a double quantum well, thereafter denoted as DQW tube, was also studied for comparison. Here the total thickness of the multilayer on top of the stressor InGaAs layer is larger (42 nm) because the SQW has been replaced by two GaAs quantum wells (4 and 4.6 nm) separated by 3.4 nm of $Al_{0.52}Ga_{0.48}As$.

Starting from such multilayer structures the fabrication process of the microtubes is sketched in Fig. 1. Firstly, narrow trenches are defined onto the sample using photolithography and wet etching. It follows the etching of the AlGaAs/AlAs sacrificial layer with diluted HF, according to the experimental procedure detailed elsewhere [5]. Once detached from the substrate, the compressively strained InGaAs layer tends to expand [Fig. 1(b)] and, as a result, the freestanding multilayer rolls up forming a tube [Fig. 1(c), (d)]. The radii of the microtubes were measured by scanning electron microscopy (SEM) [Fig. 1(d)].

Raman spectra were collected in backscattering geometry at room temperature using a confocal Jobin–Yvon LabRam HR800 μ-Raman spectrometer with the 488 nm line of an Ar^+ laser as excitation source. The size of the laser spot was about 2 μm and the laser power on the sample was 500 μW. Using a submicrometric displacement stage it was possible to accurately focus the laser beam on different regions of the samples, for example on the tubes or on the as-grown regions nearby.

3 Discussion and results

As shown in Fig. 2(a), Raman spectra collected from the microtubes of the SQW sample are characterized by strong peaks at ≈290 cm^{-1} and ≈390 cm^{-1} ascribed to GaAs-like and AlAs-like longitudinal optical (LO) phonon modes, respectively [12]. Despite of being forbidden in backscattering geometry, weaker bands at ≈260 cm^{-1} and ≈360 cm^{-1} due to scattering by transverse optical (TO) phonons are also apparent activated by disorder in the AlGaAs alloys. When moving the laser spot out of the tube and focusing onto the nearby undetached as-grown layer, we appreciate some significant changes affecting both bands. In the GaAs-like spectral range [Fig. 2(b)], for the as-grown region we find a peak at 291.7 cm^{-1} that can be ascribed to unstrained GaAs from its spectral position. In contrast, when collecting spectra

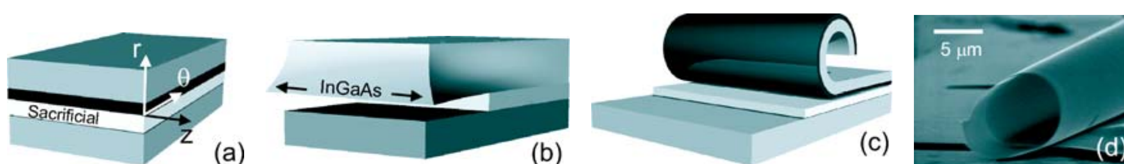

Fig. 1 (online colour at: www.pss-b.com) Sketch of the tube formation process: (a) axis system definition for the starting multilayer structure, (b) strain relaxation along the tube axis after etching of the sacrificial layer, (c) rolling up of the multilayer and (d) SEM image of the resulting microtube.

 © 2007 WILEY-VCH Verlag GmbH & Co. KGaA, Weinheim

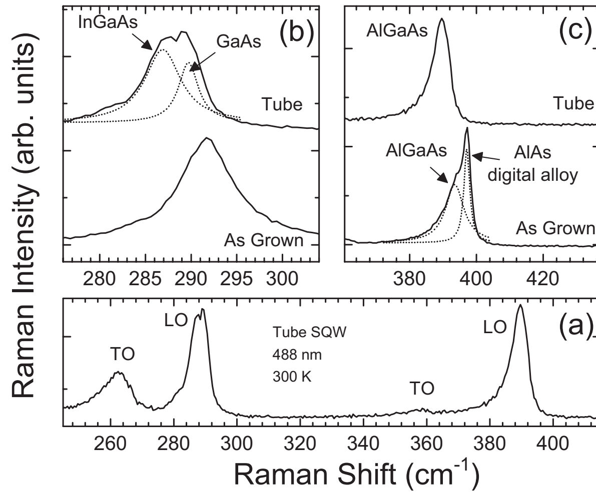

Fig. 2 (a) Representative Raman spectrum of the SQW microtube sample measured on a tube. Comparison between Raman spectra taken on the tube and in the as-grown region in the spectral range (b) of the GaAs and (c) AlAs longitudinal optical (LO) phonons.

from the tube, this band shifts to lower frequencies and it is possible to resolve two peaks, that can be attributed to InGaAs and GaAs LO modes. Both peaks are shifted from the expected bulk values due to the strain stored in the wall of the tube. Raman scattering from the 7 nm thick InGaAs layer becomes detectable in the tube spectrum because this thin strained layer is directly at the tube surface instead of being buried like in the as-grown region.

In the AlAs-like spectral range [Fig. 2(c)], we can identify two phonon modes for the as-grown region which correspond to the LO mode of the AlAs layers of the digital alloy and to the AlAs-like LO of the $Al_{0.7}Ga_{0.3}As$ QW barriers, whereas a single red-shifted peak is present when focusing on the tube. The latter is assigned to strained AlGaAs. Because the digital alloy is etched away under the tube, the fingerprint of pure AlAs disappears. Taking into account the penetration depth in InGaAs and GaAs for the 488 nm laser light (20–80 nm) and considering the exponential decay of light intensity inside the tube wall, we estimate that the measured phonon positions come from the volume of material closer to the tube external surface, whereas scattering from deeper layers would give smaller contributions forming an asymmetric shoulder not affecting the peak maxima. In contrast, the $Al_{0.7}Ga_{0.3}As$ alloy has a much smaller absorption coefficient [12] and so we assume that its peak position accounts for the average strain in the whole layer sandwiched between the InGaAs film and the GaAs QW.

From the frequency shifts of the LO phonon modes ascribed to the three different material layers it is possible to obtain quantitative information on the strain components inside the wall of the microtubes. In addition, we can cross-check the obtained strain status at different depths inside the tube wall and compare them with the strain distributions calculated in the framework of the elastic model. When a strain field is present in a zinc blende crystal lattice, the vibrational states are affected by the variation of the interatomic distances and the resulting frequency shift of the LO phonon mode can be expressed in terms of the components of strain (see Fig. 1(a) for axis definitions) as

$$\Delta\omega_{\mathrm{LO}} = \frac{\omega_0}{2}\left[\tilde{K}_{11}\varepsilon_r + \tilde{K}_{12}(\varepsilon_z + \varepsilon_\Theta)\right], \tag{1}$$

where $\tilde{K}_{ij}$ are the optical phonon deformation potentials and ω_0 is the mode frequency for the unstrained crystal. In the case of a partially freestanding microtube, the relationship between strain components cannot be described by a simple biaxial model (valid only for planar multilayers) and we must account for the fact that the rolled up multilayer strip keeps one of its ends attached to the planar as-grown region (plane-strain boundary condition), as depicted in Fig. 1(c). Then, from the generalized Hooke’s law we obtain that the radial component of strain is

$$\varepsilon_r = \frac{\nu}{1-\nu}\left[-\varepsilon_\Theta - \varepsilon_z\right], \tag{2}$$

© 2007 WILEY-VCH Verlag GmbH & Co. KGaA, Weinheim

where ε_{Θ} is the tangential (in-plane) strain and ε_z is the strain along the tube axis. With this simple model and using Eq. (1) we can obtain ε_r directly from the measured frequency shift [6]. It also follows from Eq. (2) that the hydrostatic strain can be expressed as $\varepsilon_{\text{hydro}} = \varepsilon_{\Theta} + \varepsilon_r + \varepsilon_z = ((2\nu - 1)/\nu)\,\varepsilon_r$. Notice that from Raman analysis it is possible to obtain the hydrostatic and radial strain components without knowing the strain component along the tube axis (ε_z). In contrast, some assumption on this last value (due to strain relaxation along the tube axis, for example) is needed to estimate the tangential strain component (ε_{Θ}).

By means of the elastic model [13] to treat the multilayer structures and given the mechanical properties of the materials, we can calculate the radius of curvature R and the tangential strain component at the tube wall can be expressed as a function of the depth (r) from the tube surface ($r = 0$) according to $\varepsilon_{\Theta}(r) = c + (r - r_b)/R$, where r_b is the location of the surface inside the tube wall, for which the bending strain is zero. We calculate the following radii $R = 2.5\ \mu\text{m}$ and $R = 3.8\ \mu\text{m}$ for the SQW and DQW-microtubes, respectively. Both values are lower than the experimental ones of $R = 3.5\ \mu\text{m}$ (SQW) and $R = 4.5\ \mu\text{m}$ (DQW). This discrepancy is consistent with the fact that 1 to 2 nm of the tube wall had become amorphous due to oxidation in air [10]. Nevertheless, this variation affects only little the calculated strain components and would be hardly appreciable within the experimental resolution.

The procedure we apply for the analysis of the micro-Raman data to derive the strain profile of the tube wall is illustrated for the SQW-tube sample in Fig. 3. Both components ε_r and $\varepsilon_{\text{hydro}}$ are obtained directly from the phonon frequency shifts using Eq. (2). The results are represented by the data points in Fig. 3(a), (b). The abscissa for the data symbols is set depending on the position of each material layer inside the tube wall from which comes the Raman signal, according to the sketch at the top of the figure.

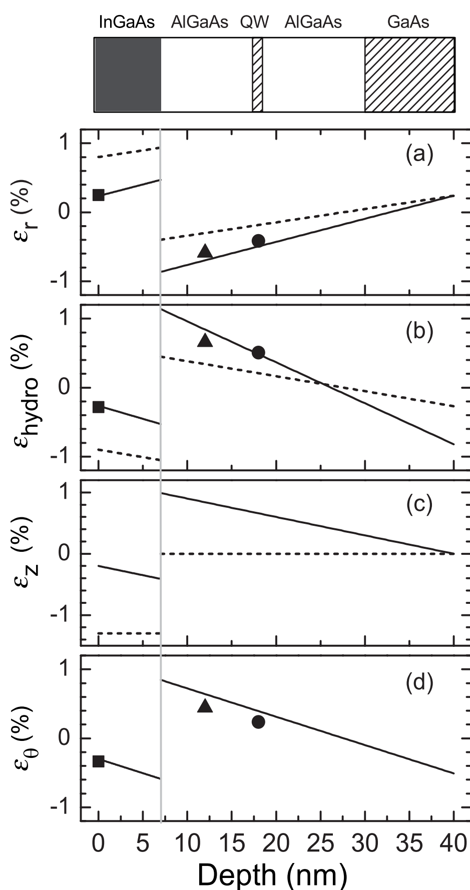

Fig. 3 (a) Radial, (b) hydrostatic, (c) axial and (d) tangential strain components inside the SQW-tube wall. Symbols are experimental data obtained from the frequency shift of the phonon modes of the InGaAs (squares), AlGaAs (triangles) and GaAs (circles) layers. Solid (dashed) lines are calculations accounting (not accounting) for strain relaxation along the tube axis. The sketch at the top represents the structure of the tube wall and the position of the different material layers.

© 2007 WILEY-VCH Verlag GmbH & Co. KGaA, Weinheim

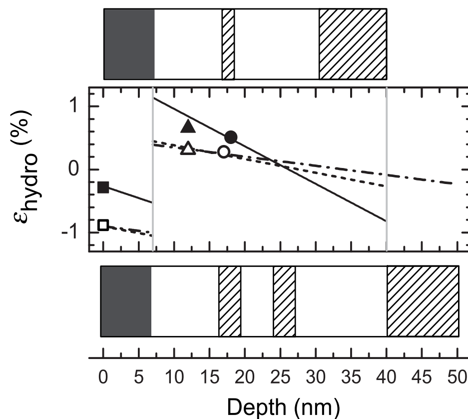

Fig. 4 Hydrostatic strain distribution inside the microtube wall for the SQW (solid symbols) and the DQW tube (open symbols). A sketch of the wall structure for each sample is shown at the top and the bottom of the graph. Symbols represent the strain obtained from Raman for the InGaAs (squares), AlGaAs (triangles) and GaAs (circles) layer. The solid line is a calculation accounting for strain relaxation along z, whereas the dashed (dot-dashed) line is calculated for the SQW (DQW) sample assuming that the InGaAs layer remains fully compressed, i.e. no relaxation takes place.

To compare with the results of the elastic model we have to make an assumption about the strain along the tube axis. Due to the boundary condition given by the constraint that one end of the tube is rigidly attached to the as-grown region one might expect, in first approximation, that ε_z is given by the lattice mismatch of -1.4% in the InGaAs region and zero otherwise (dashed lines in Fig. 3(c)). In this case, the results of the elastic model for the radial and hydrostatic components are represented by the dashed lines in the corresponding figure panels. The agreement with the experimental results is very poor. A more sound assumption is to consider that the highly compressed InGaAs layer tends to expand along the tube axis while the tube rolls up. Elasticity theory predicts for this case that such expansion would vary linearly across the tube wall, i.e. $\varepsilon_z(r)$ is a function of the depth, as depicted by the solid lines in Fig. 3(c). Note that we assumed full strain relaxation ($\varepsilon_z \sim 0$) at both the outer InGaAs and inner GaAs surfaces of the tube wall. Now the predictions of the elastic model (solid lines in Fig. 3(a), (b)) match very well the experimental data points obtained for the radial and hydrostatic strain components. Using the experimental values for the tube radii we can also apply the elastic model to calculate the tangential strain component $\varepsilon_\Theta(r)$ across the tube wall. Experimental as well as theoretical results are plotted in Fig. 3(d) and the agreement is excellent.

To check the reliability of the analysis proposed in this work, we performed comparative measurements in a second sample (DQW tube) consisting of a multilayer structure with the same stressor layer (7 nm of InGaAs) but a thicker GaAs/AlGaAs layer on top. In Fig. 4 we make a direct comparison between the results of the hydrostatic strain component for both microtube samples. Full symbols refer to the SQW structure sketched above the graph, whereas open symbols correspond to the DQW structure sketched at the bottom. Interestingly, for the DQW tube the strain values determined from the phonon shifts are best fitted by the calculation if we assume no relaxation along the tube axis (dot-dashed line for the DQW sample and dashed line for the SQW tube). This apparently contradictory result can be understood considering the mechanical behavior of a freestanding multilayer film. At fixed InGaAs thickness, if the tube wall is thick enough the thin strained layer is forced to adjust its lattice parameter to the rest of the structure. On the contrary, for a thinner tube wall, the energy gained by relaxation of the InGaAs layer can compensate for the tensile strain induced on the other material layers.

In conclusion, we demonstrate the power of micro-Raman spectroscopy as a rapid, sensitive, contactless and nondestructive diagnostic tool for the determination of the residual strain in ready 3D microdevices. By combining Raman measurements and continuum mechanics modelling we gained further insight into the strain relaxation processes occurring in strain-engineered micro-objects and obtained important feedback for the optimization of their design.

Acknowledgements We are grateful to Y. Nishidate and G. P. Nikishkov for fruitful discussions on elastic modelling of curved nanostructures. We acknowledge the Spanish Ministerio de Educación y Ciencia for support through MAT2003-00738. A.B. aknowledges a FPI fellowship and P.D.L. a I3P-CSIC grant.

© 2007 WILEY-VCH Verlag GmbH & Co. KGaA, Weinheim

References

[1] T. Kipp, H. Welsch, C. Strelow, C. Heyn, and D. Heitmann, Phys. Rev. Lett. **96**, 077403 (2006).
[2] D. J. Bell, L. X. Dong, B. J. Nelson, M. Golling, L. Zhang, and D. Grutzmacher, Nano Lett. **6**, 725 (2006).
[3] V. Prinz, V. Seleznev, A. Gutakovsky, A. Chehovskiy, V. Preobrazhenskii, M. Putyato, and T. Gavrilova, Physica E **6**, 828 (2000).
[4] O. G. Schmidt and K. Eberl, Nature **410**, 168 (2001).
[5] P. O. Vaccaro, K. Kubota, and T. Aida, Appl. Phys. Lett. **78**, 2852 (2001).
[6] A. Bernardi, A. R. Goñi, M. I. Alonso, F. Alsina, H. Scheel, P. O. Vaccaro, and N. Saito, J. Appl. Phys. **99**, 063512 (2006).
[7] R. Songmuang, N. Y. Jin-Phillipp, S. Mendach, and O. G. Schmidt, Appl. Phys. Lett. **88**, 021913 (2006).
[8] M. Hosoda, Y. Kishimoto, M. Sato, S. Nashima, K. Kubota, S. Saravanan, P. O. Vaccaro, T. Aida, and N. Ohtani, Appl. Phys. Lett. **83**, 1017 (2003).
[9] H. Paetzelt, V. Gottschalch, J. Bauer, H. Herrnberger, and G. Wagner, phys. stat. sol. (a) **203**, 817 (2006).
[10] B. Krause, C. Mocuta, T. H. Metzger, C. Deneke, and O. G. Schmidt, Phys. Rev. Lett. **96**, 165502 (2006).
[11] C. Deneke, N.-Y. Jin-Phillipp, I. Loa, and O. G. Schmidt, Appl. Phys. Lett. **84**, 4475 (2004).
[12] D. J. Lockwood and Z. R. Wasilewski, Phys. Rev. B **70**, 155202 (2004).
[13] G. P. Nikishkov, J. Appl. Phys. **94**, 5333 (2003).

© 2007 WILEY-VCH Verlag GmbH & Co. KGaA, Weinheim

On-chip Si/SiO_x microtube refractometer

A. Bernardi,[1,2] S. Kiravittaya,[3,a)] A. Rastelli,[1] R. Songmuang,[3,b)] D. J. Thurmer,[1] M. Benyoucef,[1,3] and O. G. Schmidt[1]
[1]*Institute for Integrative Nanosciences, IFW Dresden, Helmholtzstr. 20, D-01069 Dresden, Germany*
[2]*Institut de Ciència de Materials de Barcelona-CSIC, Esfera UAB, 08193 Bellaterra, Spain*
[3]*Max-Planck-Institut für Festkörperforschung, Heisenbergstr. 1, D-70569 Stuttgart, Germany*

(Received 8 July 2008; accepted 15 August 2008; published online 5 September 2008)

The authors fabricate rolled up microtubes consisting of Si/SiO_x on Si substrate and analyze the possibility to use them as a refractometric sensor. An aqueous sugar solution is inserted into the microtube, which leads to a change in refractive index and, as a result, to a detectable spectral shift of the whispering gallery modes. Experimental results can fit well with finite-difference time-domain simulations, which are used to determine the sensitivity of this tube refractometer. The ratio of spectral sensitivity to channel cross-sectional area of the refractometer is particularly striking and allows analysis of fluid volumes in the range of femtoliters. A comparative discussion with other existing refractometer schemes concludes this work. © *2008 American Institute of Physics*. [DOI: 10.1063/1.2978239]

Optofluidics is the combination of optics and fluidics.[1] Over recent years and with ever improving micro- and nanotechnologies, special attention has been paid to optofluidic systems that can be fully integrated on a single chip (optofluidic laboratories-on-a-chip).[2] Such a technology would allow for efficient biosensing[3] as well as single molecule detection[4] with highly parallel data readout. Several different approaches toward integrative optofluidic components have been put forward such as liquid core[5] and planar photonic crystal waveguides.[6] Concerning any realistic applications of integrated optofluidic laboratory-on-chip systems the fabrication process should be cheap and scalable with an intelligent strategy for positioning and integration of the optofluidic components. The potential of monolithically integrating an optofluidic function into mainstream Si technology would furthermore make high-speed Si nanoelectronics, and therefore powerful parallel data processing, available on the very same chip. In this context, we find that "rolled-up nanotech"[7,8] developed over the past years is an excellent candidate for designing cheap and reliable optofluidic systems. The strain gradient stored inside a thin layer[9] can be conveniently exploited to cause spontaneous curling of a thin film into a microtube by a simple single-step underetching procedure. The microtube acts both as a waveguide[10] with light confined in the tube walls, and as a ringlike resonator with optical resonant modes [whispering gallery modes (WGMs)] originating from total internal reflection of light at the curved surface.[11,12] The mechanism is analogous to other optical ring resonators based on microspheres,[13] microdisks,[14] or micron-sized glass capillaries.[15]

In this work, we test the possibility to use a rolled-up Si/SiO_x microtube as a refractometer by inserting an aqueous sugar solution into the microtube. The shifts of resonant mode peak positions are analyzed and compared to results from numerical simulations. The sensitivity of this refractometer is calculated. Our refractometer scheme is also discussed and compared to other proposed approaches.

The microtube resonators tested in this work were processed from a 20-nm-thick Si layer strained on top of a plastically relaxed Ge sacrificial buffer layer grown on Si(001) substrates at 300 °C by molecular beam epitaxy.[9] Subsequently, a 25-nm-thick SiO_x layer was thermally evaporated onto the strained Si layer.[16] Deep trenches into the Ge buffer were defined, and the layers were released from the substrate by selectively etching the Ge sacrificial layer with H_2O_2 (30 vol %) at 90 °C. After the formation of rolled-up microtubes by the downward bending of the Si layers (see Fig. 1), the sample was annealed at 850 °C for 30 min to induce the formation of Si nanoclusters in the SiO_x layer, creating an optically active medium inside the tube wall.[11] The resulting structure consists of a tube with 2–3 μm diameter, made out of one to two Si/SiO_x layer rotations. The tube length is typically of the order of 100 μm–1mm.

The optical response of this rolled-up Si/SiO_x was studied by microphotoluminescence (μ-PL) spectroscopy, using a frequency-doubled $Nd:YVO_4$ laser with emission wavelength of 532 nm as excitation source and collecting the emission band (600–1000 nm) associated with the Si nanoclusters embedded in the tube wall. Integrated PL intensity maps were obtained scanning the laser over the microtube

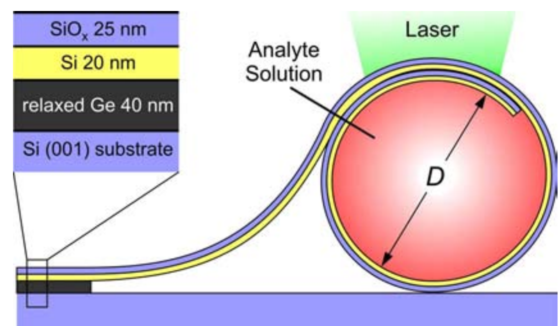

FIG. 1. (Color online) Sketch of the "LCMOR." The Si/SiO_x tube acts both as a natural pipeline and optical sensor, solidly integrated and easily positionable onto a Si chip. A microdroplet of analyte liquid can be absorbed at the tube extremity and optically probed by a laser beam.

a)Electronic mail: s.kiravittaya@fkf.mpg.de.
b)Present address: CEA-LETI, MINATEC, 17 Rue des Martyrs 38054-Grenoble Cedex 9, France.

This article is copyrighted as indicated in the article. Reuse of AIP content is subject to the terms at: http://scitation.aip.org/termsconditions. Downloaded to IP: 158.109.18.157 On: Thu, 08 Oct 2015 12:24:34

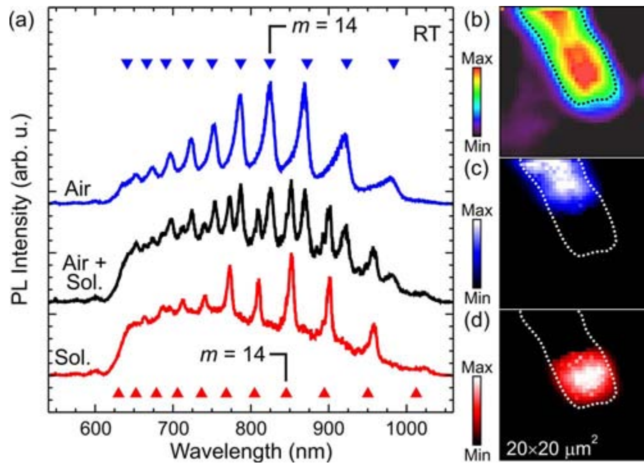

FIG. 2. (Color online) Effect produced by the presence of an aqueous sugar solution inside the tube. In panel (a) spectra with the resonant modes in presence of the solution (red) or of a bubble of air trapped in the tube (blue). The black spectrum refers to a region at the interface between liquid and air. (b) Integrated PL intensity defining the tube position. (c) Spatial regions identified by air mode and (d) solution mode (see text).

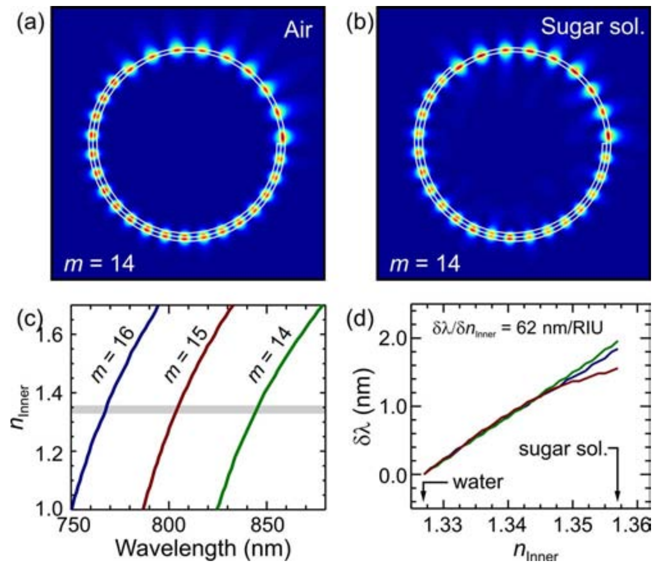

FIG. 3. (Color online) (a) Maps of the electric field intensity for mode $m = 14$ as obtained from FDTD calculation for a tube in air and (b) a tube filled with an aqueous sugar solution. In presence of solution we can notice an enhancement of the electric field spread into the tube core. (c) Calculated resonant mode wavelengths for different azimuthal mode indices as a function of the core index of refraction n_{inner}. (d) Mode shifts as a function of n_{inner}. The microtube refractometer exhibits a sensitivity of $d\lambda/dn_{\text{inner}} \sim 62$ nm/RIU.

with submicron steps, employing a two-axes microstage activated by dc motors.

In order to test the potential application as an ultra compact blood-glucose sensor, the microtube was filled with an aqueous solution of sugar by placing one open extremity of the tube in contact with a droplet deposited onto the substrate by a glass capillary, as sketched in Fig. 1. For test purposes we utilize capillary forces to rapidly incorporate liquid microdroplets into the interior of the microtube.[17,18] However, for optofluidic laboratory-on-chip applications, additional integration processing is needed for pumping liquid into and out of the tube.[18] In order to repeat several cycles of fluid filling and rinsing of the tube, we employed acetone to remove the sugar solution and dried the microstructure before filling it again in the next cycle; the microtubes are stable and robust enough to allow for a reversible multi-use operation of the device.

In Fig. 2 we show how by mapping the PL emission of the fluid-filled microtube it is possible to reveal spatial regions with two distinctive spectral fingerprints. The tube in this experiment has a diameter D of 2 μm. In Fig. 2(a), the selected spectra for different positions on the tube are presented. The integrated PL intensity map (600–1000 nm) is shown in Fig. 2(b). Figures 2(c) and 2(d) show integrated PL intensity maps of the optical modes when air is filled ("air" mode) for $m=14$ (810–840 nm) and when sugar solution is filled ("solution" mode) for $m=14$ (835–865 nm). These plots are performed after substracting the broad background emission.[19]

From the integrated PL intensity map shown in Figs. 2(c) and 2(d), it is possible to reveal spatial regions with two distinctive spectral fingerprints. At some distance from the tube opening [blue spectrum in Fig. 2(a) corresponding to region highlighted in panel (c)] we find the resonances expected for an empty tube, i.e., a bubble of air has been trapped during fluid filling. Close to the open extremity we observe redshifted resonant modes [red spectrum in Fig. 2(a) corresponding to the region highlighted in panel (d)] and we ascribe the spectrum to the presence of the aqueous sugar solution. At the interface between liquid and air we record a spectrum that is a combination of the previous ones [black spectrum in Fig. 2(a)]; this is evidence that the observed mode shift is not caused by any geometrical factors due to structural inhomogeneities of the tube wall,[19] i.e., we illuminate a specific portion of microtube and we collect both air mode and solution mode in a single shot of light.

The peak positions for the experimental resonances of the empty tube can be accurately reproduced by a finite-difference time-domain (FDTD) simulation[11] [see triangular markers in Fig. 2(a) and the associated electric field intensity maps in Fig. 3]. The WGM field profiles with $m=14$ are shown in Figs. 3(a) and 3(b). For a microtube filled with sugar solution [Fig. 3(b)], the evanescent wave penetrates more pronouncedly into the inner part of the tube and the WGMs redshift compared to the air-filled microtube. In order to extract the sensitivity of this rolled-up tube used as a refractometric sensor we varied the index of refraction of the liquid, by keeping all other simulation parameters fixed. The curves in Figs. 3(c) and 3(d) show the result of the calculation and indicate a good sensitivity to changes of the refractive index of the inner core liquid n_{inner} ($d\lambda/dn_{\text{inner}} \sim 62$ nm/RIU, RIU denotes refractive index unit) for a wide range of values. This obtained sensitivity is comparable with other existing refractometers (see Table I below). However, increasing the overlap between the WGM mode field and the analyte by thinning the tube wall thickness or increasing the tube diameter can further improve the value.[21] In addition, from the calculated sensitivity and the experimental observed linewidth (~6.6 nm for the mode $m=14$), a detection limit of ~0.05 RIU is estimated (assuming a wavelength resolution of 1/20th of the linewidth). This is due to the low Q factor of our present refractometer. Improving the Q factor will be subject of future studies.

Table I shows a comparison of various experimentally demonstrated refractometer schemes. All of the items are

This article is copyrighted as indicated in the article. Reuse of AIP content is subject to the terms at: http://scitation.aip.org/termsconditions. Downloaded to IP: 158.109.18.157 On: Thu, 08 Oct 2015 12:24:34

TABLE I. Summary of structure, sensitivity, and channel cross section of experimentally demonstrated refractometers (Refs. 13 and 20–27).

Name[Ref.] / Material System	Schematic	Sensitivity (nm/RIU)	Channel cross section (μm^2)	Monolithic integration on Si chip
Fiber Fabry-Perot interferometer[24] / Fiber		71.2	-	
Surface plasmon resonance based sensor[25]/ Al / TiO_2 / glass fiber and Ag mirror		10000	-	
Microsphere resonator[13]/ Fused silica microsphere and glass fiber		30	-	
Optical microfiber coil resonator[20]/ Glass fiber		40	$7.9\cdot10^5$	
Thin capillaries[22]/ Glass capillaries and fiber		390	69	
Cylindrical shell resonator[26]/ Polymer (polystyrene)		31.5	$1.8\cdot10^4$	
Optical liquid ring resonator[23]/ Glass capillaries and fiber		800	$3.1\cdot10^4$	
Liquid-core optical ring resonator (LCORR)[21]/ Glass fiber	LCORR	16.1	$7.9\cdot10^3$	[a]
Photonic crystal nanolaser[27]/ III-V semiconductor		266	720	
Liquid-core microtube optical resonator (LCMOR)[This work]/ Si/SiO_x		62	3.1	

[a] The authors suggested in their paper another scheme, which is compatible with monolithic integration on a chip.

based on evanescent wave coupling to the fluid. The measured sensitivities (in nm/RIU) and channel cross-sectional areas are also shown in the table. Refractometric sensors, which need to be dipped into liquid, have no channel and hence no channel cross-sectional area—and are therefore hardly compatible with any laboratory-on-a-chip integration technology. From this table, one can clearly see that the liquid core microtube optical resonator (LCMOR) has the smallest channel cross section while the sensitivity is well competitive to other systems. The former property implies that the liquid volume needed for sensing is minimum for any reported LCMOR technology. As a figure of merit, the ratios between spectral sensitivity and channel cross section are calculated based on the data given in Table I. The LCMOR shows the highest value of 20 nm/RIU μm^2, hence allowing for analysis of femtoliter fluid droplets by this technology. Moreover, this type of LCMOR can easily be positioned on a Si chip and monolithically integrated with both fluidic and optical functions.

In conclusion, we have proposed a scheme for using a rolled-up Si/SiO_x microtube as a refractometer and performed an analysis of light emitted from the tube when it is filled with aqueous sugar solution. The experimentally observed peak shifts are fitted well with FDTD simulations and the sensitivity of this rolled-up tube refractometer is extracted. Monolithic on-chip integration of this tube seems straightforward. Therefore, we expect that the combination of existing Si fabrication technologies and our approach will provide useful ways in designing and engineering improved optofludic channel networks on a single chip.

A.B. acknowledges a FPI fellowship. This work was supported by the BMBF (No. 03X5518).

[1] D. Psaltis, S. R. Quake, and C. Yang, Nature (London) **442**, 381 (2006).
[2] C. Monat, P. Domachuk, and B. J. Eggleton, Nat. Photonics **1**, 106 (2007).
[3] D. Erickson, S. Mandal, A. H. J. Yang, and B. Cordovez, Microfluid. Nanofluid. **4**, 33 (2008).
[4] D. Yin, D. W. Deamer, H. Schmidt, J. P. Barber, and A. R. Hawkins, Opt. Lett. **31**, 2136 (2006).
[5] A. Datta, I.-Y. Eom, A. Dhar, P. Kuban, R. Manor, I. Ahmad, S. Gangopadhyay, T. Dallas, M. Holtz, H. Temkin, and P. K. Dasgupta, IEEE Sens. J. **3**, 788 (2003).
[6] D. Erickson, T. Rockwood, T. Emery, A. Scherer, and D. Psaltis, Opt. Lett. **31**, 59 (2006).
[7] O. G. Schmidt and K. Eberl, Nature (London) **410**, 168 (2001).
[8] V. Ya. Prinz, V. A. Seleznev, A. K. Gutakovsky, A. V. Chehovskiy, V. V. Preobrazhenskii, M. A. Putyato, and T. A. Gavrilova, Physica E (Amsterdam) **6**, 828 (2000).
[9] R. Songmuang, Ch. Deneke, and O. G. Schmidt, Appl. Phys. Lett. **89**, 223109 (2006).
[10] S. Mendach, R. Songmuang, S. Kiravittaya, A. Rastelli, M. Benyoucef, and O. G. Schmidt, Appl. Phys. Lett. **88**, 111120 (2006).
[11] R. Songmuang, A. Rastelli, S. Mendach, and O. G. Schmidt, Appl. Phys. Lett. **90**, 091905 (2007).
[12] T. Kipp, H. Welsch, Ch. Strelow, Ch. Heyn, and D. Heitmann, Phys. Rev. Lett. **96**, 077403 (2006).
[13] N. M. Hanumegowda, C. J. Stica, B. C. Patel, I. M. White, and X. Fan, Appl. Phys. Lett. **87**, 201107 (2005).
[14] A. M. Armani and K. J. Vahala, Opt. Lett. **31**, 1896 (2006).
[15] I. M. White, J. Gohring, Y. Sun, G. Yang, S. Lacey, and X. Fan, Appl. Phys. Lett. **91**, 241104 (2007).
[16] R. Songmuang, A. Rastelli, S. Mendach, Ch. Deneke, and O. G. Schmidt, Microelectron. Eng. **84**, 1427 (2007).
[17] Ch. Deneke and O. G. Schmidt, Appl. Phys. Lett. **85**, 2914 (2004).
[18] D. J. Thurmer, Ch. Deneke, Y. Mei, and O. G. Schmidt, Appl. Phys. Lett. **89**, 223507 (2006).
[19] Ch. Strelow, C. M. Schultz, H. Rehberg, H. Welsch, Ch. Heyn, D. Heitmann, and T. Kipp, Phys. Rev. B **76**, 045303 (2007).
[20] F. Xu and G. Brambilla, Appl. Phys. Lett. **92**, 101126 (2008).
[21] I. M. White, H. Zhu, J. D. Suter, N. M. Hanumegowda, H. Oveys, M. Zourob, and X. Fan, IEEE Sens. J. **7**, 28 (2007).
[22] V. Zamora, A. Díez, M. V. Andrés, and B. Gimeno, Opt. Express **15**, 12011 (2007).
[23] M. Sumetsky, R. S. Windeler, Y. Dulashko, and X. Fan, Opt. Express **15**, 14376 (2007).
[24] W. Liang, Y. Huang, Y. Xu, R. K. Lee, and A. Yariv, Appl. Phys. Lett. **86**, 151122 (2005).
[25] Ó. Esteban, N. Díaz-Herrera, M.-C. Navarrete, and A. González-Cano, Appl. Opt. **45**, 7294 (2006).
[26] H.-J. Moon, G.-W. Park, S.-B. Lee, K. An, and J.-H. Lee, Appl. Phys. Lett. **84**, 4547 (2004).
[27] M. Adams, G. A. DeRose, M. Loncar, and A. Scherer, J. Vac. Sci. Technol. B **23**, 3168 (2005).

This article is copyrighted as indicated in the article. Reuse of AIP content is subject to the terms at: http://scitation.aip.org/termsconditions. Downloaded to IP: 158.109.18.157 On: Thu, 08 Oct 2015 12:24:34

3 Conclusions

In summary, we have studied the modified epitaxial growth mechanism of self-assembled Ge QDs in the case of submonolayer carbon predeposition. Our results point to Si interdiffusion combined with the Ge–C repulsive interaction as key factors in understanding the surface dynamics driving the whole process.
We have suggested a two-stage growth process which enables to finely tune the island density just by controlling the deposition temperature of the WL before the growth of the C-induced Ge dots. We found out that the highest dot densities are achieved at higher temperature, in apparent contradiction with previous literature results.

By means of optical characterization techniques we were able to accurately determine the composition and strain of the C-induced QD ensembles, demonstrating that the variation of island density correlates with the amount of interdiffused silicon from the substrate through the WL. The larger the amount of thermally activated silicon intermixing, the better is the carbon stability on the surface. This modifies the diffusion length of the Ge adatoms, leading to different topographies.

We have shown that the self-organized growth of Ge islands on a strained SiGe buffer layer is fundamentally affected by the predeposition of a carbon submonolayer. The relevant parameter which allows for a control of dot topography is the Ge content of the SiGe alloy. The result is a monomodal distribution of Ge rich quantum dots with an areal density which can be adjusted over a wide range 10^9 – 10^{11} cm^{-2} just by changing the Ge composition of the SiGe buffer/wetting layer. The results are explained using a kinetically limited model for the growth mechanism, which accounts for the interplay of chemical interactions among C, Si, and Ge as the determinant factor influencing Ge adatom mobility. This provides us with a powerful growth protocol for improved design of Ge quantum dot nanostructures for device applications.

We studied the strain relaxation mechanism during self-assembling of Ge QDs, comparing the conventional Ge/Si heteroepitaxy with the carbon-engineered growth. RHEED analysis permitted us to recognize three stages of strain relaxation after the growth of a pseudomorphic WL, corresponding to the nucleation of pyramids, the shape transition to domes, and dislocation formation. For the sample obtained after pre-depositing carbon on the silicon substrate, we found instead experimental evidence for a growth mode change from Stranski–Krastanow to Volmer–Weber. An ellipsometric study of the silicon cap layer was helpful to point out the presence of compressive strain associated with the local strain field in the proximity of the carbon-rich patches in between the islands. The topography of the quantum dot ensembles was correlated to the structural properties (i.e., strain and composition) measured by Raman spectroscopy. In particular, the capping process put in evidence two distinct regions of the sample with different local composition and elastic properties. We interpreted our experimental results as signals coming from two families of islands, i.e., smaller intermixed dots that get

highly recompressed and bigger domes only slightly affected by the deposition of the silicon cap layer. Optical techniques combined with RHEED and AFM permit one to obtain an overall insight into the growth mechanism of SK and C-QDs, with the possibility to capture features which hint at the local structure of single quantum dots.

We compared Raman scattering from Ge QDs under hydrostatic pressure when the dots are uncapped versus the situation when they are covered with a Si cap layer. We demonstrated that if the dots are not embedded in the Si matrix, then the measured pressure coefficient tends to the value of bulk Ge. On the contrary, just a very thin 10 nm Si cap layer is sufficient to reduce the coefficient by ~20% to values similar as previously obtained in literature for much thicker cap layers.
We considered the different boundary conditions to explain these two experimental situations, namely, we dealt with the limiting cases of fully relaxed uncapped dots (highest $d\omega/dP$) and fully compressed capped dots (lowest $d\omega/dP$). Nevertheless, the model we propose also holds for a much more complex and generalized scenario, where intermediate situations can be accounted for. Depending on the shape (aspect ratio) and on the size of the dots, the degree of relaxation (φ) is expected to vary considerably and the DAC technique for the determination of pressure coefficients turns out to be a powerful diagnostic tool for studying the mechanisms of relaxation in self-assembled nanostructures.

As an alternative route to Molecular Beam Epitaxy, we showed that combining nanostenciling with PLD provides a flexible approach to grow and pattern crystalline Ge/Si nanostructures. The location of the Ge clusters is entirely controlled by the pattern of the nanostencil, and the density and physical dimensions of the dots can be further adjusted by varying the deposition parameters. The morphological evolution of the structures with coverage follows a modified Stranski-Krastanow growth mode due to the finite size of the WL at each aperture location. Raman spectroscopy indicates that the nanostructures are crystalline Ge and that they follow the crystallographic orientation of the substrate.

We have demonstrated that micro-Raman spectroscopy is a useful tool to obtain detailed information about the local strain in microsized objects such as self-rolled microtubes. Starting from the accurate description of the elastic properties of micro-origami tubes with proper boundary conditions, a simple model has been developed to correlate the frequency shifts of the phonon modes measured by Raman with the components of the strain tensor. This model can, in principle, be applied to other micro-objects based on strain engineering, for example, microhinges in MOEMS. In the case of semiconductor microtubes, we have obtained experimental evidence that the residual hydrostatic strain at the outer part of the tube wall changes from compressive to tensile with decreasing radius of curvature, in good agreement with our calculations based on an elastic model. According to this observation the fabrication of self-rolled micro- and nanotubes appears to be a smart solution for storing intense strain fields in materials without applying any external stress.

We have proposed a scheme for using a rolled-up Si/SiO_x microtube as a refractometer and performed an analysis of light emitted from the tube when it is filled with aqueous sugar solution. The experimentally observed peak shifts are fitted well with FDTD simulations and the sensitivity of this rolled-up tube refractometer is extracted. Monolithic on-chip integration of this tube seems straightforward. Therefore, we expect that the combination of existing Si fabrication technologies and our approach will provide useful ways in designing and engineering improved optofluidic channel networks on a single chip.

4 References

[1] Phil Goldstein. (2015) Fierce Wireless. [Online]. http://www.fiercewireless.com/story/samsung-unveils-new-14-nanometer-chipset-likely-will-be-used-galaxy-s6/2015-02-17

[2] M. I. Alonso et al., *J. Phys. Chem.*, vol. 119, p. 22154–22163, 2015.

[3] V. V. Strelchuk et al., *Semiconductors*, vol. 46, no. 5, 2012.

[4] M. Ya. Valakh et al., *Applied Physics Letters*, vol. 96, p. 141909, 2010.

[5] J.-N. Aqua, I. Berbezier, L. Favre, T. Frisch, and A. Ronda, *Physics Reports*, vol. 522, no. 2, pp. 59-190, 2013.

[6] G. M. Vanacore et al., *Physical Review B*, vol. 82, p. 125456, 2010.

[7] A. Malachias et al., *Physical Review B*, vol. 79, p. 035301, 2009.

[8] Stefan M. Harazim, Wang Xi, Christine K. Schmidt, Samuel Sanchez, and Oliver G. Schmidt, *J. Mater. Chem.*, vol. 22, p. 2878, 2012.

[9] Elliot J. Smith et al., *Nano Lett.*, vol. 11, pp. 4037–4042, 2011.

[10] Stefan M. Harazim, Vladimir A. Bolaños Quiñones, Suwit Kiravittaya, Samuel Sanchez, and Oliver G. Schmidt, *Lab Chip*, vol. 12, pp. 2649–2655, 2012.

[11] Elliot J. Smith et al., *Lab Chip*, vol. 12, pp. 1917–1931, 2012.

[12] Yuze Sun and Xudong Fan, *Anal. Bioanal. Chem.*, vol. 399, pp. 205–211, 2011.

[13] Xudong Fan and Ian M. White, *Nature Photonics*, vol. 5, p. 591, 2011.

[14] Gaoshan Huang et al., *ACSNano*, vol. 6, pp. 3123–3130, 2010.

[15] Wei Qiu and Yi-Lan Kang, *Chin. Sci. Bull.*, vol. 59, no. 23, pp. 2811–2824, 2014.

[16] M. Silambarasan, S. Saravanan, and Deepak R. Nayak, *Materials Letters*, vol. 105, p. 148, 2013.

[17] T. Angelova et al., *Applied Physics Letters*, vol. 100, p. 201904, 2012.

[18] Alexander Milekhin et al., *Phys. Status Solidi C*, vol. 6, no. 9, pp. 2060– 2063, 2009.

[19] E. Bonera et al., *Physical Review B*, vol. 79, p. 075321, 2009.

[20] Raul D Rodriguez et al., *Nanoscale Research Letters*, vol. 7, no. 594, 2012.

[21] Qinglei Guo et al., *AIP Advances*, vol. 5, p. 037115, 2015.

[22] J. S. Reparaz, I. C. Marcus, A. R. Goñi, M. Garriga, and M. I. Alonso, *Journal of Applied Physics*, vol. 112, no. 023512, 2012.

5 Acknowledgements

First of all I would like to thank the members of the group of Nanostructured Optoelectronic Materials, or the so-called Optical Properties Group, when this research was started, in 2004. A decade seems to be like an eternity in nanotechnology: it's a pleasure to observe the evolution towards new exciting research lines, while I was away, busy building another career, out of physics, moving from the mystery of nanoscience towards "bigger things", the wonders of "social thermodynamics". It's nice to be back for a while again and tell the full story from a slightly different perspective.

I am especially grateful to my thesis directors Maria Isabel Alonso and Alejandro Goñi, these two cool physicists who proved that time travelling is in fact … POSSIBLE! They trusted in me and with their support I finally decided to resume the path I left behind in 2008 to cross the finish line, defending my PhD dissertation.

I thank Sebas Reparaz and Paul Lacharmoise, the "Argentinian Mafia" (Goñiometro included, of course!), my fellow labmates but mostly my good friends: we shared so many crazy adventures and deep discussions, spanning from quantum dots, to existentialism and "Fernet con cola". Our PhD felt like being with a family, really.

I dedicate my thesis to a bunch of you, colleagues from ICMAB because I know you have been waiting long for this day to happen! A special GRAZIE goes to Andrea Cavallaro, he was the first contact welcoming me in Barcelona and I am pretty sure that he will always be the last one to leave the party anytime we have a good occasion to gather. Another big GRAZIE goes to Franco Rigato, we began this "scientific journey" together in the laboratories and concert venues of Padova, back in the 90s, and it's nice to still have you around here, as part of my "extended family" in Barcelona.

I am also grateful to all the nice people I had the chance to know during my scientific stays around the world, source of inspiration and very good memories: thanks to Prof. Oliver. G. Schmidt from the Institute for Integrative Nanosciences (Dresden) and Prof. Federico Rosei from the NanoFemtoLAB (Université du Québec) for accepting me as a guest researcher, I was honoured to be part of your teams. Thanks to Fabio, Fulvio, Armando and Alexander, within many others.

Last but not the least, I would like to thank my family, in particular my parents, for always sharing the ideal of believing in education and for the unconditional support along so many years. Thanks to my brother Davide, for inspiring me since the beginning to become a scientist and for being always a fundamental reference in my life. Finally, I want to dedicate this thesis also to the future generations, my nephew Ettore and my niece Rosa, hoping that I can be a good model and a source of inspiration for your professional path and your existence.